University of Otago

Doctoral Thesis

Cognitive Impairment and Conversion to Dementia in Parkinson's Disease: An Imaging Study of Amyloid PET and Diffusion MRI

Author:
Megan Rebecca Stark

Supervisors:
Dr. Tracy R. Melzer (Primary)
Dr. Daniel J. Myall
Prof. Tim J. Anderson
Prof. John C. Dalrymple-Alford
Dr. Steven H. Marsh

A thesis submitted in fulfilment of the requirements for the degree of Doctor of Philosophy

at the

University of Otago
Department of Medicine

June 2020

Abstract

Cognitive Impairment and Conversion to Dementia in Parkinson's Disease: An Imaging Study of Amyloid PET and Diffusion MRI

by Megan Rebecca Stark

Objective

To investigate the association between amyloid deposition or white matter degeneration with cognitive impairment and conversion to dementia in Parkinson's disease (PD).

Background

Cognitive decline and dementia are common in Parkinson's disease, however the pathophysiological basis of cognitive impairment in PD is unresolved. The time-course from diagnosis to development of dementia is highly variable, and imaging biomarkers are urgently needed to assist estimation of long-term cognitive outcomes, and enable targeted therapeutic interventions in early disease. Misfolded beta-amyloid protein aggregates, or amyloid plaques, are a significant pathology in Alzheimer's disease, and may play a part in future cognitive decline in PD. Measures of cerebral blood flow and white matter micro- and macro-structural degeneration may correlate more directly with current cognitive impairment, and may interact with amyloid to affect cognitive decline in PD. This thesis comprehensively investigates these measures in PD and aims to differentiate pathology and age-related effects, using both cross-sectional and longitudinal (three-year) study designs.

Methods

We acquired [18F]-Florbetaben (FBB) amyloid PET, arterial spin labelling perfusion MRI, and structural MRI in 115 patients with Parkinson's disease, recruited from the Movement Disorders clinic at the New Zealand Brain Research Institute. Movement Disorders Society level II criteria were used to classify PD patients as having normal cognition (PDN, n=23), mild-cognitive impairment (PD-MCI, n=76), or dementia (PDD, n=16), at study baseline and over the course of three-year neuropsychological follow-up. The relationship between amyloid deposition and cognitive classification, global cognitive ability, cerebral blood flow, and conversion to dementia during the three-year follow-up was assessed using both Bayesian regression and whole-brain voxel-wise analysis. High angular resolution diffusion imaging (HARDI) MRI was acquired in a wider cohort of 123 PD participants and 37 controls, for the investigation of white matter integrity in PD across the cognitive spectrum (PDN, n=46; PD-MCI, n=66; PDD, n=11). Cross-sectional fixel-based

analysis investigated measures of fibre density, fibre cross-section, and combined fibre-density-cross-section across PD, controls, and PD cognitive subgroups. Clinical measures of global cognitive ability and motor impairment were also assessed for association with these fixel-based metrics.

Results

We observed significantly higher cortical amyloid accumulation in our PDD group relative to other cognitive subgroups, but model comparison indicated this was due to an effect of age. Cortical amyloid was seen to be present in PD at levels comparable to healthy ageing. Longitudinal assessment identified that, while increased cortical and subcortical amyloid was associated with conversion to dementia within three years, this did not represent a clinically relevant effect. There was no evidence of an interactive effect of amyloid with cerebral blood flow to affect cognition. Reduced fibre density in the substantia nigra correlated with disease, however age exhibited the most widespread association with white matter metrics in this cohort.

Conclusions

This thesis investigated the effect of amyloid on cognitive impairment within a large, well-characterised, longitudinal PD cohort, and subsequently challenged existing characterisations of regional amyloid deposition relating to cognitive decline. This work also represents the largest application to-date of fixel-based analysis for the investigation of white matter degeneration across the cognitive spectrum in PD.

Research Outputs and Activities

- Journal Publication: Tracy R. Melzer, Megan R. Stark, Ross J. Keenan, Daniel J. Myall, Michael R. MacAskill, Toni L. Pitcher, Leslie Livingston et al. (2019). Beta amyloid deposition is not associated with cognitive impairment in Parkinson's disease. *Frontiers in Neurology, 10, 391.* doi: 10.3389/fneur.2019.00391
- Poster presentation: Australasian Winter Conference on Brain Research (AWCBR), Queenstown (Sep 2017). Abstract title: *Parkinson's disease: Association between amyloid PET imaging and cognitive status.*
- Oral presentation: UOC Open Day, Christchurch, NZ (Oct 2017). Title: *Parkinson's disease: Cognitive decline, amyloid and the ageing brain.*
- Poster presentation: Human Amyloid Imaging (HAI), Miami, USA (Jan 2018). Abstract Title: *Parkinson's disease: Association between amyloid PET imaging and cognitive status.*
- Attended the BRNZ Early Career Researcher workshop, Auckland (Feb 2018).
- Three-month study period in New Haven, CT, USA, working with Dr. John Seibyl at the Institute for Neurodegenerative Disorders (May - Aug 2018). Generously funded by the The MacGibbon PhD travel fellowship.
- Attended Alzheimer's Association International conference, Chicago USA (Jul 2018).
- Attended the Global burden of Disease Brain Summit, Auckland (Oct 2018).
- Attended the BRNZ Early Career Researcher workshop, Auckland (Mar 2019).
- 3-Minute Thesis Competition: Presented at the BRNZ Conference, Auckland (Mar 2019).
- Attended Computational Anatomy Toolbox (CAT12) workshop, Auckland (Apr 2019).
- Public outreach: Presentation and panel discussion at the Christchurch Brain Awareness Day event, Turanga Library, Christchurch (Aug 2019).
- Poster presentation: The International Congress of Parkinson's disease and Movement Disorders (MDS), Nice, France (Sep 2019). Abstract Title: *Amyloid load and cognitive decline in Parkinson's disease: preliminary longitudinal findings.*
- Attended the BRNZ Early Career Researcher workshop, Dunedin (Feb 2020).

Authorship Attribution Statement

Work presented in Chapter 5 of this thesis has been published in Frontiers of Neurology (Melzer et al., 2019).

Contributing Authors

Megan Stark (MS), Tracy Melzer (TM), Ross Keenan (RK), Daniel J. Myall (DJM), Michael MacAskill (MM), Toni Pitcher (TP), Leslie Livingston (LL), Sophie Grenfell (SG), Kyla-Louise Horne (K-LH), Bob Young (BY), Maddie Pascoe (MP), Mustafa Almuqbel (MA), Jian Wang (JW), Steven Marsh (SM), David H. Miller (DHM), John Dalrymple-Alford (JD-A), Tim Anderson (TA).

Chapter 5 - Beta Amyloid Deposition Is Not Associated With Cognitive Impairment in Parkinson's Disease

MS performed the image processing, statistical analyses and interpretation of results in this chapter, and produced the primary manuscript. TM and DJM contributed to image processing, statistical analyses, results interpretation, and draft manuscript. All authors contributed to acquisition, analysis, or interpretation of data. All authors contributed to manuscript revision, read, and approved the submitted version.

Chapter 6 - Beta Amyloid Deposition and Future Cognitive Outcomes

MS performed the image processing, statistical analyses and interpretation of results in this chapter, with guidance from TM and DJM.

Chapter 7 - Diffusion Imaging of White Matter Degeneration - a Fixel-Based Analysis

MS performed all image processing, statistical analyses and interpretation of results in this chapter. TM and MA acquired the MR image data for this study.

The NZBRI Study of Parkinson's Disease

The larger study of Parkinson's disease at the New Zealand Brain Research institute was conceptualised and designed by TM, DJM, MM, TP, DHM, JD-A, and TA. TM, MM, DHM, RK, DJM, LL, JD-A, and TA obtained funding for the study. RK, LL, DJM, MM, TP, and SM provided administrative, technical, and material support.

Contributing Institutions

New Zealand Brain Research Institute, Christchurch, New Zealand
Department of Medicine, University of Otago, Christchurch, New Zealand
Brain Research New Zealand Rangahau Roro Aotearoa Centre of Research Excellence, Christchurch, New Zealand
Pacific Radiology Group, Christchurch, New Zealand
Department of Neurology, Huashan Hospital, Fudan University, Shanghai, China
Department of Physics and Astronomy, University of Canterbury, Christchurch, New Zealand
Institute of Neurology, University College London, London, United Kingdom
Department of Psychology, University of Canterbury, Christchurch, New Zealand
Department of Neurology, Christchurch Hospital, Christchurch, New Zealand

Acknowledgements

I am incredibly grateful for the exceptional support and encouragement I have received from my supervisors, Dr. Tracy Melzer, Dr. Daniel Myall, Prof. Tim Anderson, Prof. John Dalrymple-Alford, and Dr. Steve Marsh. Thank you all, for your continued guidance and expertise. Tracy and Daniel, thank you for helping me navigate the mine-field that is statistical analysis, and for basically teaching me everything I know about neuroimaging. Tracy, I thank you three times - it was your optimism, endless patience, and sheer breadth of knowledge that got me through.

Thank you to my colleagues and friends at the New Zealand Brain Research Institute. The research we do at NZBRI wouldn't be possible without the team of people putting in the hours. You made the years fly by.

I thank my friends and family for their constant love and support. To my flatmates - you're an absolute credit to the airline. Mum and Dad - I hope this means you can stop worrying now, but that's probably wishful thinking.

Thank you to the University of Otago for generously funding this study through the University of Otago Doctoral Scholarship, and allowing me to pursue study in the USA through the MacGibbon PhD Travel Fellowship.

Lastly, I thank all of the participants for taking part in this study, and continuing to give of their time and energy to further Parkinson's disease research.

Contents

Abstract i

Rsearch Outputs and Acitivities iii

Authorship Attribution Statement iv

Acknowledgements v

List of Figures x

List of Tables xii

Abbreviations xiii

1 *Introduction* 1
- 1.1 Overview . . . 1
- 1.2 Aims of this thesis . . . 2
- 1.3 Hypotheses . . . 3
- 1.4 Thesis structure . . . 3
- 1.5 Ethics Statement . . . 4
- 1.6 Funding . . . 4

2 *Background to Parkinson's Disease* 5
- 2.1 Epidemiology . . . 5
  - 2.1.1 Prevalence and incidence . . . 6
  - 2.1.2 Risk factors . . . 6
- 2.2 Neuropathology and treatment of motor symptoms . . . 9
  - 2.2.1 Nigrostriatal pathway . . . 9
  - 2.2.2 Neurodegeneration, Lewy Bodies and α-synuclein . . . 9
  - 2.2.3 Treatment . . . 10
- 2.3 Non-motor features . . . 11
- 2.4 Diagnosis . . . 13
  - 2.4.1 Diagnosis in this thesis . . . 14
    - 2.4.1.1 Cognitive subgroup classification . . . 14
    - 2.4.1.2 Mild cognitive impairment - a risk factor for PDD . . . 14
- 2.5 Imaging cognitive impairment in PD . . . 15

2.5.1 Amyloid plaques . . . 15
2.5.1.1 Amyloid PET radiotracers . . . 16
2.5.1.2 [18F]-Florbetaben . . . 16
2.5.2 Tau protein and neurofibrillary tangles . . . 18
2.5.3 Cerebral blood flow . . . 19
2.5.3.1 Arterial spin labelling MRI . . . 19
2.5.4 Metabolic changes . . . 20
2.5.5 Diffusion imaging of white matter structure . . . 21
2.5.6 Cortical thickness and grey matter atrophy . . . 22

3 *Imaging Principles of PET and MRI* 23
3.1 Positron Emission Tomography . . . 23
3.1.1 Principles of operation . . . 23
3.1.1.1 PET Detector System . . . 25
3.1.2 True annihilation coincidence detection . . . 26
3.1.3 Attenuation correction . . . 26
3.1.4 Image noise and time-of-flight . . . 28
3.1.5 Image reconstruction . . . 29
3.1.6 Quantification of PET image data . . . 31
3.1.6.1 The Centiloid scale . . . 32
3.2 Magnetic Resonance Imaging . . . 33
3.2.1 T1 and T2 relaxation . . . 34
3.2.2 MRI pulse sequence parameters . . . 36
3.2.3 Spatial localisation . . . 37
3.2.4 Image encoding in k-space . . . 40
3.2.5 Relevant MRI techniques . . . 41
3.2.5.1 Structural T1 weighted MRI . . . 41
3.2.5.2 Proton density weighted MRI . . . 42
3.2.5.3 Arterial Spin Labelling . . . 42
3.2.5.4 Diffusion weighted MRI . . . 44

4 *Pre-Processing and Analysis Methods* 47
4.1 Pre-processing of neuroimaging data . . . 47
4.1.1 Coregistration and normalisation . . . 48
4.1.2 Quantification of PET image data . . . 50
4.2 Statistical analysis in Neuroimaging . . . 51
4.2.1 The general linear model . . . 51
4.2.1.1 Mathematical basis of the GLM . . . 52
4.2.2 Frequentist vs. Bayesian regression analysis . . . 53
4.2.3 Parametric and non-parametric statistical inference . . . 56
4.2.4 Principal Component Analysis . . . 57
4.2.5 Survival analysis . . . 58

5 *Beta Amyloid Deposition Is Not Associated with Cognitive Impairment in Parkinson's Disease* 60
5.1 Author Contributions . . . 60
5.2 Abstract . . . 61

5.3 Introduction . . . 62
5.4 Materials and methods . . . 64
5.4.1 Diagnostic criteria and assessment . . . 65
5.5 Image data acquisition . . . 66
5.5.1 Magnetic Resonance Imaging . . . 66
5.5.2 Positron Emission Tomography . . . 67
5.5.2.1 Classification of FBB images . . . 67
5.6 Image processing . . . 68
5.6.1 Structural MRI . . . 68
5.6.2 Arterial Spin Labelling MRI . . . 69
5.6.3 PET data . . . 69
5.6.4 Centiloid calibration . . . 69
5.6.5 Regions of interest . . . 70
5.7 Statistical analysis . . . 71
5.7.1 ROI analysis . . . 72
5.7.2 Whole-brain voxel-wise analysis . . . 72
5.8 Results . . . 73
5.8.1 Regional amyloid distribution in PD . . . 73
5.8.2 Whole-brain voxel-wise amyloid distribution in PD . . . 75
5.8.3 CBF and grey matter volume sub-analyses . . . 75
5.8.4 Cognitive category and age: model comparison . . . 77
5.9 Discussion . . . 78
5.10 Data Availability . . . 82
5.11 Supplementary material . . . 82

6 *Beta Amyloid Deposition and Future Cognitive Outcomes* 83
6.1 Author Contributions . . . 83
6.2 Introduction . . . 83
6.3 Participants . . . 85
6.3.1 Diagnostic criteria and assessment . . . 86
6.3.2 Longitudinal protocol design . . . 86
6.4 Materials and methods . . . 87
6.4.1 Image Acquisition and Processing . . . 87
6.4.2 Calculation of principal components . . . 88
6.5 Statistical analysis . . . 89
6.5.1 Survival analysis . . . 89
6.5.2 Whole-brain voxel-wise analysis . . . 89
6.5.3 Predictors of conversion to PDD . . . 90
6.6 Results . . . 90
6.6.1 Participant conversion between cognitive subgroups . . . 90
6.6.2 Survival from PDD by clinical amyloid subgroup . . . 92
6.6.3 Predictors of Conversion to Dementia in PD . . . 93
6.6.3.1 Voxel-wise associations with Amyloid and CBF imaging . 93
6.6.3.2 Association with continuous clinical and imaging measures 94
6.6.3.3 APOE-ε4 association with amyloid load . . . 97
6.7 Discussion . . . 98

7 *Diffusion Imaging of White Matter Degeneration - a Fixel-Based Analysis* 103
7.1 Author Contributions . . . 103
7.2 Introduction . . . 103
7.2.1 Diffusion weighted imaging . . . 105
7.2.2 Fixel-based analysis . . . 107
7.3 Materials and methods . . . 109
7.3.1 Participants . . . 109
7.3.2 Image acquisition . . . 109
7.3.3 Image preprocessing . . . 110
7.3.3.1 Initial preprocessing . . . 110
7.3.3.2 Constrained spherical deconvolution . . . 110
7.3.3.3 Study-specific template creation . . . 111
7.3.3.4 Probabilistic fibre tractography . . . 113
7.3.3.5 Fixel and apparent fibre density estimation . . . 114
7.3.4 Fixel-based metrics . . . 115
7.3.4.1 Fibre-bundle cross-section . . . 116
7.3.4.2 Combined fibre density and cross-section . . . 117
7.4 Statistical analysis . . . 117
7.4.1 Connectivity-based fixel enhancement . . . 117
7.4.2 Whole-brain fixel-based analysis . . . 118
7.5 Results . . . 119
7.5.1 Demographics . . . 119
7.5.2 Whole brain FBA . . . 119
7.5.2.1 Fixel density . . . 121
7.5.2.2 Fixel cross-section . . . 125
7.5.2.3 Fixel density and cross-section . . . 126
7.5.3 HARDI + Aβ cohort (within PD only) . . . 129
7.6 Discussion . . . 131

8 *Summary and Conclusions* 137
8.1 Overview . . . 137
8.2 Key Findings . . . 138
8.3 Impact of this research . . . 140
8.4 Important considerations . . . 141
8.5 Future work . . . 144

A Anatomical Atlases 146

B Neuropsychological Battery and Participant Domain Scores 148

References 154

List of Figures

2.1 Florbetaben tracer binding specificity for Aβ plaques. 17

3.1 Flowchart of a PET imaging study. 24
3.2 Types of annihilation coincidences considered in PET imaging 27
3.3 Coincidence photon detection and time-of-flight in PET systems. 29
3.4 Transverse magnetisation decay and the free induction decay envelope. . . 35
3.5 T1 recovery and T2 decay of MR signal. 36
3.6 Spin echo pulse sequence diagram. 37
3.7 Gradient echo pulse sequence diagram. 38
3.8 Quantification of ASL MRI. 43

5.1 FBB PET images of standard uptake value ratio (SUVR), demonstrating a positive and negative scan. 68
5.2 Tissue segmentation and normalisation to standard space in T1-weighted structural MRI pre-processing. 68
5.3 Calibration of FBB SUVR values to the standard centiloid (CL) method. 70
5.4 Calibration of calculated CL values against published values. 71
5.5 Cortical FBB uptake by cognitive group. 75
5.6 Associations between cortical amyloid deposition and global cognitive ability and age. 76
5.7 Whole-brain voxel-wise correlation between amyloid deposition and age. . 77
5.8 Whole-brain voxel-wise correlation between cerebral blood flow (CBF) and amyloid deposition. 77

6.1 Dementia-free survival of FBB PET amyloid positive and negative participants. 92
6.2 Cox proportional hazard model of the effects of age and amyloid positivity on conversion to dementia within three years. 93
6.3 Whole-brain voxel-wise analyses of amyloid deposition associated with conversion to dementia 94
6.4 Whole-brain voxel-wise analyses of cerebral blood flow associated with conversion to dementia 94
6.5 Mean cortical FBB uptake in converters and non-converters to dementia . 95
6.6 Effect sizes of predictors of conversion to dementia - basic predictors. . . . 96
6.7 Effect sizes of predictors of conversion to dementia - cortical SUVR and select ROI. 96
6.8 Effect sizes of predictors of conversion to dementia - principal component 1 (PC1) 97

6.9 Effect sizes of APOE-ε4 status (carrier), in the prediction of subject amyloid load and PC1 loadings. 98

7.1 Estimated tissue volume fractions given by MSMT-CSD and SS3T-CSD. . 111
7.2 Study specific white matter fibre orientation distribution (FOD) template. 112
7.3 Study specific whole brain tractograms, given by the MSMT-CSD method and SS3T-CSD method. 113
7.4 Study specific fixel mask. 114
7.5 The principles of apparent fibre density. 115
7.6 Diagram depicting manifestation of reductions in fibre density, fibre cross-section and fibre-density-cross-section. 116
7.7 Streamline tracts demonstrating reduced FD in PD compared to controls. 122
7.8 Streamline tracts demonstrating reduced FD in PD-MCI compared to controls. 123
7.9 Streamline tracts demonstrating reduced FD in PDD compared to controls. 123
7.10 Streamline tracts demonstrating reduced FD in PD participants, associated with cognitive impairment. 124
7.11 Streamline tracts demonstrating reduced FD in PD participants, associated with motor symptoms. 124
7.12 Streamline tracts demonstrating increased FD in PD participants, associated with age. 124
7.13 Streamline tracts demonstrating reduced FD in PD participants, associated with age. 125
7.14 Streamline tracts demonstrating reduced FC in PD participants, associated with age. 126
7.15 Streamline tracts demonstrating reduced FDC in PD compared to controls. 127
7.16 Streamline tracts demonstrating reduced FDC in PD-MCI compared to controls. 127
7.17 Streamline tracts demonstrating reduced FDC in PDD compared to controls. 127
7.18 Streamline tracts demonstrating reduced FDC in PD participants, associated with age. 128
7.19 Streamline tracts demonstrating reduced FD in PD participants, associated with age and independent of amyloid load. 129
7.20 Streamline tracts demonstrating reduced FC in PD participants, associated with age and independent of amyloid load. 130
7.21 Streamline tracts demonstrating reduced FDC in PD participants, associated with age and independent of amyloid load. 130

A.1 The MNI structural atalas. 146
A.2 The JHU ICBM-DTI-81 White-Matter Labels atlas. 147
A.3 The JHU White-Matter Tractography atlas. 147

B.1 The neuropsychiatric test battery consists of a series of test within each of the five cognitive domains. 149
B.2 All participant neuropsychological cognitive domain scores and demographics at study baseline. 153

List of Tables

2.1 Non-motor features in Parkinson's disease. 12

3.1 Approximate values for T1 and T2 at B_0 =3T and 37°. 36

5.1 Baseline clinical and imaging characteristics of the cross-sectional amyloid cohort by PD cognitive group classification. 74

6.1 Baseline clinical and imaging characteristics of the longitudinal amyloid cohort by conversion to PDD status. 91

7.1 Clinical characteristics of the cross-sectional HARDI cohort by cognitive group classification. 120

7.2 Clinical and imaging characteristics of the cross-sectional HARDI + amyloid PET cohort by cognitive group classification. 120

Abbreviations

PD	Parkinson's Disease
PDN	Parkinson's Disease with Normal cognition
PD-MCI	Parkinson's Disease with Mild Cognitive Impairment
PDD	Parkinson's Disease Dementia
PET	Positron Emission Tomography
MRI	Magnetic Resonance Imaging
Aβ	Amyloid-Beta
FBB	Florbetaben
ASL	Arterial Spin Labelling
CBF	Cerebral Blood Flow
HARDI	High Angular Resolution Diffusion Imaging
SUVR	Standard Uptake Value Ratio
CL	Centiloid
BRM	Bayesian Regression Model
PCA	Principal Component Analysis
LOOIC	Leave-One-Out Information Criterion
FBA	Fixel-Based Analysis
SS3T-CSD	Single-Shell 3-Tissue Constrained Spherical Deconvolution
FOD	Fibre Orientation Distribution
FD	Fibre Density
FC	Fibre Cross-Section
FDC	Fibre-Density-Cross-Section

Chapter 1

Introduction

1.1 Overview

Idiopathic Parkinson's disease (PD) is the second most common neurodegenerative disorder behind Alzheimer's disease (AD). The clinical features of PD are dominated in the early disease stages by motor symptoms of rigidity, postural instability, bradykinesia and resting tremor. In addition to the characteristic motor features of PD, non-motor features are also common. Cognitive impairment and dementia eventuate in over 80% of 20-year survivors (Hely et al., 2008) and are significantly detrimental to patient quality of life, necessitating full-time care in many cases. The path of cognitive decline in PD is highly variable, and biomarkers are urgently needed (1) to characterize brain changes which may underlie cognitive impairment and (2) to act as surrogate outcome measures to assess treatment effectiveness.

The neuropathological basis for PDD is unclear, and may involve aspects of Alzheimer's disease pathology, such as misfolded beta-amyloid and tau proteins. Recent developments using positron emission tomography (PET) now allow in vivo imaging of abnormal beta-amyloid and tau, which were previously detectable only at autopsy or via biopsy. In this thesis, a large sample of PD patients, representative of the full cognitive spectrum, will undergo amyloid PET and MRI imaging. In-depth assessment of misfolded amyloid will contribute to a more complete understanding of dementia in Parkinson's, and may reveal shared neurodegenerative pathways with other diseases, e.g. Alzheimer's.

Many neurological disorders exhibit reduction or disruption of brain connectivity due to pathological changes to the number and density of white matter axons, or fibres. Diffusion weighted MRI allows inference of white matter microstructure based on the movement of water molecules through ordered tissues in the brain. At the voxel level, diffusion signal is complicated by the presence of multiple orientations of fibre bundles. Early modelling of DW signal lacked the directional information to resolve these crossing fibres; however, High Angular Resolution Diffusion Imaging (HARDI) acquisitions enable the estimation of multiple fibre orientations in a single voxel, through the use of many diffusion acquisition directions. In this thesis, HARDI data was obtained in an expanded cohort including both PD and healthy control participants. I focused on changes in white matter micro- and macro-structural integrity in PD, investigated using fixel-based analysis (FBA).

1.2 Aims of this thesis

This thesis aims to comprehensively investigate various imaging techniques in relation to cognitive decline and conversion to dementia in a large, well characterised Parkinson's disease cohort, followed over three years at the New Zealand Brain Research Institute.

Part One of this thesis investigates amyloid PET measures in relation to baseline cognitive assessments and measures of brain health obtained from magnetic resonance imaging (MRI). I will establish if there exists any correlation between cortical levels of misfolded protein accumulation and (i) current cognitive performance, (ii) global grey matter atrophy obtained from T1 structural MRI, and (iii) cerebral blood flow obtained from arterial spin-labeling (ASL) MRI.

Part Two revisits the cross-sectional PET cohort at three years follow-up, to investigate whether amyloid load at baseline is associated with accelerated development of dementia in PD. Cerebral blood flow is also examined for association with conversion to dementia during follow-up.

Finally, Part Three utilises high angular resolution diffusion imaging (HARDI) MRI, obtained in an expanded cohort of both PD and controls, to investigate white matter structural integrity differences in PD that may correlate with current cognition.

1.3 Hypotheses

1. Amyloid deposition may not correlate with current cognition, but may be a predictor of future dementia risk.

2. Patients with higher levels of amyloid will have lower cognitive scores and higher risk for the development of dementia over three years.

3. PD with mild cognitive impairment and dementia will exhibit reduced white matter structural integrity compared with PD with normal cognition and controls.

1.4 Thesis structure

Chapters 2-4 give an overview of Parkinson's disease, methods of imaging cognitive impairment, a technical background to the imaging methods used in this thesis, and a background to pre-processing and analysis in neuroimaging. These chapters are intended to provide a comprehensive overview of necessary concepts.

Chapters 5-7 present the results of each of the arms of this study. Work presented in Chapter 5 was published in Frontiers of Neurology (Melzer et al., 2019). I was co-first author on this publication with Tracy Melzer; the contributions of all listed authors are described in the Authorship Attribution Statement. This paper is presented in stand-alone format in Chapter 5, and thus necessarily repeats some information contained in the backgound chapters. The published supplementary material has been included in the body of the chapter, and two additional sub-analyses investigating grey matter volume and cerebral blood flow have been added. Certain aspects of the methods described in Chapter 5 also apply to future chapters, and are not reproduced. Instances of this will be noted in the body of the chapter.

Chapter 8 summarises the key findings of this thesis, and discusses research impact, important considerations and avenues of future research in the imaging of cognition in PD.

1.5 Ethics Statement

All participants gave written consent, with additional consent from a significant other when appropriate. The study was approved by the regional Ethics Committee of the New Zealand Ministry of Health (No. URB/09/08/037).

1.6 Funding

Research reported in this thesis was supported by the Health Research Council of New Zealand (14/440), a Sir Charles Hercus Early Career Development Fellowship from the Health Research Council of New Zealand (17/039), a Neurological Foundation of New Zealand Philip Wrightson Posdoctoral Fellowship (1327-WF), the Canterbury Medical Research Foundation (15/08), the New Zealand Brain Research Institute, and a University of Otago Research Grant. I was personally supported by the University of Otago Doctoral Scholarship, and the MacGibbon PhD Travel Fellowship.

Chapter 2

Background to Parkinson's Disease

The typical motor features of Parkinson's disease (PD) were first described by James Parkinson in *An essay on the shaking palsy* (Parkinson, 2002), published in 1817. In subsequent years, the essential features of parkinsonism have remained more or less constant, with the description of the disease widening to include both motor and non-motor features. This chapter gives an overview of the disease in terms of epidemiology, disease characteristics, motor and non-motor pathology, diagnosis, treatment, and imaging of cognition in PD.

2.1 Epidemiology

PD is a multi-system neurodegenerative disorder that currently affects around 12,000 individuals in New Zealand. That number is projected to quadruple by 2050 as a result of increasing lifespan (Bach et al., 2011; Myall et al., 2017). PD is a disease of later life, with less than 4% of sufferers developing clinical symptoms before the age of 50, while approximately 5% of the population over 85 develop PD (Alves et al., 2008).

2.1.1 Prevalence and incidence

A New Zealand study utilising pharmaceutical data found a 2013 prevalence of 191 per 100,000 population (95% CI 187-194), and an incidence of 29 per 100,000 person-years (95% CI 29-30)(Myall et al., 2017). Incidence rates were found to remain steady from 2006 to 2013, while prevalence increased between these two time points (6440; 95% CI, 6320-6550] to 8470; 95% CI, 8310-8620]). This indicates that disease duration is increasing, likely as a result of the ageing population.

Most European community-based studies report prevalence rates of around 100-200 per 100,000 inhabitants, although differences in methodology, diagnostic criteria and population age distribution cause this figure to vary considerably between studies (von Campenhausen et al., 2005). There are few studies investigating annual incidence, which ranged from 5 to 346 per 100,000 in the 2005 review by von Campenhausen et al. It is difficult to compare studies across research groups and countries as there is no formal framework for conducting epidemiological studies in PD, although both New Zealand and international estimates indicate a relatively common disease that is increasing as the population ages. Recent recommendations by the International Parkinson and Movement Disorders Society (MDS) for a new PD diagnostic criteria may help improve comparability across future epidemiology studies (Berg et al., 2014).

2.1.2 Risk factors

PD is a predominantly idiopathic disease, with familial forms estimated to account for less than 10% of all clinically diagnosed cases (Alves et al., 2008). As well as genetic risk factors, there are many other suspected risk factors related to gender, ethnicity, diet, environment, occupation, and many more.

Genetic factors

Genetic risk factors have been investigated for many years due to the observation that family members of those with PD are 3 to 4 times more likely to develop the disease than controls (Kurz et al., 2003). There have been at least 18 specific chromosomal loci found to be associated with PD (*PARK1-18*), with 6 of these linked to heritable, monogenic PD (C. Klein & Westenberger, 2012). Of these, autosomal dominant inheritance

has been attributed to mutations in *SNCA* (*PARK1*) and *LRRK2* (*PARK8*), while autosomal recessive inheritance is linked to the genes *Parkin (PARK2), PINK1 (PARK6), DJ-1(PARK7)* and *ATP13A2 (PARK9)*. *PARK1,2,4,6,7* manifest as juvenile or early onset, while *PARK8* appears clinically the same as idiopathic PD.

The apolipoprotein E (*APOE*) gene ε4 allele has been consistently associated with both increased risk and earlier onset of Alzheimer's disease (AD) (Pankratz et al., 2006), mainly by driving formation of β-amyloid pathology (Tachibana et al., 2019). The expression of APOE-ε4 has been associated with the development of dementia in Parkinson's disease (Williams-Gray et al., 2009; Huertas et al., 2017), and deficits in memory and verbal fluency (Nombela et al., 2014; Mata et al., 2014). The mechanistic aspect of APOE-ε4 as a risk factor for PD is largely unclear, however a recent study found that α-synuclein pathology was exacerbated in APOE-ε4 carriers independent of amyloid deposition, which may accelerate cognitive decline in Lewy Body dementias (Zhao et al., 2020).

Gender

Gender has been well investigated as a potential risk factor, although the ratio of incidence in males to females (M:F) appears to vary based on ethnicity. In New Zealand, age-standardised incidence rates are higher in the male population, at a ratio of 1.7:1(Myall et al., 2017). A meta-analysis of 17 incidence studies across various Western and Asian populations found a pooled estimate for age-adjusted M:F ratio of 1.46:1 (95% CI, 1.24-1.72), with overall larger M:F ratios in Western than Asian populations (Taylor et al., 2007). Of 14 Western studies, only two reported a M:F incidence ratio of less than 1:1, while incidence rates in men and women in Asia were almost equal (pooled M:F ratio of 0.95:1 from 3 studies, 95% CI 0.78-1.16). Pooled M:F ratio was significantly higher in those studies with a mean age of onset greater than 70 years (M:F 1.67 in age $\geq$ 70 and 1.23 in age <70), suggesting that the ratio increases with age of onset. The reason for this remains unclear, although the possible protective effect of oestrogen or hormonal changes in post-menopausal women may be an avenue of investigation.

Tobacco smoking

Cigarette smoking has been investigated as potentially protective against the development of PD (de Lau & Breteler, 2006). Most studies have been of case-control design, although these results have been confirmed by larger prospective cohort studies (Hernan et al.,

2002). A large meta-analysis (Li et al., 2015) obtained a pooled relative risk (RR) of PD of 0.59 (95% CI, 0.56-0.62) for ever smokers compared with never smokers, from 61 case-control and 8 cohort studies. Consistent findings of a protective effect across many studies argue against bias from selective mortality of smokers, poor methodology or broad eligibility criteria (de Lau & Breteler, 2006). It is now generally accepted that smoking confers some protective effect against developing PD, although the mechanism that may achieve this is poorly understood. Current theories generally centre around nicotine (Hernan et al., 2002) as a possible dopamine stimulant, antioxidant, or inhibitor of monoamine oxidase B (MAOB), an enzyme that damages neurons through oxidative stress (Jenner & Olanow, 1996). Nicotine and derivatives such as cotinine may be useful in therapeutic treatment of levodopa-induced dyskinesias, and may slow down further neurodegeneration by inhibiting fibrillation of α-synuclein and β-amyloid (Barreto et al., 2014).

Occupational exposures

Occupational and environmental exposures to toxic substances, such as herbicides and pesticides, may be related to increased risk of PD. It is thought that such toxins cause neuronal degeneration by inhibition of complex 1 (reduced nicotinamide adenine dinucleotide [NADH] coenzyme Q 1 reductase) in the mitochondrial energy cycle (Chaudhuri et al., 2011). Intravenous injection of the drug 1-methyl-4-phenyl-1,2,3,6-tetrahydropyridine (MPTP) was found in 1983 to cause parkinsonian symptoms through complex 1 inhibition, selectively damaging dopaminergic cells in the substantia nigra pars compacta (SNc) (de Lau & Breteler, 2006). Similarly, the pesticide rotenone and herbicide paraquat are complex 1 inhibitors and have been shown to induce dopamine depletion in animal studies (Betarbet et al., 2000), and pesticides have been observed to confer increased risk of PD in long time plantation workers (Petrovitch et al., 2002). Additionally, inhalation of heavy metals has been suggested as a risk factor; exposure to welding fumes containing manganese has been implicated in a few rare cases of parkinsonism (Chaudhuri et al., 2011), however epidemiological studies have failed to reveal any significant risk associated with welding (Jankovic, 2005).

2.2 Neuropathology and treatment of motor symptoms

PD is a multi-system disorder, however it is typically characterised by the presence of particular forms of motor dysfunction. These include but are not limited to bradykinesia, postural instability, rigidity and resting tremor (Docherty & Burn, 2010), and collectively comprise the 'Parkinsonian' clinical syndrome. Parkinsonism may present in a number of different neurodegenerative diseases, such as dementia with Lewy Bodies (DLB), progressive supranuclear palsy (PSP), multiple system atrophy (MSA), and many more, thus complicating diagnosis of PD from the clinical picture. A definitive diagnosis of PD is therefore performed at autopsy, where PD is characteristically accompanied by degeneration or loss of dopaminergic neurons in the ventral region of the pars compacta, located in the substantia nigra (Dickson, 2012). The primary motor symptoms of PD are attributed to this cell death and reduced production of dopamine in the nigrostriatal pathway.

2.2.1 Nigrostriatal pathway

The nigrostriatal pathway is a dopaminergic pathway that connects the substantia nigra pars compacta (SNc) to the dorsal striatum. The dorsal striatum controls movement through the expression of D1 and D2 dopamine receptors, that mediate the direct and indirect pathways, respectively, to the basal ganglia output nuclei (Niccolini et al., 2014). The direct pathway is responsible for facilitation of conscious movement, while the indirect pathway inhibits unwanted movement. The loss of dopaminergic neurons in the SNc results in a decrease in the excitatory function of the D1 receptors in the direct pathway, and an increase in the inhibitory function of the D2 receptors in the indirect pathway. The result is excess activation of the output nuclei, which manifests as the characteristic features of parkinsonism, namely bradykinesia and rigidity.

2.2.2 Neurodegeneration, Lewy Bodies and α-synuclein

While the consequences of dopaminergic neurodegeneration in the SNc are clear, the mechanism by which this occurs in PD is somewhat less so. Neuronal injury may result from a variety of pathological insults including oxidative stress, neuroinflammation, or dysfunction of protein degradation (Segura-Aguilar et al., 2014). Widely-held theories attribute SNc dopaminergic neuronal loss to mitochondrial dysfunction, or to the presence

of Lewy body pathology, commonly observed in the SNc alongside dopaminergic death in PD (J., 2018). PD is one of two dementia syndromes, the other being DLB, that present with pathological inclusions of Lewy bodies containing aggregated α-Synuclein (α-Syn) protein (Mor & Ischiropoulos, 2018). α-Syn is an abundant, inherently disordered presynaptic protein, existing in a number of conformations that may interact to cause neuronal damage in different ways. For example, early stages of aggregation involving oligomeric forms of α-Syn may influence neuronal damage by disruption of membranes, mitochondrial depolarization, cytoskeleton changes, impairment of protein clearance pathways, and enhanced oxidative stress (H. L. Roberts & Brown, 2015). There is also increasing evidence of a synergistic effect of α-Syn and Alzheimer pathology on cognitive decline, wherein the presence of both misfolded beta-amyloid and Lewy bodies at autopsy was correlated with more rapid decline and shorter survival times compared to AD without lewy-bodies (Marsh & Blurton-Jones, 2012). Work is ongoing to develop methods for imaging α-Syn *in vivo*, such that anti-α-Syn interventions may be targeted to those at high risk of developing Lewy Body dementias (Mathis et al., 2017), in order to slow or stop progression. While this work continues, treatment of the motor symptoms of PD commonly focuses on dopamine replacement therapy.

2.2.3 Treatment

Around 80% of PD patients experience significant initial improvement of motor symptoms with dopamine therapies such as levodopa, particularly rigidity and bradykinesia (Macphee & Stewart, 2012). However, as the disease progresses the brain loses the ability to store dopamine, and relief of motor symptoms with dopaminergic drug treatments becomes increasingly short-term. Patients often experience fluctuations in motor control at random times within a dosage interval, known as the 'on-off' phenomenon. Increasing dose to manage motor symptoms inevitably decreases the treatment window until the amount of levodopa required to give smooth motor control also triggers dyskinesia, as well as other side-effects such as hallucinations, psychosis, dopamine dysregulation syndrome (affecting impulse-control), and skin reactions (Chaudhuri et al., 2011). Combining or replacing levodopa with other drug therapies in early disease has been shown to decrease late motor fluctuations, and is still an area of enquiry. The individuals within our study were not required to be on or off their parkinsonian medication at the time of scanning.

2.3 Non-motor features

With careful dose management in early disease, control of motor symptoms and treatment-associated side-effects causes the burden of other PD related non-motor symptoms to become increasingly evident. The recognition of these non-motor symptoms has led to the expansion of the definition of PD as a multi-system disorder, involving not just the dopaminergic system but also the noradrenergic, serotonergic, and cholinergic systems (Grinberg et al., 2010).

PD is known to present with a large number of non-motor symptoms (NMS), which greatly impact the quality of life of individuals and often lead to full-time or institutional care. Some of these symptoms are directly disease-related and some may arise as a side-effect of treatment. The range of NMS in PD include olfactory loss, autonomic disturbances (gastrointestinal, urogenital, cardiovascular, respiratory), sleep disturbances, sensory and visual dysfunctions, and a range of neuropsychiatric disorders (K. A. Jellinger, 2015) (see table 2.1). The wide range of NMS in PD make it difficult to evaluate the total disease burden and prevalence of NMS in PD as a group. Many studies focus on examining the prevalence of specific NMS, such as depression (van der Hoek et al., 2011). Some holistic studies involving large national and international cohorts have been conducted that employ a self-completed non-motor questionnaire, notably the PRIAMO study (Barone et al., 2009) and the NMSquest study (Chaudhuri et al., 2006).

The PRIAMO study evaluated 1,072 patients diagnosed with Parkinson's disease, and found that 98.6% of participants reported at least one NMS (from 12 domains) with an average of 7.8 NMS per participant. Most patients included in this study were in the early PD stages. The NMSquest study of 123 PD and 96 age-matched controls reported an average of 10-12 NMS per patient, increasing in number with disease duration and severity. They also found that NMS were highly prevalent in PD patients compared with controls, but were unreported in over 50% of clinical consultations. The focus is now shifting to address NMS in PD and their impact on quality of life. Of particular importance is the impact of changing cognition and dementia on daily living (Kulisevsky et al., 2013). Dementia is present in over 80% of 20-year PD survivors and is known to have a major effect on quality of life, with greatly varying time from PD diagnosis to dementia onset (Anderson, 2013). Patients with worsening cognition in the category of PD with mild cognitive impairment (PD-MCI) are considered to have high risk of

Non-motor domain	Symptom
Olfactory	Hyposmia/smell loss
Circadian rhythm	REM sleep behaviour disorder
	Insomnia
	Drowsiness
	Restless leg syndrome
Gastrointestinal	Dysphagia
	Constipation
	Swallowing difficulties
	Hypersalivation
Genitourinary	Urgency
	Nocturia
	Increased frequency
	Impotence
Cardiovascular	Orthostatic hypotension
	Syncope
Skin	Seborrhoea
	Hypo/hyperhidrosis
Respiratory	Dyspnea
	Stridor
Sensory	Pain
	Abnormal sensations
Visual	Diplopia
	Blurred vision
	Reading difficulties
	Dry eyes
Neurospychiatric	Anxiety
	Depression
	Behavioral disorder
	Dysexecutive disorder
	Visuospatial deficit
	Psychosis
	Apathy, aggression
	Disinhibition
	Hallucinations
	Cognitive impairment (dementia)
Others	Light-headedness
	Fatigue
	Micrographia
	Deafness

Table 2.1: Non-motor features in Parkinson's disease (K. A. Jellinger, 2015)

conversion to PDD (Litvan et al., 2012; Wood et al., 2016), however dementia onset is still variable within this group. It is possible that those at greater risk of conversion within the PD-MCI group may display certain pathological differences, such as vascular changes or protein aggregation.

2.4 Diagnosis

There are currently no specific tests for the diagnosis of PD, and probable diagnosis remains clinical. Initial diagnosis is primarily made based on the patient's history, clinical symptoms, and a neurological and physical examination to exclude other parkinsonian disorders. Determining the appropriate diagnosis is complicated by disease co-morbidity and the difficulty in separating causes of parkinsonism that share symptomatology and structural abnormalities.

As previously mentioned, parkinsonian features are often present in a variety of neurodegenerative diseases (Chaudhuri et al., 2011). In particular, Parkinson's disease dementia (PDD) is often confused with DLB due to the similarities in clinical, morphological and pathological features. In the past, DLB has been diagnosed preferentially over PDD if the patient presented with significant cognitive impairment within 1 year of developing parkinsonian symptoms.

In response to significant advances to our understanding of PD (Berg et al., 2014), the International Parkinson and Movement Disorder Society (MDS) recently presented revised clinical diagnostic criteria for Parkinson's disease (Postuma et al., 2015). The MDS-PD diagnostic criteria retains motor parkinsonism as the core feature of the disease, with diagnosis defined at two levels of certainty based on absolute exclusion criteria that argue against a diagnosis of PD, and supportive criteria that support PD diagnosis. The MDS-PD criteria are intended for use in clinical research, but may also be used to aid clinicians and improve reproducibility between centers.

The MDS-PD criteria recommends diagnosis through a two step process:

1. Patient parkinsonism is defined as bradykinesia in combination with either rest tremor, rigidity or both;
2. The MDS-PD criteria are then applied to establish if the patient's symptoms may be attributed to PD.

Researchers may apply the criteria to either maximise specificity at the expense of sensitivity (clinically established PD), or balance specificity and sensitivity (probable PD), depending on the study requirements.

The new MDS-PD criteria removes dementia as an exclusion criteria, instead offering the option to qualify the patient as 'PD (DLB subtype)'. The aim is to clarify the features that fall under the PD umbrella and simplify diagnosis when a patient presents with dementia within one year of meeting the clinical criteria for PD (Berg et al., 2014).

2.4.1 Diagnosis in this thesis

The ongoing longitudinal study reported in this thesis commenced prior to the establishment of the new MDS-PD criteria. In this work, PD was diagnosed using the UK PD Society Brain Bank criteria (UKPDSBB) for idiopathic PD (Hughes et al., 1992). Under this criteria, patients fitting PD (DLB subtype) were excluded from participation in the study.

2.4.1.1 Cognitive subgroup classification

Following inclusion in the study, all participants are further classified by cognitive status using the MDS Task Force Level II criteria (Wood et al., 2016) (Litvan et al., 2012). This criteria examines five cognitive domains (executive function; attention, working memory and processing speed; learning and memory; visuospatial/visuoperceptual function; and language) in order to diagnose normal cognitive function, mild cognitive impairment, or dementia in PD (see Chapter 5, section 5.4.1 for methodology). The tests included within each domain can be found in table B.1; the cognitive domain scores and global cognitive scores for each participant at baseline can be found in table B.2.

2.4.1.2 Mild cognitive impairment - a risk factor for PDD

Mild cognitive impairment in PD (PD-MCI) is considered to confer higher risk of conversion to PDD, with patients fulfilling the MDS Level II criteria for PD-MCI having a 50% likelihood of developing dementia within four years (Wood et al., 2016). However the time of dementia onset is also variable within this group, indicating that some individuals may have a natural preservation of cognition. Ideally, all PD-MCI would be offered the opportunity for inclusion in trials for preventative therapies, however this is obviously impractical at early trial stages, and inclusion of those with preserved cognition may mask trial results. The goal thus becomes the elucidation of any core neuropathological features

driving conversion to PDD, that may be preserved in those PD-MCI subjects exhibiting sustained cognitive status. This thesis is but one part of a wider HRC funded study with the New Zealand Brain Research Institute (NZBRI) that aims to identify genetic, clinical and imaging biomarkers to this effect (Anderson, 2013).

2.5 Imaging cognitive impairment in PD

One of the most significant non-motor symptoms that occur in PD is that of cognitive impairment and dementia. Elucidating the cause of cognitive decline in PD has driven a large amount of research, and has led to developments in the way we categorise and diagnose PD. Imaging has a significant role in evaluating pathological changes, enabling quantification of such measures as protein deposition, cerebral metabolic rate, blood flow, cerebral atrophy, white matter structural integrity and many others. Links drawn between these measures and changes in cognition may play a vital part in future classification and staging of disease, or identification of high risk individuals for therapeutic intervention.

2.5.1 Amyloid plaques

The aggregation of misfolded β-amyloid (Aβ) proteins into plaques within the brain is a diagnostic hallmark of Alzheimer's disease (AD). Aβ accumulation has been implicated particularly in early AD as a potential precursor to neuronal damage and cortical atrophy (Nordberg, 2004), and may continue to accumulate as subjects move into the disease stage, developing memory loss, cerebral atrophy and dementia (Villain, 2012). Recent work has shown that amyloid deposition may contribute to the neuropathology underlying PD-MCI and PDD (Petrou et al., 2015). However, the causal role of amyloid in cognitive impairment is somewhat contested, as Aβ has been found to be present in 30% of cognitively normal individuals, associated with normal ageing (C. Rowe et al., 2010). This thesis will investigate the potential link of Aβ deposition with cognition in PD over a three year longitudinal study at NZBRI, which may provide another indication of dementia risk in PD.

2.5.1.1 Amyloid PET radiotracers

Historically, the radiopharmaceutical of choice for imaging amyloid deposition has been [^{11}C]-Pittsburgh Compound B (PiB) (Klunk et al., 2004). For most practical applications, imaging Aβ plaques using PiB PET is unfeasible due to the short half life of carbon-11 ($\sim$ 20 minutes), necessitating an in-house cyclotron for tracer production. Longer-lived fluorine-18 labeled radiotracers (half-life $\sim$ 110 minutes) have been developed that achieve comparable levels of binding to Aβ plaques, and may be produced commercially off-site and delivered to the PET-scanning facility. There have been three such tracers labelled with fluorine-18 approved by the US Food and Drug Administration (FDA) for imaging Aβ plaques: florbetapir, flutemetamol and florbetaben (Jeffrey, 2014). [^{18}F]-Florbetaben (FBB) in particular displays excellent linear correlation with global PiB standard uptake value ratio (SUVR) in AD ($r=0.97$, $p< 0.0001$) with a similar effect size to PiB (Cohen's d, Pib: 3.3; FBB: 3.0)(Villemagne et al., 2012). FBB tracer binding matches well with Aβ distribution given by post-mortem biopsy (Anderson, 2013). We have chosen to use FBB as our amyloid PET tracer in this study, due to these promising characteristics.

2.5.1.2 [18F]-Florbetaben

[^{18}F]-Florbetaben is a fluorine-18 (^{18}F) labeled stilbene derivative developed for use in the clinical visualisation of Aβ plaques in Alzheimer's disease. FBB was produced and transported from Cyclotek Pty Ltd in Melbourne, for use in PET scanning at Southern Cross Hospital, Christchurch.

Pharmacokinetics

Uptake within the brain is rapid, reaching a maximum ^{18}F radioactivity concentration of $\sim$6% injected dose/L at 10 minutes post intravenous bolus injection of 300 MBq of FBB. FBB is eliminated from blood plasma with a mean biological half-life of $\sim$1 hour, and is completely eliminated from the body within 24 hours post injection.

Dosimetry

^{18}F has a mean half-life of 110 minutes, resulting in a physical decay of the original activity of 99.99% at 24 hours post-inection. The mean effective radiation dose a typical patient

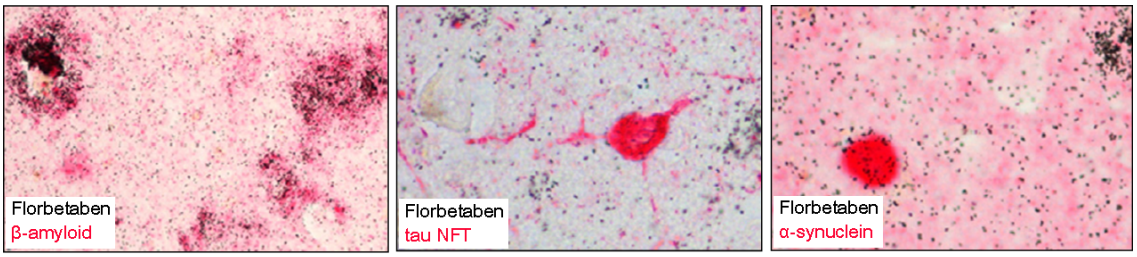

FIGURE 2.1: High-resolution emulsion autoradiography using [^{3}H]-Florbetaben (black grains) in combination with immunohistochemical staining (red) for Aβ plaques (left), tau aggregates (middle) and α-synuclein Lewy Bodies (right). FBB demonstrates high specificity for Aβ plaques over tau and α-synuclein lesions, as shown by the density of grains in the centre of the stained Aβ plaques, compared with the lack of such clusters in the tau and α-synuclein immunoreactive aggregates. Figure adapted from (Fodero-Tavoletti et al., 2012), Copyright © 2012, with permission from Elsevier.

will receive from administration of 300 MBq FBB is 5.8 ± 0.42 mSv, which has been shown to be well tolerated (Sabri, Seibyl, et al., 2015).

Binding characterisitics

Florbetaben has demonstrated high binding affinity to Aβ plaques in the brain of AD patients (Sabri, Seibyl, et al., 2015). Importantly, FBB demonstrates high specificity for Aβ plaques over tau and α-synuclein lesions, as demonstrated by (Fodero-Tavoletti et al., 2012) using high-resolution emulsion autoradiography in combination with subsequent immunohistochemical staining in brain tissue sections (figure 2.1). FBB binds highly to plasma proteins, with an unbound fraction of 1.6%, making this radiotracer well suited for imaging arterial blood supply.

The optimal scanning time window for visual assessment has been shown to be 90–110 minutes post-injection, based on blinded assessment of PET data from 25 AD subjects and 25 healthy controls by three expert readers (Tiepolt et al., 2012). Scans of three different durations (5, 10 and 20 minutes beginning at 90 minutes post-injection) were assessed in terms of diagnostic confidence, sensitivity and specificity, and inter- and intra-reader agreement. All scan durations yielded similar results, such that while a 20-minute scan duration is optimal, a reduction of time spent in the scanner can be justified without loss of diagnostic accuracy. This can be a significant advantage when scanning patient populations who have difficulty tolerating extended time in the scanner, as can be the case in patients with dementia.

2.5.2 Tau protein and neurofibrillary tangles

In a similar manner to amyloid aggregates, hyperphosphorylated tau protein is another pathological hallmark of AD, and has been hypothesised to be one of the primary drivers of neurodegeneration in AD and other disorders. In its native form, tau is an unfolded protein that is critical for maintaining structural integrity and function of axons. Alternate mRNA splicing at exons 2, 3 and 10 of the microtubule associated protein tau (MAPT) gene on chromosome 17 generate 6 isoforms of tau, present in equal proportions in the healthy adult brain. These isoforms are characterised by the presence of either three- (3R) or four-repeat (4R) sequences in the C-terminal part of the molecule (Sergeant et al., 2005). Interestingly, the relative expression of 3R or 4R isoforms has been seen to vary between tauopathies upon post-mortem examination; FTD, CBD and PSP show a relative overexpression of 4R isoforms, while all six may be found in AD (Y. Wang & Mandelkow, 2015). Both 3R and 4R isoforms bind to microtubules within the cell cytoskeleton, and assist cell stability by shifting the phase of the microtubules towards polymerisation instead of depolymerisation. Tau phosphorylation reduces the affinity of tau protein for microtubules, shifting microtubule dynamics towards depolymerisation and resulting in impaired axonal transport. This eventually leads to neuronal dysfunction and cell death. Hyperphosphorylated tau proteins aggregate to form neurofibrillary tangles (NFTs), thus the presence and number of these structures are a useful metric in the evaluation of neuronal damage and disease progression.

Examination of tau has previously been limited to post-mortem and CSF studies due to the difficulty in developing an *in vivo* PET tracer. An effective tau tracer must be able to cross the blood-brain-barrier and plasma cell membrane to bind to intracellular tau, placing restrictions on the maximum molecular size and lipophilicity of the ligand. Sites for ligand binding are further complicated by the existence of six different tau isoforms, forming fibrous polymers which may present in twisted or straight structural conformations. With the focus steadily shifting from amyloid plaques to tau NFTs, there has been a concerted effort to develop effective tau tracers for in vivo PET imaging (Okamura et al., 2018). The first generation of tau PET tracers (e.g. $[^{18}F]$THK5317, $[^{18}F]$THK5351, $[^{18}F]$AV1451, $[^{11}C]$PBB3) have been used extensively in research studies (Leuzy et al., 2019), however the presence of off-target binding compromised the utility of many of these tracers for clinical use as a diagnostic tool. A second generation of tau PET tracers (e.g.

[^{18}F]MK-6240, [^{18}F]RO-948, [^{18}F]PI-2620, [^{18}F]GTP1, [^{18}F]PM-PBB3) were developed in response to this problem (Y. T. Wang & Edison, 2019). While funding was awarded for use of [^{18}F]PI-2620 in this study, substantial delays in tracer production precluded inclusion of tau PET imaging in this thesis. It is possible that tau PET imaging in PD will be conducted in future at the NZBRI.

2.5.3 Cerebral blood flow

Perfusion refers to the capillary blood supply delivering oxygen and nutrients to brain tissue, in units of ml/min/100g (Detre et al., 1992). While technically a measure of simple flow rate (ml/min), the term CBF is somewhat synonymous with perfusion in the literature. Measuring regional CBF is a useful method of inferring neuronal function, such that decreases in ATP production and consumption due to neuronal damage are concomitant with changes in cerebral perfusion. Blood flow to the damaged region may decrease, while other regions may see compensatory increases. This same effect may also indicate disease- or age-related deficits, thus subject age is often an important factor in the analysis of perfusion data.

Imaging regional CBF (rCBF, ml/min/100g) using PET or single-photon emission computed tomography (SPECT) does not yield absolute, quantitative values, but rather relative values normalised to a reference region or global mean. This can introduce bias if there is a systematic increase or reduction in blood flow across the subject group, either globally or in the chosen reference region. Arterial spin labeling MRI (ASL MRI) provides an alternative method of imaging CBF that yields absolute perfusion values in a completely non-invasive manner (Melzer et al., 2011), and has been shown to accord well with rCBF perfusion studies using $H_2^{15}O$ PET (Ye et al., 2000).

2.5.3.1 Arterial spin labelling MRI

ASL MRI offers several advantages as a cost effective, non-invasive alternative to the more invasive $H_2^{15}O$ PET imaging of cerebral blood flow. The ASL imaging protocol offers faster scan times over PET tracer techniques and is an easily repeatable addition to existing MRI routines (Melzer, 2011). Magnetic resonance imaging deposits no radiation dose to the patient, and the required processing to extract absolute perfusion values from these

data is relatively straightforward. The resulting images are less susceptible to bias as they are not calculated based on normalisation to a global mean or reference region.

A previous study conducted at the NZBRI explored the efficacy of ASL MRI data in the construction of a disease-related covariance network in PD, relating to motor and cognitive aspects of the disease (Melzer et al., 2011). Network analysis revealed characteristic decreases in posterior and lateral-posterior parietal areas and dorsolateral prefrontal cortex, with preserved perfusion in globus pallidus. Areas of decreased perfusion indicated by the network were found to be significantly related to cognition as measured by MoCA score (P=0.001, $\beta = 0.41$), but no other variables.

2.5.4 Metabolic changes

Deficiencies in both dopaminergic and non-dopaminergic neurotransmitters, such as serotonin, norepinephrine, and acetylcholine, are frequently implicated in the pathogenesis of non-motor features in PD, notably cognition (Scatton et al., 1983; Hasselmo, 2006; J. Klein et al., 2010). As such, these possible biomarkers of cognition in PD have provided the impetus for several pharmacological interventions for the treatment of cognitive impairment and mood (Diaz & Waters, 2009). Underlying the deficiencies in these neurotransmitters is neuronal dysfunction. A properly functioning neuron utilises cerebral glucose in the production of ATP, which is in turn used by the cell in neuronal maintenance and production of neurotransmitters (Mergenthaler et al., 2013). Thus, measuring the regional cerebral metabolic rate of glucose (rCMRglc) provides a useful measure of neuronal function. Imaging rCMRglc with ^{18}F-fluorodeoxyglucose (FDG) PET has therefore been heavily explored as an avenue of disease severity assessment in neurodegenerative disorders (Eidelberg et al., 1995; Eidelberg, 2009; Eckert et al., 2007). Cortical hypometabolism has been linked to cognitive changes in PD in several independent studies using FDG PET (Huang, Mattis, et al., 2007; Ma et al., 2007; Liepelt et al., 2009). Areas known to display relative reductions in metabolic activity in PD include the lateral premotor cortex, supplementary motor area and posterior parietal association areas, while increases are seen in the globus pallidus, thalamus and pons (Eidelberg, 2009).

Due to the substantial variability in metabolic activity between brain regions, it is difficult to use regional estimates of metabolism to adequately describe response to treatment in a clinical setting. A more clinically relevant measure has been provided by network

analysis, wherein the principle components of variance in the data may be analysed to form patterns of abnormal metabolic activity that occur in PD distinct from controls. Independent patterns of metabolic activity, constructed from principle component analysis (PCA), that correlated significantly with motor dysfunction and the results of neurological testing have provided unique insight into the areas of the brain implicated in PD (Huang, Tang, et al., 2007).

2.5.5 Diffusion imaging of white matter structure

Nuclear imaging methods such as PET offer great insight into neuronal health by way of metabolic and pathologic imaging, however inherent limitations to spatial resolution inhibit the investigation of micro- and macro-structural architecture. Developments in the field of diffusion MRI offer this utility.

Many neurological disorders exhibit reduction or disruption of brain connectivity due to pathological changes to the number and density of white matter axons, or fibres (D. A. Raffelt et al., 2016). Diffusion weighted imaging aims to infer microstructure based on the movement of water molecules through ordered tissues. Diffusion tensor imaging (DTI) models the displacement of water molecules as a rotationally invariant tensor (Lanskey et al., 2018), which may be deconstructed into a number of structure-dependent metrics. These local metrics have been shown to correlate with performance on a range of motor and non-motor tasks (Danielmeier et al., 2011; Forstmann et al., 2010; Liston et al., 2005; R. E. Roberts et al., 2010, 2013; Tuch et al., 2005), and may correlate with cognitive decline in PD (Melzer et al., 2013). On a larger scale, tractography is often applied to DTI data to determine the trajectories of white matter tracts in order to infer the underlying connectome of the human brain (R. E. Roberts et al., 2013).

While DTI offers potentially powerful estimations of local structural metrics, the single tensor model suffers from a lack of multi-directional information in voxels that contain crossing fibres (Tournier, 2004). This shortcoming confounds interpretation of apparent local differences in these voxels and prohibits the successful implementation of larger scale structural analyses, such as deterministic and probabilistic tractography. High Angular Resolution Diffusion Imaging (HARDI) acquisitions enable estimation of multiple fibre orientations in a single voxel, through the use of many diffusion acquisition directions

(Descoteaux, 2015). The rationale and development of HARDI is discussed in greater detail in Chapter 7.

2.5.6 Cortical thickness and grey matter atrophy

Structural T1-weighted imaging has consistently shown evidence of reduced cortical thickness and cortical grey matter volume in PD, correlating with cognitive decline in both cross-sectional (Hong et al., 2014; Mak et al., 2014; Segura et al., 2014; Zarei et al., 2013; Gerrits et al., 2016) and longitudinal studies (Mak et al., 2015; Hanganu et al., 2016). Previous work conducted at the NZBRI investigated grey matter volume in a cognitively well-characterised cohort, examining group differences in healthy controls, PDN, PD-MCI and PDD (Melzer et al., 2012). Grey matter atrophy was found to be significantly established in PD-MCI, with more extensive loss in patients with dementia, compared to PDN and controls. Global measures of grey matter volume will be included as part of the longitudinal arm of this thesis, but are not a main focus of this study.

Chapter 3

Imaging Principles of PET and MRI

This chapter covers the operational and physical principles underlying the imaging modalities used in this study, namely positron emission tomography and magnetic resonance imaging. I discuss important factors affecting image quality in both modalities, and considerations for image acquisition, reconstruction, and quantification.

3.1 Positron Emission Tomography

Positron emission tomography (PET) is an imaging modality based on the detection of annihilation coincidence photons, following injection of a positron-emitting tracer substance. Here, I discuss the main principles of operation of PET imaging, including scientific basis, detector system components, data acquisition, image reconstruction, and quantification.

The scanner used in this study is a GE Discovery 690 PET-CT scanner.

3.1.1 Principles of operation

The general workflow of a PET image study is depicted in figure 3.1. Annihilation coincidence photons are produced when a positron emitted from the decay of a proton-rich radionuclide interacts with an electron, causing annihilation. This annihilation converts

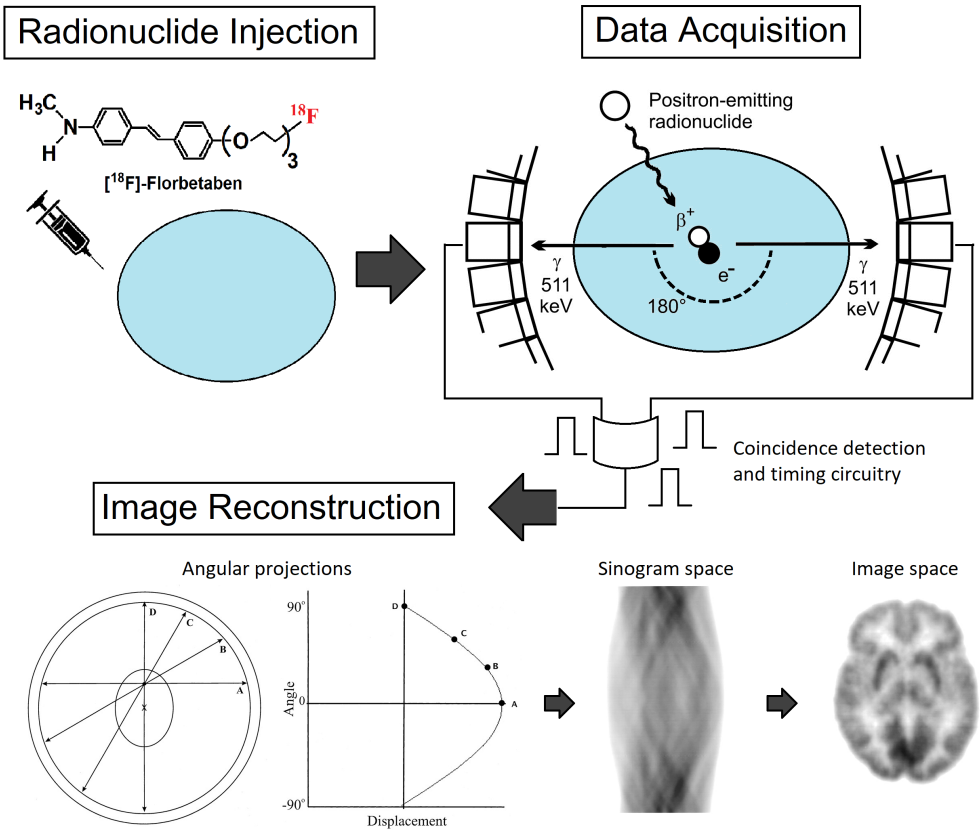

FIGURE 3.1: Flowchart of a PET imaging study. A radionuclide is injected into the patient and the emission of coincidence 511-keV annihilation photons is measured by the detector ring. Emission data are stored in a sinogram, where each line of response (is plotted as a function of angular orientation versus displacement from the gantry centre (not marked). The sinograms are reconstructed into image space to form the image volume. The image of the sinogram and reconstructed brain was originally published in JNMT. Fahey, F. H., Data Acquisition in PET Imaging. J Nucl Med Technol. 2002;30(2):39-49. © SNMMI.

the entire mass of the electron-positron pair into two 511-keV photons, travelling in nearly-opposite directions. Positrons travel only very short distances in matter before annihilation occurs, thus detection of the position of the interaction provides the approximate location of the tracer substance within the patient at the time of emission. Transverse images of the activity distribution within the patient may then be reconstructed from the acquired data by the PET system computer. Annihilation photons must escape the patient to be detected, and are thus affected by attenuation and scatter that serve to reduce image quality. Modern PET scanners are almost always coupled with x-ray CT systems to allow on-board attenuation correction, while energy-discrimination and timing circuits attempt to separate true coincidences from random coincidences and those affected by scatter (Bushberg, Seibert, Jr., & Boone, 2012, Chapter 19).

3.1.1.1 PET Detector System

A typical PET detector system consists of several rings of detectors surrounding the patient. Scintillation detectors are used in PET systems over gas-filled or semi-conductor detectors, as these have comparatively low intrinsic efficiency for the detection of 511-keV photons. Scintillation detectors generally consist of large scintillator crystals coupled to several photomultiplier tubes (PMTs). Scintillation materials absorb the energy of incident ionising radiation and re-emit it in the form of visible or ultraviolet light in a process known as luminescence (Bushberg et al., 2012, Chapter 17). Luminescence occurs as an electron drops from an excited energy state, provided by the incident 511-keV photon, to a lower energy state, ideally releasing a photon of light with energy equal to the transition. The emitted photon is converted into electrical current and amplified by the PMT electronics. This signal is rejected or accepted according to an acceptable energy window around the 511-keV annihilation energy, and passed through timing circuits which generate a time signal for each pulse. The time signal is used in coincidence circuitry to determine coincidence pairs and LOR's, and projection data are stored in sinograms. The PMTs operate in pulse-mode such that each scintillation interaction is processed separately from other interactions, yielding the time signal, deposited energy, and location of each interaction. High detection and conversion efficiency of the scintillator material for 511-keV photons is particularly important in order to accurately determine these factors, particularly in high count rates.

GE Discovery 690 PET/CT detector components

The PET detector system used in this thesis is the GE Discovery 690 PET/CT. This system consists of 24 concentric detector rings 81 cm in diameter, with a total detector width along the z-axis of 40 mm. 64 image slices may be obtained simultaneously across a 157 mm axial field of view (FOV). The entire detector system contains 13824 cerium-doped lutetium yttrium oxyorthosilicate ($Lu_2Y_{2-x}SiO_4O$, abbreviated LYSO) scintillation crystals. LYSO is an inorganic scintillation material of high density and detection efficiency, with a very short dead time (the time taken for an excited electron to decay to the ground state, during which no new interactions can be detected). The coincidence time window for this system is 4.9ns, allowing corrections for time-of-flight. This has an important effect on final image quality, which will be discussed in a later section.

3.1.2 True annihilation coincidence detection

The detector geometry encircles the patient and is designed to detect annihilation photons produced at approximately the same time. The line connecting these detected photons is termed the line of response (LOR), along which an annihilation interaction is presumed to have occurred. Annihilation coincidence detection (ACD) thus establishes the trajectories of detected photons without the use of collimation, avoiding the loss of sensitivity and reduced spatial resolution that occurs with collimated detector systems. However, the detected LOR's may provide inaccurate information as a result of scatter and random coincidence detection. Figure 3.2 depicts true, scatter and random coincidence detection. A *true coincidence* is given by the nearly simultaneous detection of two annihilation photons resulting from a single interaction, and gives the correct LOR. A *scatter coincidence* is a true coincidence resulting from a single interaction, but gives an incorrect LOR as a result of photon scatter within the patient shifting the apparent origin of the annihilation photons. A *random coincidence* detection gives a false LOR as a result of the nearly simultaneous detection of two annihilation photons produced from separate interactions, mistakenly identified as coincidence photons. Scatter and random coincidences thus reduce image contrast and increase statistical noise in PET data; to combat this, PET systems use detectors capable of energy discrimination and highly accurate timing circuits to detect true coincidence pairs, while CT attenuation correction accounts for signal loss or scatter from attenuation effects.

3.1.3 Attenuation correction

In addition to scatter and random coincidence, annihilation photons may be prevented from reaching the detectors due to attenuation within the patient tissues. Attenuation correction accounts for the loss of measured signal arising from interactions between the emitted photons and patient tissue, primarily by Compton scatter. Compton scattering is an inelastic collision, where photon interactions with unbound or valence shell electrons result in both a change in direction of the photon path (scatter) and a loss of photon energy. Primary loss of signal in PET arises as a result of scatter outside the detector ring, while detected attenuated photons contribute to noise and inhomogeneous bias in estimated tracer distribution. The effect of photon attenuation on detected signal is

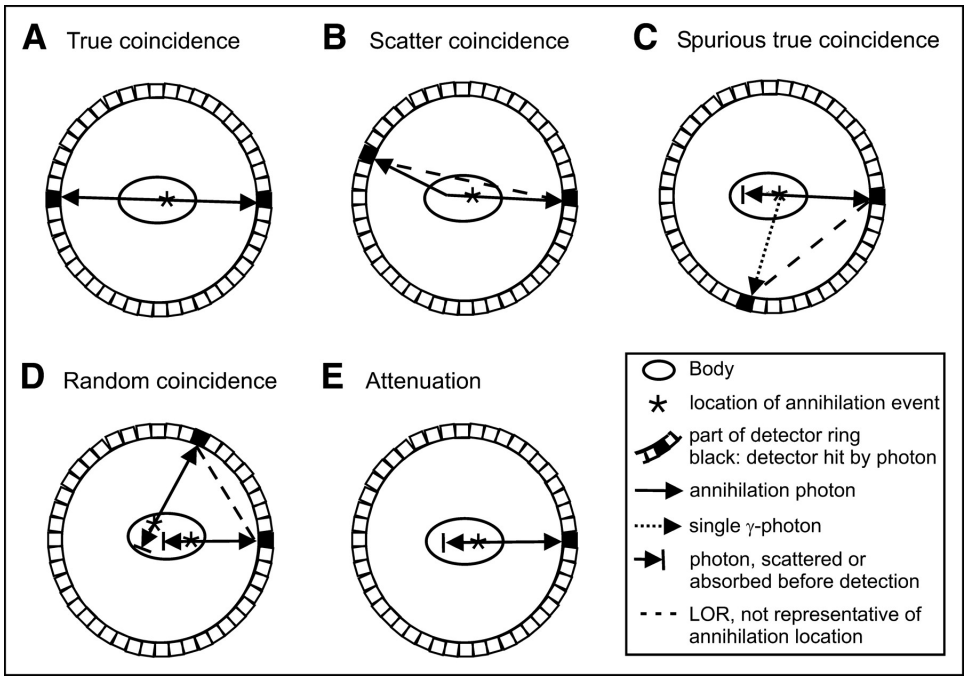

FIGURE 3.2: (A) True coincidence. Two annihilation photons, emitted from same annihilation event, travel in opposite directions without interaction with body, and are detected by opposing detectors. (B) Scatter coincidence. One photon from annihilation travels without interaction, and other annihilation photon is deflected because of scattering in body. (C) Spurious true coincidence. Single γ-photon is detected simultaneously with annihilation photon (or another single γ-photon), both emitted from same decay event. (D) Random coincidence. Two annihilation photons (or single γ-photons) emitted from 2 separate decay events are detected by chance within coincidence time window. (E) Attenuation. One (or both) annihilation photons is (are) not detected as result of scattering or absorption within body. In scatter, spurious, and random coincidences, LOR drawn between 2 detectors is not representative of annihilation location (B–D). Three or more photons (multiples) detected in coincidence are rejected by PET coincidence electronics. This figure was originally published in JNMT. Verel, I., The Promise of Immuno-PET in Radioimmunotherapy. J Nucl Med Technol. 2005;46(2):39-49. © SNMMI.

dependent on the linear attenuation coefficient μ and thickness L of a tissue or material, following the exponential relationship:

$$I/I_0 = e^{-\mu L} \tag{3.1}$$

where I is the non-attenuated signal, and I_0 is the attenuated signal (Chen & An, 2017). Estimating the linear attenuation coefficient of each voxel throughout the image volume thus allows for corrections to be made according to the magnitude of the effect I/I_0. This can be achieved using a 511 keV transmission scan, performed prior to PET acquisition using an integrated CT imaging unit. The CT scan provides an image of the radiodensities of tissues within the patient volume, where voxel intensity is quantified in Hounsfield Units

(HU):

$$HU = 1000 \times \frac{\mu - \mu_{water}}{\mu_{water} - \mu_{air}} \tag{3.2}$$

Here, μ is the linear attenuation coefficient at each voxel, and μ_{water} and μ_{air} are the linear attenuation coefficients of water and air. The CT scan is downsampled to PET resolution, transformed from HU to μ at 511 keV photon energies, and forward projected into projection space to map directly onto detector LORs. All measured emission data is corrected according to the estimated effect I/I_0, based on the value for μ at the location of each measured event, prior to image reconstruction.

3.1.4 Image noise and time-of-flight

The rate of random coincidence detection is dependent on the coincidence time window τ and the actual count rates S_1 and S_2 at the corresponding detectors, given by $R_{random} = \tau S_1 S_2$. At higher count rates, the rate of random coincidence detection increases and will decrease the signal-to-noise (SNR) ratio of the resulting images. This is a particular problem in older PET systems; in conventional PET, the probability of interactions within each voxel along the LOR is assumed to be uniform, and SNR is already reduced by the presence of noise correlations between detected events (figure 3.3 B). More modern PET systems reduce noise correlations - and improve SNR at high count rates - by spatially localising events along the LOR using time-of-flight information (Surti, 2015) (see figure 3.3). Sufficiently sensitive timing circuits are able to differentiate the arrival times t_1 and t_2 of the annihilation photons, giving an emission distance from the machine along the LOR from the scanner centre of $d = c \times (t_2 - t_1)/2$, where c is the speed of light. The uncertainty of this measurement follows a Gaussian distribution of width Δx, and is dependent on the coincidence timing resolution Δt[1] of the detector system:

$$\Delta x = c \times (\Delta t)/2$$

Thus an incremental probability of event occurrence is ascribed to each voxel along the LOR, and noise correlations between separate events are removed outside of the area Δx. Given a Δx that is equal to or less than the detector resolution (typically 4-5mm), it

[1]The coincidence timing resolution Δt of a PET detector system is given by the full-width-half-maximum (FWHM) of the histogram of TOF measurements from a point source (Surti, 2015).

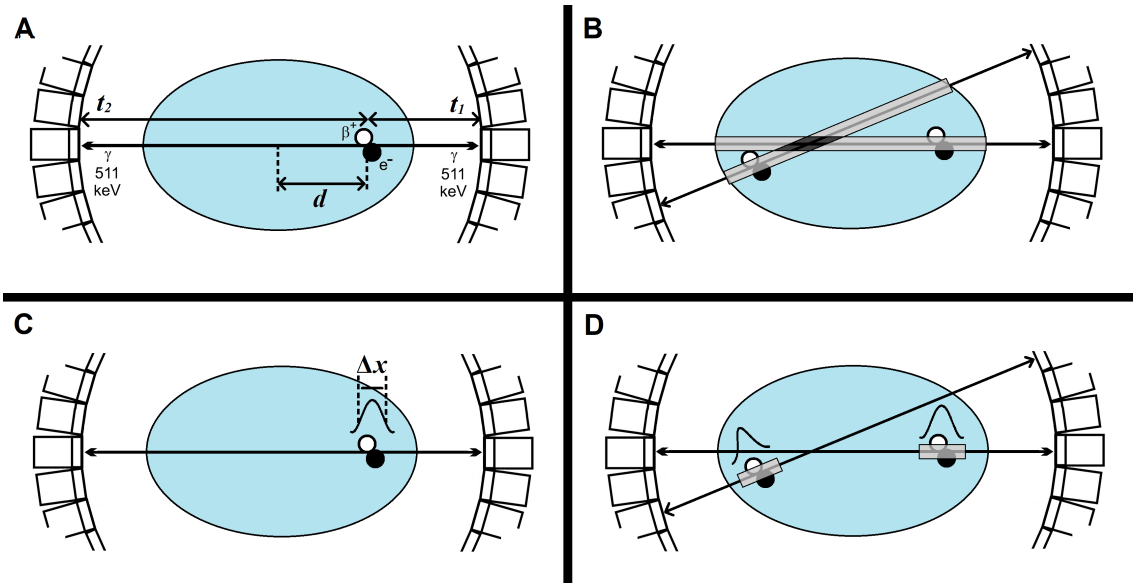

FIGURE 3.3: (A) An annihilation event at a distance d from the machine centre is detected, with coincidence photons arriving at the detectors at times t_1 and t_2. (B) In systems with no TOF capability, each point along the LOR is assumed an equal probability of having produced the annihilation. Where LOR cross, portions of the image may appear to have increased signal where no event has occurred, producing noise correlations in the image. (C) TOF information allows the probabilistic localisation of the interaction defined by width Δx, following a Gaussian distribution. (D) Noise correlations between the two events are reduced or removed by TOF localisation.

would theoretically be possible to produce a complete PET image by direct detection of localised events. In reality, Δx is generally 10 times that of the detector resolution, thus image reconstruction must be achieved through more sophisticated methods in order to produce a quality image.

3.1.5 Image reconstruction

Each LOR in a detector system gives a line of projection data, containing the sum of all detected activities within each voxel through the depth of the image volume. The projection data is stored in a sinogram, comprised of rows and columns of angular and radial samplings, respectively (Saha, 2015). Conventional image reconstruction methods 'unfold' the projection data from this polar coordinate system and translate it to a volumetric image matrix, using a direct analytical approach known as filtered back-projection (FBP). Simply, FBP assumes that the count density distribution along an LOR through the volume is equal to the line integral of the measured projection in the sinogram, and count density along the line is thus obtained through inverse mathematical operations. Counts from all LORs are projected back along the original path and summed to form

a complete PET image of tracer retention in the volume. Analytical methods are computationally inexpensive but also prone to noise and artifacts, due to being based on a simplistic model of PET that ignores the probabilistic nature of the data (see figure 3.3) and other physical factors of the detector system. Accounting for these factors requires a great number of additional equations, and solving for tracer retention through direct inversion is not realistic. Obtaining the solution through iterations of reconstruction enables the inclusion of system modeling, while being within the computational ability of most on board scanner systems.

Iterative reconstruction

As an alternative to FBP, iterative reconstruction (IR) instead looks to forward project the data, first obtaining an estimated image from a system model algorithm and comparing the computed sinogram with the measured sinogram. Discrepancies from the measured projections are corrected, and a new estimate for the next iteration is created by back-projection. This continues until an acceptable agreement between the estimated and measured sinograms is reached. IR methods vary primarily in the model algorithms used to estimate the image, the nature of the discrepancies being corrected, and the order in which corrections are applied within the full iteration (Saha, 2015). Reconstruction algorithms commonly used in PET imaging studies have two main parts; a statistical criterion estimating the image, and a numerical algorithm for convergence to the solution prescribed by the criterion. As PET is an image modality with inherently limited spatial resolution (Moses, 2011), most IR algorithms focus on optimising SNR within an acceptable convergence time.

Many IR algorithms exist that take different approaches to this problem, for example by maximum likelihood expectation maximisation (MLEM), space-alternating generalized expectation maximisation (SAGE), single-slice rebinning (SSRB) or Fourier rebinning (FORE) (see (Iriarte et al., 2016) for a thorough review). These are often used in conjunction with additional correction algorithms to inform the model, such as TOF information, or point-spread functions (PSFs) - algorithms based on the measurement of a point source at several million points across the FOV, designed to correct for detector geometry- and patient-based scatter effects. In this thesis, reconstruction is performed using General Electric's VUE Point FX + SharpIR algorithm, employing a variation of MLEM that

achieves faster convergence by dividing the data into ordered subsets (OSEM) in combination with PSF modeling, with additional correction using TOF information (a.k.a. OSEM + PSF + TOF). Images produced by this combination have been shown to improve SNR and contrast over pure OSEM and OSEM + TOF reconstruction algorithms (Vennart et al., 2017).

3.1.6 Quantification of PET image data

The raw reconstructed images output by the PET system represent the voxelwise radioactivity concentration in the image volume. Images in this form are sufficient for the purposes of clinical evaluation by visual read, however quantitative analysis between subjects or across longitudinal measurements requires that the activity be normalised for session-specific and individual variation. This is provided by the standard uptake value ratio (SUVR).

The image is initially converted into standard uptake value (SUV), given by:

$$SUV = \frac{c_{img}(t_0)}{ID \times BW} \tag{3.3}$$

where $c_{img}(t_0)$ is the activity concentration in the image voxel at time t post-injection, decay corrected to the time of injection, t_0; ID is the injected dose, calculated from activity in the syringe before and after injection; and BW is the body weight of the individual. The SUV gives a unit-less semi-quantitative measure of the activity per voxel to the activity in the whole body volume. In order to compare activity levels across subjects in an imaging study, the SUV must be further normalised to account for non-displaceable radiotracer binding. This is accomplished by normalising global values of SUV to values within a chosen reference region in the image, giving a SUV ratio (SUVR). In Aβ PET imaging, the reference region chosen must display the same level of non-displaceable binding (free plus non-specific binding) as the region of interest (ROI), show little to no variation in signal for the full duration of the scan, and be free of Aβ pathology. In this thesis, the cerebellum is chosen as the reference region for use with [^{18}F]-Florbetaben for these favourable characteristics (S. et al., 2017), and as recommended by the Centiloid Working Group for conversion of SUVR to centiloids (Klunk et al., 2015). Semi-quantitative evaluation of Aβ

PET by SUVR allows the direct comparison of tracer uptake across subjects in a study, either voxelwise or by ROI.

3.1.6.1 The Centiloid scale

The use of SUVR in quantitative analysis is prevalent in the field of PET imaging research, however considerable variation in procedure exists between studies conducted by different research groups, such that direct numerical comparison of SUVR between studies is not always valid. The centiloid (CL) scale was developed by the Centiloid Working Group (Klunk et al., 2015) in order to facilitate direct comparison of amyloid deposition across imaging centres, using different amyloid ligands (incorporating ^{11}C- and ^{18}F-based ligands), pre-processing pipelines, analysis methods and diseases. The centiloid represents a standardised quantitative amyloid imaging measure following a zero to 100 scale, anchored by young controls (displaying little to no Aβ pathology) and typical Alzheimer's disease patients. The CL scaling method was initially defined for standardisation of [^{11}C]-PiB PET, acquired using a defined 'standard' study method; groups wishing to adopt the CL scale using a non-standard tracer could do so by calibrating against PiB PET, also acquired in the same group, with additional calibration required if a non-standard method is used. Subsequent work by (C. C. Rowe et al., 2017) removed the need for comparison against PiB PET with regards to FBB PET imaging studies, and scaling from FBB SUVR to CL now only requires calibration to account for a non-standard method. Method calibration is done by processing a free-to-access FBB PET dataset (Global Alzheimer's Association Interactive Network [GAAIN:http://www.gaain.org]), and comparing resultant cortical SUVR values against published standard values using a linear model. Provided the values agree within an accepted level of variation, this gives linear method scaling factor. Scaled SUVR acquired in the study dataset can then be converted directly into CL, following the equation defined by Rowe et. al. (2017):

$$CL = 153.4 \times SUVR_{FBB} - 154.9 \tag{3.4}$$

This is known as level 3 calibration, within the framework designed by the working group. The methodology and outputs of this procedure are given in greater detail in Chapter 5, section 5.6.4. The CL scale is a relatively recent addition to the field of amyloid PET

imaging, and this study represents the first to employ the CL scale for evaluation of amyloid deposition in Parkinson's disease.

3.2 Magnetic Resonance Imaging

Magnetic resonance imaging (MRI) is an imaging technique based on the magnetic properties inherent to the nucleus of an atom. Protons and neutrons within a nucleus possess nuclear 'spin', which can be understood as magnetic dipoles. In stable nuclei containing equal numbers of protons and neutrons, these magnetic dipoles sum to zero and cancel out. When there are uneven numbers of protons and neutrons, a nuclear magnetic moment exists about the nucleus, often visualised as an arrow vector with magnitude and direction. Under the influence of an external magnetic field B_0, a large number of nuclei possessing random magnetic orientation will assume a non-random alignment resulting in a small net magnetisation parallel to the external magnetic field. By convention, the magnetic field B_0 is applied in the z-direction of a three-dimensional cartesian coordinate system; the net magnetisation in the direction of the applied magnetic field is thus denoted M_z and is known as the longitudinal magnetization. This magnetisation is maximal under equilibrium conditions and is denoted M_0, the equilibrium magnetisation.

An applied external magnetic field B_0 also causes a magnetic spin to have a certain precessional frequency about its axis, proportional to the strength of the magnetic field and determined by the gyromagnetic ratio unique to each element. This relationship may be written as:

$$\omega = \gamma B_0 \tag{3.5}$$

where ω is the resonant or Larmour frequency and γ is the gyromagnetic ratio (for hydrogen, ω = 127.7 MHz at 3T, γ = 42.57 MHz T^{-}). Equation 2.1 describes the behaviour of a magnetic spin within an external magnetic field, and is thus the key relationship underpinning MRI (Bushberg et al., 2012).

The net magnetisation of spins within a magnetic field is not sufficient to produce signal in MR. To obtain signal, the net longitudinal magnetisation must be tipped into the transverse plane. Application of a radio frequency (RF) electromagnetic pulse perpendicular

to B_0 and tuned to the resonant frequency causes the net magnetisation to rotate away from the longitudinal plane. This results in a perpendicular magnetisation vector rotating at the applied RF frequency, known as the transverse magnetisation M_{xy}. Immediately following a 90° RF pulse, M_z is at a minimum and M_{xy} is at a maximum. The gradual return to equilibrium (loss of M_{xy} and regrowth of M_z) ensues, and receiver coils detect the change in this rotating magnetisation as MR signal. The rate at which the transverse and longitudinal magnetisation decay occur are dependent on the structural and magnetic characteristics of the sample, and enable the large amount of tissue selectivity available using MR. These characteristics determine the so-called T1 and T2 relaxation times of tissues, and relate to longitudinal magnetisation recovery and transverse magnetisation decay respectively.

3.2.1 T1 and T2 relaxation

T1: spin-lattice

Immediately following the excitation pulse, longitudinal magnetization M_z will begin to recover as a result of excitation energy being released from the spin back to the lattice of molecules surrounding it; it is thus termed *spin-lattice relaxation*. T1 is the time taken for the exponential recovery of M_z to reach 63% of equilibrium following a 90° excitation pulse. Spin-lattice relaxation is highly dependent on the molecular structure and composition of tissue; long T1 times are given by dense structures and watery fluids, while viscous fluids possess the shortest T1 times. The recovery of longitudinal magnetisation may be described by the following equation (Brown et al., 2014):

$$M_z = M_z(0)e^{-t/T1} + M_0[1 - e^{-t/T1}] \tag{3.6}$$

where $M_z(0)$ is the longitudinal magnetisation at the time of the excitation pulse and t is the elapsed time from the excitation pulse.

T2: spin-spin

The initial transverse magnetisation M_{xy} induces a sinusoidal signal in the receiver coil that becomes damped as M_{xy} relaxes, known as the free induction decay (FID) envelope (figure 3.4). The T2 relaxation time of a tissue is the time taken for the FID envelope to

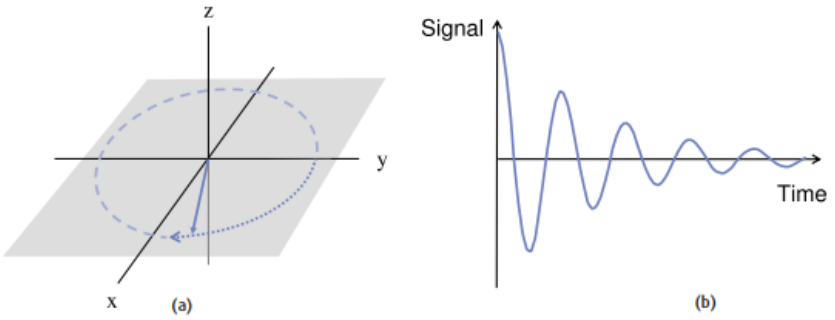

FIGURE 3.4: (a) Precession of the flipped magnetization in the transverse plane. (b) Signal induced in the receiver coil – the Free Induction Decay (FID) envelope. Figure reused with permission from (McRobbie et al., 2002).

exponentially decay to 37% of the peak level following the excitation pulse. Transverse magnetisation decay occurs due to macromagnetic inhomogeneities in the local magnetic field of the tissue causing spin ensembles to lose phase coherence, thus earning the moniker, *spin-spin relaxation*. The decay of transverse magnetisation due to T2 effects may be described by the following equation (Brown et al., 2014):

$$M_{xy} = M_{xy}(0)e^{-t/T2} \tag{3.7}$$

Loss of phase coherence occurs faster in tight structures able to support local magnetic field variations, and slower in free moving amorphous structures. Thus, dense structures such as bone exhibit very short T2, while fluids such as cerebrospinal fluid (CSF) exhibit long T2. Dephasing may also be caused by inhomogeneities in the applied magnetic field B_0, characterised by the time constant T'. The transverse magnetisation decay constant due to both intrinsic and extrinsic inhomogeneities is termed T2*, and is always shorter than T2. T2* is related to T2 and T' by

$$\frac{1}{T2^*} = \frac{1}{T2} + \frac{1}{T2'} \tag{3.8}$$

T1 is typically on the order of 5 to 10 times longer than T2 (see table 3.1); the difference in decay time of longitudinal and transverse magnetisation in the same tissue is depicted in 3.5. While both longitudinal recovery and transverse decay occur simultaneously, M_{xy} decreases significantly faster.

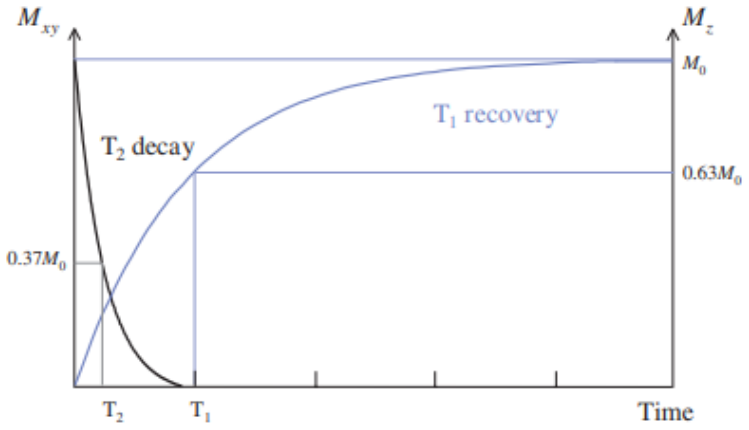

FIGURE 3.5: T1 and T2 decay for the same tissue. T1 recovery is on the order of 5-10 times longer than T2, although they both occur simultaneously. Figure reused with permission from (McRobbie et al., 2002).

The tuning of various imaging parameters in an MR pulse sequence makes use of these differences in the T1 and T2 constants of different tissues in order to obtain the desired tissue contrast.

Tissue	T1 (ms)	T2 (ms)
Grey matter	1820	100
White matter	1084	70
Cerebrospinal fluid	4163[a]	500[b]
Fat	371	133
Blood	1932	275

a. Value retrieved from (Lin et al., 2001)
b. Value retrieved from (Piechnik et al., 2009)

TABLE 3.1: Approximate values for T1 and T2 at B_0 =3T and 37° (Stanisz et al., 2005).

3.2.2 MRI pulse sequence parameters

There are many different pulse sequences used in MRI to emphasise differences in proton density, T1 times, and T2 times of tissues. There are several important parameters employed to this effect that vary depending on the imaging objective.

The *repetition time* (TR) is the period of time between excitation pulses, during which T1 recovery and T2 and T2* decay occur. The length of TR varies depending on the pulse sequence employed, and may be on the order of milliseconds to thousands of milliseconds.

The *echo time* (TE) is the time between the excitation pulse and the peak amplitude of the FID echo. The echo is produced by applying a 180° inversion pulse at TE/2, causing

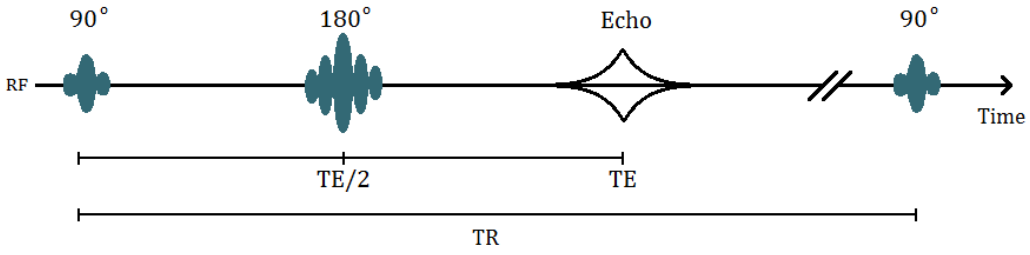

FIGURE 3.6: Spin echo pulse sequence diagram, demonstrating the repetition time TR between excitation pulses and the echo time TE. A 180° pulse is applied at time TE/2 to produce the echo at TE.

rephasing of the spins and subsequent regrowth of the FID envelope, producing an 'echo' with peak amplitude at time TE. This is known as a *spin echo* pulse sequence (figure 3.6). Some pulse sequences use magnetic field gradients in place of an inversion pulse to produce an echo; in these sequences, a negative magnetic field gradient applied directly after the 90° RF pulse causes rapid loss of phase coherence, which is then reversed by switching the polarity of the applied gradient. When the effects of the negative gradient have been completely reversed by the positive gradient, an echo is produced; however, this and subsequent echoes will decay exponentially according to T2*, as the gradients do not correct for the effects of intrinsic and extrinsic magnetic field inhomogeneities (T2 and T2* effects). This sequence is known as a *gradient echo* sequence.

The *inversion time* (TI), employed in *inversion recovery* sequences, is the time between the 180° inversion pulse and a 90° readout pulse that converts the recovered longitudinal magnetisation to transverse magnetisation. Subsequently, an additional 180° pulse is required at TE/2 to refocus the transverse magnetisation and generate the echo of the readout pulse. Careful selection of the TI may be used to nullify the signal of certain tissues, and is selected according to the T1 relaxation time of the undesired tissue.

3.2.3 Spatial localisation

MR signal localisation is achieved through the use of magnetic field gradients superimposed over the main field B_0, that induce position-dependent changes in precessional frequency and phase of the spins within that gradient. Magnetic field gradients are produced within the magnet bore by a 3-axis gradient system, wherein three magnetic coils directed along each of the x, y and z directions produce magnetic gradients G_x, G_y and G_z, which spatially modify the magnetic field within the bore. The magnetic field strength

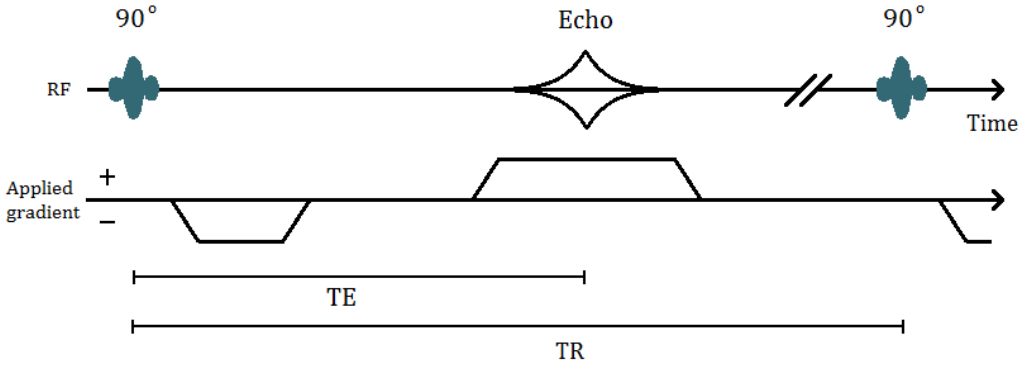

FIGURE 3.7: Gradient echo pulse sequence diagram, demonstrating the creation of an echo using reversed polarity magnetisation gradients. The magnetisation gradients decrease or increase the precessional frequency of the spins depending on their spatial position within the gradient, causing rapid loss of phase coherence. Phase coherence is re-established using a magnetic field gradient of reversed polarity applied for an equal amount of time, producing an echo.

in the z-direction experienced by a spin at position (x,y,z) within this net gradient is thus (Brown et al., 2014):

$$\bar{B} = (B_0 + G_x x + G_y y + G_z z)\hat{z} \tag{3.9}$$

There are three gradients applied over the course of a pulse sequence; the slice select gradient (SSG), the frequency encode gradient (FEG) and the phase encode gradient (PEG).

Slice select gradient - G_z

The slice select gradient is applied concurrently and in the same direction as the RF excitation pulse to select an imaging slice in the z-direction. Application of G_z causes a shift in resonant frequency of the spins in the z-direction following the linear variation of the gradient. Given that the RF pulse confers energy only to those spins precessing at the defined centre frequency, the frequency shift will result in spin excitation limited to a specific slice within the gradient. The following equation describes the spatial dependency of the spin resonant frequency (MHz T^{-1}) within G_z (McRobbie et al., 2002):

$$\begin{aligned} f(z) &= \gamma B(z) \\ &= \gamma(B_0 + z \cdot G_z) \end{aligned} \tag{3.10}$$

The width of the slice is determined by the strength of the magnetic gradient across the FOV and the bandwidth (BW) of the excitation pulse:

$$width = \frac{BW}{\gamma G_z} \tag{3.11}$$

Thus the same slice width may be achieved using a narrow BW as a wide BW, by altering the SSG strength accordingly. A narrow bandwidth is generally desired, due to the inverse relationship of bandwidth with signal to noise ratio (SNR $\propto \frac{1}{\sqrt{BW}}$). However, the wide slice widths required to image a desired volume would necessitate a low gradient strength, which may result in chemical shift artifacts (Bushberg et al., 2012). The width of the SSG is thus a matter of trade-off between the desired SNR and the propensity for chemical shift artifacts in the image volume.

Frequency encode gradient - G_x

The frequency encode gradient, or readout gradient, is applied perpendicular to G_z during the growth and decay of the induced echo. Either of the orthogonal directions may be chosen, but here it is defined in the x-direction as G_x. The frequency encode gradient causes the precessional frequency of the spins within the selected slice to vary according to their position on the x-axis. Acquiring the signal of the echo simultaneously with application of the readout gradient thus assigns spatial information in the x-direction to detected signal intensities.

Phase encode gradient - G_y

Lastly, the phase encode gradient induces a frequency shift in the y-direction, resulting in a spatially dependent phase-shift when the gradient is turned off and all spins revert to the resonant frequency. Applied prior to signal acquisition, this enables readout of spatial information in y based on the degree of phase shift experienced by the spins. A 'rewinder' gradient of opposite polarity is generally applied after signal acquisition to re-establish phase conditions prior to the next excitation.

Multiple phase and frequency encode steps are applied with incremental changes in field strength to acquire the MR signal produced by different tissues, the frequency of which will be dependent on the parameters used in the sequence. This method of image construction is known as filling k-space.

3.2.4 Image encoding in *k*-space

The encoding of MR signal into an image is dependent on the frequency and phase encode gradients (G_x and G_y). The phase shift θ accumulated by the spins over time is dependent on the position (x, y) within the applied gradients, and is proportional to the integrated area of G_x and G_y, such that (Pipe, 2009):

$$\theta = 2\pi(k_x + k_y) \tag{3.12}$$

where

$$k_x = \gamma \int G_x(t)dt \tag{3.13}$$

$$k_y = \gamma \int G_y(t)dt \tag{3.14}$$

The net magnetisation across a slice as a result of the frequency and phase encode gradients may be represented as a function $f(x, y)$. Thus, the signal $s(t)$ measured by the receiver coil is the integrated signal from all excited spins within the slice, expressed as the Fourier transform:

$$s(t) = F(k_x, k_y) = \int f(x, y)e^{i2\pi[k_x x + k_y y]}dxdy \tag{3.15}$$

The signal is dependent on the net magnetisation $f(x, y)$, and the variables k_x and k_y, and may be written $F(k_x, k_y)$. Taking the inverse fourier transform of F for a sufficient variety of k_x and k_y allows the function $f(x, y)$ to be recovered - this function then produces the MR image. Sampling signal frequencies F as a function of k_x and k_y is known as filling k-space.

The sampling of signal for different values of k_x and k_y is accomplished by manipulating the gradient strength while the receiver coil current is being measured, populating signal measurements in k-space relating to the selected slice. In an image f, low values of k represent the lower spatial frequencies (making up most of the image), while high values of k reflect high frequencies (found at edges and details). The filling of k-space follows

measurement trajectories determined spatially by the sequence in which k_x and k_y are varied, with acquisition speed dependent on gradient amplitude.

The k-space trajectory forms an important parameter affecting final image quality and resolution, with different pulse sequences approaching this in different ways to obtain the desired contrast with minimal artefacts, while optimising scanning efficiency. A standard approach in most clinical MR sequences is to fill one line of k-space (a single k_y position) per TR by changing the area of G_y, requiring a number of 'shots' to produce an image. Fast sequences such as echo-planar imaging (EPI) fill multiple or even all lines of k-space in a single shot by oscillating the frequency encoding gradient G_x, while slowly moving along k_y. While this method greatly reduces the time to acquire a full image, the necessarily long TR makes EPI sequences vulnerable to image artefacts from magnetic field inhomogeneities. These effects are discussed later in the chapter in the context of diffusion-weighted imaging, a widely used application of EPI.

3.2.5 Relevant MRI techniques

3.2.5.1 Structural T1 weighted MRI

T1-weighted acquisitions, such as 3D spoiled gradient recalled echo acquisition (3D SPGR), maximise the differences in T1 characteristics of tissues and minimise the differences in T2 characteristics (see figure 3.1) using short TR and TE. Due to the short TR, T2* effects dominate and allow a build up of transverse magnetisation to occur in tissues with long T2 times. These steady-state contributions are prevented in 3D SPGR by introducing a semi-random phase change in subsequent RF excitation pulses in the acquisition. This shifts the residual transverse magnetisation components out of phase, preventing build up of the transverse steady-state signal and effectively removing T2* effects from the acquisition(Bushberg et al., 2012, Chapter 12). This leaves a T1-weighted image with 1 mm isotropic resolution and good contrast rendition of grey and white matter acquired over a very short TR, with very low contribution from CSF.

Grey matter volume from T1-weighted MRI

The good contrast between grey matter and white matter offered by T1-weighted MRI allows the estimation of several measures pertaining to grey matter morphology, namely

cortical thickness, cortical surface area and grey matter volume. These measures are calculated in this thesis using the surface-based parcellation package offered by FreeSurfer (FreeSurfer, 2017; Fischl et al., 1999; Dale et al., 1999). Following initial pre-processing, the structural image is parcellated into its constituent tissues using a series of algorithms and atlases, wherein the skull is stripped, white matter segmented and grey matter boundaries with white matter (white surface) and cerebrospinal fluid (pial surface) defined.

Cortical thickness is calculated as the shortest distance from the white surface to the pial surface at each vertex across the cortical mantle, measured in millimeters. To measure cortical surface area, the natural folds of the cortical ribbon are inflated and mapped onto a spherical coordinate system, and registered to a surface atlas of 68 regions-of-interest (34 ROI per hemisphere) based on the geometry of the inflated gyri. The pial surface area (in mm^2) of each ROI is automatically calculated at this step. The grey matter volume is estimated as the product of the cortical thickness and the pial surface area, which may be obtained for each ROI or summed to give a global estimate of cortical grey matter volume (mm^3). This measure of grey matter volume is applied in cross-sectional analysis in relation to cortical amyloid deposition in this thesis.

3.2.5.2 Proton density weighted MRI

Proton density weighted MR imaging highlights the differences in the number density of protons in magnetised tissues. This is done by minimising the differences in signal caused by the T1 and T2 characteristics of the different tissues in the imaging slice (3.1). Choosing a long TR allows the longitudinal magnetisation to recover for all tissues, thus reducing the effect of T1 characteristics. Choosing a short TE minimises T2 and T2* effects as it does not allow enough time for significant transverse magnetisation decay to occur.

3.2.5.3 Arterial Spin Labelling

Arterial spin labelling (ASL) is a non-invasive method for quantitative measurement of perfusion, eliminating the need for potentially harmful exogenous or intravenous radiotracers such as those used in PET imaging (Dai et al., 2008).

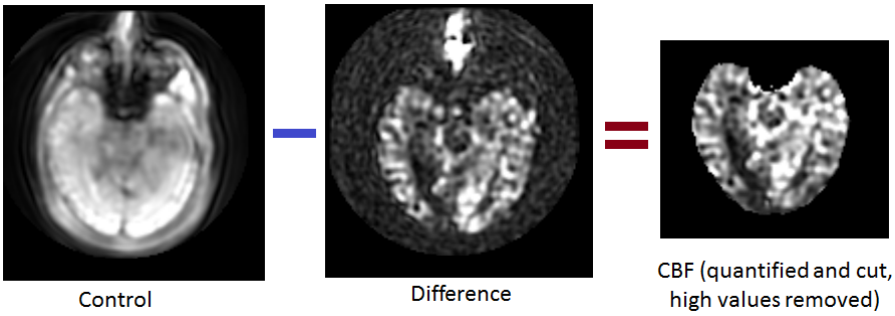

FIGURE 3.8: A very simple representation of the ASL quantification process. Subtracting the difference image (tagged blood water - no tag) given by ASL from the control (proton density weighted M_0) image given yields a quantified measure of perfusion, cut to include only the brain volume. This process includes the consideration of many factors not represented in this graphic (see equation 3.16).

ASL methods acquire perfusion data through the use of external RF and magnetic field gradient pulses applied across a chosen labelling plane. The RF and gradient pulses invert the magnetic spins of water molecules in the feeding arteries within the labelling plane, which then flow into the imaging volume. The longitudinal magnetisation of the tagged blood water entering the image volume acts in the opposite direction to the non-labelled tissue magnetisation, causing a reduction of the longitudinal magnetisation in that region. Areas of high perfusion thus see a greater reduction in signal, captured by the so-called *difference* image. Subtracting the difference image from a proton-density weighted image acquired without any labelling (M_0) is used to produce a quantified measure of the cerebral blood blow through the volume.

Methods of ASL acquisition usually fall into the 'pulsed' and 'continuous' categories, depending on how the blood water is labeled - pulsed ASL (PASL) inverts spins using a single applied RF pulse, while continuous ASL (CASL) inverts spins as they pass through a continuous RF field, applied across the labelling plane. PASL has the advantage of increased efficiency and multi-slice imaging capability, while CASL is able to achieve a higher signal-to-noise ratio (SNR), however specialist hardware is required to operate RF pulses in continuous mode (Dai et al., 2008). Pseudo-continuous ASL (P-CASL), a combination of the two strategies using both pulsed RF and gradient fields, is able to achieve the flow-driven adiabatic inversion strategy without the need for specialist hardware. This is the acquisition mode used in this study.

An estimate of the CBF within each voxel is quantified from ASL signal based on the equation:

$$cbf = 6000 \cdot \left(\frac{\lambda \cdot \left(1 - e^{(-2/1.2)}\right) \cdot e^{(w/T1)}}{2 \cdot T1 \cdot \left(1 - e^{(-1.5/T1)}\right) \cdot \epsilon} \right) \cdot \left(\frac{diff}{(g \cdot nex) \cdot cont} \right) \tag{3.16}$$

where λ is the brain-blood partition coefficient of water, set to the whole brain average of 0.9; w is the post-labelling decay time, which is 1.525 seconds in this study; $T1$ is the spin-lattice relaxation time of blood, set to 1.6 seconds at 3T; ϵ represents the combined efficiency of labelling and suppression in the acquisition sequence, defined as 0.8*0.75; the constants 1.5 and 2 represent the labelling and background saturation/suppression time in seconds respectively, with the suppression time corrected for the T1 time of grey matter (1.2 seconds); $diff$ and $cont$ are image matrices containing the voxel values of the difference (tagged - no tag) and control (M_0) images; NEX is the number of excitations or signal averages, set to 5. The quantified perfusion values are scaled by a factor of 6000 to convert L/kg/s to ml/100g/min.

3.2.5.4 Diffusion weighted MRI

Diffusion-weighted imaging makes use of the variation in T2* signal that arises in differently structured tissues, that is, the rate of decay of water signal due to extrinsic and intrinsic field inhomogeneities. The diffusion of water molecules in neural tissue, while essentially isotropic in nature, is influenced by the presence of cell membranes, cytoskeleton, and macro-molecules (Basser & Özaslan, 2009), such that movement through tissue architecture is hindered in recognisable ways. As a water molecule diffuses through neural tissue during an MR sequence, T2* signal will be lost proportional to the ease of that diffusion, thus very little signal will remain in watery tissues such as CSF, and high signal will remain in complex or dense structures such as white matter or bone.

This thesis uses a spin echo EPI (SE-EPI) sequence to acquire diffusion images. This can be considered a modified spin echo sequence (figure 3.6), with the addition of a bipolar diffusion weighting gradient following initial excitation, and a series of oscillating phase and frequency encoding gradients at readout following the 180° echo pulse. Diffusion signal is obtained in an MR acquisition by first acquiring at least one T2* weighted image with no diffusion weighting applied, known as the b=0s/mm^2 image (b quantifies the strength and duration of diffusion weighting). Diffusion weighting is applied in subsequent acquisitions using a bipolar field gradient, oriented in a different direction for each repetition.

Diffusion weighting

Immediately following the excitation pulse, all spins are in phase. The positive gradient causes the precessional frequency of spins on one side of the gradient to experience a stronger magnetic field than spins on the other side, inducing a phase shift proportional to their position within the gradient field. When the positive gradient is turned off, the spins precess at the same frequency, but retain the phase change. With the application of an equal (but opposite) negative field gradient, the direction of the induced phase-change is reversed, again proportional to the spin's position within the gradient field. If a spin has changed location between the first and second gradient lobes, there will be a net loss of magnetisation from b=0 due to loss of phase, proportional to the magnitude of displacement. T2* signal is preserved in tissues where spin motion is constrained, and lost from freely diffusing tissues. It is important to remember that the magnitude of this signal loss only relates to movement in the direction of the applied gradient. For standard diffusion tensor imaging, the diffusion signal must be sampled in at least 6 different directions to ensure sufficient angular resolution, however it is common to acquire many more - in fact, the HARDI protocol used in this thesis acquired 64 unique diffusion directions.

Image distortion in diffusion MRI

Fast data acquisition methods are required in order to capture the decay of T2* following diffusion weighting, therefore most diffusion imaging studies employ EPI sequences for signal readout. As previously mentioned, these sequences are vulnerable to image artifacts associated with local field perturbations due to the long repetition time for each sequence. These include: signal variation and geometric distortion in the phase-encode direction (known as EPI distortion) due to variations in magnetic susceptibility, usually around tissue/air boundaries or metal implants; spatial distortion or ghost images due to field perturbations from the build up of induced eddy currents in the main or gradient fields; and signal loss from spin dephasing over the length of the acquisition, reducing the signal contribution from high frequencies acquired later in the readout trajectory, causing image blur. Modern MR hardware operates parallel arrays of receiver coils to reduce the time taken to traverse k-space in acquisition, helping to mitigate these effects. Additionally, re-phasing gradients are commonly applied at the end of each frequency encoding gradient oscillation to prevent the build-up of phase-incoherence. While modern

acquisition methods have reduced the magnitude of common EPI artifacts, it is always necessary and beneficial to apply corrections in pre-processing to minimise the impact of these well known artifacts. Notably, the diffusion acquisition used in this thesis includes at least one image taken in the reverse phase-encoding direction, used to correct for the EPI distortion that occurs in the direction of phase-encoding (Andersson & Sotiropoulos, 2016; Andersson et al., 2003). Other corrections include denoising (Tustison et al., 2010), bias field correction (Tustison et al., 2010) and removal of ring artifacts (Kellner et al., 2016).

Chapter 4

Pre-Processing and Analysis Methods

The field of neuroimaging research has greatly expanded as new and more sophisticated technologies become available, with almost countless ways to examine brain structure, function and pathology through the use of MRI, PET, diffusion imaging, single-photon emission computerized tomography (SPECT), functional MRI (fMRI), electroencephalography (EEG), and magnetoencephalography (MEG), among others. Different imaging methods offer unique opportunities to probe characteristics of the human brain in vivo, however each presents its own challenges in the path from raw image to meaningful inference. This chapter will discuss key steps from the MRI and PET pre-processing pipeline used in this thesis, and describe approaches to analysis of neuroimaging data.

As pre-processing and analysis of high angular resolution diffusion imaging (HARDI) MRI data required a highly specialised approach, this will be discussed in the HARDI chapter (Chapter 7).

4.1 Pre-processing of neuroimaging data

Pre-processing of PET and MR image data in this study was carried out using using CAT12 (r934, (Gaser, 2020)), a toolbox of Statistical Parametric Mapping (SPM12) (v6685, (FIL, 2016)), in MATLAB (v9.0.0 [R2016a]), designed specifically for the analysis of brain images.

4.1.1 Coregistration and normalisation

In order for inter- or intra-subject voxel-wise analysis to take place, subject image data must first be pre-processed to align all images into a common anatomical space, accounting for individual differences in brain shape, size, and location in the scanner geometry. Spatial alignment of image data is generally performed over several steps, known collectively as co-registration and normalisation. Co-registration generally refers to the mapping of within-subject data to a structural image of high anatomical resolution, while normalisation refers to the spatial warping of inter-subject data to a common anatomical space. Both are required in order to extract robust comparisons across the whole brain from image data spanning multiple modalities.

Co-registration

Within-subject co-registration to structural MRI is achieved using an iterative least squares approach, optimising a 6 parameter rigid body (affine) spatial transformation (Ashburner et al., 2015). Transformation parameters are estimated to best match the input image to the structural reference image by convergence to selected matching criterion, in this case mutual information (MI) of voxel pairs (Collignon et al., 1995). MI is a measure of the mutual dependence of two variables and is assumed to be maximised when the two images are in register. In order to obtain faster convergence, the images and the histogram were smoothed slightly by the routine to make the cost function as smooth as possible (Ashburner et al., 2015). This also reduced the chance of the algorithm getting caught within local minima.

Normalisation

Spatial normalisation to standardised space is a multi-step process that involves some initial processing of the structural image, in order to reduce the effect of noise and bias, estimate tissue segments, and produce individual subject warp fields, that may then be used in normalisation. Segmentation of the brain into the main tissue classes (grey matter, white matter, cerebrospinal fluid and bone) is an important step in quantitative morphology, as many brain structures are anatomically defined by the boundaries of these tissues. It is important that warp fields are informed by these segments in order to accurately warp specific structures, and retain individual anatomical characteristics in normalised space.

The CAT12 processing pipeline includes denoising, internal resampling, and bias correction, and obtains a starting estimate of tissue segments using unified tissue segmentation (Ashburner & Friston, 2005). Unified segmentation is initialised using maximum likelihood (ML) estimation from standard tissue probability maps (TPMs). The output segments from this step merely provide a starting point for more refined segmentation, that will ultimately be performed independent of tissue priors. This has the benefit of being less sensitive to tissue-specific noise, as can occur in segmentation via maximum likelihood estimation.

The output from unified segmentation is first skull-stripped, parcellated into the left and right hemisphere, subcortical regions and the cerebellum, and a local intensity normalisation applied within each parcel to reduce the effect of artifactual tissue-specific variation. Final tissue segmentation is performed using an adaptive maximum a posteriori (AMAP) model (Rajapakse et al., 1997), refined by partial volume estimation of the tissue fraction within each voxel (Tohka et al., 2004). The AMAP segmentation method avoids the use of tissue priors by applying an iterative conditional model, where initial model parameters are estimated using local information from the image data, and the output segmentation then informs the model parameters for the next iteration.

The segments are then spatially normalised to the corresponding segments in MNI space[1] using DARTEL (Diffeomorphic Anatomical Registration using Exponentiated Lie algebra (Ashburner, 2007)). The spatial deformations required to align an individual set of segments to MNI space are output by DARTEL as a subject-specific warp field, which may be applied within SPM to any image that has been co-registered to subject structural space to warp that image to standard space. This ensures voxel-level correspondence across the study-dataset.

The normalisation of image data may be applied with or without modulation. This refers to a rescaling of the spatially normalised image by the Jacobian determinant of the deformation (Ashburner et al., 2015), in order to compensate for any dilution/concentration of image intensity that may arise from spatial normalisation. It is a good idea to apply this when normalising structural images such as the grey matter segments, so that total tissue volume is preserved, however modulation of lower resolution or non-structural data

[1]The current standard MNI template used in this study is ICBM152, an average brain template of 152 MRI scans of normal brains registered by a 9-parameter affine transformation to the previous MNI template, MNI305 (created from the average of 305 normal brains registered to the Talairach Atlas). MNI space has largely replaced Talairach coordinates as the standard template for brain image normalisation.

may result in a loss of disease-related image variance. In this thesis, grey matter images are normalised to standard space with modulation, while quantified ASL MRI and FBB PET are normalised without.

Note that the co-registration and normalisation methods described here are not applied in the pre-processing of HARDI data for fixel-based analysis (FBA), as direct voxel-wise comparisons are not being carried out between HARDI and the other imaging datasets. HARDI subject data are co-registered to a study-specific space without the use T1-weighted MRI, which will be described in Chapter 7.

4.1.2 Quantification of PET image data

As discussed in the previous chapter (see section 3.1.6), PET images of the activity concentration within the brain must be normalised according to whole body activity and individual variance in non-specific and unbound radiotracer fraction. Converting spatially normalised PET image data to standard uptake value ratio (SUVR) allows between subject comparison and inter-modality correlation analysis. Here the reference region was chosen as the whole cerebellum (Bullich et al., 2017), as recommended by the Centiloid Working Group for later conversion to centiloids (CL) (Klunk et al., 2015). This thesis uses the Centiloid project whole cerebellum and standard centiloid cortical grey matter masks for extraction of mean voxel values from the cerebellum and grey matter cortex respectively.

The creation of SUVR images from spatially normalised images of FBB radioactivity is carried out using SPM PET, and is relatively straightforward. Firstly, the average activity concentration within the voxels defined by the whole cerebellum mask is extracted. All other values within the PET image are then normalised to the mean within this reference region, giving the SUVR image. Mean SUVR values in selected regional ROI may be extracted following the same process used for the reference region, for analysis of regional amyloid deposition.

The SUVR images are then converted to CL, by first applying a method-scaling factor (derived in centiloid calibration, see section 5.6.4) to account for a non-standard acquisition and processing method, followed by scaling to CL using the FBB-to-CL conversion

equation (C. C. Rowe et al., 2017). Mean cortical values of both SUVR and CL are extracted from the standard centiloid cortical region - these values are thereafter referred to as global values for SUVR and CL respectively. In order to carry out whole-brain voxelwise analysis, images must be smoothed to reduce the proportion of residuals exhibiting non-normal distribution, and to reduce the effect of any remaining inter-subject misalignment. The amount of smoothing applied is a matter of trade-off between spatial resolution and normality of the data. Here, an 8 mm isotropic Gaussian kernel is used to smooth images.

4.2 Statistical analysis in Neuroimaging

There are many ways to approach analysis of neuroimaging data, and methods must be carefully considered based on the data type and analysis objectives. In neuroimaging, the goal may be classification, prediction, treatment response, or determining the functional, pathological or structural basis for a particular neurological disease or psychiatric disorder. To that end, studies often investigate many aspects of the clinical disease picture, such as cognition, learning and memory, structural connectivity, functional connectivity or localisation through response to stimuli or task performance, resting state brain function, language, or mood. Here, I investigate brain structure and pathology as it relates to measures of cognition and risk of developing dementia, with the overall future objective to be able to classify or predict cognitive impairment in PD from imaging data. Robust statistical methods are required to extract meaningful inferences from highly complex and often vast amounts of data, and in some cases facilitate inter-modality comparisons.

4.2.1 The general linear model

Statistical tests of association are typically based on variations of the general linear model (GLM). The GLM refers to a group of statistical analysis methods centred on inferential tests of hypothesis or analysis of variance (Friston et al., 2007). Analysis of variance and multiple regression analysis are both implementations of the GLM. More generally, the GLM also includes a number of types of analyses; these include simple t-tests, one-way ANOVA or more complex correlation and linear regression analyses.

4.2.1.1 Mathematical basis of the GLM

The core idea behind the GLM is that an observed response variable Y may be expressed in terms of a linear combination of independent explanatory variables X, weighted by an optimised coefficient β, plus a well behaved error term ϵ, usually representative of noise in the dataset (Friston et al., 2007). The basic form of the GLM for the i^{th} observation in Y, in the case of p multiple regressors, is as follows:

$$y_i = \beta_0 + \beta_1 X_{i,1} \cdots + \beta_p X_{i,p} + \epsilon_i \tag{4.1}$$

where β_0 is a dummy variable providing an intercept. This can be written in matrix form as:

$$y = \beta^T X + \epsilon \tag{4.2}$$

where the intercept and coefficients to be estimated are gathered within the transpose of the weight matrix, β^T. The goal of linear regression is to compute the coefficient values $\beta^T X$, or model parameters, that achieve the best fit of the model given by the design matrix X to the observed set of data points y.

The GLM is heavily dependent on the form of the design matrix X, wherein the columns of explanatory variables correspond to experimental confounds or covariates. Columns are defined as confounds or components of interest by the form of the contrasts applied within the GLM. For example, a multiple linear regression of the amyloid FBB PET data with subject cognitive score may be performed by accounting for any variation in voxel intensity related to age and sex, as these are known confounds in brain perfusion, and testing for a positive association between FBB PET data and cognitive score. Significance on this contrast would thus indicate a positive correlation of the data with cognitive score, accounting for age and sex. The form that the design matrix of the GLM takes allows for a wide variety of study designs, and is employed in this thesis to investigate group differences, as well as association with continuous metrics.

Methods of estimating the model parameters, and thus formulating statistical inferences from the GLM, generally fall into either the 'frequentist' or 'Bayesian' category, which are primarily distinct in terms of their treatment of probability.

4.2.2 Frequentist vs. Bayesian regression analysis

The choice of frequentist or Bayesian inference methods is one that must be made based on the known properties and limitations of the data, with both providing advantages and drawbacks in certain situations. It is useful to consider both approaches, and decide which is appropriate.

Frequentist regression

The frequentist approach to linear regression is based on long-run sampling frequencies, such that the probability of an event occurring is representative of the number of observations of that event within a population. In the context of multivariate regression analysis, unknown parameters are assumed to have a fixed non-random value, and the model attempts to obtain point-estimates of those values (with associated error estimates), given knowledge about the population - that is, the probability of the data, given the model. A frequentist may approach solving the GLM given by equation 4.2 by obtaining the parameters β^T that minimise the squared residual differences (SRD) between the known data-points y and the estimated model outputs $\hat{y}$:

$$SRD(\beta) = \sum_{i=1}^{N}(y_i - \hat{y})^2 = \sum_{i=1}^{N}(y_i - \beta^T x_i)^2 \tag{4.3}$$

thus the summation is given by, and dependent on, the number N of training data points. There is assumed to be one 'true' solution for the parameters β that minimise the error - however, as this cannot be known exactly, we estimate the most probable β given the inputs X and outputs y. The solution to equation 4.3, giving an estimate of the model parameters $\hat{\beta}$, takes the form:

$$\hat{\beta} = (X^T X)^{-1} X^T y \tag{4.4}$$

This is known as ordinary least squares (OLS) estimation. This method thus gives a single estimate for the model parameters, fitting the chosen design matrix, based only on the training data points in y. New data points may then be estimated by simple application of the predictive model, $\hat{y} = \hat{\beta}^T X$.

For sufficiently large sample sizes and relatively simple model designs, a frequentist approach is an efficient method of accurately estimating effects within the data. These models are also relatively easy to interpret by way of generated p-values, where given that the null hypothesis is true, the p-value represents the probability of obtaining results as extreme as the observed results. Sufficient evidence to reject the null hypothesis is assumed when p-values are less than a selected cut-off, by convention, $p < 0.05$, 0.01, or 0.001, such that there is 95%, 99% or 99.9% confidence in the result, respectively. However, this method assumes that all information required to accurately estimate the model parameters is contained within the data, and in the context of small sample sizes (as in many neuroimaging studies) or increasing model complexity, a frequentist approach can lead to nonconvergence, inadmissible parameter solutions, or inaccurate estimates (Smid et al., 2020).

In these instances, a better estimate may be obtained if the model is supplied with additional information. Bayesian regression achieves this with the use of prior information.

Bayesian regression

A Bayesian model instead assumes the model parameters to have a probability distribution rather than a fixed value. For an observed set of data points, there exists a set of solutions given by the so-called posterior probability distribution - the probability of the model, given the data.

As an example, the observed data points y may be assumed to be generated by a normal (Gaussian) distribution:

$$y \sim N(\beta^T X, \sigma^2 I) \tag{4.5}$$

where the distribution is characterised by a mean (given by the product of the transpose correlation matrix β^T and the design matrix X) and a variance (given by the square of the standard deviation σ in matrix form). Here, the goal is to determine the posterior

distribution of the model parameters that best explains the probability distribution of the data, given some prior knowledge about the form the posterior should take. Bayes theorem states that the posterior distribution is equal to likelihood of the data, multiplied by the prior probability of the posterior, and divided by a normalisation constant:

$$Posterior = \frac{Likelihood \times Prior}{Normalisation} \tag{4.6}$$

Or, more formally:

$$P(\beta|y, X) = \frac{P(y|\beta, X) \times P(\beta|X)}{P(y|X)} \tag{4.7}$$

The use of prior information is important for low numbers of data points, where the probability distribution of the data contains less information to inform the model. Deriving the full shape of the posterior distribution involves randomly sampling posteriors in parameter space, and allowing the estimate to change as more evidence is gathered. The prior estimate provides an original starting point for this process, and subsequent posteriors are selected to improve the estimate through a method known as Markov chain Monte Carlo (MCMC). MCMC algorithms sample random posteriors in parameter space, selecting a posterior only if it improves upon the model estimation from the previous step, thus a chain of posteriors is formed. All points have an equal chance of being sampled, thus the density of accepted points in the estimated posterior distribution is more likely to be proportional to the actual posterior distribution. Furthermore, as the number of data points in the sample increases, the posterior estimation becomes less dependent on priors and the solution converges to that given by the frequentist approach. However, if one is confident in the chosen prior applied to the data, this can be a robust method of estimating model parameters for small data sets.

The output of a Bayesian model fit is a distribution of possible parameters based on the data and the prior, where the uncertainty in our estimation is quantified by the range of the distribution, known as the credible interval (CI), somewhat analogous to the confidence interval in frequentist statistics. Here, the 95% credible interval for a parameter is the range of values for which the subjective probability of the parameter lying between those values is 95%, considered in this context to convey strong evidence. Thus, a positive

or negative net effect given by a parameter, where the 95% CI does not include zero, conveys strong evidence for the existence of the effect (or is 'significant' from a frequentist approach), suggesting an association between the independent variable and the response variable.

It should be noted that, while there may be a 'significant' effect associated with a variable, the range of possible values within the 95% CI might be large, representing a large uncertainty in our estimation of the effect. It is useful to evaluate predictive model fits to the data using analytic methods, such as by evaluating leave-one-out information criterion (LOOIC). In R, the output of leave-one-out cross validation gives the estimated predictive accuracy of a Bayesian model fit (expected log predictive density, denoted $elpd_{loo}$), and the approximate standard error (SE). The LOOIC is simply -2*$elpd_{loo}$ (converted to deviance scale). These values take on meaning when compared against the output from another model - a lower LOOIC score, by at least twice the standard error of the estimated difference between the two models, indicates a model with a better fit. This process will be used to compare different models to determine the importance of individual predictors.

In this thesis

Both frequentist and Bayesian methods are used for statistical analysis in this thesis. Simple group differences and voxel-wise analysis with minimal covariates are investigated using a frequentist model, and a Bayesian method is used to generate more complex predictive models, investigating the effect of multiple continuous variables.

Bayesian model estimation is performed in this thesis using the "brms" (v2.2.0) package (Bürkner, 2017), and model comparison was carried out using the loo package (Vehtari et al., 2015, 2016) in R (v3.4.4).

4.2.3 Parametric and non-parametric statistical inference

This study used both parametric and non-parametric methods for voxelwise statistical inference. The difference between the two rests on certain distributional assumptions (or lack thereof) made by each method, the fulfilment of which affects the power of each method to obtain significant results. Parametric methods assume that the data and model residuals come from a population that follows a known probability distribution, described

by a fixed set of parameters. Non-parametric methods do not make distributional assumptions and allow these parameters to change, and thus may supervene in terms of sensitivity when distributional assumptions are violated. This may occur when degrees of freedom are small and voxel sizes are large in relation to smoothness. Should the probability distribution assumptions remain true, parametric methods yield greater accuracy and sensitivity and require less computing power, but are regarded as somewhat less robust in a general sense.

In this thesis, non-parametric methods are used in the voxel-wise analysis of image data, performed using a permutation-based inference tool. For each contrast, the null distribution is generated over 5000 permutations, corrected for multiple comparisons using a family-wise error correction method known as threshold-free cluster enhancement (TFCE) (Winkler et al., 2014).

4.2.4 Principal Component Analysis

Principal component analysis (PCA) is a data reduction method based on orthogonal linear transformation, wherein a large number of correlated variables are transformed to give a smaller number of uncorrelated principal components. The objective when using PCA is to achieve useful dimension reduction by extracting a few principal components that describe most of the variance with the least loss of information (Razifar et al., 2009).

The data is shifted onto an axis that best fits the variance, and a set of uncorrelated eigenvectors are formed to describe the data according to this new axis. The eigenvectors along which the variation in the data is maximal are known as the principal components (PCs) (Ringnèr, 2008). The number of PCs will initially equal the number of samples in the data, and the associated size of the eigenvalue represents the amount of unit variance encompassed by that PC. The first few principal components usually account for much of the variance within a data-set, thus the remaining principal components may be rejected to reduce dimensionality without significant loss of information(Razifar et al., 2009). The number of principal components chosen is often done based on the number of components that represent a certain percentage of the variance. By convention, this is usually in the range of 70%-90%, however in the case of high dimensionality of the sample this may result in an overly large number of necessary PCs, and the percentage should be set lower (Jolliffe, 2002). Another method is by selecting only those components that have

an eigenvalue greater than 1, representing a non-trivial contribution of that PC in the overall data variance. Both methods are somewhat arbitrary, and decisions should be made based on the data and extracted PCs (Jolliffe, 2002).

This thesis aims to select the principal components of the baseline amyloid FBB data that represent at least 70% of the total variance in the data. The relative expression of each component within each subject is examined in Bayesian regression analysis to determine if the variance they represent within each subject is statistically associated with the variable of interest, in this case, conversion to dementia during longitudinal follow-up. Thus, PCA represents another method of spatially analysing amyloid deposition, that may be more sensitive to existing patterns within the data than direct voxel-wise methods.

4.2.5 Survival analysis

Survival analysis refers to a set of statistical models used to evaluate duration of time until the occurrence of an event of interest. While the classic application of survival analysis is concerned with survival to a time t after a disease diagnosis, one can also examine the effect of variables of interest on the probability of an individual experiencing an event (not necessarily death) at time t. This is known as the hazard probability, investigated using Cox proportional hazards regression analysis, and can be applied to evaluate both quantitative or categorical variables.

The Cox proportional hazards model is expressed by the hazard function, h(t), and is similar in form to the GLM described previously. In the case of i covariates, the hazard function may be given by:

$$h(t) = h_0(t) \times exp(b_1x_1 + b_2x_2 + ... + b_ix_i) \tag{4.8}$$

Where t is the survival time to event, the coefficients b_i of variables x_i represent the effect size of the covariates, and $h_0(t)$ is the baseline hazard, representing the risk of the event occurring in the absence of the examined covariates.

The quantities $exp(b_i)$ are known as hazard ratios, and a value greater than 1 indicates a positive association between the i_{th} variable and the event hazard, and a negative association with length of survival.

The purpose of hazard regression in this thesis is to examine the relative risk presented by amyloid positivity at baseline in the development of dementia over time, given observations of conversion to dementia in our cohort over four years longitudinal follow-up. Survival analysis was carried out using the survival (v2.44-1.1) package in R (v3.4.4).

Chapter 5

Beta Amyloid Deposition Is Not Associated with Cognitive Impairment in Parkinson's Disease

Please note

The following Chapter has been published in Frontiers of Neurology (Melzer et al., 2019), and is presented here in journal format, with some modification. These include all supplementary material and the addition of two sub-analyses that were not included in the original publication.

The methods used for participant recruitment, neuropsychological assessment, image acquisition and image processing described in Chapter 5 are also relevant to the longitudinal arm of this study, detailed in Chapter 6.

5.1 Author Contributions

I performed the image processing, statistical analyses and interpretation of results in this chapter, and produced the primary manuscript.

TM and DJM contributed to image processing, statistical analyses, results interpretation, and draft manuscript. All authors contributed to manuscript revision, read, and approved the submitted version.

The NZBRI Study of Parkinson's Disease

The larger study of Parkinson's disease at the New Zealand Brain Research institute was conceptualised and designed by TM, DJM, MM, TP, DHM, JD-A, and TA. TM, MM, DHM, RK, DJM, LL, JD-A, and TA obtained funding for the study. RK, LL, DJM, MM, TP, and SM provided administrative, technical, and material support. All authors contributed to acquisition, analysis or interpretation of data.

5.2 Abstract

The extent to which Alzheimer neuropathology, particularly the accumulation of misfolded beta-amyloid, contributes to cognitive decline and dementia in Parkinson's disease (PD) is unresolved. Here, we used [^{18}F]-Florbetaben PET imaging to test for any association between cerebral amyloid deposition and cognitive impairment in PD, in a sample enriched for cases with mild cognitive impairment. This cross-sectional study used Movement Disorders Society level II criteria to classify 115 participants with PD as having normal cognition (PDN, n = 23), mild cognitive impairment (PD-MCI, n = 76), or dementia (PDD, n = 16). We acquired [^{18}F]-Florbetaben (FBB) amyloid PET and structural MRI. Amyloid deposition was assessed between the three cognitive groups, and also across the whole sample using continuous measures of global cognitive status, average performance in memory domain tests, and total grey matter volume (normalised by individual total intra-cranial volume). Outcomes were cortical FBB uptake, expressed in centiloids and as standardized uptake value ratios (SUVR) using the Centiloid Project whole cerebellum region as a reference, regional SUVR measurements, and grey matter volume. Additionally, arterial spin labelling (ASL) MRI of perfusion was investigated for association with amyloid deposition using whole-brain analysis. FBB binding was higher in PDD, but this difference did not survive adjustment for the older age of the PDD group. We established a suitable centiloid cut-off for amyloid positivity in Parkinson's disease ($CL_{cut\text{-}off}$=31.3), but there was no association between FBB binding and global cognitive or memory scores.

The failure to find an association between PET amyloid deposition and cognitive impairment in a moderately large sample, particularly given that it was enriched with PD-MCI patients at risk of dementia, suggests that amyloid pathology is not the primary driver of cognitive impairment and dementia in most patients with PD.

5.3 Introduction

Motor impairment is the cardinal feature of early Parkinson's disease (PD), but progressive cognitive impairment and dementia (PDD) eventually become major debilitating symptoms for patients (Aarsland et al., 2017). PDD arises in over 80% of 20-year survivors (Hely et al., 2008), leading to substantial caregiver and financial burden, reduced quality of life, early institutionalization and premature death (Jones et al., 2017). Progression to PDD involves a complex, multisystem brain degeneration (Aarsland et al., 2017; Irwin et al., 2013). Alzheimer's disease (AD) neuropathology, including misfolded beta-amyloid (Aβ), may influence the emergence of PDD by acting synergistically with α-synucleinopathy (Compta et al., 2011; Irwin et al., 2013, 2018; P. T. Kotzbauer et al., 2012; Lashley et al., 2008). Neuropathological investigations of Aβ suggest an association with cognitive impairment and increased deposition in PDD, at least in a subset of patients (Compta et al., 2011, 2014; Irwin et al., 2013; Sabbagh et al., 2009; Shah et al., 2016). Similarly, increased concentrations of Aβ in cerebrospinal fluid have been associated with cognitive dysfunction and dementia in PD (Buongiorno et al., 2011; Compta et al., 2012; Goldman et al., 2018; McMillan & Wolk, 2016; Siderowf et al., 2010), although some studies have not found this relationship (Dolatshahi et al., 2018; Kang, 2018). While both neuropathological and CSF markers suggest an association with cognitive decline, the cerebral deposition of amyloid is, however, not ubiquitous and the neuropathology underlying the development of PDD remains heterogeneous (Compta et al., 2013; Adler et al., 2010; K. Jellinger, 2012).

In vivo imaging of α-synuclein is currently not possible, but positron emission tomography (PET) imaging allows an in vivo test of an association between amyloid deposits and cognition in PD (Gomperts et al., 2013; Petrou et al., 2015). Amyloid PET imaging, however, has produced conflicting results in PD, especially with respect to cognitive decline. Gomperts and colleagues (Gomperts et al., 2013), found no difference in amyloid accumulation in the precuneus between a group of PD patients with mild cognitive impairment

(PD-MCI) and cognitively normal patients at baseline, but the baseline presence of amyloid was weakly associated with cognitive decline an average of 2.5 years later, suggesting that amyloid may be a better marker of future rather than current cognitive status in PD. While Fiorenzato et al. (Fiorenzato et al., 2018), suggest a modest association with cognitive decline, other in vivo amyloid imaging studies suggest that amyloid deposition may occur in only a minority of PD patients, even in PDD (Akhtar et al., 2017; Edison et al., 2013; Gomperts et al., 2012; Lee et al., 2018; Mashima et al., 2017; Petrou et al., 2015, 2012; Winer et al., 2018). However, these previous PET studies have used relatively small samples and the robustness of their findings may be compromised by low statistical power, lack of thorough cognitive characterization, or not accounting for age.

We therefore investigated the relationship between amyloid deposition and cognitive impairment in a cohort of PD participants using [^{18}F]-Florbetaben (FBB) PET imaging. Participants were recruited from a large, cognitively well-characterized clinical population that included cases with normal cognition (PDN), mild cognitive impairment (PD-MCI) and dementia (PDD). Patients meeting PD-MCI criteria are at a 7-fold higher risk of conversion to PDD over a 4-year period compared to patients who do not meet these criteria (Wood et al., 2016). Thus, the sample was enriched by recruiting a large proportion of PD-MCI patients; this is a group in whom intervention to prevent progression to dementia is particularly pertinent.

Since previous studies have suffered from inconsistent and variable standardization procedures, we used centiloid scaling in the present investigation. The centiloid scale facilitates direct comparison of amyloid deposition across different imaging centers, analysis methods, amyloid ligands (incorporating ^{11}C- and ^{18}F-based ligands), and diseases (Klunk et al., 2015; C. C. Rowe et al., 2017). This is achieved by applying a linear scaling to amyloid PET data to an average value of zero in high-certainty amyloid-negative subjects, and to an average of 100 in typical AD subjects (Klunk et al., 2015). In this first application of centiloid standardization in PD, we (1) investigated the relationship between amyloid deposition and cognitive impairment in a group of well-characterized PD participants representative of the broad cognitive spectrum, and (2) established the distribution of centiloid values across the cognitive spectrum in PD.

Additional sub-analyses

Cerebral blood flow measured by arterial spin labelling MRI (ASL MRI) has been reported to show associations with cortical Aβ deposition in the context of Alzheimer's disease and mild cognitive impairment, in subjects ranging from cognitively normal (CN), to early MCI, late MCI and AD (Mattsson et al., 2014). In a study of 182 participants from the Alzheimer's Disease Neuroimaging Initiative (ADNI), Mattson et. al. reported a reduction in CBF associated with higher amyloid load measured with [^{18}F]-Florbetapir within several ROI, independent of study subgroup, suggesting that amyloid deposition and CBF may interact in healthy aging and early MCI. They noted a possible early and late effect of elevated amyloid, with reductions in CBF occurring in early disease, and loss of grey matter volume occurring in late MCI and dementia. Another study of non-demented older adults (27 CN and 16 amnestic MCI) reported lower global CBF in those displaying higher levels of amyloid measured using [^{11}C]-PiB PET (Bangen et al., 2017). These studies suggest that reduced CBF may be an important mechanism leading to cognitive decline, and that this affect may be exacerbated by the presence of high amyloid load. As our cohort is enriched for PD with mild cognitive impairment, it will be of use to examine any possible interactive effect between CBF and amyloid that occurs in early disease, ahead of development of dementia. I investigated both whole brain CBF, measured with ASL MRI, and global grey matter volume in relation to abnormal amyloid load in this cohort.

5.4 Materials and methods

As part of an ongoing longitudinal study, a convenience sample of 118 PD participants meeting the UK Parkinson's Disease Society's criteria for idiopathic PD (35)(Hughes et al., 1992) was recruited from volunteers at the Movement Disorders Clinic at the New Zealand Brain Research Institute, Christchurch, New Zealand. We invited people representative of the broad spectrum of cognitive status in PD to participate, i.e., from normal cognition to dementia, although we particularly encouraged participation from individuals with PD-MCI. Exclusion criteria included atypical Parkinsonian disorders; prior learning disability; previous history of other neurological conditions including moderate-severe head injury, stroke, vascular dementia; and major psychiatric or medical illness in the previous 6 months. Neuroradiological screening (RJK) excluded two participants

with multifocal infarcts and one in whom part of the bolus injection extravasated into the soft tissue. Participants completed a neuropsychological battery, MRI scanning session, and [^{18}F]-Florbetaben (FBB) PET imaging. MRI was not acquired for one subject due to having titanium implants. A previous T1-weighted structural image obtained before the injury was used in pre-processing. All participants gave written informed consent, with additional consent from a significant other when appropriate. The study was approved by the regional Ethics Committee of the New Zealand Ministry of Health (No. URB/09/08/037).

5.4.1 Diagnostic criteria and assessment

Comprehensive neuropsychological assessment fulfilling the Movement Disorders Society (MDS) Task Force Level II criteria was used to diagnose PD-MCI (Wood et al., 2016; Litvan et al., 2012). Five cognitive domains were examined (executive function; attention, working memory and processing speed; learning and memory; visuospatial/visuoperceptual function; and language; see table B.1 in the Appendix for tests included in each domain) (Wood et al., 2016). Within each cognitive domain, standardized scores from the constituent tests were averaged to provide individual cognitive domain scores; global cognitive performance for each participant was then expressed as an aggregate z score obtained by averaging four domain scores (language domain excluded). PD-MCI cases had unimpaired functional activities of daily living, as verified by interview with a significant other, and scored 1.5 SD or more below normative data on at least two measures within at least one of the five cognitive domains (Wood et al., 2016). Dementia was defined using MDS criteria as significant cognitive impairments (2 SD below normative data) in at least two of five cognitive domains, plus evidence of significant impairment in everyday functional activities, not attributed to motor impairments (Emre et al., 2007). Participants also completed the Montreal Cognitive assessment (MoCA). All assessments and scans were performed with no disruption to participants' usual medication regimen. PD participants were classified as either cognitively normal (PDN, n = 23), with mild cognitive impairment (PD-MCI; n = 76), or with dementia (PDD; n = 16). Assessors were blinded to amyloid status.

Cognitive subgroup classification

Performance on each neuropsychological test is evaluated in terms of z-score, or the number of standard deviations (SDs) of the result from the mean in age, education and gender normative data for that test. Normal cognitive performance is indicated by test scores within 1.5 SDs of normative data. Failure to meet this threshold in two tests within a single domain is sufficient to classify a patient as PD with mild cognitive impairment. PD-MCI can also be diagnosed without this requirement, given noticeable deterioration in cognition over time in serial neuropsychological testing, exceeding the reliable change index (Litvan et al., 2012). In order to classify a patient as having PD with dementia, an impairment of the participants' ability to function in daily life unassisted must be indicated by their significant other. A score of at least 2 SDs below normative data in any single test within two of the five cognitive domains, in combination with impaired daily living, is sufficient to classify an individual as PDD.

5.5 Image data acquisition

5.5.1 Magnetic Resonance Imaging

T1-weighted MRI

MR images were acquired on a 3T General Electric HDxt scanner (GE Healthcare, Waukesha, USA) with an eight-channel head coil. A volumetric T1-weighted (inversion-prepared spoiled gradient recalled echo (SPGR), TE/TR=2.8/6.6ms, TI=400ms, flip angle = 15 deg, acquisition matrix = 256 × 256 × 170, FOV = 250mm, slice thickness = 1mm) was acquired to facilitate spatial normalization of FBB PET images. Additional T2-weighted and T2-weighted fluid-attenuated inversion recovery (FLAIR) images were acquired to enable a clinical read.

ASL perfusion MRI

Quantified whole brain perfusion was acquired by removing background contributions (proton density weighted images) from spiral, fast spin echo images prepared using pseudo-continuous arterial spin labelling (repetition time = 6 s, echo spacing 9.2 ms, post-labelling delay = 1.525 s, labelling duration = 1.5 s, eight interleaved spiral arms with 512 samples

at 62.5 kHz bandwidth and 30 phase encoded 5mm thick slices, NEX = 5, total scan time = 6 min 46 s, units: ml/100 g/min) (Dai et al., 2008). These images were acquired with the subject at rest with their eyes closed.

5.5.2 Positron Emission Tomography

[^{18}F]-Florbetaben (FBB) was manufactured in Melbourne, Australia, by Cyclotek Pty Ltd, and transported by air freight to Christchurch, New Zealand, with sufficient radioactivity for three participant doses, despite the passage of three half-lives in transit. After receiving an intravenous injection of 300 MBq ± 20% FBB, participants were scanned for 20 minutes in "list mode" on a GE Discovery 690 PET/CT scanner, at 90 minutes post-injection. Images were reconstructed using an iterative time-of-flight plus SharpIR algorithm. Standardized uptake value (SUV), defined as the decay-corrected brain radioactivity concentration normalized for injected dose and body weight, was calculated at each voxel. A low dose CT scan was acquired immediately prior to PET scanning for attenuation correction. Voxel size in the reconstructed 20 min PET image was 1.2 × 1.2 × 3.2 mm^3.

5.5.2.1 Classification of FBB images

Visual classification of FBB scans as positive or negative is accurate and reliable for detection of cases with histology-defined plaques (Seibyl et al., 2016). A neuroradiologist (RJK, with both in-person and e-training), blinded to cognitive status, rated each scan as amyloid-positive or -negative. That judgment was based on the assessment of FBB uptake in gray vs. white matter in the lateral temporal, frontal, posterior cingulate/precuneus, and parietal lobes (in accordance with the NeuraCeq^{TM} guidelines: `https://www.accessdata.fda.gov/drugsatfda_docs/label/2014/204677s000lbl.pdf`). Example images of FBB positive and negative scans, displaying either very high or very low cortical uptake of FBB, can be found in figure 5.1.

An additional approach using standardized uptake value ratios (SUVR) or centiloids (see below) was also used to categorize FBB scans. An ROC analysis [using the R package "pROC" (Robin et al., 2011)] was used to identify the optimum centiloid cut-off to separate positive and negative scans.

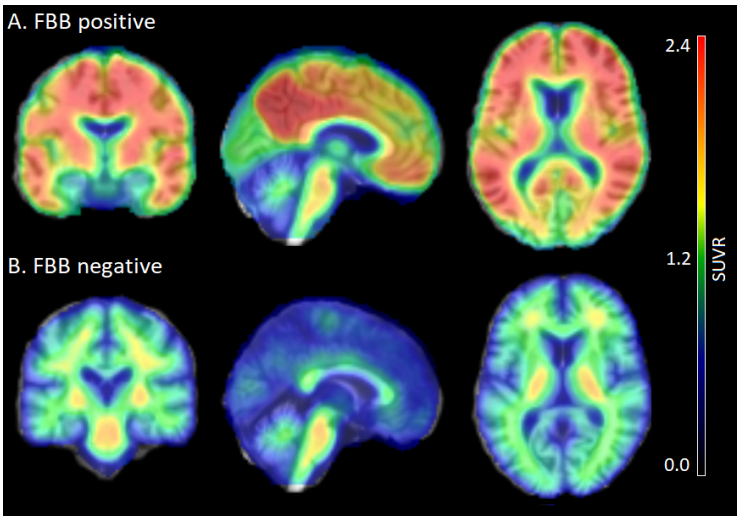

FIGURE 5.1: Example FBB PET images given in standard uptake value ratio (SUVR) normalised to the cerebellum, overlaid on skull-stripped T1-weighted structural MRI images. Visual assessment by a trained neuroradiologist classified these subjects as either (A) FBB PET positive, or (B) FBB PET negative.

5.6 Image processing

5.6.1 Structural MRI

CAT12 (r934, http://www.neuro.uni-jena.de/cat/), a toolbox of SPM12 (v6685, http://www.fil.ion.ucl.ac.uk/spm/), running in Matlab 9.0.0 (R2016a), was used to process T1-weighted structural images (figure 5.2[A]). Images were bias corrected, spatially normalized via DARTEL (using the MNI-registered template provided within CAT12), modulated to compensate for the effect of spatial normalization, and classified into gray matter (GM), white matter (WM), and cerebrospinal fluid (CSF), all within the same generative model (Ashburner & Friston, 2005) (figure 5.2). Estimated total grey matter volume was extracted from the segmented grey matter images and normalised by the total intracranial volume (TIV) of each subject (to account for individual head-size), giving a global measure of grey matter volume (GM_{vol}).

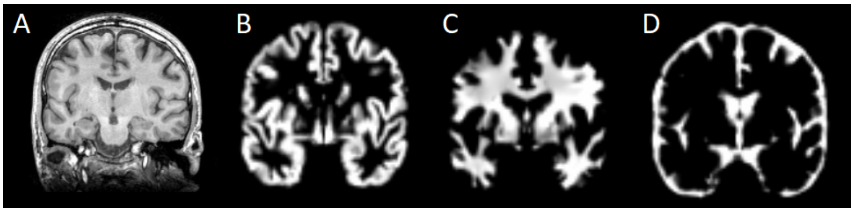

FIGURE 5.2: Tissue segmentation and normalisation to standard space in T1-weighted structural MRI pre-processing. Raw T1-weighted images (A) display considerable anatomical variation between subjects. Co-registration and normalisation aligns subject anatomy with standard MNI space, and produces tissue segments of (B) grey matter, (C) white matter and (D) cerebrospinal fluid (CSF).

5.6.2 Arterial Spin Labelling MRI

ASL perfusion images were first quantified to give absolute perfusion values at each voxel, following the quantification process described in Chapter 3, using equation 3.16. The quantified CBF images were then co-registered to subject T1-weighted structural images and normalised to MNI space using the MRI-derived deformation fields. Mean cortical CBF was extracted from the standard centiloid cortical region. Lastly, CBF images were smoothed using an 8 mm isotropic Gaussian kernel for whole-brain analysis.

5.6.3 PET data

FBB PET images were coregistered to subject T1-weighted images and normalised to MNI space using the MRI-derived deformation fields. We then created a standardized uptake value ratio (SUVR) image in each individual by scaling to the mean radioactivity in the Centiloid project whole cerebellum reference region of interest. Mean cortical SUVR was extracted from the standard centiloid cortical region. SUVR images were also smoothed using an 8 mm isotropic Gaussian kernel for whole-brain analysis (figure 5.1).

5.6.4 Centiloid calibration

We performed a level 3 centiloid (CL) calibration to verify agreement between the 'standard' CL processing method (which utilized SPM8) and our 'non-standard' processing method (Klunk et al., 2015; C. C. Rowe et al., 2017), which utilized CAT12 normalisation.

FBB and structural MR images in 25 elderly subjects and 10 young controls (C. C. Rowe et al., 2017), and standard CL regions (whole cerebellum and cortex), were downloaded from the Global Alzheimer's Association Information Network (GAAIN: http://www.gaain.org). We created cortical SUVR values using our non-standard CAT12 normalization methodology for all FBB images, following the steps outlined above. We then compared our 'non-standard' cortical SUVR values to the published 'standard' cortical SUVR values available from the GAAIN images using a linear model, per (Klunk et al., 2015). We demonstrated that our non-standard processing pipeline does not introduce errors into the data, as required for correct calibration (Klunk et al., 2015). A scatter plot is displayed in figure 5.3, showing the relationship and linear equation linking $SUVR_{NS}$ (our

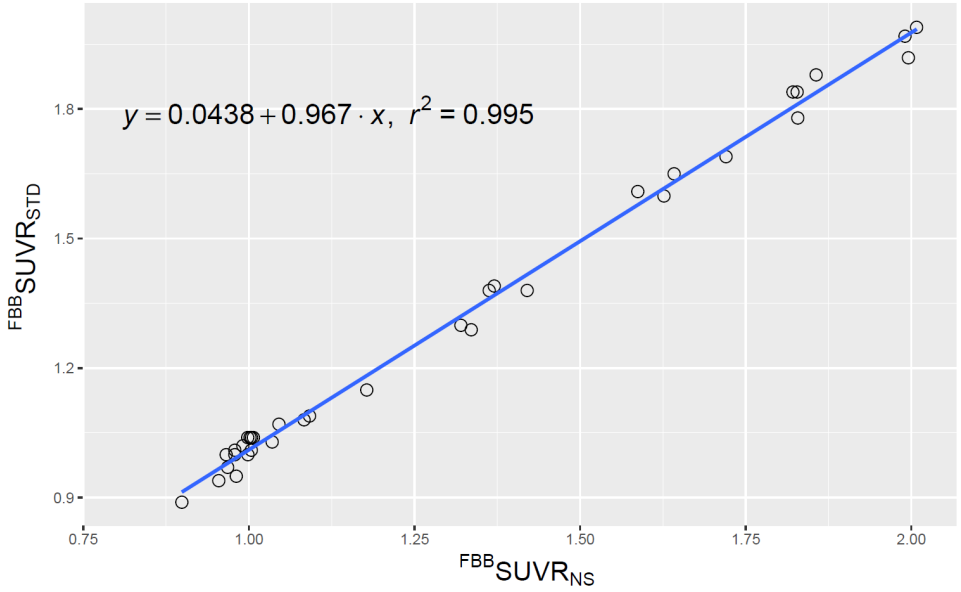

FIGURE 5.3: Scatterplot of published 'standard' cortical FBB SUVR values (FBB SUVR$_{STD}$) versus our 'non-standard' cortical FBB SUVR values (FBB SUVR$_{NS}$) using CAT12 normalization and from 25 elderly subjects and 10 younger controls described by Rowe and colleagues (C. C. Rowe et al., 2017) and downloaded from the GAAIN website. SUVR values were created using the Centiloid Project whole cerebellum reference region and cortical region. The calculated linear equation was used to correct our SUVR$_{NS}$ values to the standard method described by (Klunk et al., 2015). Previously produced in Supplementary material of (Melzer et al., 2019).

processing) and SUVR$_{\text{STD}}$ (standard processing (Klunk et al., 2015; C. C. Rowe et al., 2017)). This equation was then used to convert our cortical FBB SUVR$_{\text{NS}}$ values to cortical FBB SUVR$_{\text{STD}}$ values; these cortical SUVR$_{\text{STD}}$ values were then converted into CL units using the FBB-to-CL conversion equation (C. C. Rowe et al., 2017) (CL units = 153.4 $\times$ SUVR$_{\text{FBB}}$- 154.9). We then plotted calculated CL values obtained from our non-standard processing against the published CL values (figure 5.4). The expectation is that the slope will be between 0.98 and 1.02 (actual: 1.000), the intercept will be between -2 and 2 CL (actual: -0.0357), and $R^2 > 0.98$ (actual: 0.995). All parameters were well within the expected values for level 3 calibration of a non-standard method; hence, CL values reported in the current manuscript meet all specifications and can therefore be interpreted as a standardized, quantitative measure of amyloid deposition.

5.6.5 Regions of interest

While our principal analysis focused on cortical Aβ deposition, a number of both pathological and imaging studies suggest a potential relationship between Aβ accumulation in the

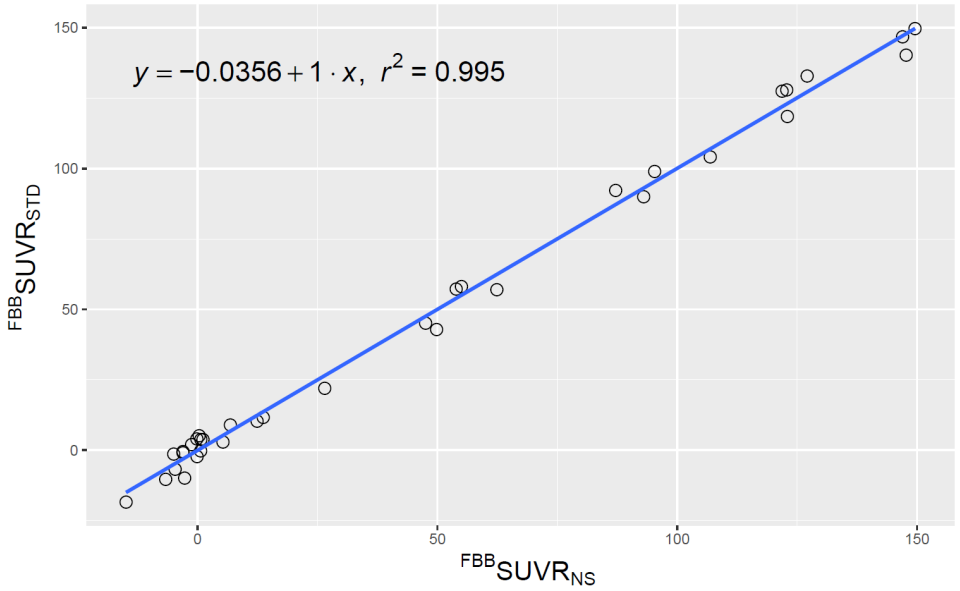

FIGURE 5.4: Scatterplot of the published CL values given by 'standard' processing (FBB CL_{STD}) versus our calculated CL values (FBB CL_{NS}) from the GAAIN dataset (C. C. Rowe et al., 2017). The plot shows excellent agreement between the two processing streams. Previously produced in Supplementary material of (Melzer et al., 2019).

striatum, thalamus, and globus pallidus and cognitive decline (Shah et al., 2016; Fiorenzato et al., 2018; Dugger et al., 2012; Kalaitzakis et al., 2008; Chen et al., 2017). We therefore specifically investigated *a priori* regions of interest (ROIs), including the caudate, putamen, thalamus, globus pallidus, and precuneus. The precuneus was included as a representative cortical region that exhibits very high amyloid load in AD (Becker et al., 2013). As standard centiloid regions do not exist for these structures, we calculated average SUVR within these regions defined by the Harvard-Oxford cortical and subcortical atlases in MNI152 space (Makris et al., 2006; Frazier et al., 2005; Desikan et al., 2006; Goldstein et al., 2007).

5.7 Statistical analysis

Bayesian models were fitted using the "brms" (v2.2.0) package (Bürkner, 2017) in R (v3.4.4). In each model, four chains with 2,000 iterations each were used to generate the posterior sample. Model comparison using LOOIC (leave-one-out information criterion) was performed when models included correlated predictors or predictive performance was being evaluated (Vehtari et al., 2017). A lower LOOIC score, by at least twice the standard error of the estimated difference between the two models, indicated a model with a better fit, and consequently whether a specific predictor significantly improved model fit.

Baseline demographic and neuropsychological group differences were analyzed using linear models (in brms). Analysis code and data are available at https://osf.io/5fqb9/.

5.7.1 ROI analysis

We investigated the relationship between FBB uptake and cognition in PD using Bayesian regression models, including age and sex as covariates.

1. We first tested for evidence of varying cortical amyloid deposition (centiloid) across the cognitive subgroups (PDN, PD-MCI, PDD).

2. We aimed to predict a continuous measure of global cognitive ability (aggregate cognitive z score) as a function of age, sex, and cortical FBB binding (centiloid). We evaluated the importance of predictors by model comparison, using LOOIC. That is, we compared a model predicting global cognitive ability with and without cortical FBB binding in order to determine whether cortical FBB binding improved prediction of global cognitive ability. This same procedure was repeated for the memory domain score.

3. Lastly, regional SUVR from the *a priori* ROIs was modeled as a function of age, age-by-ROI, sex, and global cognitive ability-by-ROI interaction, in order to investigate the relationship between FBB uptake and cognition in the different ROIs.

5.7.2 Whole-brain voxel-wise analysis

We used a standard, frequentist ANCOVA model (with age and sex as covariates) to assess the spatial distribution of amyloid deposition across the cognitive subgroups (we specifically investigated the contrasts: PDD > PD-MCI, PDD > PDN, and PD-MCI > PDN). In addition, we ran three multiple linear regression models to investigate the association between voxel-wise FBB SUVR and continuous measures of (1) global cognitive ability (cognitive z score), (2) memory domain score, and (3) age. Age and sex were included as covariates in the global cognitive ability and memory domain models; only sex was included in the age model. Voxel-wise comparisons were performed using a gray matter mask and a permutation-based inference tool for non-parametric thresholding (*randomise* (Winkler et al., 2014) in FSL v5.0.9). For each contrast, the null distribution was

generated from 5,000 permutations and the alpha level set at $p< 0.05$, corrected for multiple comparisons (family-wise error correction using threshold-free cluster-enhancement (TFCE)).

Additional analyses

These analyses were not included in the original publication of this work (Melzer et al., 2019).

A standard, frequentist ANCOVA model was used to assess the spatial distribution of differences in voxel-wise CBF between the amyloid positive and amyloid negative subgroups (testing the contrast, Aβ positive < Aβ negative). A multiple linear regression investigated the voxel-wise association between CBF and global cognitive ability as a continuous measure (cognitive z score). The association between voxel-wise SUVR and a continuous measure of global grey matter volume (GM_{vol}) was also investigated in multiple linear regression. Age and sex were included as covariates in all models.

ASL MRI was not acquired for one subject due to the presence of titanium implants in the skull, therefore the data set for analysis of CBF has one fewer subject (n=114) than the primary analysis (n=115).

5.8 Results

Table 5.1 summarizes the demographic and clinical information for PD participants. Twenty-one of 115 (18%) had positive FBB scans on visual assessment. We identified a centiloid cut-off of 31.3 (equivalent SUVR = 1.21), which yielded sensitivity (to visually assessed positive scans) = 100%, specificity = 92.6%, and AUC [95% confidence interval] = 0.98 [0.97, 1.0]. We also identified a significant association between centiloid and age (r = 0.011 [0.005, 0.017] SUVR/year, or 9.3% per decade).

5.8.1 Regional amyloid distribution in PD

With a simple model that only considered the discrete cognitive groups, we found evidence of increased cortical amyloid accumulation in PDD relative to PDN and PD-MCI (Figure 5.5; Table 5.1). However, adding age as a covariate to the model and using LOOIC to

Demographics	PDN	PD-MCI	PDD	Linear model
n	23	76	16	-
Female, No. [%]	8 (35)	18 (24)	3 (19)	-
Age, years	70 (6)	72 (6)	77 (6)	PDD > PDN & PD-MCI
Education, years	12 (2)	13 (3)	12 (2)	∼
PD symptom duration, years	7.4 (5)	7.3 (4)	8.5 (5)	∼
MoCA	26 (2)	23 (3)	16 (5)	PDN > PD-MCI > PDD
Cognitive Z score	0.28 (0.48)	-0.81 (0.53)	-1.89 (0.57)[a]	PDN > PD-MCI > PDD
Memory Domain score	0.52 (0.86)	-0.82 (0.85)	-1.82 (0.67)[a]	PDN > PD-MCI > PDD
Dose, MBq	294 (20)	300 (16)	290 (27)	∼
Aβ positive, No. [%][b]	4 [17]	11 [14]	6 [38]	-
Cortical $SUVR_{NS}$	1.11 (0.13)	1.12 (0.18)	1.28 (0.30)	PDD > PDN & PD-MCI
Cortical CL	16 (19)	18 (27)	42 (44)	PDD > PDN & PD-MCI
Normalised GM_{vol}	0.39 (0.02)	0.38 (0.02)	0.36 (0.02)	PDN & PD-MCI > PDD
Cortical CBF[c], ml/100g/min	494 (88)	440 (121)	320 (112)	PDN & PD-MCI > PDD

TABLE 5.1: Values are mean (standard deviation) unless specified; [a]Cognitive z scores and memory domain scores for seven PDD participants were imputed from restricted neuropsychological data due to their inability to complete the full cognitive assessment; [b]Visual assessment of amyloid positive/negative reported; [c] ASL MRI was not obtained in one subject, here n=114; ∼, no evidence of a difference; -–, no statistical test applicable or was not performed. Pairwise group estimates were considered different if 95% uncertainty intervals did not overlap. MBq, megabecquerel; MoCA, Montreal Cognitive Assessment; Aβ, Amyloid beta; $SUVR_{NS}$, Standardized uptake value ratio with "non-standard" processing (see Supplementary Material); CL, centiloid.

compare models, showed that age, rather than cognitive group, was predictive of increased cortical amyloid accumulation (Figure 5.6 B). When attempting to predict cognition from cortical amyloid deposition, the addition of FBB uptake (centiloid) to the model resulted in marginally worse out-of-sample prediction of global cognitive score [LOOIC (standard error) = 1.8 (0.8), Figure 5.6 A] and memory score [0.7 (2.1), data not shown] than simpler models, which only included age and an intercept. This indicates FBB uptake has little, if any, relationship with cognitive impairment in our PD sample. In *a priori* ROIs, including age and sex, we saw no evidence of association between FBB uptake (SUVR) and either global cognitive or memory score (Figure 5.6 C).

We also considered the potential of using symptom duration as a model covariate in the place of age, however this was found to have little effect on the results of the regression. Similarly to the above comparison, the addition of global CL to a model containing only symptom duration and an intercept gave a worse out-of-sample prediction, as indicated by LOOIC [0.8 (0.4)]. Furthermore, we compared these two models directly (considering age

or symptom duration in combination with amyloid) and found that there was no evidence of a difference between the two models [LOOIC = 0.6 (1.3)].

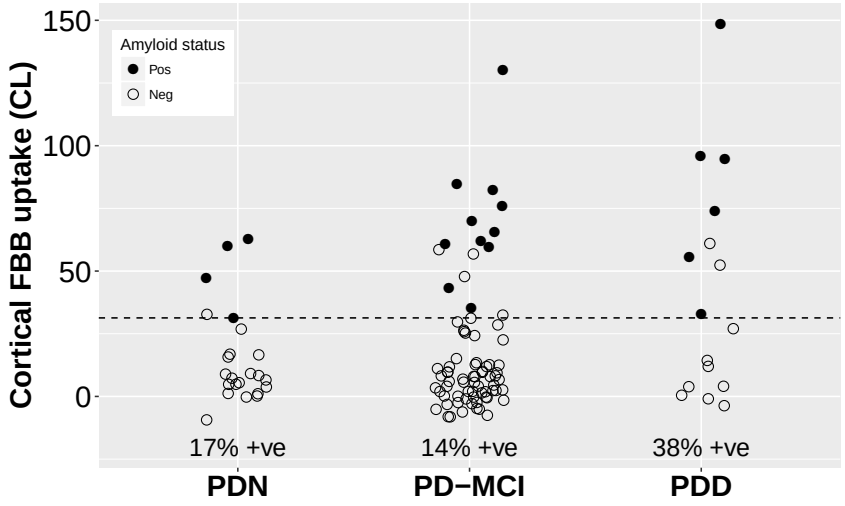

FIGURE 5.5: Cortical FBB uptake by cognitive group. We found evidence of increased cortical amyloid accumulation in PDD relative to PDN and PD-MCI, however this was explained by the older age of the PDD group (Table 5.1). The dashed line at CL = 31.3 indicates the ROC-defined optimal centiloid cut-off in this sample, with sensitivity to clinically positive cases = 100%, specificity = 92.6%, AUC [95% confidence interval] = 0.98 [0.97, 1.0]. Previously produced in (Melzer et al., 2019).

5.8.2 Whole-brain voxel-wise amyloid distribution in PD

We identified no evidence of a difference in amyloid deposition across PD cognitive groups (TFCE-corrected, $p < 0.05$). Furthermore, we identified no evidence of an association between SUVR and either global cognitive ability or memory domain scores. There was, however, a widespread positive association between SUVR and age over the cortex (figure 5.7).

5.8.3 CBF and grey matter volume sub-analyses

Using a simple frequentist model that only considered the discrete cognitive groups, pair-wise group estimates found significantly reduced mean cortical CBF in PDD compared to PDN and PD-MCI (table 5.1). However, voxel-level investigation is likely more appropriate in the analysis of CBF than by investigation of extracted mean values, given there is considerable variation associated with inter-subject values, as evidenced by large standard deviations (table 5.1). Mean normalised GM_{vol} was also significantly reduced in PDD compared to PDN and PD-MCI.

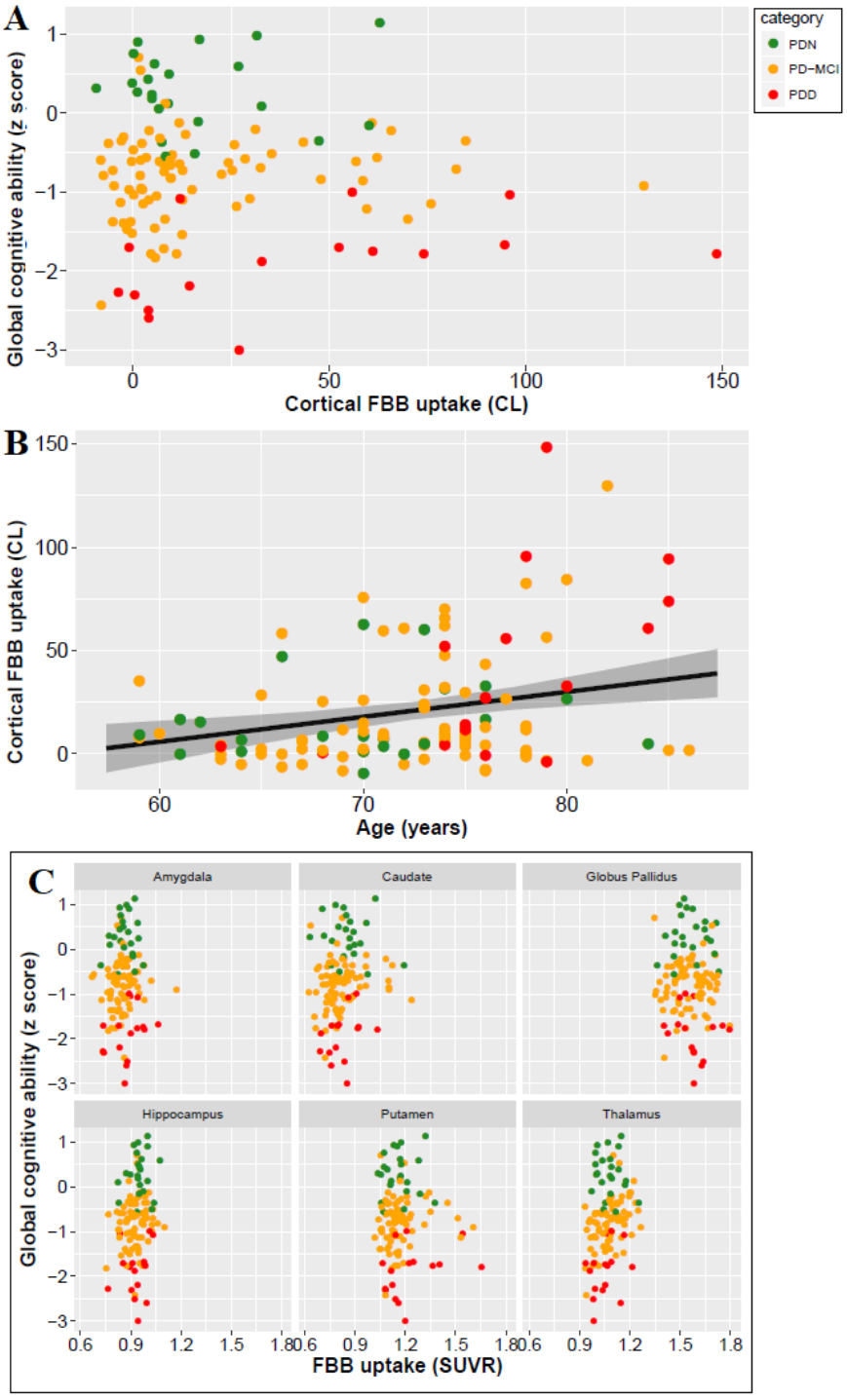

FIGURE 5.6: Associations between cortical amyloid deposition and global cognitive ability and age. (A) Scatter plot showing no evidence of a significant association between global cognitive ability (Cognitive z score) and cortical amyloid (CL; Table 5.1). (B) Scatter plot of cortical amyloid (CL) vs. age (years). FBB uptake was associated with age (slope = 1.5 CL/year, 95% uncertainty interval [0.6, 2.3], equivalent to SUVR of 0.011/year [0.005, 0.017]). The black line depicts the estimate from the Bayesian model fit and the shaded area indicates the 95% credible interval. (C) Cognitive performance as a function of mean FBB SUVR within a number of brain regions. While different regions exhibited different levels of amyloid deposition, there was a clear lack of relationship between cognitive performance (cognitive z score) and SUVR within all of the regions examined. Color represents cognitive status: green - PDN, orange - PD-MCI, red - PDD. Previously produced in (Melzer et al., 2019).

Whole-brain voxel-wise analysis of CBF identified no evidence of an effect of amyloid positivity on CBF, accounting for age and sex (TFCE-corrected, $p < 0.05$). Furthermore, where SUVR showed no evidence of association with global cognitive ability, voxel-wise analysis of CBF displayed a widespread positive association with cognitive z score, such that reduced CBF across the cortex was correlated with poorer cognition in this sample (figure 5.8).

Voxelwise analysis of FBB PET images revealed no evidence of an association with mean cortical GM_{vol}.

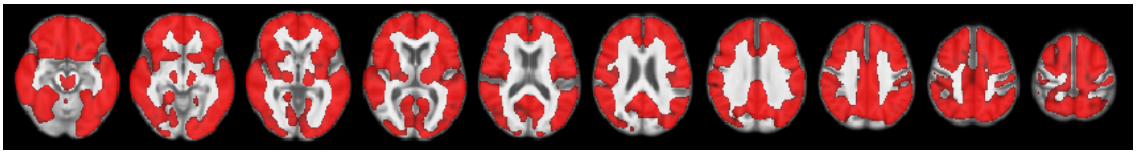

FIGURE 5.7: Red indicates voxels with a significant positive association between FBB uptake and age (TFCE-corrected $p < 0.05$), overlaid on a study-specific average structural image. This association was evident throughout the cortex and in the thalamus but not in the striatum.

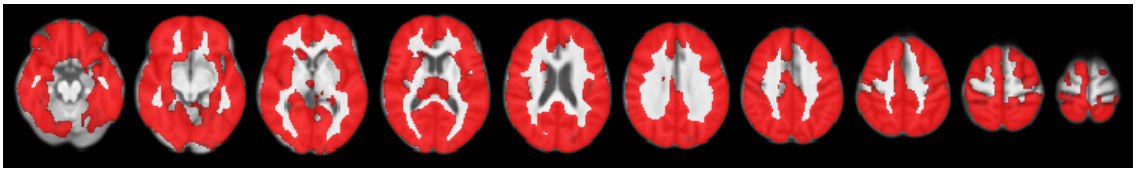

FIGURE 5.8: Red indicates voxels with a significant positive association between quantified CBF value from ASL MRI, and global cognitive z score (TFCE-corrected $p < 0.05$), overlaid on a study-specific average structural image. There was evidence of sparing in select regions of the left frontal lobe (juxtapositional lobule cortex, superior region of the paracingulate gyrus, medial region of the superior frontal gyrus) and the cingulate gyrus.

5.8.4 Cognitive category and age: model comparison

As cognitive status and age are correlated (PDD are on average older than PD-MCI who are on average older than PDN), care is required in interpreting a model that includes both of these predictors. Comparing models using LOOIC allows the determination of relative predictive information contained in variables. Adding cognitive category to a model with only an intercept resulted in an increase in LOOIC of 5.5 ± 7.0. In comparison, adding age to a model with only an intercept gave an increase in LOOIC of 10.6 ± 6.0. Adding cognitive category to a model which included age resulted in a small increase of 1.5 ± 5.3. The effects of age and cognitive category are small effects on the LOOIC scale, indicating that neither has a large predictive ability. However, these results indicate that cognitive

category has minimal predictive value once age is known, suggesting that age is more likely the stronger predictor.

5.9 Discussion

Using FBB PET imaging in 115 PD patients across the cognitive spectrum, we observed significantly higher cortical amyloid accumulation in our PDD group relative to other cognitive subgroups, but model comparison indicated this was due to the older age of the PDD group.

Visual assessment revealed amyloid positive proportions of 17%, 14%, and 38% in PDN, PD-MCI, and PDD groups, respectively. The prevalence of amyloid positivity reported in the literature is variable, ranging from 0 to 53% in PDN (Winer et al., 2018; Mashima et al., 2017; Lee et al., 2018; Akhtar et al., 2017; Gomperts et al., 2016), 0 to 47% in PD-MCI (Petrou et al., 2015; Winer et al., 2018; Mashima et al., 2017; Lee et al., 2018; Akhtar et al., 2017; Gomperts et al., 2016), and an estimated point prevalence of 34% in PDD (Petrou et al., 2015). Nevertheless, these proportions of amyloid positivity across the cognitive spectrum in PD are substantially lower than levels seen in Alzheimer's dementia (88%) (Ossenkoppele et al., 2015) or amnestic MCI (69%) (Villemagne et al., 2011), and are closer to levels seen in elderly controls (11.6% at age 60, 23.8% at 70, and 34.5% at 80 years) (Ossenkoppele et al., 2015). The association we observed between amyloid deposition and age (r = 0.011 [0.005, 0.017] SUVR/year, or 9.3% per decade) is similar to that reported in the healthy elderly population ([^{11}C]-PiB uptake increased at 0.016 SUVR/year, 10% per decade) (Villemagne et al., 2011), indicating that a PD-specific influence on amyloid accumulation is unlikely. Although global SUVR measures obtained from PiB and FBB PET in the same subjects have excellent linear correlation, the above rates are not directly comparable as different reference regions were used to define SUVR (for example, we used the whole cerebellum while Villemagne et al. (Villemagne et al., 2011), used the cerebellar cortex). Nevertheless, amyloid load in our PD sample appears to be consistent with levels seen in the general elderly population, as well as previous PD studies (Hely et al., 2008; Petrou et al., 2015; Akhtar et al., 2017), and any increases in our PDD group can be explained by their older age. Not accounting for age may help explain the recent report of association between amyloid deposition and global cognition in a subset of the Parkinson's Progression Marker Initiative (Fiorenzato et al., 2018).

Ideally we would have used a predefined centiloid threshold derived from a large population study to define amyloid positivity in our PD sample. However, to the best of our knowledge, this is not currently possible. SUVR cut-off values are well established, but recent work demonstrates that specific thresholds are, as expected, highly dependent on the reference regions and processing methodology (Lashley et al., 2008; Su et al., 2018). Therefore, a threshold derived using a particular method should not necessarily be applied to a different processing methodology, even after centiloid standardization (Su et al., 2018). Many potential thresholds are available: a phase III FBB study identified a histopathologically-confirmed amyloid positivity cut-off of SUVR = 1.478 (Sabri, Sabbagh, et al., 2015); Jack et al. (Jack et al., 2017), report a Pittsburgh Compound B-derived cut-off of SUVR = 1.42 and CL = 19; Bullich et al. (Bullich et al., 2017), reported FBB thresholds using cerebellar cortex (SUVR = 1.43) and non-centiloid whole cerebellum (SUVR = 0.96) as reference regions. However, it would be inappropriate to apply these cut points to our current dataset as image processing and reference regions differed from the standard centiloid SUVR method. Su et al. presented a centiloid cut-off using standard reference regions (CL = 6.8) based on an ROC analysis to classify young, amyloid negative participants from AD patients in the GAAIN dataset (Su et al., 2018). This surprisingly low threshold may be driven by differences in non-specific binding and tracer delivery differences between young and old participants. In any case, standardized centiloid analyses of large cohorts are needed to establish appropriate centiloid thresholds, which will lead to greater applicability of the centiloid scale.

In this study, we used a well-validated visual assessment to clinically rate scans as being amyloid positive or negative (Seibyl et al., 2016). As there is not an accepted threshold based on standardized centiloid reference regions, we defined an amyloid positivity centiloid cut-off threshold in our sample. Our cut-off (CL = 31.3, SUVR = 1.21) corresponds well to the estimated value proposed by Rowe and colleagues (C. C. Rowe et al., 2017) in the context of AD (CL = 25-30), however our estimated threshold may be biased by the low number of Aβ-positive patients.

Our results suggest a lower prevalence of amyloid-positive PDD individuals than in dementia with Lewy bodies (DLB); neither of these two conditions exhibit the proportions of amyloid-positive cases reported in Alzheimer's dementia (Petrou et al., 2015; Lee et al., 2018; Donaghy et al., 2018; Gomperts et al., 2008). While some have reported an association between cognitive ability and cortical SUVR in DLB (Gomperts et al., 2012),

the largest study (including the most thoroughly profiled group of DLB to date) did not find an association between amyloid deposition and clinical profile, despite showing increased amyloid accumulation vs. controls (Donaghy et al., 2018). We confirm here a similar lack of association in PD between amyloid deposition and cognitive impairment, with age explaining the increased FBB-uptake observed in our PDD group.

Most of our PD patients were within the normal centiloid range (compared to control data from the Global Alzheimer's Association Information Network used for level 3 centiloid standardization: http://www.gaain.org/centiloid-project), with few showing AD-like levels of cortical amyloid. Hence Aβ pathology is unlikely to be a dominant causal factor in the majority of individuals with PD or PDD.

PET measures of amyloid do not suggest plaques as a primary pathology for dementia in PD, but amyloid may play a part in conjunction with other pathologies, such as alpha-synuclein and hyper-phosphorylated tau. It is expected that tau deposition will correlate more directly with current cognitive ability, due to its association with accelerating neuronal injury. Initial tau PET imaging in PD and DLB demonstrates a spectrum of deposition, with reports of both association (Lee et al., 2018; Gomperts et al., 2016) and lack of association (Winer et al., 2018; Hansen et al., 2017) with cognitive impairments in PD. Thus, consideration of amyloid, tau, and alpha-synuclein deposition in the same individuals may ultimately provide a more complete description of how pathological processes potentially interact to affect cognition in PD. A potential scenario for prediction of future outcomes will most likely synthesize an array of biomarkers representative of these and other pathologies (Compta et al., 2013; Lanskey et al., 2018).

I investigated two other potential pathological correlates of amyloid deposition, namely cerebral blood flow and grey matter volume. Reductions in cerebral blood flow and grey matter volume are known to correlate with cognitive impairment (Meyer et al., 2000), and previous observations of interaction between CBF and amyloid load (Mattsson et al., 2014; Bangen et al., 2017) in cognitively unimpaired individuals suggested a possible exacerbating effect of amyloid in reducing cerebral blood flow, such that those with high amyloid may experience greater risk of future cognitive impairment. In this PD group, amyloid positivity was not seen to confer any additional risk of abnormal cerebral blood flow, and higher amyloid load was not associated with reduced cortical grey matter volume. We noted that levels of amyloid in this PD cohort were comparable to those seen in

healthy ageing, thus it is interesting that the CBF/Aβ interaction effect seen in cognitively unimpaired controls does not appear to occur in PD. While current cognitive ability was strongly associated with reduced cerebral blood flow across the cortex, this effect did not appear to be exacerbated by amyloid deposition in this group. Mattsson et al. found that the interaction effect was significant independent of diagnostic group in several brain regions, however was strongest in controls and MCI. It may be that the interaction effect is small, and the power of this investigation doubly suffered from low prevalence of amyloid positivity and conducting analysis independent of diagnostic group. However, as this study is enriched with PD-MCI and the number of PDD is relatively small, it is unlikely that the presence of PDD subjects in the analysis washed out this effect. Therefore, cognitive decline associated with cerebral blood flow in this study is not likely tied to amyloid deposition, however a more targeted approach including a higher proportion of amyloid positive individuals is required to verify this finding in PD.

Our results suggest that amyloid deposition is neither necessary nor sufficient to explain cognitive decline and dementia in PD. The current study cannot address the role that amyloid accumulation plays in AD, but it does raise the question as to the fundamental relationship between amyloid plaques and dementia. While the amyloid cascade hypothesis remains the leading candidate to explain the pathophysiology of AD, it not universally accepted (Herrup, 2015; Harrison & Owen, 2016). Amyloid beta may be a downstream result, and not necessarily the cause, of AD (Drachman, 2014).

Limitations

Limitations of this study include the absence of a healthy control group. Analyses were restricted to the effects of varying levels of cognitive impairment within PD. All comparisons to healthy controls were based on comparable reports from the literature. However, the primary aim of this work was to investigate the relationship between amyloid deposition and cognitive impairment within a group of well-characterized PD participants. Even when following level II criteria for PD-MCI, considerable variability exists across those diagnosed as PD-MCI; some exhibit single domain and others multi-domain impairment (Wood et al., 2016). It is possible that different subtypes may exhibit greater or lesser underlying Aβ. Nonetheless, Aβ was not associated with global cognitive ability or memory function.

Expression of the apolipoprotein E (APOE) gene ε4 allele has been shown to correlate with amyloid deposition (Akhtar et al., 2017; Villemagne et al., 2011), and the development of dementia in PD (Williams-Gray et al., 2009; Huertas et al., 2017). At the time of writing, the APOE-ε4 genotype of our participants was not known. We also did not have histopathological confirmation of amyloid plaque accumulation, although recent work demonstrates tight agreement between visual assessment of amyloid PET and histopathological evidence in AD (Bullich et al., 2017). Lastly, recent work suggests that partial volume correction can improve the ability of FBB PET to discriminate between AD patients and healthy controls (Rullmann et al., 2016). We did not perform this step because partial volume correction methods are still highly variable across centers, with no consensus on optimal methods, and have not been incorporated into centiloid standardization procedures yet (Klunk et al., 2015).

In this cross-sectional investigation of a large, cognitively well-characterized PD group, we found increased cortical amyloid accumulation in PDD, but this was explained by the older age of the PDD group. We found no associations between amyloid load and continuous measures of cognitive performance. This suggests that Aβ accumulation is not the primary cause of cognitive impairments in PD. Low levels of amyloid may, however, still interact synergistically with other PD pathological processes, thereby accelerating other pathways to dementia.

5.10 Data Availability

Analysis code and data are available on the Open Science Framework at https://osf.io/5fqb9/.

5.11 Supplementary material

The original Supplementary Material for this article has been added into the body of this work. It may also be found online at:
https://www.frontiersin.org/articles/10.3389/fneur.2019.00391/full#supplementary-material

Chapter 6

Beta Amyloid Deposition and Future Cognitive Outcomes

6.1 Author Contributions

I performed the image processing, study design, statistical analysis and results interpretation in this study, with guidance from TM and DJM.

The NZBRI Study of Parkinson's Disease

The larger study of Parkinson's disease at the New Zealand Brain Research institute was conceptualised and designed by TM, DJM, MM, TP, DHM, JD-A, and TA. TM, MM, DHM, RK, DJM, LL, JD-A, and TA obtained funding for the study. RK, LL, DJM, MM, TP, and SM provided administrative, technical, and material support. All authors contributed to acquisition, analysis or interpretation of data.

6.2 Introduction

While many studies have been carried out over the nearly three decades since the discovery of widespread amyloid deposits in AD, the field has yet to fully determine the mechanism by which misfolded beta-amyloid may affect cognitive function, and intervention studies aimed at reducing amyloid load in the early stages of AD have only shown to be successful in slowing cognitive decline in one recent study (Swanson et al., 2018).

Amyloid accumulation in Parkinson's disease is generally much less pronounced than in AD; many cross-sectional studies of cortical amyloid across the cognitive spectrum, and indeed the cross-sectional arm of this thesis, have largely found accumulation comparable to age-matched healthy controls.

Cross-sectional analysis of misfolded beta-amyloid in this thesis identified increased cortical amyloid accumulation in subjects with Parkinson's disease dementia, but found that this was explained by the older age of the PDD group. While cortical Aβ accumulation does not appear to be the primary driver of cognitive impairments in this PD group, low levels of amyloid may accelerate other pathways to dementia through synergistic involvement of multiple pathologies (Mao & Reddy, 2011; Pascoal et al., 2017). A possible mechanism of future cognitive impairment in those with high amyloid is induced fibrillary changes in α-synuclein, leading to increased Lewy-body related pathology and thereby accelerating development of dementia (Toledo et al., 2016). The presence of co-morbid lewy-body pathology occurs in approximately 50% of AD cases, and is recognised to accelerate cognitive decline and shorten survival time compared to AD without lewy-bodies (Marsh & Blurton-Jones, 2012). The impact of cortical amyloid load on future cognition in PD is less well characterised, as some longitudinal studies have found an association between baseline amyloid load and future cognitive decline (Lee et al., 2018; Gomperts et al., 2013), while others have not (Winer et al., 2018; Hansen et al., 2017). Notably, Gomperts et al. found baseline amyloid accumulation to be positively associated with cognitive decline at an average of 2.5 years follow-up, after having identified no difference in precuneal or frontal amyloid between PDN and PD-MCI subjects in cross-sectional analysis (a finding echoed here in the previous chapter). This suggests that early amyloid load in PD may represent a better marker of future rather than present cognitive ability, may provide useful information for clinicians in advising patients on long-term outcomes and enable more targeted management of symptoms. However, the result reported by Gomperts et al. was obtained from a relatively small sample (n = 46), thus validation using a larger, well characterised cohort is required.

We therefore investigated the relationship between amyloid deposition and conversion to dementia over a mean 3.2 years follow-up using [^{18}F]-Florbetaben (FBB) PET imaging. Subjects included all participants investigated in the cross-sectional arm of this thesis, for which at least one follow-up neuropsychological assessment was acquired, and who were not classified as having Parkinson's disease dementia (PDD) at baseline. This sample

was enriched for PD with mild-cognitive impairment (PD-MCI), and thus investigates a particularly high-risk population (Wood et al., 2016). This study aims to clarify the potential role of amyloid load in accelerating conversion to dementia within these subjects, using robust statistical methods accounting for a range of risk factors implicated in the development of PDD.

Additionally, cerebral blood flow measured using arterial spin-labelling MRI was assessed for association with conversion to dementia. Previous studies have identified an interactive effect between CBF and amyloid load, such that non-demented individuals classified as amyloid-positive experienced greater reductions in CBF (Bangen et al., 2017), a known correlate of cognitive impairment (Meyer et al., 2000). A voxel-wise interactive effect between amyloid-positivity and cortical CBF was not identified in this sample at baseline, however baseline cognition in this PD cohort was associated with widespread reductions in CBF. It will be useful to also examine the role of early reductions in CBF in the progression of cognitive decline in PD, given that lower CBF has similarly been implicated in the acceleration of cognitive decline in AD (Benedictus et al., 2017).

6.3 Participants

This study follows a subset of participants originally included in the cross-sectional analysis of amyloid deposition in this thesis. All PD participants met the UK Parkinson's Disease Society's criteria for idiopathic PD (Hughes et al., 1992). The original exclusion criteria for recruitment in this study is detailed in the previous chapter. Participants who fulfilled the criteria for a probable diagnosis of PDD at baseline were excluded from this analysis, as were those for which no follow-up neuropsychological assessments had been obtained. Of the original cross-sectional cohort (n=115), n=99 were non-demented. Two participants were deceased before any follow-up assessments could be obtained, thus, the final cohort included in this chapter consists of n=97 participants, having completed the baseline neuropsychological battery (+1), baseline MRI scanning session, and baseline [^{18}F]-Florbetaben (FBB) PET imaging. As in the cross-sectional analysis, sub-analyses investigating CBF were performed with one fewer subject (n = 96), due to no acquisition of ASL MRI for that subject.

6.3.1 Diagnostic criteria and assessment

As at baseline, Movement Disorders Society (MDS) Task Force Level II criteria was used to classify PD participants as cognitively normal (PDN), with mild cognitive impairment (PD-MCI), or with dementia (PDD) (Wood et al., 2016; Litvan et al., 2012). A global measure of cognitive performance was created by averaging scores across the cognitive domains (aggregate cognitive z score) measured in each full cognitive assessment session. This method is described briefly in Chapter 5 (see Wood et. al. 2016 for a detailed description). Assessors were blinded to amyloid status. Participants also completed the Montreal Cognitive assessment (MoCA). All assessments and scans were performed with no disruption to participants' usual medication regimen.

6.3.2 Longitudinal protocol design

All subjects underwent comprehensive neuropsychological (NP) assessments at baseline and annually thereafter, with an aim to obtain longitudinal cognitive data spanning at least 3 years for each subject. A truncated assessment battery performed biannually was used as a screening measure for dementia; a probable diagnosis of dementia prompted a full NP assessment. Following a diagnosis of dementia, PDD subjects underwent only short assessments due to inability to complete the full assessment. This truncated battery included the MoCA as a measure of cognitive function, demonstrated in a recent study of common cognitive screening measures (MoCA, Mattis Dementia Rating Scale (DRS-2), and Mini Mental Status Examination (MMSE)) to offer the best overall diagnostic accuracy for PD-MCI (AUC = 0.79, sensitivity = 76.4) and for PDD (AUC = 0.89, sensitivity = 81.0)(Kim et al., 2019).

Where measures of global cognitive z score were missing due to short assessments, the score for that session was imputed using the Multivariate Imputation via Chained Equations (MICE, v3.6.0) package in R (v3.4.4), by predictive mean matching (PMM). Imputation is a widely used method for providing plausible data points, drawn from a distribution specifically designed for the missing variable. PMM is used to infer continuous values based on an observed value from a donor with a similar predictive mean.

6.4 Materials and methods

6.4.1 Image Acquisition and Processing

This study revisits the imaging measures acquired at baseline, and thus much of the methodology described in Chapter 5 for the acquisition, pre-processing, and quantification of image data was employed in this longitudinal investigation with no methodological changes. Previously described imaging outputs of relevance to this chapter are:

- FBB PET amyloid-positive or amyloid-negative visual classification, performed by a trained neuroradiologist;
- Standardised uptake value ratio (SUVR) images of [^{18}F]-Florbetaben (FBB) PET radiotracer activity, normalised by values in the Centiloid whole cerebellum region;
- Mean cortical SUVR, extracted from the standard centiloid cortical region of the processed SUVR images;
- Mean regional SUVR, extracted from selected *a priori* brain regions for use in region-of-interest (ROI) analysis, including the caudate, putamen, thalamus, globus pallidus, and precuneus;
- Mean cortical centiloid (CL) values, extracted from the standard centiloid cortical region of CL-converted SUVR images;
- Cortical grey matter volume (GM_{vol}), extracted from T1-weighted structural MRI and normalised by individual total intra-cranial volume;
- Quantified cerebral blood flow (CBF) images, given by arterial spin labelling (ASL) MRI;
- Mean cortical CBF, extracted from the standard centiloid cortical region of the quantified CBF images.

In addition to these outcomes, principal component analysis (PCA) gave the expression of each principal component of variance within the FBB SUVR dataset for each individual. The objective of PCA in this context is to identify independent patterns of amyloid deposition, derived from variance in the data, and to test whether those spatially related

patterns are associated with conversion to dementia. This method has been shown to be sensitive in detecting patterns of amyloid deposition in AD compared to controls (Fripp et al., 2008).

6.4.2 Calculation of principal components

PCA was performed to extract the principal patterns of spatial variance within the amyloid FBB PET (SUVR) dataset. The data were restricted to voxels within a study-specific grey matter mask (created from averaging all subject grey matter segments) and twice demeaned (subject followed by group demean). This yielded the subject residual profile, a matrix representing the deviation of each subject from the subject and group mean image matrices. Computing the covariance between each pair of rows, representing each subject residual, yielded the covariance matrix for the SUVR dataset.

The eigenvectors and corresponding eigenvalues of the covariance matrix were calculated. Scaling each eigenvector by the square-root of its corresponding eigenvalue produced components of unit variance; these were the principal components of the dataset. The inverse scaled eigenvectors indicated the expression (or loading) of each component within each subject image, while the relative size of each eigenvalue quantified the total unit variance encompassed by that particular spatially fixed principal component (Melzer et al., 2011). The principal components were ordered by how much of the variance they represent, with the first principal component capturing the most variance. The first few principal components generally account for a large amount of the total variance in the data, in which case the remaining components may be rejected to reduce dimensionality without significant loss of data (Razifar et al., 2009).

We aimed to select the components that accounted for at least 70% of the variance - however, the first two components were found to account for only 21% and 19.4% of the variance respectively, with subsequent proportional contributions rapidly decreasing thereafter to less than 5%. Thus the number of components required to reach 70% cumulative variance was impractical for statistical analysis. This may occur when data dimension is high, or when spatially-related variances in the data are low (Jolliffe, 2002). The cut-off proportion was revised to a cumulative proportion of at least 50%. This resulted in selection of the first five PCs for analysis, representing approximately 53% of the variance (PC1 = 21%, PC2 = 19.4%, PC3 = 4.7%, PC4 = 4.5%, PC5 = 3.3%).

6.5 Statistical analysis

This study focused on longitudinal conversion to dementia in PD. Only those that had converted to dementia, and not to any other cognitive classification, were considered 'converters' in this study; all other subjects were classified as 'non-converters' for the purposes of this analysis. A non-conversion classification provided the reference level for the analyses, thus conversion to dementia was the predicted effect of each model.

6.5.1 Survival analysis

A survival curve was fitted using the *survival* (v2.44-1.1) package in R. Survival from dementia over time was examined within the amyloid positive and the amyloid negative groups, taking into account subject age and right-censoring of the data. A Cox proportional hazards model assessed the relative risk conveyed by amyloid-positivity compared with amyloid-negativity for conversion to dementia over the course of longitudinal follow-up.

6.5.2 Whole-brain voxel-wise analysis

We used a standard, frequentist ANCOVA model (with age and sex as covariates) to assess the spatial distribution of amyloid deposition across the convert and non-convert subgroups, specifically testing Convert>Non-Convert. Images of quantified CBF were analysed in the same manner (testing Non-Convert>Convert). Voxel-wise comparisons were performed using a study-specific gray matter mask and a permutation-based inference tool for non-parametric thresholding (*randomise* (Winkler et al., 2014) in FSL v5.0.9). For each contrast, the null distribution was generated from 5,000 permutations and the alpha level set at $p < 0.05$, corrected for multiple comparisons (family-wise error correction using threshold-free cluster-enhancement (TFCE)). Corrected voxel-wise association maps were displayed over a study-averaged structural T1-weighted image, and associated brain regions were identified from the MNI structural atlas (Mazziotta et al., 2001) (figure A.1).

6.5.3 Predictors of conversion to PDD

Baseline demographic and neuropsychological group differences between converters and con-converters were analyzed using simple frequentist linear models, considering no other covariates.

We then used Bayesian multiple regression models to investigate potential predictors of conversion to dementia in our sample, including baseline age, sex, and baseline cognitive ability as covariates. Investigated predictors included continuous measures of (1) mean cortical FBB SUVR, (2) regional FBB SUVR extracted from *a priori* ROIs, (3) principal component expression, (4) baseline MoCA scores, (5) mean normalised grey matter volume (GM_{vol}), and (6) only the nuisance covariates, for the purposes of model comparison and evaluation of primary predictors. I additionally investigated the effect of APOE-ε4 status as a predictor of (1) mean cortical FBB SUVR, and (2) expression of the first principal component, including baseline age and sex as covariates.

Bayesian models were fitted using the "brms" (v2.9.0) package (Bürkner, 2017) in R. In each model, four chains with 2,000 iterations each were used to generate the posterior sample. Resultant model parameters associated with each variable were considered to have a predictive effect if the 95% credible interval did not include zero. Model comparison using LOOIC (leave-one-out information criterion) was performed when models included correlated predictors or predictive performance was being evaluated (Vehtari et al., 2017). A higher expected log predictive density, by at least twice the standard error of the estimated difference, indicated a model with a better fit, and consequently whether a specific predictor significantly improved model fit.

6.6 Results

Table 6.1 summarizes the baseline demographic, clinical and imaging characteristics of PD participants, stratified by conversion status.

6.6.1 Participant conversion between cognitive subgroups

At a mean of 3.2 ± 1 years follow-up (median 3.1 years, range 0.5 - 4.9 years), 46 participants had remained stable at their baseline cognitive classification (PDN, n = 13;

Demographics at study baseline	PDD convert status		
Total n=97	Non-convert	Convert	Linear model
n	65	32	-
PD-MCI, No. (%)	42 (65)	32 (100)	-
Female, No. (%)	20 (30)	6 (19)	-
Age, years	71 (6)	72 (5)	∼
Latest follow-up, years	3.2 (1)	3.2 (0.9)	∼
Education, years	13 (3)	13 (3)	∼
PD symptom duration, years	14 (5)	11 (5)	Non-Convert > Convert
Hoehn and Yahr	2.5 (0.5)	3 (0.6)	Convert > Non-Convert
MoCA	24 (4)	17 (4)	Non-Convert > Convert
Cognitive Z score	-0.33 (0.7)	-1.03 (0.5)	Non-Convert > Convert
UPDRS Part III	40 (12)	50 (12)	Convert > Non-Convert
APOE-ε4 carrier, No. (%)	16 (25)	14 (44)	-
Dose, MBq	300 (16)	301 (17)	∼
AB-positive, No. (%)	7 (11)	8 (25)	∼
Cortical $SUVR_{NS}$[c]	1.09 (0.1)	1.18 (0.2)	Convert > Non-Convert
Cortical CL	13 (19)	27 (33)	Convert > Non-Convert
Normalised GMvol	0.38 (0.02)	0.37 (0.02)	Non-Convert > Convert
Cortical CBF[d], ml/100g/min	478 (117)	410 (94)	Non-Convert > Convert
Regional SUVR			
Caudate	0.82 (0.1)	0.84 (0.1)	∼
Putamen	1.15 (0.09)	1.20 (0.1)	∼
Thalamus	1.08 (0.07)	1.08 (0.08)	∼
Globus pallidus	1.55 (0.1)	1.57 (0.1)	∼
Hippocampus	0.93 (0.06)	0.93 (0.07)	∼
Amygdala	0.85 (0.07)	0.85 (0.09)	∼
Precuneus	0.97 (0.13)	1.08 (0.23)	Convert > Non-Convert

TABLE 6.1: Baseline demographics, clinical and imaging characteristics of the longitudinal follow-up cohort. Values are mean (standard deviation) unless specified; [a]Cognitive z scores for three PDD participants were imputed from restricted neuropsychological data due to their inability to complete the full cognitive assessment; [b]Visual assessment of amyloid positive/negative reported; [c]Tested using Fisher's exact test; [d]ASL MRI was not obtained in one subject, here n=96; ∼, no evidence of a difference; -–, no statistical test applicable or was not performed. Pairwise group estimates were considered different if 95% uncertainty intervals did not overlap.

PD-MCI, n = 33), 10 participants had converted from PDN to PD-MCI, and 32 participants had converted from PD-MCI to PDD. Nine participants had reverted from PD-MCI to PDN; this may be due to the sensitivity of the PD-MCI criteria to small variations in NP scores in those less-impaired, thus those that have reverted likely reflect the noise inherent in the classification of these cases rather than a true improvement in cognition. Only conversion to PDD was investigated in this study, thus there were a total of 65 participants in the non-convert subgroup, and 32 participants in the convert subgroup.

Of the 97 participants included in this analysis, 24 were lost to further follow-up over the course of the study due to death, or following a diagnosis of dementia. Of these, 14 participants had converted to PDD during the period for which data was obtained, and thus contribute to conversion statistics. Of the remaining 10 subjects, 6 were lost to follow-up before three years, and therefore contribute to right censoring of the data in that

respect. However, as this study is focused on identifying factors that influence conversion to dementia during life, this effect has little impact on the overall interpretation of results. These subjects were not removed from the analysis, to avoid introducing bias.

6.6.2 Survival from PDD by clinical amyloid subgroup

The proportion of participants classified as FBB amyloid-positive was 11% in the non-convert subgroup, and 25% in the convert subgroup (figure 6.5). A Fisher's exact test of independence found no evidence of a difference between these proportions (p-value = 0.1) within the sample. This test does not take into account the time points at which conversion occurred for each participant, thus survival analysis was used to gain a more complete understanding of the role of amyloid positivity in the acceleration of cognitive decline to dementia.

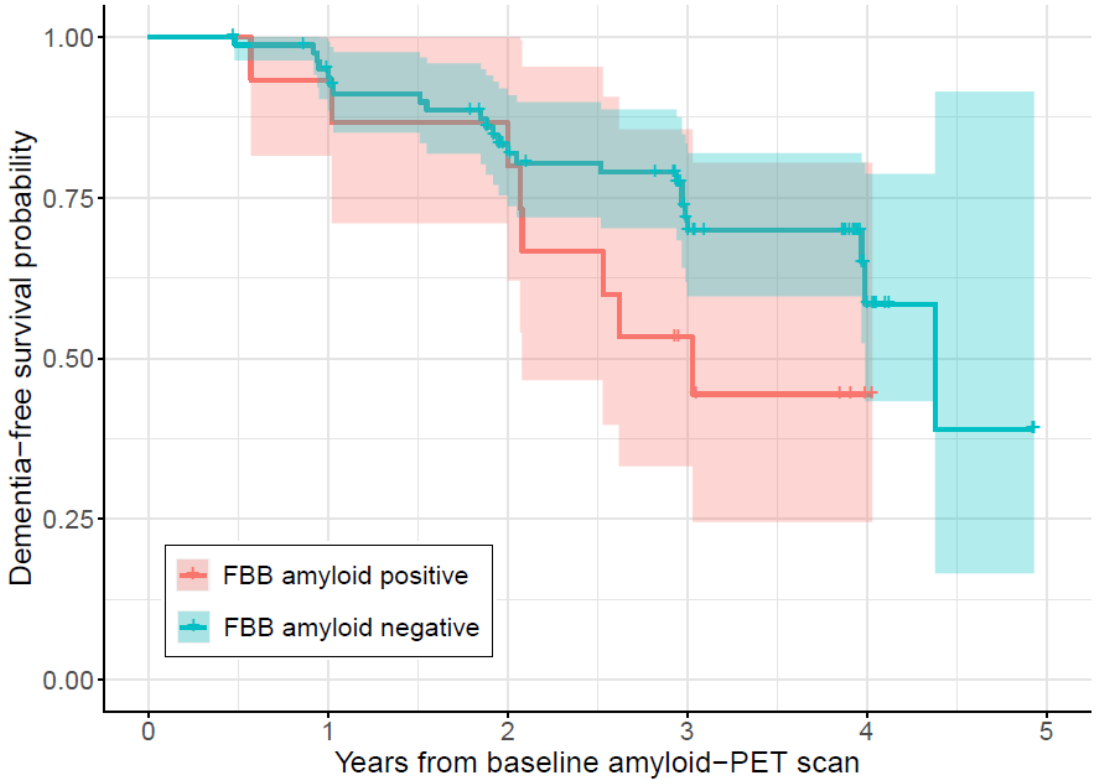

FIGURE 6.1: The survival curve depicts dementia-free survival over time within the amyloid-positive and amyloid-negative subgroups, accounting for age. Clinically positive levels of amyloid load appear to convey greater risk of conversion to dementia than clinically amyloid negative, however the associated error of the amyloid-positive survival curve is inclusive of the amyloid-negative survival curve throughout the course of follow-up. Points on the line indicate the last session for subjects who had not converted to dementia.

We found that Aβ-positive subjects displayed poorer survival from PDD over time, however the estimated survival of the Aβ-negative subjects was within the error estimates of the Aβ-positive time-course (Figure 6.1). Survival analysis therefore did not support that a clinically positive amyloid PET scan at baseline is a major contributing factor in conversion to dementia in PD.

The Cox proportional hazard analysis similarly showed that neither greater age (hazard ratio = 1.8, 95% confidence interval = 0.97 - 3.3; $p = 0.06$) nor amyloid positivity (hazard ratio = 1.9, 95% confidence interval = 0.84 - 4.2; $p = 0.1$) at baseline accelerated conversion to dementia in this subject group (Figure 6.2).

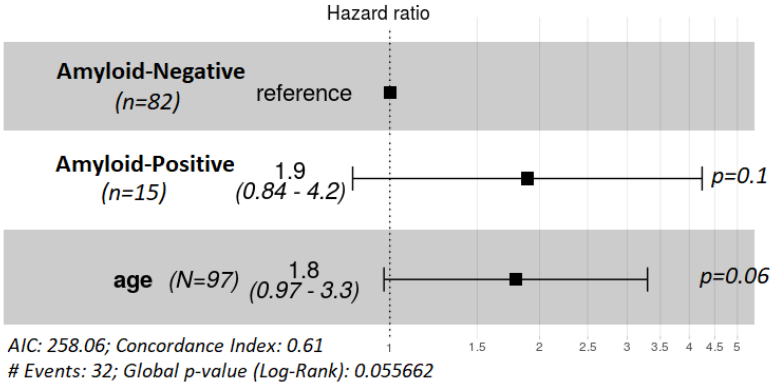

FIGURE 6.2: Cox proportional hazard ratios obtained from the model fit of the survival analysis provided no evidence that amyloid positivity at baseline is related to an increased risk of conversion to dementia within a mean of 3.2 years.

6.6.3 Predictors of Conversion to Dementia in PD

6.6.3.1 Voxel-wise associations with Amyloid and CBF imaging

Whole-brain non-parametric voxel-wise analysis examined the association between conversion to dementia during follow-up with two baseline imaging data-sets: baseline amyloid deposition, as given by FBB SUVR, and baseline cerebral blood flow (CBF), measured with ASL MRI. Both baseline measures displayed voxel-wise associations with future conversion to dementia (TFCE-corrected, $p < 0.05$), specifically, increased amyloid deposition in the occipital lobe, parietal lobe (precuneus), lateral occipital cortex, and frontal lobe (superior frontal gyrus, pre and post-central gyrus) (figure 6.3), and decreased CBF in the

frontal lobe (paracingulate gyrus), insula, and temporal lobes (primarily right side) (figure 6.4). The cerebellum also demonstrated reduced CBF, however this region contained spiral artifacts and thus is not reliable.

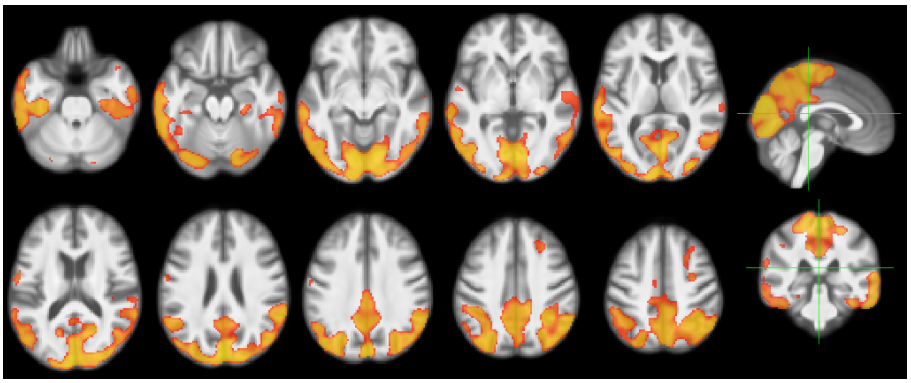

FIGURE 6.3: Whole-brain voxel-wise analysis found amyloid deposition in the occipital lobe, parietal lobe (precuneus), lateral occipital cortex, and frontal lobe (superior frontal gyrus, pre and post-central gyrus) to be positively associated with conversion to dementia during mean 3.2 years follow-up.

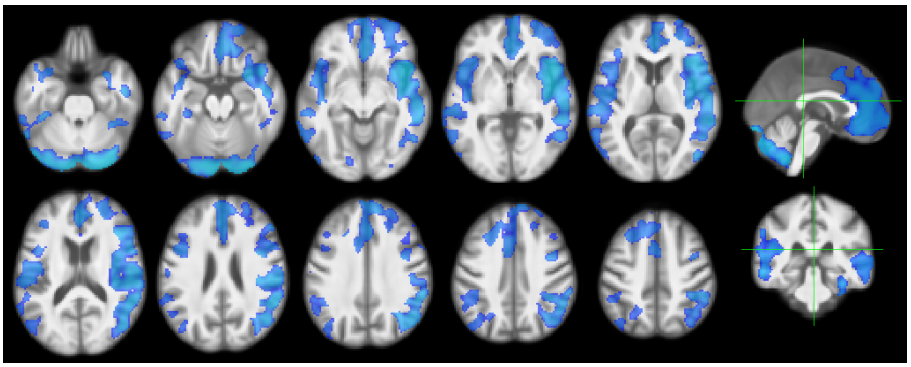

FIGURE 6.4: Whole-brain voxel-wise analysis found cerebral blood flow within several cortical regions at study baseline to be negatively associated with conversion to dementia within a mean 3.2 years follow-up. Reductions were demonstrated in the frontal lobe (paracingulate gyrus), insula, and temporal lobes (primarily right side).

6.6.3.2 Association with continuous clinical and imaging measures

Group differences between convert/non-convert

Pairwise group estimates given by a simple frequentist ANOVA model, without considering any other covariates, identified significant differences between the conversion subgroups in baseline Hoehn and Yahr (H & Y) score, MoCA score, global cognitive z score, UPDRS Part III score, mean cortical amyloid load (FBB SUVR and CL (figure 6.5) measures), normalised GM_{vol}, mean cortical CBF, and mean SUVR in the precuneus, such that converters had worse baseline expression of these measures. There was no difference

in age at baseline, years of education or APOE-ε4 status between convert and non-convert groups. Converters to PDD had displayed PD symptoms for a shorter duration, indicating a more rapid worsening of cognitive impairment in this group.

Figure 6.5 depicts the mean cortical CL values within the convert and non-convert subgroups, coloured by clinical amyloid classification.

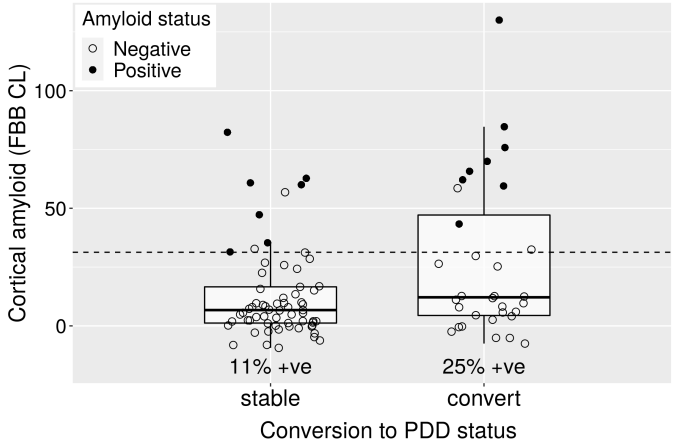

FIGURE 6.5: Cortical FBB uptake in Centiloids by conversion status, stratified within group by amyloid positivity. We found evidence of increased cortical amyloid accumulation at baseline in converters relative to non-converters. Proportional amyloid positivity was not significantly different between the two groups (Fisher's exact test: *p-value*=0.1). The dashed line at CL = 31.3 indicates the ROC-defined optimal centiloid cut-off in this sample defined in cross-sectional analysis, with sensitivity to clinically positive cases = 100%, specificity = 92.6%, AUC [95% confidence interval] = 0.98 [0.97, 1.0].

Predictive model analysis

In a Bayesian regression model estimating the potential predictive effects of select risk factors (baseline age, sex, baseline cognitive ability), only baseline cognitive ability was found to have an effect on conversion to dementia (estimate: −2.5, 95% CI: −3.8 - −1.4, figure 6.6). This model formed the basis of comparison with the primary predictive model fits.

Of the primary predictors applied in Bayesian regression model analysis, accounting for potential predictive effects of the above risk factors, the predictors of interest to demonstrate an effect on conversion to dementia within our sample were mean cortical SUVR (estimate: 5.7, 95% CI: 2.0 - 9.9, figure 6.7[A]), mean SUVR within the caudate (estimate: 6.0, 95% CI: 1.1 - 11.3, figure 6.7[B]), mean SUVR within the putamen (estimate: 6.2, 95% CI: 0.7 - 12.3, figure 6.7[C]), mean SUVR within the precuneus (estimate: 5.30, 95% CI: 2.0 - 9.2, figure 6.7[D]) and PC1 loadings (estimate: −17.4, 95% CI: −24.0 - −1.8, figure 6.8[A]). Examined predictors that demonstrated no evidence of an association with

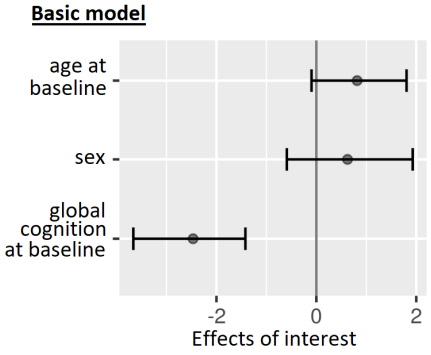

FIGURE 6.6: Effect sizes of predictors of conversion to dementia, obtained by Bayesian regression model (BRM) analysis. A model examining only the basic predictors found baseline global cognitive ability to be a negatively associated predictor.

conversion to dementia were SUVR within the thalamus, globus pallidus, amygdala and hippocampus, PCs 2-5, mean cortical CBF, and global grey matter volume. The respective figures depict the estimated effect of each of the parameters within the models, where the error bars reflect the 95% credible interval. Global cognition at baseline remained a negatively associated predictor within all models.

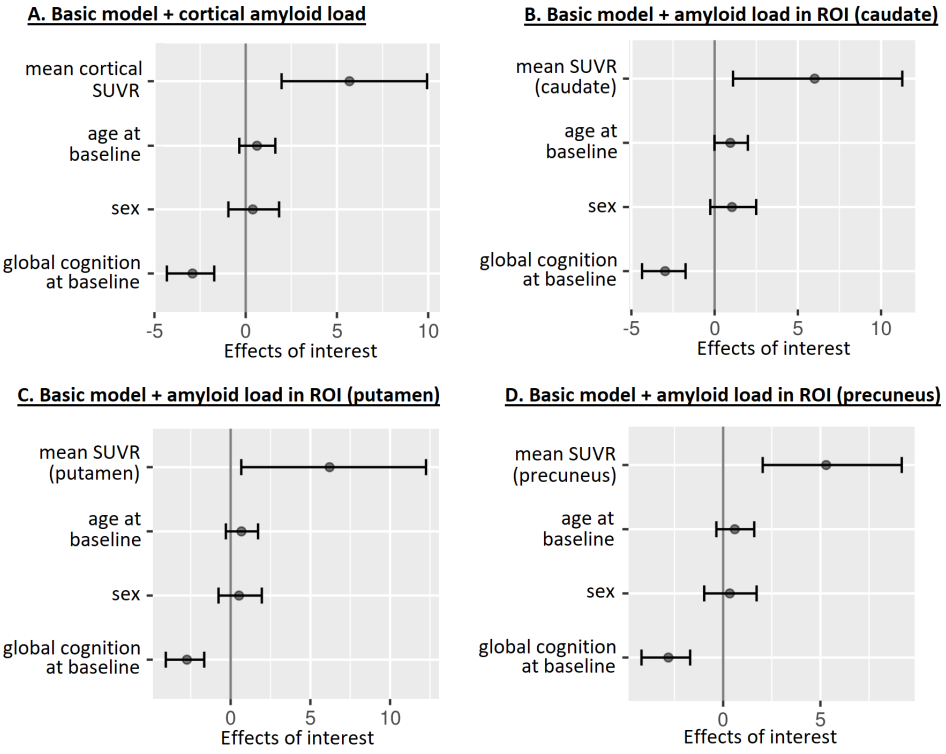

FIGURE 6.7: Effect sizes of predictors of conversion to dementia, obtained by Bayesian regression model (BRM) analysis; Adding mean SUVR values (extracted from the cortex and *a prior* ROI) into the model found SUVR to be associated with conversion to dementia within (A) cortex, (B) caudate, (C) putamen and (D) precuneus. Global cognitive ability also remained a negatively associated predictor in these models.

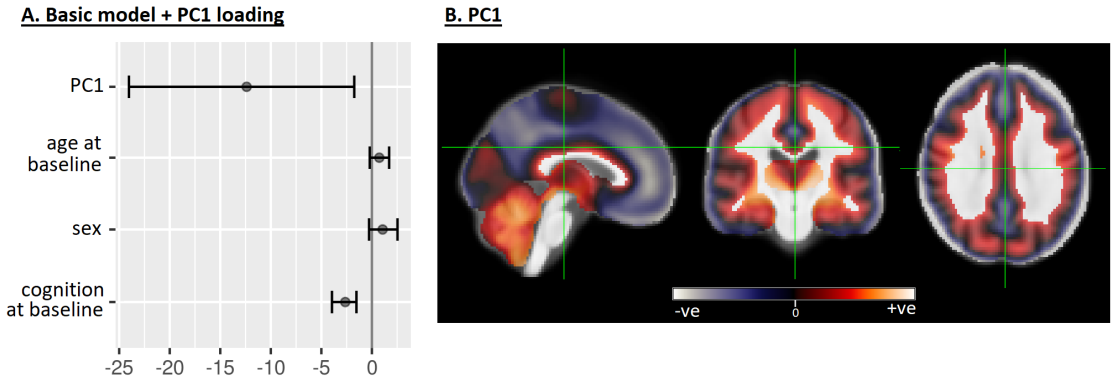

FIGURE 6.8: Effect sizes of predictors of conversion to dementia, obtained by Bayesian regression model (BRM) analysis; (A) Principal component 1 (PC1) was found to be an associated predictor. (B) PC1 represents the highest proportion of variance in the data, where negative (blue) values indicate regions of relative AB accumulation increase, which appear associated with conversion to dementia (parietal lobe, including the precuneus, frontal lobe, and paracingulate gyrus).

Comparing SUVR model predictive accuracy by LOOIC

When compared with the model including only the standard covariates by leave-one-out information criterion (LOOIC), there was no evidence that the cortical SUVR model improved prediction of future development of dementia. This is reflected by the difference in expected log predictive density ($elpd_{diff}$) between the two models, where the elpd difference was within the standard error ($elpd_{diff} = -3.1 \pm 3.6$). Additionally, I compared the predictive accuracy offered by the cortical SUVR model to the three ROI SUVR models. There was no evidence the ROI models performed better or worse than the cortical model in the prediction of conversion to dementia (precuneus $elpd_{diff} = -0.3 \pm 1.3$; caudate $elpd_{diff} = -1.8 \pm 2.2$; putamen $elpd_{diff} = -2.3 \pm 1.7$).

6.6.3.3 APOE-ε4 association with amyloid load

One likely influence on SUVR is the expression of the APOE-ε4 allele, which has been shown to correlate with amyloid deposition in PD (Akhtar et al., 2017; Villemagne et al., 2011). Bayesian regression analysis investigating APOE-ε4 carrier status as a predictor of mean cortical SUVR and PC1 loadings found evidence of a positive association between APOE-ε4 expression and SUVR (estimate: 0.15, 95% CI: 0.08 - 0.22, figure 6.9A), and a negative association with PC1 loadings (estimate: −0.05, 95% CI: −0.07 - −0.03, figure 6.9A).

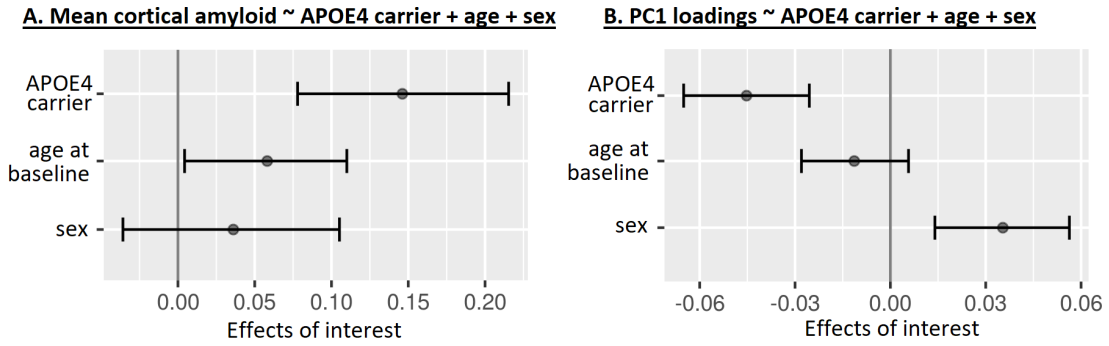

FIGURE 6.9: Effect sizes of APOE-ε4 status (carrier) and nuisance predictors of age and sex, obtained from Bayesian regression investigating mean cortical SUVR and PC1 loadings. (A) APOE-ε4 was (A) positively associated with mean cortical SUVR, and (B) negatively associated with PC1 expression. This is in line with the same relationship found between these measures and conversion to dementia given in figures 6.7[A] and 6.8[A].

6.7 Discussion

This longitudinal study analysed the role of beta-amyloid in conversion to dementia in PD, investigating multiple different metrics relating to amyloid deposition, and taking into account a number of known risk factors using sophisticated statistical methods. We found that, while baseline amyloid load was associated with conversion to dementia within a mean of 3.2 years follow-up, amyloid information likely provides limited predictive value in estimating the likelihood of imminent conversion to dementia in PD, once cognitive ability is known.

One rationale for pathophysiological involvement of amyloid in cognitive decline is based on the observation of high levels of Aβ deposition in AD, such that early deposition is followed by a cascade of pathological events leading to cognitive impairment and dementia. In this PD group, the time course of conversion to dementia within this sample was analysed with respect to amyloid classification. Unfortunately, the survival analysis was affected by the low proportion of amyloid positive participants in this study, such that estimated error on the survival trajectory of the amyloid-positive subgroup encompassed the amyloid-negative trajectory. This became more apparent as time went on, and the data became more right-censored. Observing the trajectories themselves, amyloid positive participants were seen to have shortened survival time over the course of the study, however this does not constitute significant evidence to support improved long-term outcomes in amyloid negative subjects with respect to conversion to dementia in PD. Given the prevalence of amyloid at 'positive' levels in PD is comparable to that seen in healthy

controls, retrospective studies targeting amyloid positivity may be better equipped to determine the time-course of associated risk for conversion to dementia.

This study did find that cortical amyloid deposition, investigated both in bayesian regression analysis and whole-brain voxel-wise analysis, appears to have a stronger association with future rather than current cognitive impairment, considering the results of cross-sectional analysis in this thesis. Specifically, high amyloid load across the whole cortex, and regionally in the precuneus, putamen and caudate, was associated with conversion to dementia in this sample. However, the results of predictive model analysis argue against a region-specific effect of amyloid deposition, as model comparison found no evidence of an improvement in the prediction of conversion to dementia when these values were included in the model. Furthermore, there was no evidence to suggest that amyloid deposition in one region was more informative than any other. The parameter estimates for all regions were similar in size, suggesting a global, rather than regional, effect of amyloid accumulation on future cognition. We found that a basic model containing only baseline age, global cognitive ability and sex was not significantly outperformed by the amyloid models, when compared in out-of-sample tests. In addition, voxels found by whole-brain voxelwise analysis of SUVR images to be positively associated with conversion were not restricted to these regions, nor was the variance encompassed by the the first principal component, where negative expression correlated with conversion. This result - finding an associated effect of the parameter, but no evidence of an improvement in model predictive performance - is not contradictory. This can result when there are correlated variables, such as amyloid and age (Melzer et al., 2019). In this case, age can effectively provide some of the information related to SUVR, with the addition of SUVR only providing a marginal further improvement in predictive accuracy. These results do not fully confirm those found previously in a similar longitudinal study of 46 non-demented PD patients, where amyloid load in the precuneus did not distinguish PDN and PD-MCI at baseline, but predicted conversion to a more severe diagnosis (Gomperts et al., 2013). Our investigation of a much larger prospective cohort, where a high proportion converted to dementia during follow-up, suggests that while amyloid accumulation in the precuneus does exhibit an association with future dementia, this effect is not specific to the precuneus or any other distinct region. If the ultimate goal of characterisation of amyloid in PD is to assist clinicians in advising non-demented PD patients with regard to their expected outcomes, the value of a model including this information is likely not sufficient to outweigh the cost

of PET imaging, invasive nature of the procedure, and radiation dose imparted to the patient.

We were able to identify a pattern of conversion-related variance within the amyloid data, using principal component analysis. While informative with respect to analysing regional and voxel-wise aspects of this data, the PC as a predictor had similarly large associated error in the prediction as was found in the other models. Examining the principal component revealed a pattern of negative voxel loadings within (but not limited to) the precuneus, paracingulate gyrus, and large portions of the frontal lobe, such that a negative association of the component relates to an over expression of this spatial pattern in converters to dementia (figure 6.8[B]). Visually comparing this pattern to that obtained by voxel-wise analysis with conversion to dementia (figure 6.3), it is apparent that much of the variance encompassed by the image is unlikely to be related to conversion to dementia alone. Subsequent investigation of PC1 loadings in association with APOE-ε4 carrier status found that this PC captures variance associated with both conversion to dementia and the expression of APOE-ε4. APOE-ε4 carrier status was associated with increased levels of cortical amyloid in this cohort, but there was no evidence of a difference in the number of APOE-ε4 carriers within the convert subgroups. A recent study of APOE-ε4 expression in a mouse model of synucleinopathy identified a possible facilitator effect of APOE-ε4 on α-synuclein pathology and related toxicity, observed to be independent of amyloid deposition, and correlating with faster cognitive decline in Lewy Body dementia (Zhao et al., 2020). In contrast, APOE-ε4 status does not seem to accelerate cognitive decline in the absence of β-amyloid in this cohort. It is possible that bias in our sample weakened our ability to detect an effect of APOE-ε4 on conversion status, as the cohort was originally enriched at baseline for PD-MCI, a known risk factor for conversion to dementia in PD. Thus our low sample size of PDN at baseline may not be inclusive enough to detect the effects of APOE-ε4 on cognitive decline in those not already classified as PD-MCI.

While we found evidence of reduced cortical cerebral blood flow in converters within several brain regions using voxel-wise regression, there was no evidence of an effect when examining mean cortical CBF in Bayesian regression analysis. Extracting mean values of CBF may not be an appropriate method of examining group differences with this type of data, in that regional or network based differences may be occluded by taking the mean over a broad region. Analysis at the voxel level is more apt, and the results here are in line with similar findings of reduced CBF in parietal areas associated with

accelerated cognitive decline in AD (Benedictus et al., 2017). Previously, PD-related networks of cerebral hypoperfusion at baseline have been shown to correlate with cognitive impairment (Melzer et al., 2011) - these results perhaps support the application of this method in deriving a conversion-related network of cerebral hypoperfusion in PD. The evidence of reduced perfusion in converters at baseline may also provide an explanation for the difference in duration of symptoms between converters and non-converters, with converters seen to progress more rapidly along the disease course.

Limitations

Limitations of this study, in addition to those discussed in the previous chapter, include a comparatively high number of PD-MCI participants compared to PDN (PD-MCI, n = 74; PDN, n = 23). Participants fulfilling the requirement for PD-MCI were preferentially recruited at study outset, based on an observed increased risk of cognitive decline and development of PD in those individuals. This represents one of the primary strengths of this study, as this enabled comprehensive prospective investigation of a reasonably large number of individuals who had converted to PDD during follow-up. However, it is possible that our study lacked the strength to detect subtle changes occurring in the cognitively normal stages of PD that influence future cognition. While we recruited across the cognitive spectrum due to a particular interest in the pathological basis of cognitive impairment at baseline, a future possible de novo design examining cognitive decline in PD may recruit at diagnosis of PD, and follow through to conversion to dementia, thus increasing sensitivity to true effects in the population.

Prospective analysis of survival from dementia during this longitudinal study, stratified by amyloid positivity at baseline, was affected by the comparatively low prevalence of amyloid positivity in PD, comparable to levels seen in healthy ageing (Ossenkoppele et al., 2015). This increases the error associated with this analysis, particularly where amyloid positive patients were lost to follow-up before progressing to dementia (first instance at approximately 2 years from baseline scan). While an apparent increased risk was detected, this does not represent evidence of improved long-term outcomes in PD in those individuals exhibiting low levels of cortical amyloid load.

Low statistical power is an increasing concern in the field of neuroimaging research (Poldrack et al., 2017). Where cognitive neuroscience benefits from a high degree of reproducibility, many imaging studies face cost-restrictions that limit the availability of

high sample sizes and multiple trials per subject. While this study represents one of the largest of it's type, our sample size was likely a primary factor increasing the error of our cross-validation analysis, which can be as high as ±10% in studies containing 100 samples (Varoquaux, 2018). This limitation is well-understood in this thesis, and care has been taken in interpreting the results of these statistical models. Group-level voxel-wise analysis employing permutation testing, as applied here in the voxel-wise analysis of SUVR and CBF images, has been shown to provide good statistical control on prediction accuracy (Stelzer et al., 2013). Considering these analyses in concert thus increases our confidence in the interpretation of the results presented here.

This longitudinal analysis of a large, cognitively well-characterised PD cohort, found evidence of increased cortical amyloid accumulation in PD that correlated with future cognitive decline to dementia within approximately three years. However, the practical merit of this measure in estimating the three-year probability of conversion to dementia is likely minimal. The primary pattern of spatial variance of amyloid load was found to be associated with both conversion to dementia and APOE-ε4 expression, suggesting that involvement of other pathologies associated with this gene expression may affect patterns of amyloid deposition in PD.

Chapter 7

Diffusion Imaging of White Matter Degeneration - a Fixel-Based Analysis

7.1 Author Contributions

I performed the image processing, study design, statistical analysis and interpretation of results in this chapter. TM and MA acquired the MR image data for this study.

The NZBRI Study of Parkinson's Disease

The larger study of Parkinson's disease at the New Zealand Brain Research institute was conceptualised and designed by TM, DJM, MM, TP, DHM, JD-A, and TA. TM, MM, DHM, RK, DJM, LL, JD-A, and TA obtained funding for the study. RK, LL, DJM, MM, TP, and SM provided administrative, technical, and material support. All authors contributed to acquisition, analysis or interpretation of data.

7.2 Introduction

Parkinson's disease is a neurodegenerative disorder characterised by the progressive formation of alpha-synuclein aggregates and death of dopaminergic neurons in the substantia

nigra, manifesting in a broad spectrum of motor and non-motor clinical features, including progressive cognitive decline and dementia. Thus far this thesis has focused mainly on the imaging of global and cortical pathological changes that may be associated with cognitive decline in PD, such as beta-amyloid protein accumulation, grey matter atrophy and cerebral perfusion. While investigation of amyloid accumulation has not identified any major effect on current or future cognitive status within our cohort, it may be that the primary driver of neurodegeneration (and thus, cognitive decline) in PD is alpha-synuclein aggregate-related synaptic and neuronal dysfunction, in addition to organelle dysfunctions (mitochondrial, lysosomal, and endoplasmic reticulum impairments) and metallomic imbalances resulting in degenerative neurotoxicity (oxidative stress and neuroinflammation). Modern imaging techniques enable changes in white matter to be quantified in vivo, offering potential analogues of overall white matter health, including myelin damage and axonal degeneration.

MR imaging offers perhaps the most potential for in vivo investigations of white matter changes over the disease course in PD. For example, lesions in white matter are visible on T2-weighted fluid-attenuated inversion recovery (FLAIR) MRI as areas of increased brightness, or white matter hyperintensities (WMH). Comorbid WMH's are expected to contribute to balance, gait, mobility and cognitive impairments, both in PD and in otherwise normal elderly individuals (Bohnen & Albin, 2011). In recent years, diffusion-weighted imaging, specifically diffusion tensor imaging (DTI), has garnered widespread interest as a way to potentially quantify white matter microstructural integrity in vivo, but has been plagued with difficulties including a lack of anatomical accuracy in small subcortical structures, large potential for error over a long, complicated workflow, and failure to model complex fibre orientations at the voxel level. Nevertheless, DTI has been applied incredibly widely, reporting white matter integrity to be differentially reduced in PD with dementia (PDD) compared with cognitively normal PD (PDN) (Atkinson-Clement et al., 2017). DTI tractography revealed anterior cingulum fibre tracts to be more affected in PDD compared with both healthy controls and PDN (Kamagata et al., 2012), while another study has shown evidence of a possible sequential relationship, wherein brain hypoperfusion precedes WM microstructural degeneration, grey matter atrophy, and consequently cognitive decline (Hattori et al., 2012). This suggests that WM changes imaged using diffusion MR may have potential as a biomarker of future development of dementia in PD.

However, there is a lack of consensus in the literature as to when in the PD disease course microstructural changes become differentiable from age-matched controls; (Melzer et al., 2013) observed increased WM structural abnormalities compared to controls, beginning from PDN and increasing with severity of cognitive impairment; while (Hattori et al., 2012) found WM to be detrimentally affected in PD-MCI, PDD and dementia with lewy bodies (DLB), but not in PDN, compared to controls. Studies thus run the range of little to no differences in WM at the cognitively normal stage, to showing extensive changes that correlate with poorer cognitive performance at longitudinal follow-up (Auning et al., 2014; Sterling et al., 2017). Some of this variation may be due to differences in the characterisation of the cognitive groups, small sample sizes and the limitations inherent to DTI imaging, requiring the use of more sensitive and accurate methods for modelling subtle changes in early disease. In recent years, higher order methods of diffusion imaging have been developed in an attempt to mitigate the aforementioned limitations associated with DTI, which may help to define a clearer picture of WM changes that occur prior to cognitive impairment.

7.2.1 Diffusion weighted imaging

It is useful at this point to discuss the primary tenets underlying DTI, in order to understand both the potential value and the limitations that can be addressed by improvements in acquisition and modelling. DTI refers to a specific type of modelling of diffusion weighted magnetic resonance imaging (DW MRI) that enables the quantification of tissue architecture based on the movement of water (water diffusion) through those tissues. DTI models the displacement of water molecules as a rotationally invariant tensor (Lanskey et al., 2018), with the diffusion of water assumed to be essentially random, following Gaussian free diffusion. Deconstruction of the diffusion tensor allows the estimation of water diffusion in the directions sampled by the diffusion signal. This information is used to estimate several main properties of interest within tissues, namely radial diffusivity (RD), axial diffusivity (AD), mean diffusivity (MD) and fractional anisotropy (FA).

DTI metrics may be used to infer structure based on what we know of interactions of water with cellular membranes, macromolecules and white matter fibres. Fractional anisotropy (FA) in particular is often used as a summary measure of white matter integrity, and quantifies the degree to which water diffusion is directionally restricted within a voxel,

following a scale of zero (fully isotropic) to one (fully anisotropic). WM tends toward anisotropy, consisting of parallel bundled axons, where diffusion perpendicular to the axon is restricted in part by the myelin sheath. This facilitates preferential diffusion along the main direction of the fibre bundle. In the ideal DTI case where unrestricted diffusion of water is assumed, water diffusion through the brain will be completely directionally restricted in WM (but free to diffuse along the WM pathway), and essentially free to diffuse in CSF. This is clearly an over-simplification, and one that impacts the biological interpretability of DTI, both in terms of local metrics such as FA, and more global tractographical analysis.

Tractography has been applied to DTI data to determine the trajectories of white matter tracts, in order to infer the underlying connectome of the human brain (R. E. Roberts et al., 2013). In theory, white matter fibres may be inferred where the principal direction of diffusion is maintained through a number of contiguous voxels. In practice, both accurate tractography and evaluation of the above DTI metrics suffer from the assumptions underlying the model. The traditional diffusion tensor model is a poor fit to describe voxels containing partial volumes, or multiple distinct fibre bundles oriented in different directions, as DTI models only a single principal direction of diffusion within each voxel. Crossing, kissing, fanning, or curving fibres are difficult for many diffusion reconstruction algorithms to correctly distinguish, leading to incorrect estimation of fibre orientations (Daducci et al., 2014). The 'crossing fibre' problem is expected to affect approximately 90% of voxels in a DW image (Jeurissen et al., 2013). This has severe implications for interpretation of diffusion tensor modelled data, and strongly argues for a move away from such simplified models.

High angular resolution diffusion imaging (HARDI) was introduced in part to address the crossing fibre problem, particularly in the context of fibre tracking. Here, fibre orientation information is paramount, in order to effectively follow a single fibre as it curves and intersects with other fibres through the brain. While diffusion signal can be improved in many ways (for example, using multiple b-values, or 'shells', applied over the same direction, multiple repeats of the same direction, or any mixture of the two), HARDI primarily focuses on improving directional information by sampling directional space as densely as possible. Traditional DTI is acquired using as few as 6 unique diffusion directions plus at least one image without diffusion weighting (b=0), while HARDI acquisition protocols

sample over 50 unique directions for any one b-value (Berman et al., 2013). HARDI signal, acquired in this way, can be thought of as the spherical convolution of the amplitude of directional responses of tissues within a voxel to an applied magnetic field gradient. It follows that the fibre population in a voxel can be modelled by performing the spherical deconvolution of the DW signal by the WM response function, constrained to non-negative values (Tournier et al., 2007). This yields the fibre orientation distribution (FOD) of the WM tissue within the voxel. Constrained spherical deconvolution (CSD) methods have been shown to offer superior fibre tracking compared to conventional DTI methods, in the context of neurosurgical planning (Farquharson et al., 2013; Mormina et al., 2015). While effective in addressing the crossing fibre problem, voxels containing partial volumes, particularly at the WM/GM border, require additional consideration. To address this, specialised applications of CSD allow not only the FOD pertaining to WM and CSF to be estimated, but also GM. Until recently, 3-tissue FOD estimation has been limited to data acquired using multiple b-values, or 'shells'. Dhollander and Connelly (2016) have developed a method to obtain these 3-tissue FODs using only single-shell data (Single-Shell 3-Tissue CSD [SS3T-CSD] (Dhollander & Connelly, 2016)), using MRtrix3Tissue (https://2Tissue.github.io), a new branch of MRtrix3 (Tournier et al., 2019). The ability to obtain multi-shell-like estimation from single-shell data presents highly desirable clinical advantages, both in reduced scanning-time and cost. The SS3T-CSD method shows clear improvements over standard single-shell CSD, as will be shown in this chapter.

7.2.2 Fixel-based analysis

Previous chapters in this work have employed voxel-based analysis (VBA) for investigating whole-brain voxel-wise tests across and within our subject groups, using statistical parametric mapping (SPM). While VBA has the ability to identify local group differences and test specific hypotheses, voxel-averaged metrics such as FA lack the within-voxel specificity required to compare specific fibre populations, especially in the context of crossing fibres and partial volumes. In response to this limitation, fixel-based analysis (FBA) was proposed (D. A. Raffelt et al., 2016) as a method that improves biological interpretability in these areas by breaking down voxels into their composite fibre populations, represented as 'fixels' (D. Raffelt et al., 2015). The fixel not only provides a representation of the potentially multiple fibre population orientations within a standard voxel, but also may be used to examine degeneration by way of reduced fibre density (FD) or fibre-cross-section

(FC). Changes in fibre density may be interpreted as an alteration of the intra-axonal volume of an axon, with a decrease in FD indicating axonal degeneration. Changes in fibre bundle cross-section may occur as a consequence of atrophy, wherein a loss of extra-axonal space may reflect a loss of axons (D. A. Raffelt et al., 2016) or hypomyelination and disorganisation of axons (Malhotra et al., 2019). A combined measure of these two processes, fibre-density-cross-section (FDC) may serve as an average measure of neuronal health, much as FA does in voxel-based DTI analysis. These metrics are expected to provide a more readily interpretable measure of neuronal health from DW imaging than voxel-average metrics, and also allow tract-specific statistical testing.

To that end, this chapter investigates tract specific changes in FD, FC and FDC in an expanded cohort of both Parkinson's disease and controls. This cross-sectional application of FBA represents one of the largest and most well-characterised PD cohorts examined using this new technique, including subjects across the cognitive spectrum from normal cognition, mild cognitive impairment, and dementia. The aim of this study was to (1) identify specific fibre tracts affected in PD, (2) investigate the role of ageing in white matter changes, and (3) identify any tracts that relate specifically to cognitive performance. Additionally, I restricted the cohort to those for which amyloid imaging was also acquired (n=84) and (4) investigated if the presence of amyloid deposition was related to fibre tract degeneration by these same metrics.

Previous results from cross-sectional analysis of amyloid load in these subjects identified cognitive deficits to be primarily age rather than amyloid-driven. Given the close relationship between cognitive decline and white matter degeneration, it will be of use to investigate any association between amyloid load and measures of WM degeneration given by FBA, which may further support our previous findings. Using the most up-to-date techniques, we aim to construct a more accurate picture of WM degeneration in PD, and elucidate the driving forces behind those changes.

7.3 Materials and methods

7.3.1 Participants

A convenience sample of 171 participants, including both healthy controls and patients representative of the full cognitive spectrum in PD, was recruited as part of an ongoing longitudinal study of Parkinson's disease at the New Zealand Brain Research Institute (NZBRI), Christchurch, New Zealand. Parkinson's disease participants met the UK Parkinson's Disease Society's criteria for idiopathic PD (Hughes et al., 1992), and were recruited from volunteers at the Movement Disorders Clinic at the NZBRI. Exclusion criteria included atypical Parkinsonian disorders; prior learning disability; previous history of other neurological conditions including moderate-severe head injury, stroke, vascular dementia; and major psychiatric or medical illness in the previous 6 months. Participants completed a comprehensive neuropsychological battery and MRI scanning session. In addition to HARDI MRI, a subset of 84 also completed [^{18}F]-Florbetaben (FBB) PET imaging. Of the original sample, there were a number of exclusions; 2 due to patient motion; 5 due to acquisition error; 2 due to a later diagnosis of progressive supranuclear palsy (PSP); and 2 withdrew from the study. The final HARDI cohort included a total of 160 participants, including controls with normal cognition (CN; n=34), otherwise healthy controls with MCI (C-MCI; n=3), cognitively normal PD (PDN; n=46), PD with mild cognitive impairment (PD-MCI; n=66) and Parkinson's disease dementia (PDD; n=11). All participants gave written informed consent, with additional consent from a significant other when appropriate. The study was approved by the regional Ethics Committee of the New Zealand Ministry of Health (No. URB/09/08/037).

7.3.2 Image acquisition

MR images were acquired on a 3T General Electric HDxt scanner (GE Healthcare, Waukesha, USA) with an eight-channel head coil. High angular resolution diffusion weighted imaging (spin echo, echo planar imaging (SE-EPI) sequence, TE/TR=94.4/10000ms, flip angle = 90 deg, acquisition matrix = 128 × 128 × 74, slice thickness = 2mm, voxel size of 1.95 × 1.95 × 2 mm3, phase encoding = anterior-posterior) was performed over 64 uniformly distributed non-co-planar gradient-encoding directions (b = 2500 s/mm2). Six volumes without diffusion weighting (b = 0s/mm2) were also acquired, for a total

scan time of approximately 13 minutes. At least one scan with reversed phase encoding (posterior-anterior) was also acquired (b=0 s/mm2), to be used in EPI distortion correction.

PET images of [^{18}F]-Florbetaben (FBB) uptake were also acquired in a subset of subjects. These acquisition parameters are detailed in chapter 5, section 5.5.2.

7.3.3 Image preprocessing

Software used in this study for image preprocessing and statistical analysys included MATLAB R2018b v9.5.0.1175774, SPM12 v6685 (http://www.fil.ion.ucl.ac.uk/spm/), FMRIB Software Library (FSL) v5.0 (Jenkinson et al., 2012), MRtrix3 (https://www.mrtrix.org) (Tournier et al., 2019), Mrtrix3Tissue v5.1.0 (https://2Tissue.github.io) and RStudio v1.2.1335. Unless stated otherwise, the program used to perform image processing or statistical analysis on diffusion-weighted data was MRtrix3.

7.3.3.1 Initial preprocessing

Diffusion weighted images underwent denoising (Veraart, Fieremans, & Novikov, 2016; Veraart, Novikov, et al., 2016), removal of Gibbs ring artifacts (Kellner et al., 2016), correction for motion and distortion due to eddy currents and field inhomogeneities using the acquisition with reverse phase encoding (Andersson & Sotiropoulos, 2016; Andersson et al., 2003), and bias field correction (Tustison et al., 2010). Voxel size was then up-sampled to 1.3mm isotropic in order to increase anatomical contrast (Dhollander et al., 2016). Brain masks were computed for these up-sampled images using FSL's BET (S. M. Smith, 2002), at a fractional intensity threshold value of f=0.25. Images were visually inspected after each step.

7.3.3.2 Constrained spherical deconvolution

Tissue response functions were estimated for WM, GM and CSF for each subject using an unsupervised method (Dhollander et al., 2019, 2016), and averaged to create a single set of three study-specific tissue response functions. Single-Shell 3-Tissue CSD (SS3T-CSD) was then performed within the brain mask to obtain WM-like FODs as well as GM-like

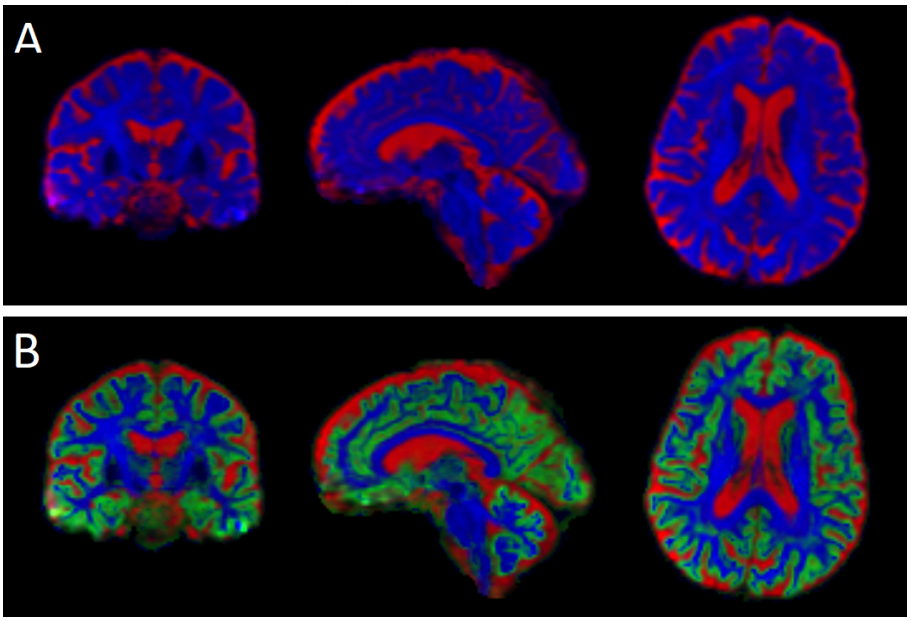

FIGURE 7.1: Volume fraction images obtained through FOD estimation using a) MSMT-CSD b) SS3T-CSD. Red is the volume of tissue estimated to be CSF, blue is estimated to be WM, and green is estimated to be GM. MSMT-CSD is unable to estimate GM from a diffusion weighted data consisting of a single b-value +b=0. SS3T-CSD performed on the same data yields multi-shell-like estimation of tissue volume fractions.

and CSF-like compartments in all voxels (Dhollander & Connelly, 2016), using the group-averaged response functions for each tissue. In brief, SS3T-CSD achieves multi-shell-like FOD estimation by using an iterative approach in the estimation of tissue boundaries. Firstly, WM is initialised to 0 and used as a prior constraint to fit a CSF+GM mixture, yielding an underestimate of CSF; this underestimate is then used as a constraint to fit a WM+GM mixture, which will also yield an underestimate of WM; this new estimate is then applied as the WM constraint in the next iteration. This process, carried out over 3 iterations, avoids overestimation of WM and allows estimation of GM, which cannot be estimated by simply applying the MSMT-CSD algorithm to single-shell data. Figure 7.1 shows the volume fractions estimated for each tissue using (a) MSMT-CSD and (b) SS3T-CSD. The ability to estimate GM-FOD information greatly improves the spatial resolution of WM in the generation of the study specific WM-FOD template, as evidenced in figure 7.2.

7.3.3.3 Study-specific template creation

The resulting 3-tissue FODs for each subject were then intensity-normalised in order to make the FODs comparable between subjects. A study-specific unbiased FOD template

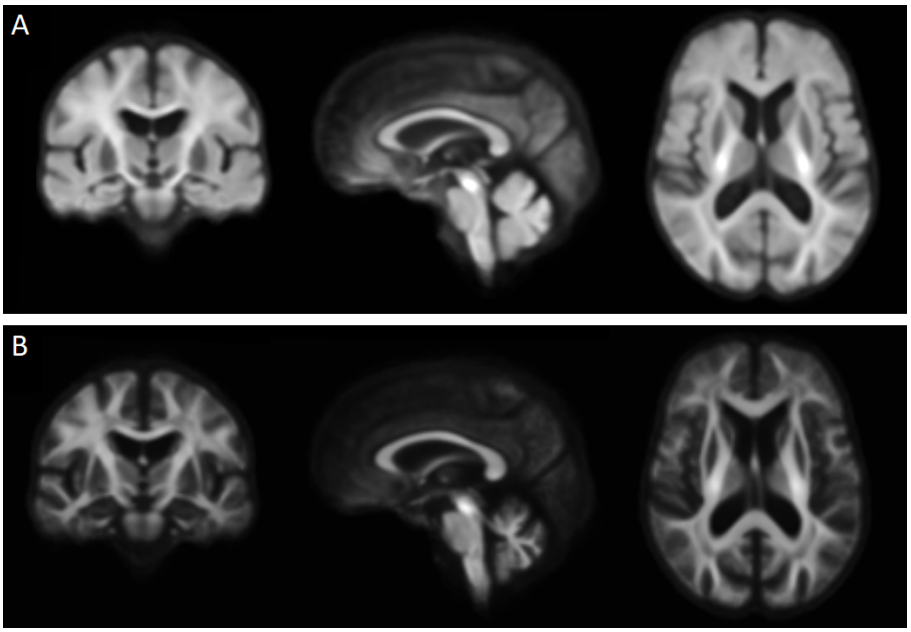

FIGURE 7.2: Study-specific WM FOD template images created from a subset of 32 subjects, using (a) WM FODs derived from MSMT-CSD, and (b) WM FODs derived using SS3T-CSD. The sagital slice was placed directly in the midline of the brain. Image (a) is included here to demonstrate the efficacy of SS3T-CSD over MSMT-CSD in distinguishing WM from GM in FOD generation.

was created from a subset of 32 subjects (8 each from CN, PDN, PD-MCI and PDD) by first applying an affine registration, then applying an iterative non-linear registration to bring all subjects into a common space (D. Raffelt et al., 2011). Figure 7.2(B) depicts the output averaged FOD template image from SS3T-CSD derived 3-tissue FODs. The 2-tissue FODs output from employing the MSMT-CSD method with this data were also used to generate a study-specific WM-FOD template (figure 7.2[A]), in order to compare the efficacy of the two methods. There is a clear improvement in the delineation of WM tissue using the SS3T-CSD method, with WM significantly over-estimated by the MSMT-CSD method.

Non-linear, apodised point-spread reorientation was then used to coregister all subject FOD images to the template image (D. Raffelt et al., 2011; D. Raffelt, Tournier, Crozier, et al., 2012). Subject brain masks were then warped to template-space using the output warp fields from this step, and a template mask computed from the intersection of all subject masks. This defined areas in which all participants had usable data.

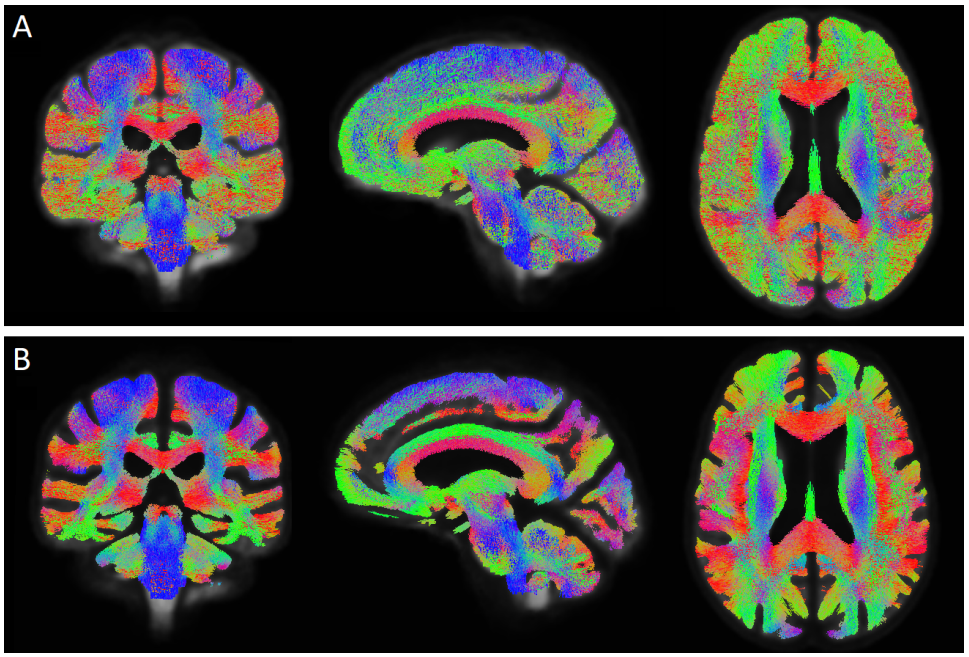

FIGURE 7.3: A whole brain tractogram created from study specific WM FOD templates, given by (A) the MSMT-CSD method, which estimates only WM and CSF-like compartments when used with single-shell data, and (B) the SS3T-CSD method, which estimates WM, CSF and GM-like compartments from single-shell data. 20 million tracts were originally generated, and filtered to 2 million by SIFT. For ease of display in this figure, streamlines were further reduced to 200 thousand. Colour indicates the direction of streamline orientation: red indicates left-right; green indicates anterior-posterior; blue indicates superior-inferior.

7.3.3.4 Probabilistic fibre tractography

A whole-brain tractogram including twenty million streamlines was then generated from the FOD template, using probabilistic fibre tractography. Tracts were generated using the WM-FOD template mask as both seed region and restrictive mask, ensuring all possible WM voxels are included in fibre tractography estimation. The number of streamlines was filtered to 2 million using spherical-deconvolution informed filtering of tractograms (SIFT) (R. E. Smith et al., 2013), in order to reduce the effect of biases inherent to reconstruction. Figure 7.3 shows the output of fibre tractography and SIFT, colour-coded based on streamline orientation, when performed using (A) the WM-FOD template generated from employing MSMT-CSD with single-shell data, and (B) the WM-FOD template generated from employing SS3T-CSD with the same data. This figure demonstrates the effect of over-estimation of WM, leading to probabilistic tractography failing to accurately terminate tracts at the GM/WM boundary, resulting in lack of delineation of WM tracts and a diffuse loss of directional information.

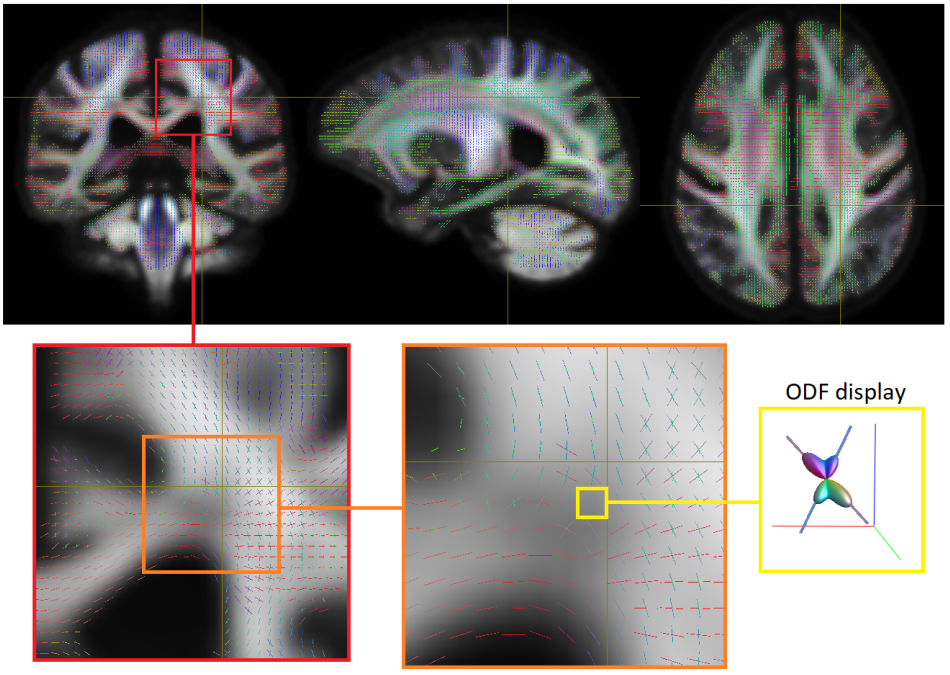

FIGURE 7.4: The generated fixel mask, designating all fixels that will be examined in fixel-based analysis. The magnified section (red, orange inset) contains crossing fibres. The fixels contain information relating to multiple fibre orientations, rather than the single primary orientation that would be given by DTI. The yellow inset depicts the estimation of two crossing fixels from segmentation of the FOD lobe peaks and troughs for that voxel. Colour indicates the direction of fixel orientation: red indicates left-right; green indicates anterior-posterior; blue indicates superior-inferior.

7.3.3.5 Fixel and apparent fibre density estimation

The template FOD was then segmented into fixels based on lobe peaks and troughs, producing a 'fixel mask' (figure 7.4). This mask designates all fixels that will be included in statistical analyses, and hence also which fixels' statistics can contribute to others via the mechanism of connectivity-based-fixel enhancement (CFE) (D. Raffelt et al., 2015). Individual subject fixels were estimated by segmenting each FOD lobe to identify the number and orientation of fixels in each voxel (figure 7.4: ODF display inset). This step also provides the first estimate of apparent fibre density (AFD) within each fixel in subject space. The resulting fixels were then reoriented based on the local warps used previously, to ensure the fixel directions remain consistent with the surrounding anatomy following a non-linear spatial transformation. Each subject's individual fixel FD values were then assigned to the corresponding fixels in the template fixel mask. Fixel-based metrics computed for each subject will now correspond in space, and specific tracts can be directly compared in statistical analysis.

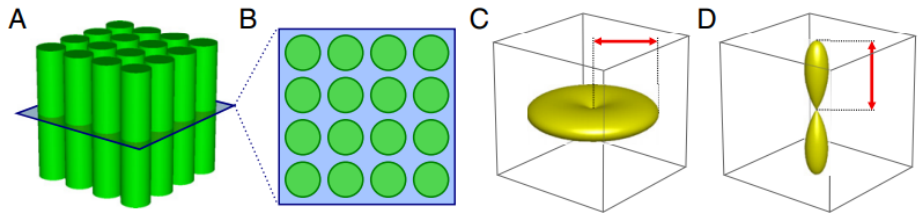

FIGURE 7.5: The principles of AFD. (A) A given voxel containing coherently ordered axons. (B) Radial diffusion of water is restricted by the intra-cellular compartment (green circles) in the perpendicular plane. (C) Diffusion weighted signal is proportional to the intra-cellular compartment, independent of axonal diameter. (D) The amplitude of the FOD in the radial direction is proportional to the magnitude of the radial DW signal, and therefore also to the intra-axonal volume occupying the perpendicular plane. Reprinted from (D. Raffelt, Tournier, Rose, et al., 2012), Copyright © 2012, with permission from Elsevier.

7.3.4 Fixel-based metrics

Fixel-based metrics were computed for each subject across all white matter fixels, including apparent fibre density, fibre-bundle morphology (cross-section), and a combined fibre density and cross-section metric, following the methodology described by (D. A. Raffelt et al., 2016). All three metrics provide different yet complimentary information relating to white matter health, which will be summarised here.

Computation of AFD for any given coherently ordered fibre bundle is based on the assumption that intra-axonal water is radially restricted within fibres (figure 7.5[A-B]), and the observation that radial DW signal emanating from a restricted compartment is independent of axonal diameter (D. Raffelt et al., 2011) (figure7.5[C]). As the FOD amplitude is approximately proportional to the radial DW signal (figure7.5[D]), the integral of the FOD lobe in any given direction will then be proportional to the intra-axonal volume of axons aligned in that direction (Mito et al., 2018). Thus, the apparent fibre density represents the volume of a bundle actually occupied by fibres (Figure 7.6[a]), providing within-voxel specificity to microstructural changes in WM.

The AFD value of each subject fixel is mapped to a corresponding fixel in template space, and thereafter referred to by the shortened acronym Fibre Density, FD. If no subject fixel can be found that corresponds to a template fixel within a maximum angle of 30 degrees, then a value of zero is assigned (D. Raffelt et al., 2015), as absent fixels most likely occur due to a very low, or zero, FD.

7.3.4.1 Fibre-bundle cross-section

While FD is sensitive to microstructural changes in intra-axonal volume at the sub-voxel level, it is independent of the macro-structural changes to the cross-sectional size, or morphology, of the bundle. In certain cases, as in figure 7.6(b), a loss of axons may result in a reduced overall macro-structural area of the fibre bundle, while FD is preserved. Macro-structural morphology is evaluated in the fixel-based framework using the fibre-bundle cross-section (FC) metric (D. A. Raffelt et al., 2016).

In short, FC is derived completely from the warp fields generated by the coregistration of subject FODs to template space. In the plane perpendicular to the fixel direction, the template-to-subject warp fields contain information about the local transformation required to spatially normalise a given fibre bundle in template space to the corresponding fibre bundle in subject space. FC is estimated as the overall factor of volume change (or the expansion or contraction of a cross-sectional area) required to transform a template fibre bundle to subject anatomy. Thus, a value greater than 1 implies the subject FC is larger than the corresponding template fibre bundle, and likewise a value less than one indicates a reduced subject FC. It is important to keep in mind that FC is a relative metric - it is only valid to directly compare FC between subjects whose fixel data corresponds to the same study-specific template. This precludes the comparison of tract specific FC values with those obtained in other studies. It is valid, however, to compare the results of

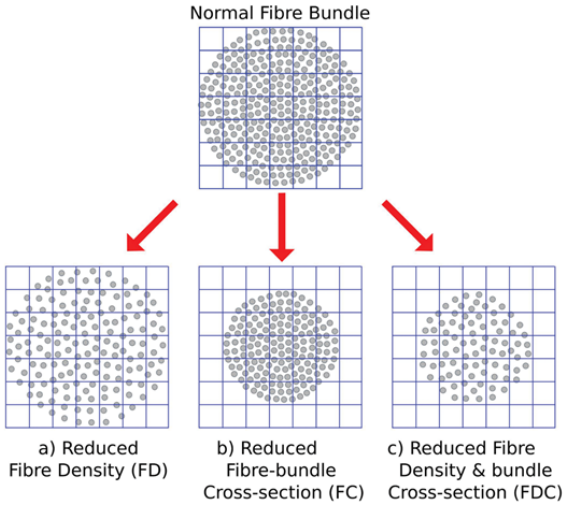

FIGURE 7.6: Fixel-based metrics allow the varying manifestations of changes to the intra-axonal volume of a fibre bundle to be differentiated. Each square represents a voxel, containing a certain number of fibres. This figure originally appears in (D. A. Raffelt et al., 2016), Copyright © 2017, Elsevier. Reused under Creative Commons licence.

between-subject statistical analyses with results from other groups. For group statistical analysis, the log of FC is computed such that the data are centered normally around zero.

7.3.4.2 Combined fibre density and cross-section

Both FD and FC are important factors affecting the total intra-axonal volume across a bundle's full cross-sectional extent (figure 7.6(c)), and hence both effect the overall capacity of that fibre bundle to carry information. As all subjects fixels correspond to the same set of template fixels, it is a simple matter to compute a combined measure for each fixel, resulting in a fibre-density and cross-section metric (FDC). This metric can be thought of as a more complete measure of intra-axonal volume, accounting for both within-voxel density of fibres, and macro-structural area (D. A. Raffelt et al., 2016).

7.4 Statistical analysis

7.4.1 Connectivity-based fixel enhancement

Connectivity-based smoothing and statistical inference were performed using connectivity-based fixel enhancement (CFE). CFE uses the study-specific tractogram output from probabilistic tractography to structurally connect neighbouring fixels, identifying those that likely share underlying anatomy. In smoothing, probabilistic connectivity information is used to preferentially smooth values along structurally connected fixels (as opposed to applying a standard isotropic Gaussian kernel), ensuring that smoothing occurs locally with fixels belonging to the same fibre tract. Spatially restricting the Gaussian kernel helps to prevent smoothing with neighbouring fixels that may belong to crossing fibres, or remote fixels outside of the WM structure that may contain very different values. Here, CFE smoothing was applied using the template-derived whole-brain tractogram, containing 2 million streamlines, using the default parameters (FWHM = 10mm, C = 0.5, E = 2, H = 3) (D. Raffelt et al., 2015). CFE also applies probabilistic connectivity information in statistical inference, to mimic conventional threshold-free cluster enhancement. All P-values derived from FBA analysis were thus corrected for family-wise error using non-parametric permutation testing over 5000 permutations (D. Raffelt et al., 2015).

7.4.2 Whole-brain fixel-based analysis

Using CFE-supported whole-brain FBA, I first applied a standard ANCOVA model (with age and sex as covariates) to assess fixel-wise differences in FD, log(FC) and FDC, specifically testing the following contrasts within the full PD/controls cohort: PD > CN, C-MCI > CN, PD-MCI > CN, and PDD > CN. In the cohort restricted to those with amyloid PET imaging, I investigated differences in these metrics between clinically amyloid positive and amyloid negative participants (Aβ-positive > Aβ-negative).

In addition, I ran three multiple linear regression models, restricted to PD, to investigate the association between the fixel-wise metrics and continuous measures of (1) global cognitive ability (cognitive z score), (2) motor impairment (UPDRS Part-III score), (3) global Aβ load (average global FBB CL value), and (4) age. Age was included as a covariate in models (1-3); models (1) and (2) were assessed specifically in the HARDI only cohort; model (3) was assessed specifically in the HARDI + Aβ cohort; Global Aβ load was included as a covariate in model (4) for the HARDI + Aβ cohort; sex was included as a covariate in all models. I tested for both a positive and negative association between the HARDI metric and the variable of interest in all models.

The fixel-level statistical inference maps were corrected for family-wise error using non-parametric permutation testing over 5000 permutations (D. Raffelt et al., 2015), and thresholded at a FWE-corrected P-value < 0.05. The output statistical inference maps for each contrast were mapped to associated streamline points in the whole-brain tractogram, and the resulting track scalar files displayed over the study-specific template using the mrview tool in MRtrix3, cropped to the slice in view. Significant tracts (FWE-corrected P-value < 0.05) were coloured by streamline orientation (red, left-right; green, anterior-posterior; blue, superior-inferior). Significant tracts were visually matched to corresponding anatomy defined by the John's Hopkins University (JHU) ICBM-DTI-81 White-Matter Labels atlas (Oishi et al., 2008) and the JHU White-Matter Tractography Atlas. Select axial slices of these atlases can be found in the appendix for reference (see figures A.2 A.3) .

7.5 Results

7.5.1 Demographics

Table 7.1 and table 7.2 summarize the demographic and clinical information for the HARDI only cohort and the HARDI + Aβ PET cohort respectively, where control and PD participants are grouped by cognitive status. No significant pairwise group differences were found between the cognitive groups in education and duration of PD symptoms for either cohort. Within the HARDI cohort: (1) CN were significantly older than PDN, otherwise no group differences in age were observed; (2) significant decreases in MoCA score by worsening cognitive status were observed across all groups; (3) significant decreases in cognitive z score were observed across most cognitive groups, however C-MCI and PDN showed similar cognitive z scores. Within the HARDI + Aβ PET cohort: (1) PDD were significantly older than PDN; (2) significant decreases in MoCA score by worsening cognitive status were observed across all groups; (3) significant decreases in cognitive z score by worsening cognitive status were observed across all groups.

7.5.2 Whole brain FBA

Whole-brain CFE-supported analysis of fixel level associations with FD, FC and FDC revealed widespread age-related reductions in all three metrics in PD, while reductions in PD compared to controls were much more constrained. Fixel density was found to increase with increasing age in the posterior commissure and left thalamic nuclei, but no other positive associations were found.

The right ventral tegmental area (VTA), including the substantia nigra, showed reduced FD and FDC in PD, an association that remained significant in PD-MCI and PDD compared to controls, but was not significant in PDN. FC was not found to be reduced in PD compared to controls, or within the cognitive subgroups.

Cognitive impairment was associated with reduced FD in the left fornix (cres) and stria terminalis (FX-ST), while motor impairment (UPDRS Part III) was associated with reduced FD in the left splenium, left tapetum, and left sagittal stratum. No other metric was found to show alterations associated with cognitive ability or motor control.

HARDI (n=160)	Control		PD			
	CN	C-MCI	PDN	PD-MCI	PDD	Linear models
n	34	3	46	66	11	-
Age, years	74 (7)	82 (9)	69 (7)	73 (6)	75 (7)	CN > PDN
Female, No. (%)	10 (30)	3 (100)	16 (35)	21 (32)	2 (18)	-
Education, years	14 (3)	15 (4)	13 (3)	13 (3)	13 (3)	∼
PD symptom duration, years	NA	NA	11 (5)	10 (6)	10 (6)	∼
MoCA	27 (2)	22 (2)	26 (2)	23 (3)	17 (3)	CN & PDN > C-MCI & PD-MCI > PDD
Cognitve Z score	0.69 (0.39)	0.15 (0.35)	0.21 (0.42)	-0.76 (0.44)	-1.91 (0.54)[a]	CN > C-MCI & PDN > PD-MCI > PDD

Table 7.1: Demographics table for the HARDI only cohort. Values are mean (standard deviation) unless specified; [a]Cognitive z scores for three PDD participants were imputed from restricted neuropsychological data due to their inability to complete the full cognitive assessment; ∼, no evidence of a difference; -–, no statistical test applicable or was not performed. Pairwise group estimates were considered different if 95% uncertainty intervals did not overlap. MoCA, Montreal Cognitive Assessment.

HARDI + Aβ PET (n=84)				
	PDN	PD-MCI	PDD	Linear models
n	20	55	9	-
Age, years	70 (6)	73 (6)	76 (7)	PDD > PDN
Female, No. (%)	6 (30)	15 (27)	2 (22)	-
Education, years	13 (2)	13 (3)	12 (2)	∼
PD symptom duration, years	10 (6)	9 (5)	10 (6)	∼
MoCA	26 (2)	23 (3)	16 (4)	PDN > PD-MCI > PDD
Cognitve Z score	0.073 (0.42)	-0.75 (0.45)	-2.01 (0.47)[a]	PDN > PD-MCI > PDD
Dose	296 (20)	301 (17)	288 (35)	∼
Aβ Positive, No. (%)[b]	4 (0.25)	8 (15)	1 (11)	-
Mean cortical CL	15 (21)	18 (29)	27 (34)	∼

Table 7.2: Demographics table for the HARDI + amyloid PET cohort. Values are mean (standard deviation) unless specified; [a]Cognitive z scores for three PDD participants were imputed from restricted neuropsychological data due to their inability to complete the full cognitive assessment; [b]Visual assessment of amyloid positive/negative reported; ∼, no evidence of a difference; -–, no statistical test applicable or was not performed. Pairwise group estimates were considered different if 95% uncertainty intervals did not overlap. MBq, megabecquerel; MoCA, Montreal Cognitive Assessment; Aβ, Amyloid beta; $SUVR_{NS}$, Standardized uptake value ratio with "non-standard" processing (see Supplementary Material); CL, centiloid.

There was no evidence of an association between amyloid positivity and alterations in any FBA metric, when investigated within the HARDI + Aβ restricted cohort. A linear regression with mean cortical amyloid load as a continuous measure supported this groupwise comparison. Age-related effects, independent of mean cortical amyloid load, followed similar patterns as seen in the wider cohort however were less extensive. This may suggest an amyloid-facilitated, age-related pattern in PD, encompassing some of the variance seen in the larger group for whom amyloid status is not known. This hypothesis was not verified within the current scope of this study, given the low proportion of amyloid-positive subjects in this cohort.

7.5.2.1 Fixel density

PD versus healthy controls

In the fixel-wise comparison of FD between PD and CN participants, there were no areas found to have increased FD in the PD group. Reduced FD in the PD group was observed in the splenium of the corpus callosum, right ventral tegmental area (including the substantia nigra [SN]), and bilateral tapetum (figure 7.7).

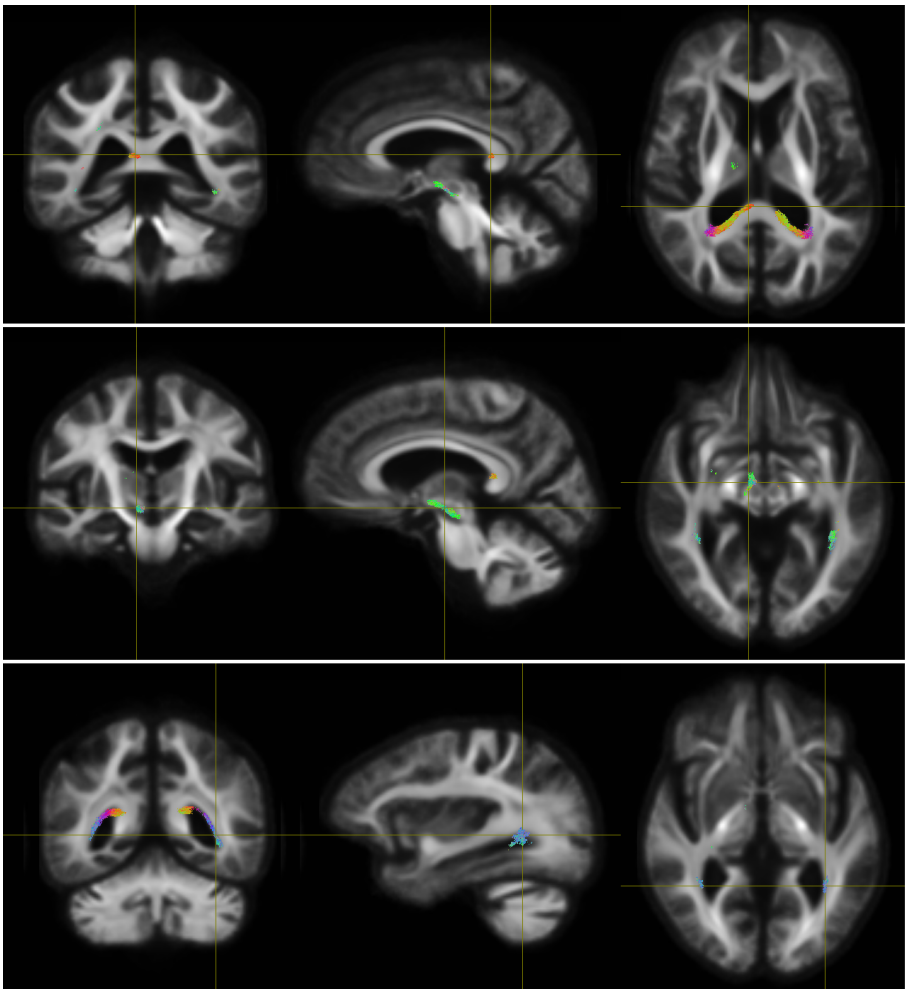

FIGURE 7.7: Fixels identified by FBA to have reduced FD in PD participants compared to cognitively normal controls, mapped to corresponding streamlines and coloured by direction. The structures identified are the splenium of the corpus callosum, tapetum and right ventral tegmental area, including the substantia nigra (SN).

Cognitive subgroups

When investigating the cognitive subgroups, I identified no evidence of any fixel-wise differences in FD between CN and C-MCI or PDN. FD was found to be reduced in both PD-MCI (figure 7.8) and PDD (figure 7.9) compared to CN, again within a small area of the ventral tegmental area (including the SN).

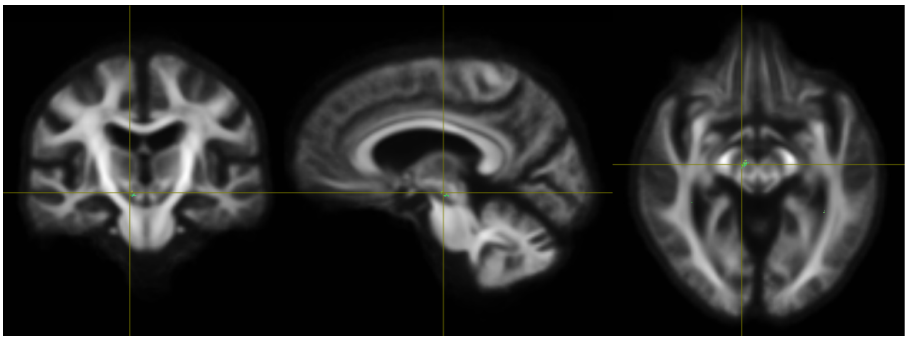

FIGURE 7.8: Fixels identified by FBA to have reduced FD in PD-MCI participants compared to cognitively normal controls, mapped to corresponding streamlines and coloured by direction. The structure identified is the right ventral tegmental area, including the SN.

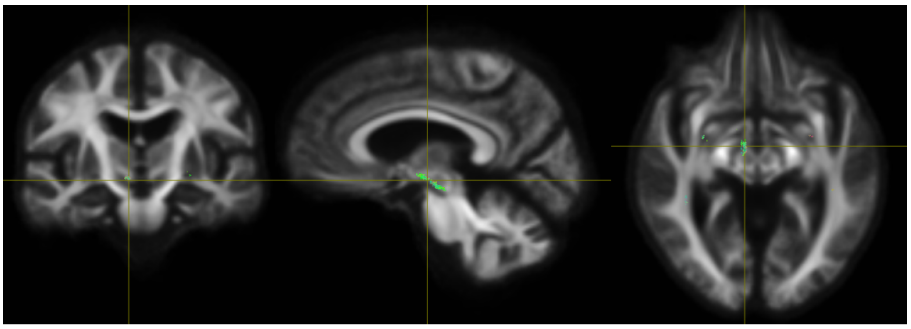

FIGURE 7.9: Fixels identified by FBA to have reduced FD in PDD participants compared to cognitively normal controls, mapped to corresponding streamlines and coloured by direction. The structure identified is the right ventral tegmental area, including the SN.

Cognitive and clinical associations with PD

When restricted to the PD group, reduced FD in the left fornix (cres) and stria terminalis (FX-ST) was significantly associated with global cognitive ability (global cognitive z score) (figure 7.10). Reduced FD in the tapetum (extending slightly into the splenium), and in a region of the inferior longitudinal fasciculus was associated with reduced motor function in PD, as defined by performance on part III of the UPDRS (figure 7.11).

Age exhibited positive association with FD in the posterior commissure and thalamic WM (figure 7.12), and a negative association in the forceps major, splenium, genu and body of the corpus callosum, fornix, tapetum, saggittal stratum (including the inferior longitudinal fasciculus and the inferior fronto-occipital fasciculus), external capsule, anterior commissure and the anterior thalamic radiation (figure 7.13).

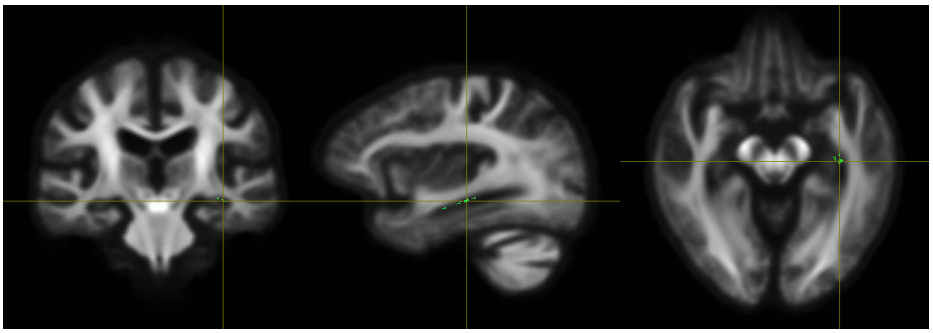

FIGURE 7.10: Fixels identified by FBA to have reduced FD associated with cognitive impairment in the PD participants, mapped to corresponding streamlines and coloured by direction. The structure identified is the fornix (cres) and stria terminalis.

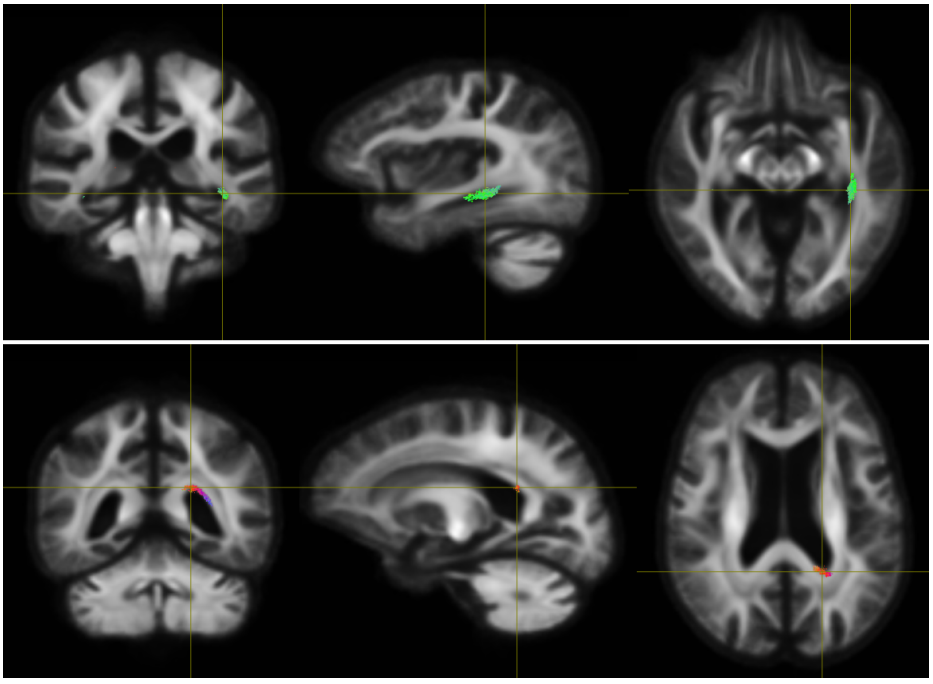

FIGURE 7.11: Fixels identified by FBA to have reduced FD associated with poorer motor control in the PD participants, mapped to corresponding streamlines and coloured by direction. The structures identified are the left splenium and tapetum, and the sagittal stratum (inferior longitudinal fasciculus).

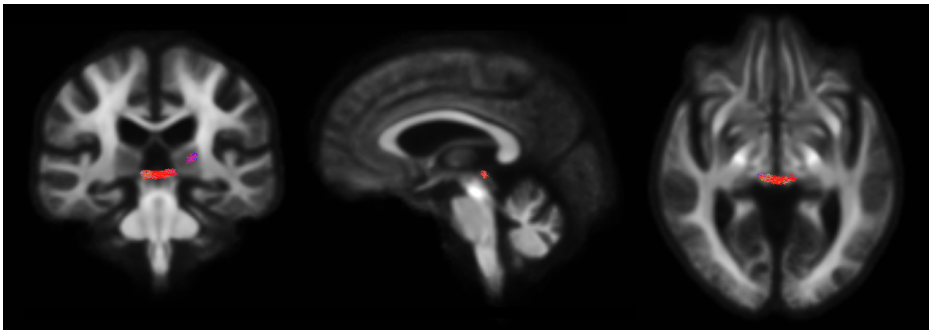

FIGURE 7.12: Fixels identified by FBA to have increased FD associated with increasing age, mapped to corresponding streamlines and coloured by direction. The structures identified are the posterior commissure and thalamic WM.

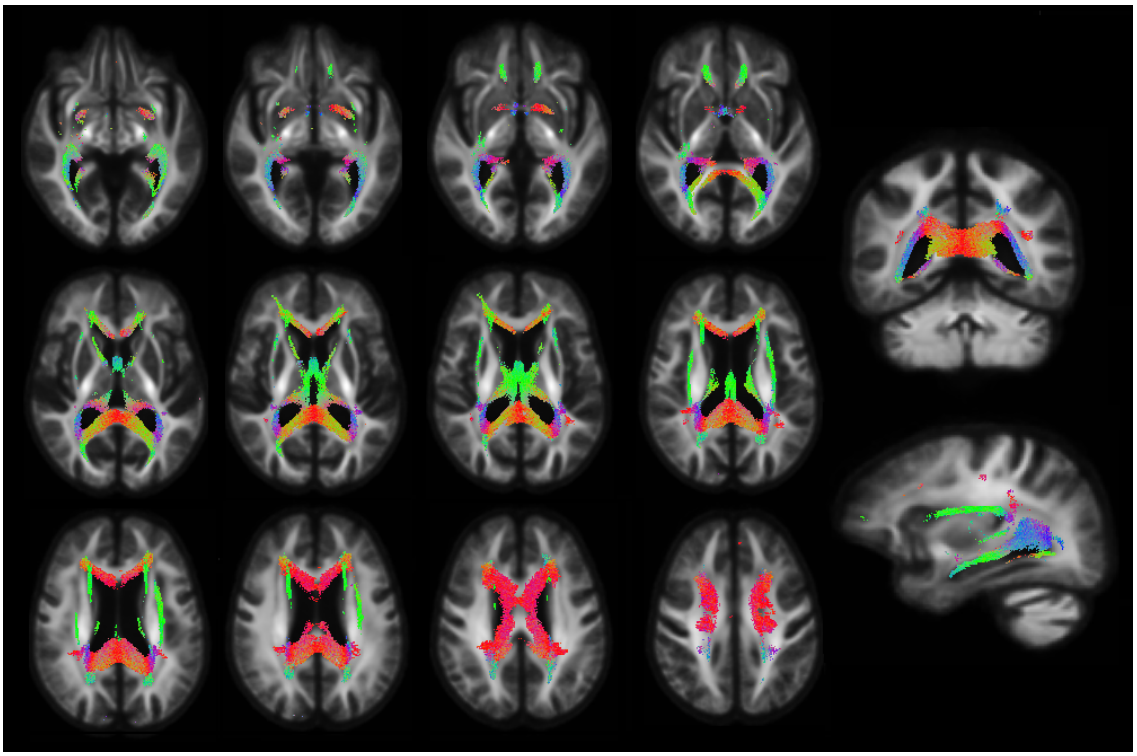

FIGURE 7.13: Fixels identified by FBA to have reduced FD associated with increasing age, mapped to corresponding streamlines and coloured by direction. The structures identified are the forceps major, splenium, genu and body of the corpus callosum, fornix, tapetum, saggittal stratum (including the inferior longitudinal fasciculus and the inferior fronto-occipital fasciculus), external capsule, anterior commissure and the anterior thalamic radiation.

7.5.2.2 Fixel cross-section

PD versus healthy controls

There was no evidence of any fixel-wise differences in FC between PD and cognitively normal controls.

Cognitive subgroups

There was no evidence of any fixel-wise differences in FC between any of the groups examined.

Cognitive and clinical associations with PD

When restricted to the PD group, there was no evidence of any fixel-wise association between FC and global cognitive performance (cognitive z score) or motor performance (UPDRS Part III score). FC showed reductions associated with increasing age in the splenium and body of the corpus callosum, cingulate gyrus, corticospinal tract, sagittal

stratum (including the inferior longitudinal fasciculus and inferior fronto-occipital fasciculus), external capsule, anterior commissure, uncinate fasciculus, and forceps minor (figure 7.14).

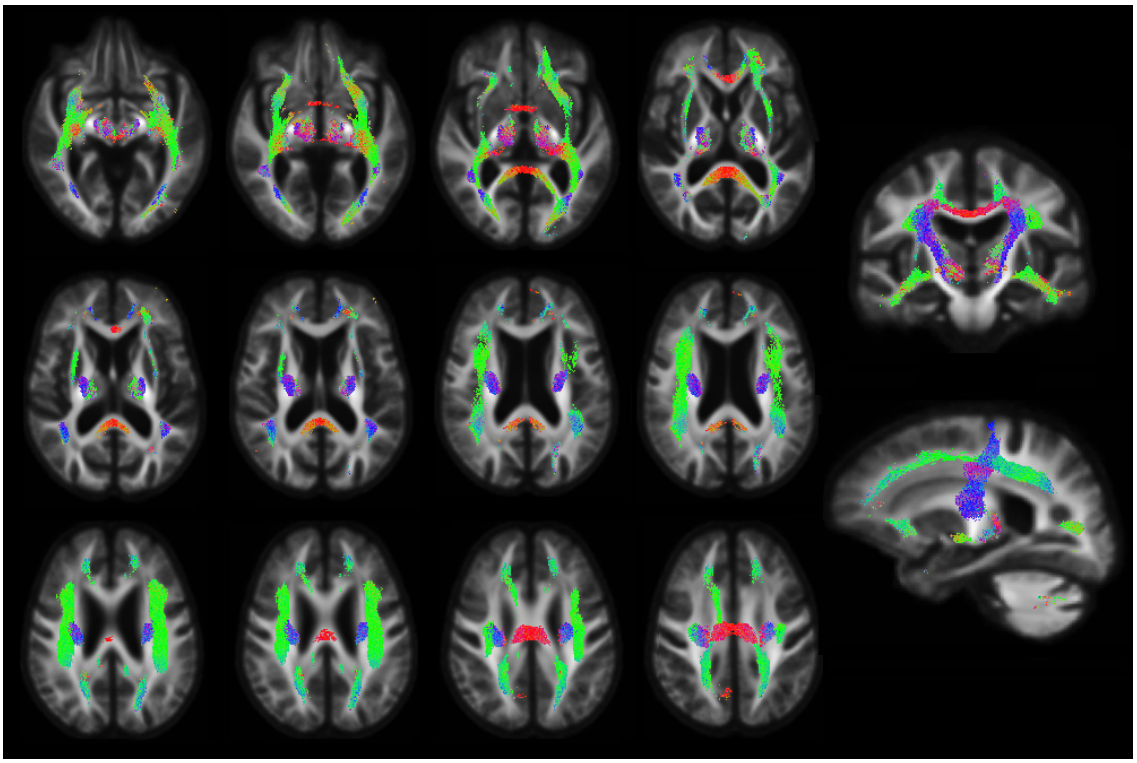

FIGURE 7.14: Fixels identified by FBA to have reduced FC associated with increasing age, mapped to corresponding streamlines and coloured by direction. The structures identified are the splenium and body of the corpus callosum, cingulate gyrus, corticospinal tract, sagittal stratum (including the inferior longitudinal fasciculus and inferior fronto-occipital fasciculus), external capsule, anterior commissure, uncinate fasciculus, and forceps minor.

7.5.2.3 Fixel density and cross-section

PD versus healthy controls

In the fixel-wise comparison of FDC between PD and CN participants, there were no areas found to have increased FDC in the PD group. Reduced FDC in the PD group was observed in the right ventral tegmental area, including the substantia nigra (figure 7.15).

Cognitive subgroups

There was no evidence of any fixel-wise differences in FDC between CN and C-MCI or PDN. Fixel cross-section was found to be reduced in the right ventral tegmental area, including the substantia nigra (SN) in the PD-MCI (figure 7.16) and PDD (figure 7.17) cognitive groups, compared to CN. The reduction in FDC found in both PD-MCI and

PDD encompassed a lesser extent than that given by the comparison of all PD versus controls.

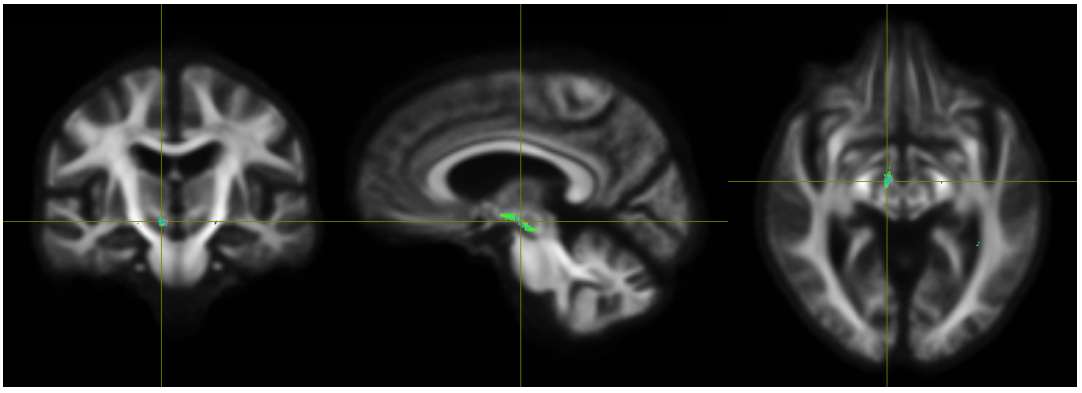

FIGURE 7.15: Fixels identified by FBA to have reduced FDC in PD participants compared to cognitively normal controls, mapped to corresponding streamlines. The structure identified is the right ventral tegmental area, including the SN.

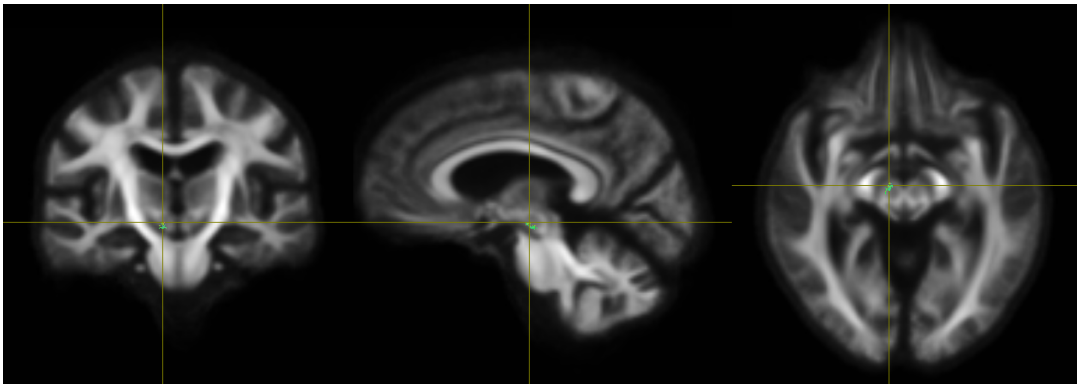

FIGURE 7.16: Fixels identified by FBA to have reduced FDC in PD-MCI participants compared to cognitively normal controls, mapped to corresponding streamlines. The structure identified is the right ventral tegmental area, including the SN.

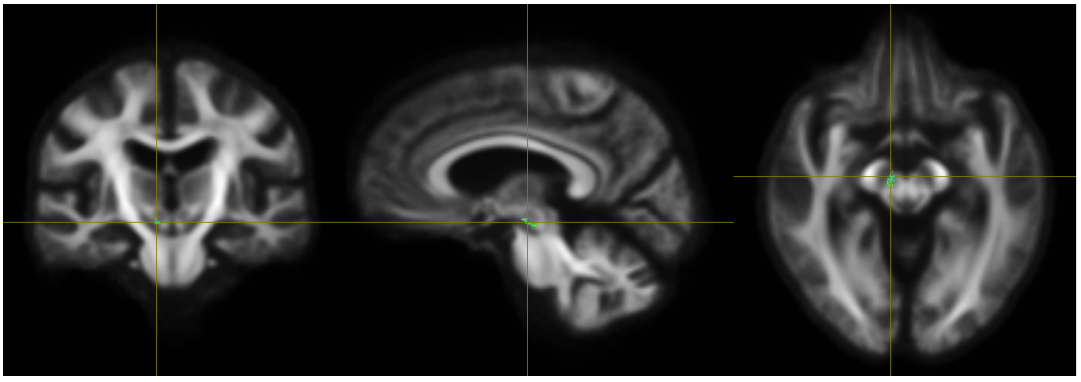

FIGURE 7.17: Fixels identified by FBA to have reduced FDC in PDD participants compared to cognitively normal controls, mapped to corresponding streamlines. The structure identified is the right ventral tegmental area, including the SN.

Cognitive and clinical associations with PD

There was no evidence of any fixel-wise association between FDC and global cognitive performance (cognitive z score) or motor performance (UPDRS part III score). FDC was observed to decrease with increasing age in the sagittal stratum (including the inferior longitudinal fasciculus and inferior fronto-occipital fasciculus), external capsule, uncinate fasciculus, cingulum (hippocampus), forceps major and minor, fornix, tapetum, the corpus callosum body, genu and splenium, hippocampus and anterior commissure (figure 7.18).

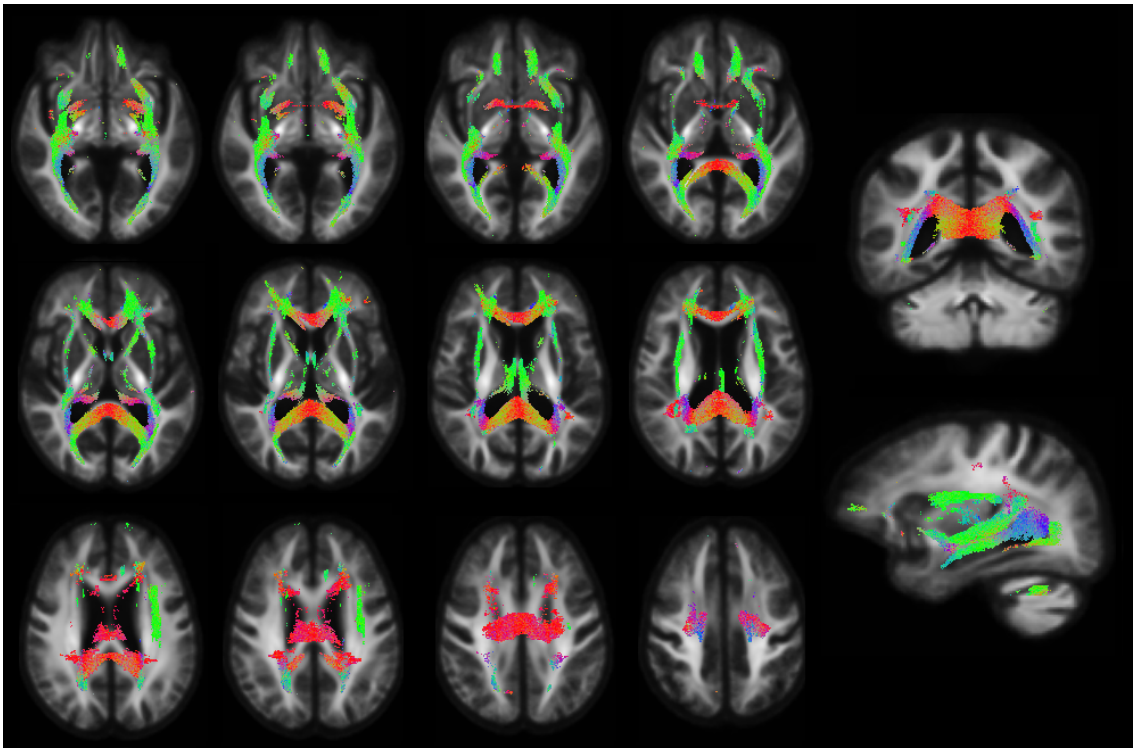

FIGURE 7.18: Fixels identified by FBA to have reduced FDC associated with increasing age, mapped to corresponding streamlines. The structures identified are the sagittal stratum (including the inferior longitudinal fasciculus and inferior fronto-occipital fasciculus), external capsule, uncinate fasciculus, cingulum (hippocampus), forceps major and minor, fornix, tapetum, the corpus callosum body, genu and splenium, hippocampus and anterior commissure.

7.5.3 HARDI + Aβ cohort (within PD only)

Aβ+ versus Aβ-

I identified no evidence of a difference in FD, FC or FDC between Aβ-positive and Aβ-negative subjects in this cohort.

Associations with amyloid load and age

There was no evidence of a fixel-wise association of any metric with CL (a continuous measure of cortical amyloid deposition). Age association with all three metrics (FD, figure 7.19; FC, figure 7.20; FDC, figure 7.21) showed a widespread pattern of positive association, similar to the findings previously presented in the investigation of the full cohort (see figures: FD, 7.13; FC, 7.14; FDC, 7.18). These associations were found independent of amyloid load.

Fixel density

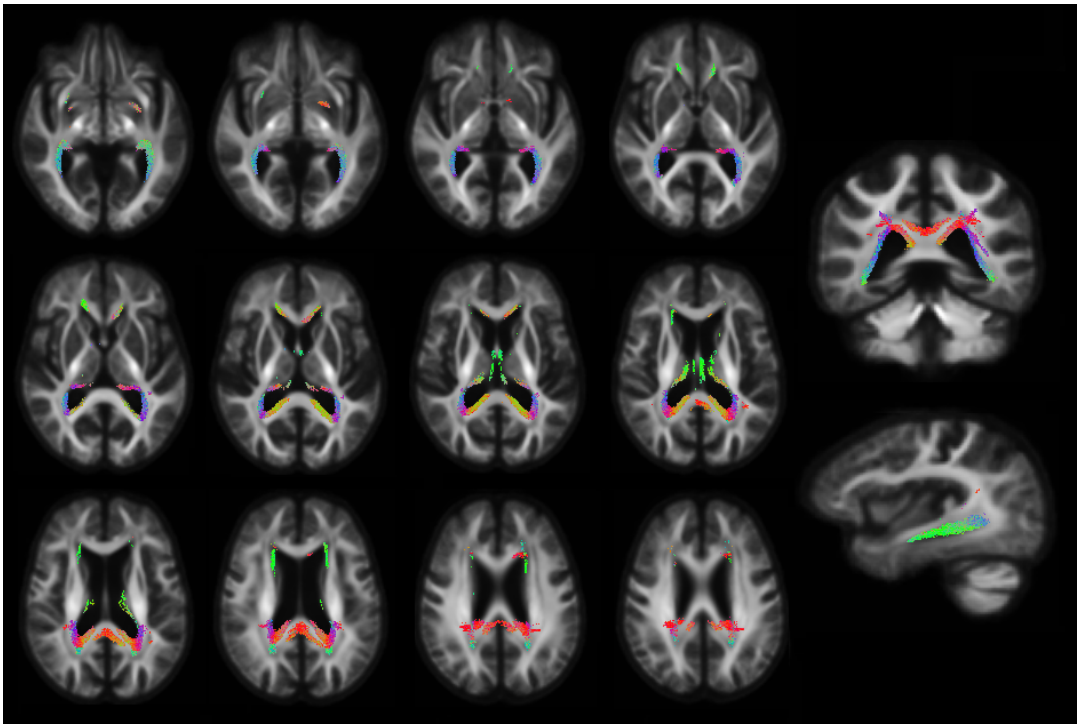

FIGURE 7.19: Fixels identified by FBA to have reduced FD associated with increasing age, independent of amyloid load, and mapped to corresponding streamlines. The structures identified are the fornix, tapetum, hippocampus, splenium and body of the corpus callosum, anterior corona radiata, fornix cres/stria terminalis, sagittal stratum (including the inferior longitudinal fasciculus and inferior fronto-occipital fasciculus), and putamen.

Fixel cross-section

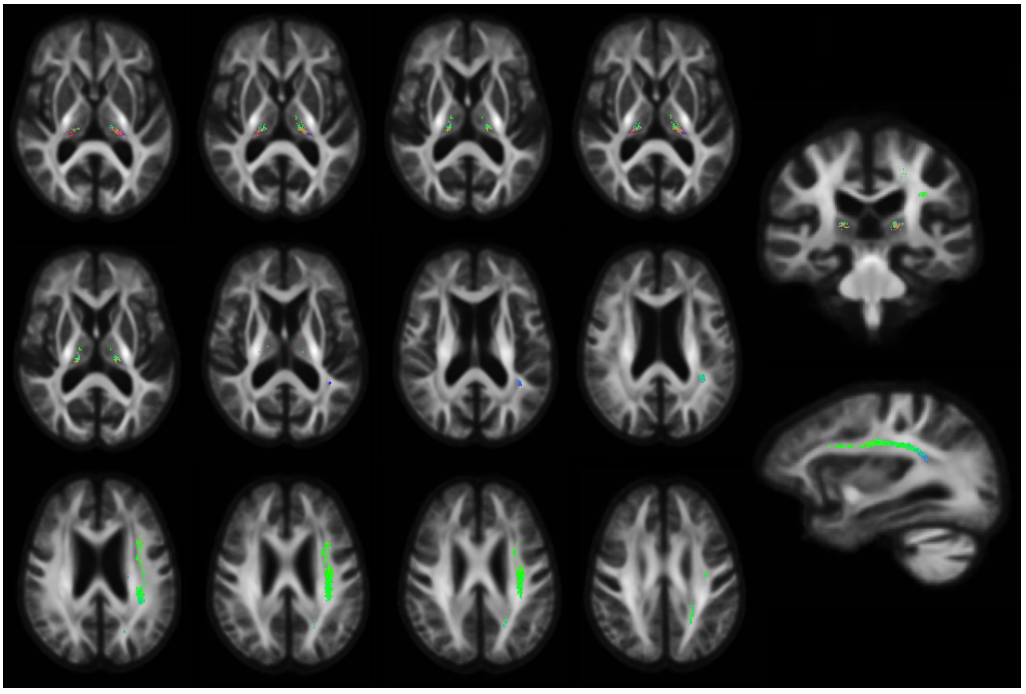

FIGURE 7.20: Fixels identified by FBA to have reduced FC associated with increasing age, independent of amyloid load, and mapped to corresponding streamlines. The structures identified are the anterior corona radiata extending into the posterior corona radiata, and thalamic white matter.

Fixel density and cross-section

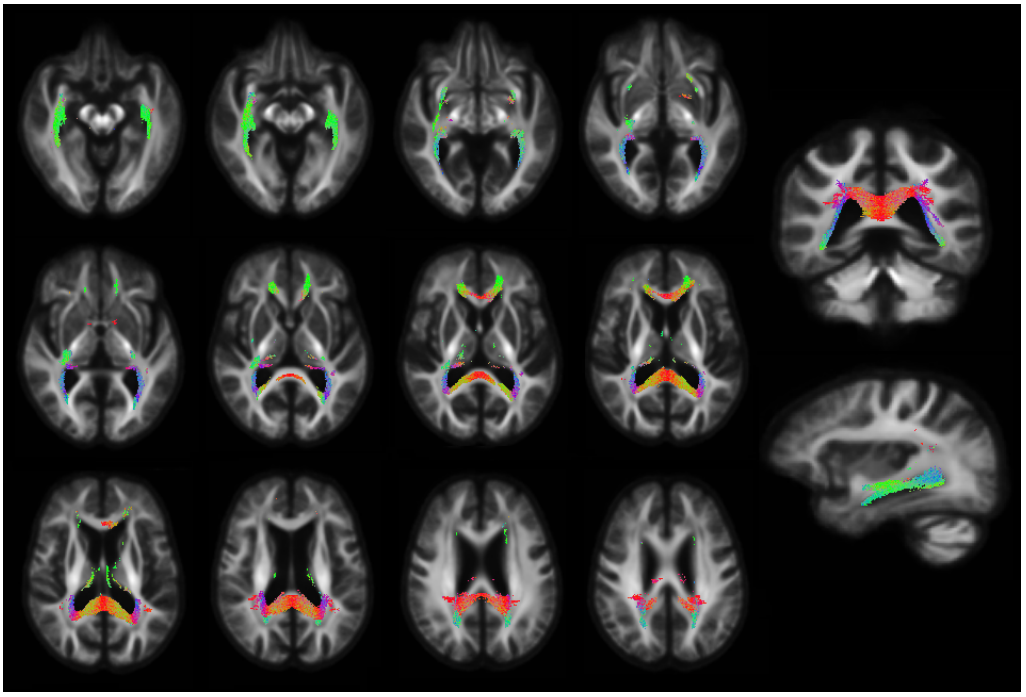

FIGURE 7.21: Fixels identified by FBA to have reduced FDC associated with increasing age, independent of amyloid load, and mapped to corresponding streamlines. The structures identified are the splenium and body of the corpus callosum, tapetum, forceps minor and major, and the sagittal stratum (including the inferior longitudinal fasciculus and inferior fronto-occipital fasciculus).

7.6 Discussion

This study undertook a whole-brain FBA of HARDI data to examine micro- and macrostructural changes that occur in the white matter of PD patients, and investigated those changes with respect to disease, amyloid pathology, and age. Overall, while there were limited regions that exhibited changes related to PD or worsening cognitive performance, those identified have been shown to have clinical relevance in PD, particularly in relation to non-motor symptoms. Age was seen to be extensively associated with fixel-wise decreases in all three metrics, representing a strong effect of subject age on tissue micro- and macrostructure.

In the analysis of fixel-wise differences across the cognitive groups within the full cohort, a decrease in FD and FDC was noted in the right ventral tegmental area (VTA), including the substantia nigra (SN), in PD, PD-MCI and PDD, compared to cognitively normal controls. Loss of dopaminergic neurons in the SN is one of the known pathological hallmarks of PD (Dickson, 2012), while the tegmental midbrain and other deep subcortical WM structures have been postulated to undergo an accelerated rate of loss of microstructural integrity in nondemented PD patients compared to controls (Pozorski et al., 2018). This pattern of WM change is consistent with Braak stage 3 and 4 of sporadic PD (Braak et al., 2003), and precedes widespread cortical involvement at the later stages. The VTA has been identified as being involved in PD, however the clinical contribution of neuronal loss in the VTA is the topic of some speculation (Alberico et al., 2015). The review by Alberico et al. hypothesised that PD patients exhibiting non-motor symptoms of anxiety, depression and executive dysfunction are likely to show extensive VTA/medial nigral loss of dopamine neurons, while other case studies of VTA lesions have indicated an importance of the VTA in cognitive function (Adair et al., 1996; Nishio et al., 2007).

Structural changes in the VTA in this cohort appear to be driven by neuronal loss in the absence of atrophy (FD rather than FC), distinguishable in PD versus controls and becoming more extensive with severity of cognitive impairment. However, there was no evidence of a fixel-wise association of any FBA metric with cognitive performance within the VTA or SN, and other non-motor symptoms such as depression were not examined with FBA. The clinical contribution of observed neuronal loss in the VTA is therefore difficult to comment upon within the current scope of this research. While this study was focused on WM damage associated with cognition in PD, future work may examine

other non-motor aspects with respect to WM, or investigate each of the cognitive domains separately. For example, WM integrity in the hippocampus may be more associated with performance in the learning and memory domain than the visuospatial domain. It would also benefit future studies to recruit a higher number of PDD participants, as the low number included here (n=11) may have impacted the statistical power of the analyses, especially when investigating subtle group differences.

We found no significant WM alterations in PD with normal cognition compared to controls, a finding that is in line with previous DTI results from (Hattori et al., 2012), in a cohort consisting of controls and PD, age- and sex- matched across the cognitive spectrum. These results fall in the most conservative end of the spectrum concerning involvement of WM degeneration in PDN, contrasting with studies showing mild involvement limited to the corpus callosum (Melzer et al., 2013), or extensive involvement in the temporal, parietal and occipital cortices (Auning et al., 2014), for example. In terms of group differences from controls in PD-MCI and PDD, Hattori et al. found WM to be altered in the superior longitudinal fasciculus, inferior longitudinal fasciculus, inferior fronto-occipital fasciculus, uncinate fasciculus, and cingulum - areas which (with the exception of the superior longitudinal fasciculus) we have identified in this study to show micro- and macro-structural changes related to age in PD. While the Hattori et al. cohort was age-matched, and age included as a covariate in statistical analysis of group differences, the authors did not examine the possible effect of age as a variable of interest. In a recent study of age- and disease- related WM changes in PD (de Schipper et al., 2019), the authors found DTI measures (FA and MD) to be significantly associated with age in both PD and controls, with no significant difference between the two groups in the spatial distribution of WM changes. Our findings, taken with those of de Schipper et al., would appear to support a conclusion that WM changes in PD have a strong association with age, perhaps suggesting that they may be primarily driven by age and not disease presence or progression. However, the cross-sectional design of both studies may be a limitation in the assessment of disease and age-related decline in WM, due to a reliance on between-person comparisons rather than intra-individual change over time. Additionally, our cohort would benefit from the inclusion of a larger number of control subjects, perhaps enabling greater statistical power to detect disease-related differences in PD. The result here, while supported by advanced diffusion imaging and analysis methods, would be strengthened by the addition of individual longitudinal data.

The potential of longitudinal FBA in identifying longitudinal WM degeneration in PD has been demonstrated in a recent study of 50 non-demented PD and 76 healthy controls, implementing both FBA and DTI (Rau et al., 2019). There are several key findings to note from this study. Firstly, there was no evidence of group differences between PD and controls in either set of metrics at baseline. All PD subjects followed by Rau et al. were early in the disease course at study baseline, and while neuropsychological metrics were not extensive enough to determine a cognitive subgroup classification, these findings likely support the conservative estimate of WM changes in PDN as presented here. The authors also identified a PD-facilitated pattern of age-related cognitive decline, distinct from the age-related pattern seen in controls. However as controls were not followed longitudinally, it was not known what interaction there might be between PD and normal ageing in these metrics. Nevertheless, areas identified by Rau et al. to be associated with age in PD that were also identified for the same metrics in our PD subjects were: reductions in FD within the splenium and genu of the corpus callosum, tapetum, bilateral fornix and sagittal stratum; reductions in FC in the bilateral cingulum and left sagittal stratum; and reductions in FDC in the splenium of corpus callosum, bilateral fornix and tapetum. The identification of these same regions may serve to validate the findings of this study in regards to particular age associations. Also, the observation that FBA may be able to discriminate healthy and disease related patterns of age-associated degeneration would imply greater sensitivity to these effects, compared with the lack of distinct differences in associated areas previously identified using DTI ((de Schipper et al., 2019)). The identification of an age-related pattern of WM degeneration in healthy controls was not a focus of this study, however this potential application of FBA warrants further investigation.

In a recent large cross-sectional FBA study of healthy ageing, including 293 subjects from ages 21 to 86 years old, widespread age-related alterations were identified in FD, FC and FDC (Choy et al., 2020), demonstrating some similarity in affected regions with those identified here. Notably, specific differences in some tracts showing reductions in one metric but not another were also found here, with reductions in FC but not FD in the cingulate gyrus, and reductions in FD but not FC in the fornix. The authors also identified higher values of FC associated with age in tracts connecting the hippocampus to the cingulum, postulating that this may be attributable to the benefits of exercise-induced increase in brain neurotrophic factor (BDNF), linked to increased hippocampal volume

(Erickson et al., 2011). I identified an increase of FD in the posterior commissure and left thalamic white matter associated with age in this PD cohort. This is somewhat difficult to explain, but may be a consequence of FBA misinterpreting changes in thin white matter structures (such as the commissural fibres), where insensitivity to macro-structural changes in FC can sometimes present as micro-structural changes in FD (D. A. Raffelt et al., 2016). This may also be exacerbated by partial volume effects in these thin structures (D. A. Raffelt et al., 2016), thus the supposed increase in fibre density in this region may not be a reliable interpretation.

The efficacy of FBA over traditional voxel-based morphometry (VBM) in the investigation of cognitive decline in PD is difficult to fully evaluate given the lack of existing research using both methods. To the best of my knowledge, there have been no comprehensive studies employing both FBA and VBM in the analysis of cognitive decline in PD. Rau and colleagues compared the results offered by both FBA and DTI metrics over the course of 40-month follow-up, but did so in early PD, and did not investigate differences between cognitive subgroups. In the comparison of FBA and DTI metrics, longitudinal follow-up revealed increases of MD and decreases of FA consistent with alterations of FDC in the same regions, with several additional areas showing changes in FDC not identified by DTI analysis. The authors noted a potential increase in sensitivity to longitudinal WM changes offered by the morphology metrics of FBA (FC and FDC) over traditional voxel-based morphometry, in support of the initial hypotheses by (D. A. Raffelt et al., 2016). In a study of mild cognitive impairment and AD (Mito et al., 2018), the authors demonstrated the ability of FBA to distinguish subtle degeneration in the posterior cingulum of MCI subjects, a region that has been implicated to show early functional disruption (Zhou et al., 2012) and hypometabolism (Nestor et al., 2003) associated with later cognitive decline and development of AD. Mito et al. additionally demonstrated misleading increases in FA within the centrum semiovale in the direction of the corticospinal tract, that were identified to be fixel specific decreases once appropriately resolved using CSD. These two separate studies appear to support the use of FBA over DTI, with regards to improved sensitivity to subtle changes in WM, detection of alterations that may predict future cognitive decline, and proven efficacy in regions of large crossing fibre populations.

This study found no evidence of an association between amyloid positivity and reduced FD, FC or FDC in any regions of the brain within the restricted HARDI + Aβ PET cohort. This result adds to that observed by Mito et al. (2018), wherein amyloid-positive MCI

subjects, representing prodromal AD, did not display any decreases in FDC compared to AD, amyloid-negative MCI, amyloid-positive healthy subjects or amyloid-negative controls, surviving correction for multiple comparisons. These results argue against an interaction effect of amyloid in the pathogenesis of WM degeneration, in PD irrespective of cognitive ability and in early AD. The age-related results obtained from investigation within the restricted cohort were also significant independent of amyloid load, however encompassed a less widespread extent than that found in the wider PD group. It is possible that some of the variance associated with age in the wider cohort was captured by the presence of amyloid load in the restricted cohort. An amyloid-facilitated pattern of age-related WM degeneration in PD could be identified by examining age effects within amyloid-positive and amyloid-negative groups specifically and comparing the two, however this analysis was not judged to be viable in this study due to a low proportion of amyloid positive subjects (15%).

Limitations

The results of groupwise ANCOVA investigating the PDD cognitive subgroup may have suffered from low statistical power due to a low number of participants (n=11). Low statistical power can arise as a result of small sample sizes, small statistical effects, or large standard error, and may reduce the chance of detecting a true effect within the sample, or conversely reduce the likelihood that a statistically significant result reflects a true effect (Button et al., 2013). In this PDD subgroup, the significant result aligns very closely with that observed in the larger PD-MCI subgroup (n=66), therefore it seems unlikely that a false positive has arisen in this case. Rather, there may be small effects in the PDD subgroup that have not been detected. Increasing the number of the PDD participants to be more comparable with the other subgroups may reveal these subtle affects, or otherwise will increase confidence in the result reported here.

While this study included controls, there was a significant difference in the age of the control group and the PD group with normal cognition, being 8 years older on average. While age was included as a covariate in all relevant analyses, it is possible that this method may not have entirely accounted for these differences. The increased age of the control group may have the effect of obfuscating more subtle disease affects in PDN, due to the strong dependence of WM integrity on advancing age. It is difficult to untangle age effects from pathological disease effects in PD, as PD is inherently an age-related disease (Myall et al.,

2017). This also makes obtaining a fully age-matched cohort across the cognitive groups difficult, compared with larger retrospective studies of international cohorts. Future work would nevertheless benefit from the inclusion of older PDN participants or younger controls. Additionally, obtaining individual longitudinal data would reduce the reliance on inter-subject comparison, and may mitigate the effect of such group differences.

Tract-specific statistical comparisons were not performed in this study. Comparative analysis of mean FD, FC and FDC values within major associated fibre tracts may reveal a more nuanced view of the extensive association with age found in this study.

The use of FBA, while offering distinct advantages over tensor-derived analysis methods, is a relatively new technique, and as such there are few studies with which to compare our findings. Direct comparison of FD, FC and FDC values with DTI metrics such as FA or MD is inappropriate, as they do not always reflect the same pathological change. Here, I have compared the results of FBA with those of DTI studies in terms of the authors' interpretation of WM degeneration in their cohort. It would be beneficial to carry out DTI with this same subject group in order to observe the points of difference given by FBA, and perhaps replicate the increased sensitivity to morphological changes seen by Rau and colleagues. DTI was not able to be performed using the single-shell HARDI data acquired in this study, as the modeling of the diffusion tensor is not appropriate for high b-value acquisitions (Hui et al., 2010); the diffusion tensor model assumes linear decay of the magnetisation signal, which is true for low b-values (e.g. b=1000) but not true for high b-values (b=2500). Thus, while this study has reaped the clinical benefits of single-shell data in obtaining MSMT-like results using the SS3T-CSD method, a notable benefit of acquiring true multi-shell data is being able to perform both DTI and CSD from the same acquisition.

This cross-sectional study represents the largest application of FBA for the analysis of white matter micro- and macro-structural changes in PD to date, investigating both controls and cognitively well-characterised PD across the cognitive spectrum.

Chapter 8

Summary and Conclusions

8.1 Overview

Parkinson's disease is now well recognised as a multi-system neurodegenerative disorder, with a broad range of clinical features that encompass both motor and non-motor symptoms. Cognitive decline and dementia is expected to occur in over 80% of 20-year survivors (Hely et al., 2008), however the pathological and physiological basis underlying this is not well understood, and the time-course from diagnosis to development of dementia is highly variable. Imaging biomarkers of cognitive decline are urgently needed, such that individuals may be targeted for intervention therapies, or to improve prediction of long-term cognitive outcomes. This thesis investigated misfolded beta-amyloid protein deposition, imaged using [^{18}F]-Florbetaben (FBB) positron emission tomography (PET), in combination with multiple different imaging metrics that may correlate with cognitive impairment, with the aim to characterise potential imaging biomarkers related to cognitive decline in PD. White matter micro- and macro-structural changes occurring in PD were also investigated, in the first large cohort study employing novel fixel-based analysis methods for the analysis of cognition across the cognitive spectrum in PD.

Participants investigated in this thesis were well-characterised at study baseline, and represent the full cognitive spectrum in PD, including normal cognition (PDN), mild cognitive impairment (PD-MCI) and dementia (PDD). While the primary analysis of beta-amyloid in this thesis was focused on evaluating cognitive group differences and future conversion to dementia in PD, control participants were additionally included in the analysis of white

matter structural changes, enabling the comparison of PD subjects against healthy controls. In the cross-sectional analysis of amyloid with respect to cognitive impairment in PD, 115 participants were examined, in a cohort enriched for PD-MCI in recognition of the increased risk of cognitive decline in these individuals. Subsequent longitudinal cognitive assessments allowed the investigation of amyloid load in relation to conversion to dementia over a mean of 3.2 years, within a subset of 97 participants who were non-demented at study baseline. Investigation of white matter structural changes was performed in an expanded cohort of 37 controls and 123 PD participants, for which high angular resolution diffusion imaging was obtained as part of the larger longitudinal study of PD underway within our research group. Within the subset of these participants that were also included in the primary study of amyloid (n = 84), I was able to investigate a potential interactive effect of amyloid in the pathogenesis of WM degeneration.

8.2 Key Findings

Part one of this study identified increased cortical amyloid accumulation in PDD in cross-sectional analysis, however this was found to be due to an effect of older age of the PDD participants. Amyloid load was found to increase in our cohort at a rate of 9.3% per decade, comparable to the rate of increase identified in healthy ageing of 10% (Villemagne et al., 2011), and was not found to correlate with cognitive impairment at baseline when age was considered in the analysis. In contrast, longitudinal follow-up in Part two revealed that higher levels of cortical and subcortical amyloid deposition at baseline were associated with developing dementia within three years. However, comparison with simpler predictive models did not endorse the use of cortical or regional amyloid information in determining individual three-year outcomes in a clinical setting, as the value added may not outweigh potential harm from radiation dose or the high cost of PET scanning. The relatively small proportion of PD patients with significant amyloid load may benefit from the anti-amyloid therapy trials currently underway, aiming to slow or halt cognitive decline by reducing cortical amyloid load - however continued efforts in this field have met with little success (Hardy & De Strooper, 2017). It is unlikely that amyloid load is a primary driver of cognitive decline, particularly with respect to PD, however amyloid may interact synergistically with other pathological processes in PD, thereby accelerating other pathways to dementia.

Cerebral blood flow (CBF), as measured using arterial spin labeling (ASL) MRI, was investigated in this thesis as one potential correlate of amyloid deposition, given observations of greater reductions in CBF in the presence of amyloid at clinically positive levels in non-demented or early MCI participants (Mattsson et al., 2014; Bangen et al., 2017). There was no evidence of an interactive effect between amyloid deposition and CBF in this sample at cross-sectional analysis, however baseline reductions in CBF within several cortical areas were found to be associated with conversion to dementia over longitudinal follow-up. Taken with our results from longitudinal analysis of amyloid deposition, this suggests that the two pathologies may be concomitant in PD but act independently to affect cognitive impairment.

The first two parts of this thesis focused on pathophysiological changes occurring within the grey matter in PD. Part three expanded this investigation to include measures of white matter micro- and macro-structural integrity, in this first large-cohort application of fixel-based analysis (FBA) of high angular resolution diffusion imaging (HARDI) for the evaluation of PD across the cognitive spectrum. Traditional diffusion imaging following voxel-based methods, while widely used, suffer from a lack of anatomical and physiological accuracy due in large part to inaccurately modeling crossing white matter fibres within each voxel. FBA makes use of the high angular resolution offered by HARDI to estimate multiple fibre orientations within each voxel using constrained spherical deconvolution (CSD), by which process the fixel is created. A novel method of performing CSD, optimised for diffusion data acquired using a single b-value, was demonstrated to improve fibre orientation estimation and probabilistic fibre tractography in this thesis.

Measures of fibre density (FD), fibre cross section (FC), and a combined measure of fibre-density-cross-section (FDC), extracted from the subject fixel data, were investigated for changes associated with PD, clinical features, amyloid pathology and age. Similarly to the cross-sectional analysis of amyloid deposition, there was a widespread association between reduced values of these metrics and age in this cohort, representing a strong effect of subject age on tissue micro- and macro-structure. Neuronal loss in the right ventral tegmental area (VTA), including the substantia nigra (SN), was associated with disease, beginning in PD-MCI and increasing the extent of the involvement in PDD. There were no observations of reductions in these metrics in PDN compared to controls, consistent with conservative estimates of white matter degeneration in PD with normal cognition.

Additionally, amyloid positivity was not seen to be associated with white matter degeneration, indicating an age-related pattern of white matter axonal and morphological change that occurs independent of amyloid deposition. There was no evidence of an association between any HARDI metric and global cognitive ability as a continuous measure. The results of cross-sectional analysis support a primary effect of age rather than disease presence or amyloid pathology on observed white matter structural changes in PD.

In summary, this thesis comprehensively investigated the effect of amyloid on cognitive impairment within a large, well-characterised PD cohort, and subsequently challenged existing characterisations of regional amyloid deposition relating to cognitive decline. This work also represents the largest application to-date of fixel-based analysis for the investigation of white matter degeneration across the cognitive spectrum in PD.

8.3 Impact of this research

The publication resulting from this thesis contributed to the literature concerning the application of the Centiloid scale to amyloid imaging in PD and derived a potential threshold value for amyloid positivity based on our sample. There is not yet widespread application of the CL scale in PD studies of amyloid, and no standard threshold value yet exists that has been validated in a large international PD cohort, as has been done in AD (Salvadó et al., 2019). Our value provides a reference against which other research groups may compare their own derived thresholds, until such time as a focused PD study can be completed. Such a study may consider amyloid-PET visual classification in conjunction with $A\beta_{42}$, tTau, pTau and their ratios in cerebrospinal fluid in order to derive a potential threshold from ROC analysis.

Deducing that PET imaging of amyloid is not necessary to characterise cognitive impairment in PD has a number of benefits that impact both the patient in a clinical setting, and those conducting research in this field. Chiefly, the patient would not be subjected to an ultimately unnecessary imaging procedure that (a) necessitates exposure to harmful ionising radiation, (b) may be stressful, painful or otherwise difficult to complete, and (c) requires an extended time commitment compared to other modalities such as MRI. Additionally, classification of an individual as 'amyloid-positive' comes with considerable negative connotations, as a result of the focus and media coverage emphasising the role

of amyloid pathology in Alzheimer's disease. Knowledge of a positive amyloid PET scan may be deeply affecting for the individual but have minimal real implications for their expected future outcomes in PD.

From an economic standpoint, PET imaging is a costly endeavour and requires a number of logistical considerations, both in research and clinical applications. Overall, the cost of amyloid PET imaging in research is approximately three times that of research MRI, which requires considerable investment on the part of the funding entity or research body. Fluorine-18 based amyloid PET tracers are also not currently produced in New Zealand, therefore there is a cost associated with sourcing the required tracer from Australia or elsewhere. In addition, transport of radioactive materials requires care to reduce the risk of radiation incidents and prevent exposures to the public or transport personnel. All of these factors must be weighed against the potential for clinical application of amyloid PET in PD, found here to be limited.

This thesis also applied a novel algorithm allowing the segmentation of multi-tissue admixtures from single-shell (+b=0) diffusion-weighted MRI, in one of the first applications of this new technique in a large clinical population. Verification of this algorithm and its effectiveness in crossing-fibre regions has great implications for future research utilizing this diffusion MR protocol. Acquiring only single-shell data reduces the overall time required for the scan, a factor that has great benefit in reducing the costs associated with research MRI, where cost is often dictated by the length of time set aside from clinical use of the scanner. Reducing the time of one sequence also has the benefit of potentially enabling other imaging sequences in the time allowed, improving cost-effectiveness and expanding the research benefit obtainable from a single series of scans.

8.4 Important considerations

Parts One and Two

The study of amyloid in this thesis was limited by the absence of a healthy control group. This necessitated restriction of the analysis to within-PD differences associated with cognitive impairment and cognitive group classification. Thus, evaluating levels of amyloid in PD with respect to healthy aging was performed by comparison with the literature. However, the primary aim of parts one and two of this thesis was to investigate

the association between amyloid deposition and cognitive impairment in a cognitively well-characterised PD cohort. In this respect, the characterisation of PD-MCI is subject to considerable variability, with both single-domain and multi-domain impairment subtypes (Wood et al., 2016), and an observed sensitivity of the MDS level II criteria to small variations in neuropsychological test scores in less-impaired individuals. PD-MCI subtypes were not examined in this thesis, and it is possible that these subtypes may exhibit greater or lesser Aβ pathology. In addition, several participants classified as PD-MCI at baseline were seen to revert to PDN over the course of longitudinal follow-up, reflecting the noise inherent in this classification in these borderline cases. The combination of these two effects may have reduced the strength of our cross-sectional analysis of amyloid deposition across the cognitive groups. Nonetheless, cortical amyloid deposition was not associated with global cognitive ability or memory function across the wider cohort, so these effects were likely negligible.

The enrichment of this cohort for PD patients fulfilling the criteria for mild cognitive impairment represents both a strength and a limitation of this study. PD-MCI participants are considered to be at higher risk of developing dementia, with an estimated conversion rate of 50% within four years (Wood et al., 2016). This effect is apparent in our sample, where all those who developed dementia during longitudinal follow-up were classified PD-MCI at baseline. The enrichment of PD-MCI participants in our cohort thus benefited our statistical power to examine correlates of conversion to dementia within a large subgroup of the original cohort over three years. However, it is possible that there are pathological changes occurring in cognitively normal PD related to conversion to dementia that were not detected due to a comparatively low recruitment of PDN. The lack of any PDN subjects in the convert subgroup may have introduced bias in some aspects of longitudinal group comparison.

Expression of the apolipoprotein E (APOE) gene ε4 allele has been shown to correlate with amyloid deposition (Akhtar et al., 2017; Villemagne et al., 2011), and the development of dementia in PD (Williams-Gray et al., 2009; Huertas et al., 2017). The APOE-ε4 genotype of our participants was obtained subsequent to completion of cross-sectional analysis, and the possible effect of APOE-ε4 expression on amyloid load in this PD group was not examined in baseline analysis. Three subjects included in the cross-sectional analysis were deceased before APOE genotyping could be performed. As these subjects were also excluded from longitudinal analysis due to either a diagnosis of dementia at

baseline or insufficient follow-up, APOE-ε4 carrier status was able to be investigated in the longitudinal arm of this study without excluding any meaningful data.

This thesis examined amyloid deposition by quantification of FBB tracer retention, using the standardised uptake value ratio (SUVR) and recently developed centiloid (CL) scale (Klunk et al., 2015), as well as visual assessment as clinically positive or negative by a trained neuroradiologist. Amyloid accumulation was not confirmed by histopathological assessment, however there is evidence of a tight agreement between visual assessment of amyloid PET and histopathological reports (Bullich et al., 2017). Amyloid load in this study of PD was found to be approximately comparable to levels observed in healthy ageing (Ossenkoppele et al., 2015), thus the analysis of survival from dementia in those demonstrating high levels of amyloid had a large associated error. Over time, this error increased as the data became right-censored. Thus, we were not able to definitively conclude that a negative amyloid scan at baseline represents a greater probability of improved long-term cognitive outcomes.

Part Three

While this investigation of white matter structural changes in PD was conducted within an expanded cohort of PD participants, the number of participants classified as having PD dementia was low compared to the other subgroups (PDN, n=46; PD-MCI, n=66; PDD, n=11), potentially reducing the chance of detecting a true effect associated with PDD due to low statistical power. Additionally, the lack of an association between cognitive impairment and white matter degeneration may reflect a limitation of our cross-sectional study design, in that analyses were reliant upon inter-subject comparisons and may have reduced sensitivity to detect subtle differences in individual anatomy relating to cognitive ability. Group comparison of PDN participants against controls may also have been affected by the increased age of the control group, being 8 years older on average. There is a strong dependence of white matter integrity on advancing age, thus this may have had the effect of obfuscating more subtle disease effects in PDN. Extending the study to include longitudinal data may increase the sensitivity of this analysis to identify white matter structural changes, both with regards to group analysis and in association with cognitive decline.

HARDI acquisitions may be performed using multiple different diffusion weightings, including both the high b-values required for spherical deconvolution and low b-values appropriate for modeling with the traditional diffusion tensor (b=1000 s/mm2 or less) (Hui et al., 2010). In this study, HARDI acquisition was performed at a single high value of diffusion weighting (b=2500 s/mm2), chosen to give the best resolution capability for crossing white matter fibres in the brain, while remaining clinically feasible (Xie et al., 2015). As low b-value data were not acquired, I was not able to apply DTI methods in the same subjects and thereby evaluate the points of difference between the two methods. Fixel-based analysis is a relatively new and unproven technique compared to the widely adopted diffusion tensor model, and it would be beneficial to demonstrate the benefit offered by improved discrimination of crossing fibres compared with DTI within a large PD subject group.

8.5 Future work

This work found that amyloid plaque deposition is likely not a primary pathology driving cognitive decline in PD, but amyloid may act in conjunction with other pathologies, thereby accelerating the pathway to dementia. Two such pathologies that may interact synergistically with beta-amyloid to affect cognition are alpha-synuclein, in the form of Lewy bodies, and hyper-phosphorylated tau. In AD, the presence of co-morbid beta-amyloid and Lewy body pathology detected at autopsy has been demonstrated to shorten survival times and accelerate disease progression, compared with AD patients without comorbidity (Marsh & Blurton-Jones, 2012). Effective PET radiotracers able to selectively bind to alpha-synuclein over amyloid and tau is a current unmet need in neuroimaging of Lewy body disorders (P. Kotzbauer et al., 2017), and development of such would have great benefit in diagnosis and staging of PD. Hyper-phosphorylated tau is expected to correlate more directly with current cognitive ability, and second-generation tau PET radiotracers show much improved specificity and reduced off-target binding compared to first generation tracers (Okamura et al., 2018). Initial tau PET imaging in PD and DLB demonstrates a spectrum of deposition, with reports of both association (Lee et al., 2018; Gomperts et al., 2016) and lack of association (Winer et al., 2018; Hansen et al., 2017) with cognitive impairments in PD. Tau PET imaging using a second generation radiotracer, $[^{18}F]$PI-2620, was originally planned in this study, however substantial delays in tracer

production prevented inclusion in this thesis. It is possible that imaging of tau using this tracer may be conducted within the ongoing study of Parkinson's disease within this research group, in order to fully characterise the deposition of tau and effect on cognition in PD.

This thesis verified the use of a novel method of constrained spherical deconvolution for obtaining multi-shell-like estimates from single-shell data, demonstrating clear improvement over standard single-shell methods. However, future work incorporating multiple b-value acquisitions (b=0, b=1000, b=2000, and b=3000 s/mm2 for example) would allow comparison with traditional DTI methods, as discussed above, and also allow validation of the single-shell method against multi-shell data acquired in the context of PD. Multi-shell data and CSD methods will offer improved characterisation of voxel-level fibre orientation distributions compared with the novel single-shell method, however the single-shell method may represent an excellent compromise regarding acquisition efficiency. The single-shell method has been verified against multi-shell data during development (Dhollander & Connelly, 2016), however application in the context of imaging white matter degeneration associated with cognition in PD may verify its effectiveness in the elucidation of subtle disease effects.

Appendix A

Anatomical Atlases

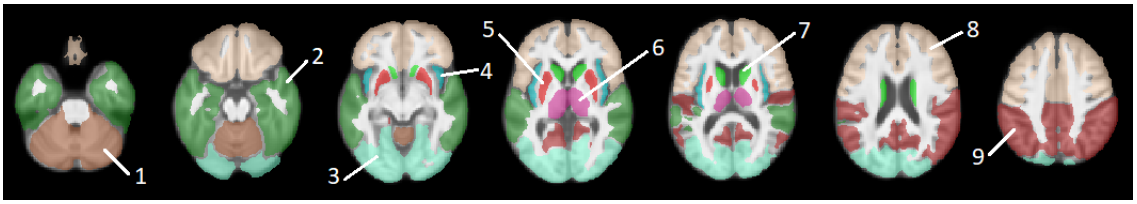

FIGURE A.1: The MNI structural atlas (Mazziotta et al., 2001), overlaid on a mean structural image. Labelled regions defined by the atlas are: (1) cerebellum; (2) temporal lobe; (3) occipital lobe; (4) insula; (5) putamen; (6) thalamus; (7) caudate; (8) frontal lobe; (9) parietal lobe.

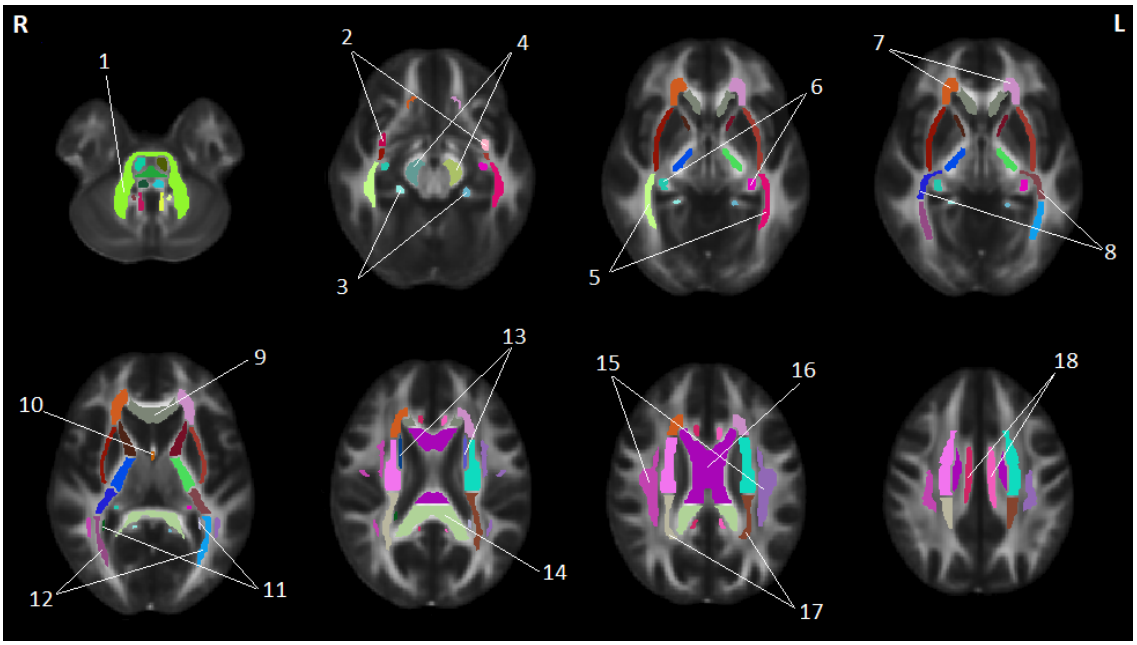

FIGURE A.2: Select axial slices from the JHU ICBM-DTI-81 White-Matter Labels atlas, overlaid on the FMRIB58_FA_1mm mean FA image. Those regions identified as significant in whole brain fixel analysis have been numbered: 1) Middle cerebellar peduncle; 2) Uncinate fasciculus; 3) Cingulum (hippocampus); 4) Cerebral peduncle; 5) Sagittal stratum; 6) Fornix cres/stria terminalis; 7) Anterior corona radiata; 8) Retrolenticular part of internal capsule; 9) Genu of the corpus callosum; 10) Fornix (body); 11) Tapetum of the corpus callosum; 12) Posterior thalamic radiation; 13) Superior fronto-occipital fasciculus; 14) Splenium of the corpus callosum; 15) Superior longitudinal fasciculus; 16) Body of the corpus callosum; 17) Posterior corona radiata; 18) Cingulate gyrus.

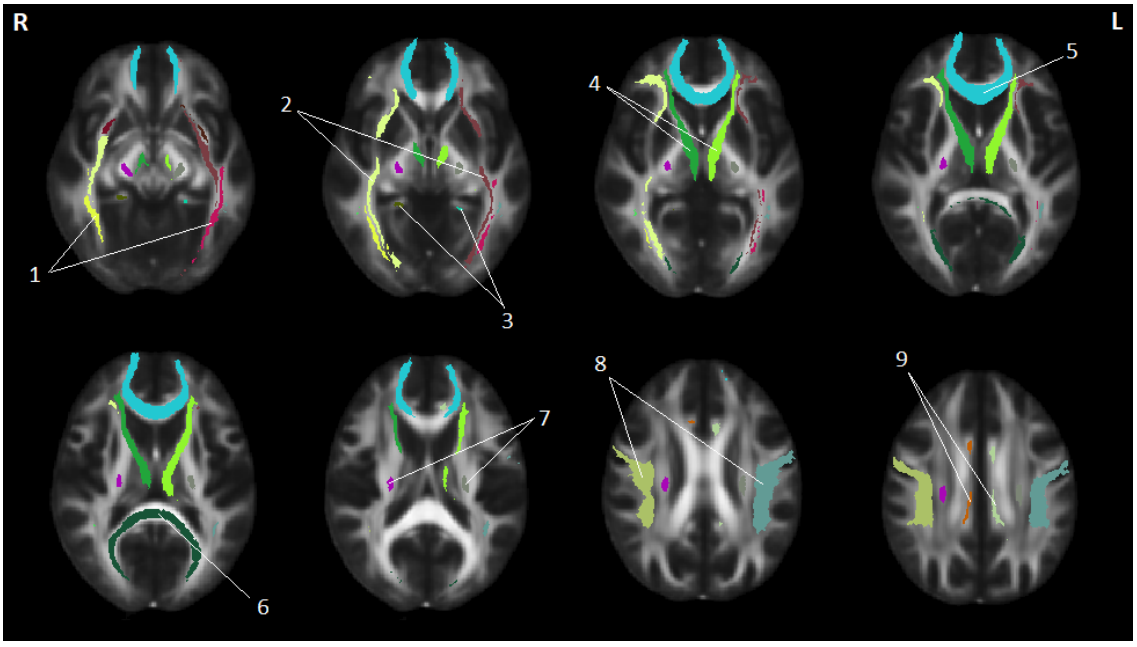

FIGURE A.3: Select axial slices from the JHU White-Matter Tractography atlas, overlaid on the FMRIB58_FA_1mm mean FA image. Those regions identified as significant in whole brain fixel analysis have been numbered: 1) Inferior longitudinal fasciculus; 2) Inferior fronto-occipital fasciculus; 3) Cingulum (hippocampus); 4) Anterior thalamic radiation; 5) Forceps minor; 6) Forceps major; 7) Corticospinal tract; 8) Superior longitudinal fasciculus; 9) Cingulum (cingulate gyrus).

Appendix B

Neuropsychological Battery and Participant Domain Scores

Executive Function	Attention & working memory	Episodic Memory	Visuospatial	Language
Stroop interference	Digits forwards/backwards	California Verbal Language Test-II Short Form; acquisition, short and long delays	Judgement of line orientation (JLO)	Boston Naming test
Letter fluency	Digit ordering	Rey Complex Figure test; short and long delays	Fragmented letters test	Dementia Rating Scale-2 similarities sub-test
Category fluency	Map search task		Picture completion test	Alzheimer's Dementia Assessment Cognitive Scale; object/finger naming, commands, comprehension, spoken language, word finding difficulties
Category switching	Stroop colour reading		RCF-Copy	
Action fluency	Stroop word reading			
Trails B	Trails A			

FIGURE B.1: The neuropsychiatric test battery consists of a series of test within each of the five cognitive domains.

Cross-sectional FBB PET amyloid imaging cohort

AnonID	Group	Cognitive group	PDD convert	Age	Sex	Education	Symptom (yrs)	MoCa	H&Y score	UPDRS-III	Attention	Executive	Visuospatial	Learning	Language	Global Cognitive Z	Amyloid
NZ000681	PD	PD-MCI	Convert	72	M	10	20	21	2	26	-1.04	-1.36	-1.01	-2.09	-0.6	-1.38	neg
NZ001620	PD	PDD	Excluded	80	M	10	8	23	3	55	-2.11	-1.96	-1.16	-2.28	-1.02	-1.88	pos
NZ001939	PD	PD-MCI	Convert	67	M	17	2	27	2.5	36	-0.63	-0.83	-0.24	-1.24	0.16	-0.73	neg
NZ002344	PD	PDD	Excluded	75	F	10	19	18	3	52	-1.37	-1.21	-1.49	-0.3	-1.09	-1.09	neg
NZ002568	PD	PDD	Excluded	79	M	12	3	12	3	38	-2.95	-2.6	-1.83	-1.76	-2.56	-2.28	neg
NZ003197	PD	PD-MCI	Non-convert	69	M	14	3	16	3	39	-2.67	-2.64	-2.24	-2.22	-2	-2.44	neg
NZ003283	PD	PD-MCI	Non-convert	65	M	10	7	24	2	36	-0.85	-0.66	-0.09	-2.32	-0.15	-0.98	neg
NZ004050	PD	PD-MCI	Convert	73	F	10	2	15	3	29	-0.82	-1.02	-1.46	-2.32	-0.27	-1.4	neg
NZ006471	PD	PD-MCI	Non-convert	76	M	11	20	22	NA	NA	-0.48	-0.84	-1.02	-0.02	-0.28	-0.59	neg
NZ007195	PD	PD-MCI	Convert	80	M	15	1	21	2	21	-0.76	-1.06	0.47	-0.1	0.2	-0.36	pos
NZ009306	PD	PDN	Non-convert	62	M	12	6	25	2.5	44	-0.47	0.14	-0.6	-1.1	-1.3	-0.51	neg
NZ011098	PD	PD-MCI	Convert	76	F	13	15	20	3	33	-0.27	-1.81	-1.67	-0.66	-0.57	-1.1	neg
NZ011417	PD	PD-MCI	Non-convert	60	F	11	13	25	3	46	-0.68	-1.07	-1.31	-0.2	0.16	-0.82	neg
NZ012046	PD	PD-MCI	Convert	74	M	18	4	25	1.5	19	-0.36	-0.75	0.1	-1.28	-0.71	-0.57	pos
NZ012580	PD	PD-MCI	Convert	75	M	13	12	18	2.5	37	-0.8	-1.88	-1.92	-1.58	-1.89	-1.54	neg
NZ012761	PD	PD-MCI	Non-convert	74	F	11	17	27	3	49	-0.92	-0.05	-0.6	-0.84	0.51	-0.6	neg
NZ012804	PD	PD-MCI	Non-convert	72	M	12	8	24	2.5	41	0	-0.84	-0.2	0.52	-0.6	-0.13	pos
NZ012899	PD	PD-MCI	Convert	75	M	10	4	25	2	33	-0.46	-0.94	-1.2	-0.72	-0.39	-0.83	neg
NZ013933	PD	PD-MCI	Convert	74	M	10	10	23	2	52	-0.64	-0.78	0.59	-0.08	-1.15	-0.23	pos
NZ014157	PD	PD-MCI	Non-convert	63	M	10	20	23	2	56	-0.91	-1.38	-0.97	-0.88	-0.7	-1.03	neg
NZ016044	PD	PD-MCI	Non-convert	70	F	10	10	26	3	50	-0.39	0.28	-0.54	-0.94	0.48	-0.4	neg
NZ016397	PD	PD-MCI	Non-convert	81	F	10	10	21	2.5	25	0.34	0.65	-0.61	-1.78	0.05	-0.35	neg
NZ017526	PD	PD-MCI	Non-convert	63	F	12	11	26	4	65	-0.72	-1.07	-1.29	-1.36	-0.26	-1.11	neg
NZ018060	PD	PD-MCI	Convert	74	M	11	8	22	3	62	-1.03	-0.7	-0.4	-0.68	0.51	-0.7	neg
NZ018155	PD	PDN	Non-convert	64	M	12	3	27	1.5	25	-0.43	-0.54	0.34	0.84	0.52	0.05	neg
NZ020395	PD	PD-MCI	Non-convert	78	M	17	12	23	2	45	-0.36	-0.71	0.38	-0.38	0.54	-0.27	neg
NZ021748	PD	PD-MCI	Convert	73	M	9	2	16	2	23	-2.47	-2.08	-1.48	-1.08	-1.49	-1.78	neg
NZ023006	PD	PD-MCI	Non-convert	86	M	13	6	23	2.5	43	-1.49	-1.38	0.33	-1.3	-0.24	-0.96	neg
NZ025117	PD	PD-MCI	Convert	59	M	10	5	21	2	20	-1.29	-1.68	-0.77	-1.62	0.16	-1.34	neg
NZ025427	PD	PDN	Non-convert	71	F	11	11	27	2.5	36	-0.32	0.66	0.56	0.84	0.15	0.43	neg
NZ025522	PD	PDN	Non-convert	73	M	11	5	24	4	63	-0.26	-0.62	0.02	0.2	-1.05	-0.16	pos
NZ026909	PD	PDN	Non-convert	74	M	10	9	27	2.5	36	-0.03	0.21	0.99	2.78	0.51	0.98	pos
NZ027495	PD	PDD	Excluded	77	M	12	8	20	NA	NA	NA	NA	NA	-1.5	NA	-1	pos
NZ028167	PD	PD-MCI	Convert	70	F	12	8	21	2.5	51	-1.52	-1.15	-1.28	-0.64	-0.31	-1.15	neg
NZ029425	PD	PD-MCI	Excluded	75	M	12	12	27	5	14	-0.55	-1.23	1.02	1.22	-0.72	0.12	neg
NZ030278	PD	PD-MCI	Non-convert	70	M	15	10	21	2	35	-0.74	-1.49	-0.72	-0.98	-0.9	-0.98	neg
NZ030373	PD	PD-MCI	Convert	75	M	11	6	20	2	36	-0.69	-0.67	-1.43	-1.58	-1.16	-1.09	neg
NZ030726	PD	PDN	Non-convert	84	M	13	12	25	2.5	58	-0.05	-0.07	-0.66	1.54	0.54	0.19	neg
NZ030907	PD	PDN	Non-convert	71	M	15	20	26	4	68	-0.54	-0.4	-0.45	-0.1	-0.64	-0.37	neg
NZ031355	PD	PDD	Excluded	74	M	11	15	9	NA	NA	NA	NA	NA	-1.9	NA	-2.6	neg
NZ031536	PD	PD-MCI	Non-convert	74	M	10	13	23	3	76	-0.69	-0.81	-0.81	-0.14	0.51	-0.61	neg
NZ031760	PD	PDN	Non-convert	80	F	15	17	24	NA	51	-0.29	1.35	0.25	1.04	0.36	0.59	neg
NZ032484	PD	PD-MCI	Convert	74	M	16	5	22	2	35	-1.12	-0.97	0.08	-0.9	-1.56	-0.73	neg
NZ032613	PD	PD-MCI	Non-convert	69	M	13	20	19	2.5	33	-1.68	-1.28	-0.99	-1.92	-0.71	-1.47	neg
NZ032889	PD	PD-MCI	Non-convert	66	M	10	11	24	2	38	-1.72	-1.3	0.43	0.74	-0.45	-0.46	neg

AnonID	Group	Cognitive group	PDD convert	Age	Sex	Education	Symptom (yrs)	MoCa	H&Y score	UPDRS-III	Attention	Executive	Visuospatial	Learning	Language	Global Cognitive Z	Amyloid
NZ034595	PD	PD-MCI	Non-convert	64	M	10	6	23	2	43	-1.6	-1.66	-0.17	-0.28	-1.56	-0.93	neg
NZ034905	PD	PD-MCI	Convert	76	M	19	15	26	2	32	-1.02	-1.31	0.79	0.66	-0.02	-0.22	neg
NZ035224	PD	PD-MCI	Non-convert	66	M	18	5	19	2.5	25	-0.37	-0.38	-0.04	-0.76	-0.67	-0.39	neg
NZ037111	PD	PD-MCI	Non-convert	70	F	12	4	30	2	20	-0.16	1.17	0.84	0.94	-0.09	0.7	neg
NZ038093	PD	PDN	Non-convert	74	F	16	10	27	2	25	0.38	0.72	1.02	0.34	0.06	0.62	neg
NZ038274	PD	PD-MCI	Non-convert	69	F	12	18	26	3	53	-0.84	-0.36	-0.52	-0.84	0.15	-0.64	neg
NZ038593	PD	PDD	Excluded	79	M	11	15	16	2.5	61	-1.47	-1.76	-2.22	-1.72	-0.8	-1.79	pos
NZ038903	PD	PDN	Non-convert	70	F	11	10	28	2	31	0.67	1.34	0.71	1.84	0.48	1.14	pos
NZ039222	PD	PD-MCI	Convert	76	M	11	5	25	3	62	-0.52	-0.81	-0.22	0.06	0.18	-0.37	pos
NZ040704	PD	PD-MCI	Convert	74	M	11	9	19	2.5	36	-1.6	-2.23	-1.74	-1.3	-1.49	-1.72	neg
NZ040833	PD	PDD	Excluded	85	M	11	14	19	3	52	-2.27	-1.97	-1.32	-1.14	-0.28	-1.67	pos
NZ041014	PD	PDN	Non-convert	70	M	17	8	23	2.5	35	0.14	0.55	0.63	-0.26	0.48	0.26	neg
NZ041109	PD	PDN	Non-convert	76	F	10	6	26	2	19	1.24	0.96	0.34	1.22	0.31	0.94	neg
NZ042496	PD	PDD	Excluded	74	M	16	14	19	NA	NA	NA	NA	NA	-1.6	NA	-1.7	neg
NZ042591	PD	PD-MCI	Convert	75	M	10	3	17	2.5	51	-1.51	-2	-1.67	-0.34	-0.5	-1.38	neg
NZ043754	PD	PD-MCI	Non-convert	67	M	14	8	22	2	26	-1.2	-0.47	0.17	-0.04	-0.67	-0.38	neg
NZ044383	PD	PDN	Non-convert	70	M	11	11	25	1	6	-0.02	0.87	0.04	0.34	0.15	0.31	neg
NZ045107	PD	PD-MCI	Non-convert	75	M	11	9	22	3	54	-0.82	-0.06	-0.44	-0.98	0.16	-0.57	neg
NZ045193	PD	PDN	Non-convert	70	M	11	17	28	2.5	31	0.25	0.16	0.15	-0.06	-0.18	0.12	neg
NZ049458	PD	PDD	Excluded	85	M	12	9	14	NA	NA	-1.39	-1.5	-1.82	-2.42	-2.33	-1.78	pos
NZ050182	PD	PD-MCI	Convert	71	M	13	9	22	2.5	44	-1.51	-1.48	0.2	-2.04	-0.87	-1.21	pos
NZ052474	PD	PDD	Excluded	75	F	11	4	18	3	57	-1.78	-2.09	-2.43	-2.48	-1.09	-2.19	neg
NZ052698	PD	PDD	Excluded	84	M	13	3	20	3	65	-2.61	-2.06	-1.71	-0.62	-0.83	-1.75	neg
NZ053551	PD	PD-MCI	Convert	70	F	15	4	19	2	13	-2.05	-1.89	-1.34	-1.86	-0.55	-1.78	neg
NZ053680	PD	PD-MCI	Non-convert	75	F	13	23	20	3	32	-1.32	-1.19	-2.24	-1.1	0.16	-1.46	neg
NZ054585	PD	PDN	Non-convert	76	M	12	0	28	3	45	-0.6	-0.11	0.8	0.26	-0.02	0.09	neg
NZ054671	PD	PD-MCI	Non-convert	78	M	13	5	21	2.5	46	-0.92	-1	-1.04	-0.92	-1.05	-0.97	neg
NZ055438	PD	PD-MCI	Non-convert	73	M	18	12	20	2.5	34	-0.88	-0.45	-0.41	-1.32	-0.05	-0.77	neg
NZ056601	PD	PDD	Excluded	63	M	17	11	16	NA	NA	NA	NA	NA	-2.6	NA	-2.5	neg
NZ057325	PD	PD-MCI	Non-convert	79	M	19	4	23	4	64	-1.05	-0.76	-0.38	-0.28	-0.66	-0.62	neg
NZ059436	PD	PDN	Non-convert	66	M	12	3	23	2.5	23	-0.5	-0.21	-0.33	-0.36	-0.61	-0.35	pos
NZ059660	PD	PD-MCI	Non-convert	68	M	10	10	28	3	56	-0.86	-0.54	-1.18	-0.6	-0.06	-0.79	neg
NZ059789	PD	PDN	Non-convert	61	M	9	14	27	2.5	61	-0.03	0.65	0.34	0.56	0.49	0.38	neg
NZ060065	PD	PD-MCI	Non-convert	78	M	10	5	23	2.5	42	-0.82	-1.21	0.19	-1.02	0.2	-0.71	pos
NZ060918	PD	PD-MCI	Non-convert	65	M	11	6	27	2	41	-0.93	-0.88	-0.6	0.1	-0.7	-0.58	neg
NZ061452	PD	PD-MCI	Convert	70	F	18	14	21	2.5	37	-0.9	-1.53	-0.53	-1.62	-1.33	-1.15	pos
NZ061547	PD	PD-MCI	Non-convert	71	M	15	16	27	2.5	46	-0.19	-0.21	-1.16	-1.44	0.24	-0.75	neg
NZ062081	PD	PD-MCI	Non-convert	78	M	12	13	23	3	53	-0.81	-0.89	-0.32	-0.38	-0.42	-0.6	neg
NZ062891	PD	PD-MCI	Non-convert	73	M	12	14	23	3	41	0.53	0.1	-0.21	-1.28	-0.94	-0.21	neg
NZ063968	PD	PD-MCI	Non-convert	75	F	10	9	23	3	23	-0.38	-0.61	-0.08	-1.62	-0.83	-0.67	neg
NZ064821	PD	PDD	Excluded	76	F	12	14	15	NA	NA	NA	NA	NA	-2.1	NA	-1.7	neg
NZ065140	PD	PDD	Excluded	78	M	15	8	20	3	41	-0.73	-1.09	-0.35	-1.98	-0.57	-1.04	pos
NZ066803	PD	PD-MCI	Excluded	74	M	9	4	22	2.5	38	-0.92	-0.43	-0.28	-1.74	-0.04	-0.84	neg
NZ067027	PD	PDN	Non-convert	61	M	13	9	24	2.5	36	-0.69	0.33	0.07	-0.16	-0.06	-0.11	neg
NZ067656	PD	PDN	Non-convert	68	F	13	7	24	2	25	-0.23	-0.24	-0.98	-0.76	-0.06	-0.55	neg
NZ068914	PD	PDN	Non-convert	72	F	10	21	26	2.5	32	0.6	0.75	0.87	0.8	0.51	0.75	neg
NZ069543	PD	PDD	Excluded	68	M	11	4	16	3	57	-1.99	-2.28	-2.54	-2.42	-1.17	-2.31	neg

AnonID	Group	Cognitive group	PDD convert	Age	Sex	Education	Symptom (yrs)	MoCa	H&Y score	UPDRS-III	Attention	Executive	Visuospatial	Learning	Language	Global Cognitive Z	Amyloid
NZ070706	PD	PD-MCI	Non-convert	71	F	10	7	23	NA	NA	0.01	-0.29	-0.56	-1.8	-1.07	-0.66	neg
NZ070930	PD	PD-MCI	Convert	78	F	11	10	26	2.5	35	-0.05	-0.87	-0.33	0.78	0.54	-0.12	neg
NZ072283	PD	PD-MCI	Non-convert	85	M	19	8	28	2.5	32	0.04	1.08	-0.17	1.22	-0.17	0.54	neg
NZ072912	PD	PDN	Non-convert	64	M	13	3	28	2	37	0.74	1.29	0.95	0.64	0.19	0.9	neg
NZ073446	PD	PD-MCI	Non-convert	73	F	16	7	21	3	6	-1.26	-0.89	-0.67	0.3	-0.05	-0.63	neg
NZ074299	PD	PD-MCI	Non-convert	59	M	14	10	23	2	35	-0.71	-0.03	-0.5	-0.82	-0.14	-0.51	pos
NZ074394	PD	PD-MCI	Convert	76	M	16	7	28	2.5	40	-1.63	-1.58	-0.18	0.24	0.13	-0.79	neg
NZ074523	PD	PD-MCI	Convert	66	M	11	10	23	2.5	27	-0.93	-1.09	-0.88	-0.56	-0.67	-0.86	neg
NZ074618	PD	PD-MCI	Convert	68	M	12	11	24	2	39	-1.17	-1.17	0.24	-0.78	-0.61	-0.72	neg
NZ075652	PD	PD-MCI	Non-convert	67	M	11	6	27	2.5	35	-0.67	-0.25	-0.08	-0.26	-0.33	-0.32	neg
NZ075876	PD	PD-MCI	Convert	73	M	11	5	18	2.5	49	-1.21	-1.93	-2.03	-2.16	-0.6	-1.83	neg
NZ076505	PD	PD-MCI	Convert	67	M	11	5	22	2	44	-1.49	-1.54	-0.36	-0.84	-0.61	-1.06	neg
NZ076815	PD	PD-MCI	Non-convert	63	M	17	15	24	NA	NA	-0.47	-0.02	-0.22	-0.56	-0.03	-0.31	neg
NZ077039	PD	PDN	Non-convert	73	M	12	11	27	2.5	47	-0.72	-0.1	0.93	0.84	0.51	0.24	neg
NZ077134	PD	PD-MCI	Convert	65	M	12	10	20	2.5	52	-0.68	-1.82	-1.67	-1.9	-1.26	-1.52	neg
NZ077668	PD	PD-MCI	Non-convert	79	M	16	10	24	3	59	-1.89	-1.54	-1.34	0.22	-0.02	-1.14	neg
NZ078435	PD	PD-MCI	Non-convert	78	F	8	9	24	3	52	-0.42	-0.73	-0.12	-1.18	0.2	-0.61	neg
NZ078926	PD	PD-MCI	Convert	74	M	10	9	16	2	49	-1.56	-1.73	-0.94	-1.18	-1.26	-1.35	pos
NZ079021	PD	PD-MCI	Convert	82	M	17	5	20	3	41	-0.55	-0.26	-1.27	-1.62	-1.37	-0.92	pos
NZ079874	PD	PDN	Non-convert	59	F	13	4	30	2.5	41	0.37	0.77	0.14	0.68	0.49	0.49	neg
NZ080227	PD	PDD	Excluded	76	M	10	15	4	NA	NA	NA	NA	NA	-2.3	NA	-3	neg
NZ082390	PD	PD-MCI	Convert	77	M	11	1	24	2.5	35	-1.08	-1.53	-0.64	-1.48	-0.06	-1.18	neg
NZ084406	PD	PD-MCI	Non-convert	74	M	11	17	24	3	24	-0.86	0.48	-1.25	-0.5	-0.16	-0.53	neg
Additional subjects included in White Matter analysis																	
NZ001034	Control	CN	NA	64.8	M	11	NA	27	NA	NA	0.49	0.67	1.01	0.82	0.52	0.59	NA
NZ001086	PD	PDD	NA	71.4	M	17	12.9	15	3	46	-2.45	-2.39	-1.58	-2.66	-0.99	-2.07	NA
NZ001715	PD	MCI	NA	67	M	17	6.2	18	2.5	42	-1.88	-2.21	0	-0.84	-1.72	-1.58	NA
NZ002792	PD	MCI	NA	69.5	F	15	26.1	23	3	26	-0.75	0	-1.67	-0.92	0.48	-0.57	NA
NZ005213	PD	PDN	NA	72.8	F	14	16.9	25	3	49	-0.13	0.57	0.01	1.32	0.51	0.34	NA
NZ005661	Control	CN	NA	72.8	M	16	NA	29	NA	NA	1.26	0.88	1.13	2.3	0.51	1.04	NA
NZ009211	PD	PDN	NA	65.1	F	17	11.6	29	2	31	0.27	1.08	0.67	1.56	0.52	0.69	NA
NZ011503	PD	PDN	NA	80.4	F	16	7.6	24	3	41	-0.25	0.73	0.07	1.48	-0.02	0.31	NA
NZ011770	Control	CN	NA	77.1	F	11	NA	26	NA	NA	-0.17	0.96	0.84	0.22	0.16	0.47	NA
NZ012175	Control	CN	NA	64.5	M	17	NA	30	NA	NA	-0.1	0.74	0.71	2.24	0.52	0.56	NA
NZ013028	PD	PDN	NA	78.2	F	13	15.1	28	NA	NA	0.19	-0.2	0.03	1.07	0.54	0.17	NA
NZ013028	PD	PDN	NA	80.2	F	13	17.1	29	NA	NA	0.08	0.34	0.35	-0.32	0.54	0.4	NA
NZ016216	Control	CN	NA	74.2	F	10	NA	28	NA	NA	-0.23	0.78	1.45	2.32	0.51	0.66	NA
NZ017207	PD	PDN	NA	61.5	M	10	8.1	26	2	32	-0.13	0.42	0.2	1.64	0.49	0.26	NA
NZ018017	Control	CN	NA	57.1	M	18	NA	30	NA	NA	0.19	0.53	0.89	0.38	0.49	0.44	NA
NZ018689	PD	PDN	NA	66.9	F	12	9.8	28	3	49	-0.05	0.14	0.81	0.38	0.22	0.3	NA
NZ020619	Control	CN	NA	82.1	F	18	NA	29	NA	NA	0.81	0.76	1.51	2.22	0.54	0.98	NA
NZ022101	Control	CN	NA	72.2	M	15	NA	25	NA	NA	-0.03	0.35	0.79	1.04	-0.27	0.31	NA
NZ023411	PD	PDN	NA	63.1	M	11	9.2	28	2	19	0.15	0.99	0.51	-0.36	-0.59	0.44	NA
NZ024574	Control	CN	NA	80.8	F	13	NA	29	NA	NA	0.47	-0.49	0.32	2.18	0.54	0.25	NA
NZ025022	Control	CN	NA	65	M	17	NA	29	NA	NA	0.26	0.9	0.7	1.76	0.52	0.66	NA
NZ025022	Control	CN	NA	66.9	M	17	NA	28	NA	NA	0.64	0.79	0.61	2.08	0.5	0.74	NA

AnonID	Group	Cognitive group	PDD convert	Age	Sex	Education	Symptom (yrs)	MoCa	H&Y score	UPDRS-III	Attention	Executive	Visuospatial	Learning	Language	Global Cognitive Z	Amyloid
NZ025470	Control	CN	NA	84.9	M	18	NA	25	NA	NA	0.32	0.79	0.87	1.96	0.54	0.72	NA
NZ027133	PD	PDN	NA	67.1	M	15	25.3	25	2	28	0.72	0.74	-0.18	0.08	0.22	0.47	NA
NZ027581	Control	CN	NA	76.5	F	12	NA	30	NA	NA	1.44	1.76	1.28	2.18	0.5	1.39	NA
NZ028839	Control	CN	NA	85.2	M	13	NA	20	NA	NA	-0.29	0.27	1.35	1.76	-0.13	0.27	NA
NZ031312	Control	CN	NA	75.9	M	10	NA	27	NA	NA	0.18	1.07	0.77	0.66	0.5	0.64	NA
NZ032208	Control	CN	NA	80.5	F	15	NA	23	NA	NA	0.45	0.65	0.6	1.86	-0.32	0.41	NA
NZ032389	Control	CN	NA	79.4	M	15	NA	29	NA	NA	0.85	1.03	1.32	2.5	0.36	1.01	NA
NZ032794	PD	PDN	NA	67.1	M	14	8.1	28	2	31	0.66	1.86	0.89	1.86	0.5	1.16	NA
NZ034724	PD	PDN	NA	57.4	M	10	13.7	25	3	55	-0.7	-0.59	0.82	-0.16	-0.11	-0.25	NA
NZ035577	Control	CN	NA	71.5	M	16	NA	27	NA	NA	1.28	1.75	1.03	2.06	0.51	1.31	NA
NZ037912	Control	CN	NA	78.3	M	12	NA	28	NA	NA	-0.13	-0.01	1.03	1.5	0.36	0.27	NA
NZ037964	PD	PDN	NA	62.9	M	13	7.3	23	2	31	-0.98	-0.03	0.68	0.24	-0.15	-0.21	NA
NZ038636	Control	CMCI	NA	71.6	F	13	NA	24	NA	NA	-0.88	0.05	0.05	-0.2	0.51	-0.16	NA
NZ038636	Control	CN	NA	73.4	F	13	NA	26	NA	NA	-0.54	0.61	-0.02	0.14	-0.27	0	NA
NZ042944	Control	CMCI	NA	86.1	F	12	NA	21	NA	NA	0.54	0.23	0.24	-1.74	-0.72	0.08	NA
NZ044340	Control	CN	NA	80.2	F	13	NA	25	NA	NA	0.52	1.03	0.06	0.02	0.2	0.53	NA
NZ045460	PD	PDN	NA	61.8	M	16	11.5	29	2	32	0.66	0.52	0.67	2.42	0.16	0.66	NA
NZ046494	PD	PDN	NA	79.6	M	18	12.9	26	2	35	-0.13	1.24	0.43	1.22	0.54	0.51	NA
NZ048424	Control	CN	NA	84.6	M	16	NA	24	NA	NA	-0.55	0.78	0.7	-0.5	-0.35	0.21	NA
NZ049053	Control	CN	NA	53.5	M	14	NA	28	NA	NA	-0.04	2.04	1.02	1.66	0.47	0.97	NA
NZ050492	PD	PDN	NA	59	F	17	12.8	26	2.5	45	-0.49	0.47	0.42	0.34	-0.14	0.13	NA
NZ054533	Control	CN	NA	77.5	M	12	NA	26	NA	NA	0.11	0.41	0.71	1.5	0.54	0.47	NA
NZ054533	Control	CN	NA	79.4	M	12	NA	26	NA	NA	0.17	-0.11	0.62	1.9	-0.02	0.26	NA
NZ054809	PD	PDN	NA	67.4	M	12	15.5	28	2	37	-0.42	-0.06	0.26	0.36	-0.11	-0.14	NA
NZ055791	Control	CN	NA	70	M	19	NA	30	NA	NA	1.48	2.16	1.2	2.62	0.48	1.53	NA
NZ056196	Control	CN	NA	82.5	M	18	NA	28	NA	NA	0.37	0.78	0.19	2.28	0.54	0.51	NA
NZ056825	PD	MCI	NA	81.9	M	10	10.6	26	3	66	-0.16	-1.2	-0.78	0.26	-0.51	-0.49	NA
NZ057902	Control	CN	NA	73.9	F	11	NA	28	NA	NA	0.44	1.41	-0.22	0.02	0.51	0.57	NA
NZ059970	PD	PDN	NA	65.4	M	18	10.2	26	2	27	0.35	1.07	1.07	2.48	-0.15	0.77	NA
NZ060289	PD	PDN	NA	62.6	F	13	15.1	26	2	29	-0.4	-0.14	-0.8	-1.4	-0.03	-0.38	NA
NZ061228	PD	PDN	NA	63.4	M	13	7.4	24	2.5	35	0.28	0.47	-0.76	-1.18	0.52	0.13	NA
NZ063158	PD	MCI	NA	77.7	F	15	16	19	4	49	-1.25	-2.27	-1.2	-1.34	-1.04	-1.56	NA
NZ064011	Control	CN	NA	74.6	M	13	NA	30	NA	NA	0.9	2.51	0.94	2.28	0.5	1.4	NA
NZ064640	Control	CN	NA	72.4	F	10	NA	27	NA	NA	0.21	1.08	0.57	1.16	0.51	0.61	NA
NZ065269	Control	CMCI	NA	87.4	F	19	NA	21	NA	NA	0.02	1.01	0.31	1.64	0.26	0.53	NA
NZ072188	PD	PDN	NA	55	M	18	9.2	29	2	42	1.32	1.17	1.07	0.8	0.47	1.12	NA
NZ072188	PD	PDN	NA	53.1	M	18	7.3	29	1.5	15	0.84	0.3	0.99	0.54	-0.09	0.59	NA
NZ073765	PD	MCI	NA	75.7	F	10	16.2	26	2.5	34	-0.4	-0.5	-0.81	-1.32	-0.06	-0.52	NA
NZ077220	Control	CN	NA	77.3	M	12	NA	29	NA	NA	0.86	1.67	0.7	1.68	0.5	1.07	NA
NZ077220	Control	CN	NA	75.3	M	12	NA	27	NA	NA	1.35	1.98	1.31	1.8	-0.06	1.32	NA
NZ080632	PD	PDN	NA	75.4	F	11	11.7	27	2.5	29	-0.28	0.87	0.17	0.52	0.16	0.26	NA
NZ081037	PD	PDN	NA	79.2	M	12	10.5	23	2.5	28	-0.47	-0.4	0.55	0.66	0.36	-0.11	NA
NZ081666	PD	MCI	NA	62.4	F	14	10.3	24	2.5	35	-0.84	-0.71	-1.35	-1.52	-0.17	-0.82	NA
NZ082967	Control	CN	NA	69.7	M	11	NA	27	NA	NA	0.56	1.07	0.46	1.04	0.48	0.78	NA
NZ083372	Control	CN	NA	74.9	M	11	NA	24	NA	NA	0.21	-0.37	1.18	1.34	0.5	0.33	NA

FIGURE B.2: All participant neuropsychological cognitive domain scores and demographics at study baseline. Those included in longitudinal follow-up have PD dementia conversion status specified. Cognitive groups are Parkinson's disease with normal cognition (PDN), mild cognitive impairment (PD-MCI), or dementia (PDD), and control with normal cognition (CN) or mild cognitive impairment (CMCI).

References

Aarsland, D., Creese, B., Politis, M., Chaudhuri, K. R., ffytche, D. H., Weintraub, D., & Ballard, C. (2017). Cognitive decline in parkinson disease. *Nature Reviews Neurology*, *13*(4), 217.

Adair, J. C., Williamson, D. J., Schwartz, R. L., & Heilman, K. M. (1996). Ventral tegmental area injury and frontal lobe disorder. *Neurology*, *46*(3), 842-843.

Adler, C., Caviness, J., Sabbagh, M., Shill, H., Connor, D., Sue, L., ... Beach, T. (2010). Heterogeneous neuropathological findings in parkinson's disease with mild cognitive impairment. *Acta Neuropathologica*, *120*(6), 827-828. doi: 10.1007/s00401-010-0744-4

Akhtar, R., Xie, S., Chen, Y., Rick, J., Gross, R., Nasrallah, I., ... Weintraub, D. (2017). Regional brain amyloid-β accumulation associates with domain-specific cognitive performance in parkinson disease without dementia. *PLOS ONE*, *12*(5). doi: 10.1371/journal.pone.0177924

Alberico, S. L., Cassell, M. D., & Narayanan, N. S. (2015). The vulnerable ventral tegmental area in parkinson's disease. *Basal Ganglia*, *5*(2-3), 51-55. doi: 10.1016/j.baga.2015.06.001

Alves, G., Forsaa, E. B., Pederson, K. G., Gjerstad, M. D., & Larsen, I. P. (2008). Epidemiology of parkinson's disease. *Journal of Neurology*, *255*(5), 18-32. doi: 10.1007/s00415-008-5004-3

Anderson, T. J. (2013). *Genetics, brain imaging, and cognitive decline in parkinson's disease.* Research Project Full Application (GA214F) to the Health Research Council of New Zealand.

Andersson, J. L., Skare, S., & Ashburner, J. (2003). How to correct susceptibility distortions in spin-echo echo-planar images: application to diffusion tensor imaging. *NeuroImage*, *20*(2), 870-888. doi: 10.1016/S1053-8119(03)00336-7

Andersson, J. L., & Sotiropoulos, S. N. (2016). An integrated approach to correction for off-resonance effects and subject movement in diffusion mr imaging. *NeuroImage*, *125*, 1063-1078. doi: 10.1016/j.neuroimage.2015.10.019

Ashburner, J. (2007). A fast diffeomorphic image registration algorithm. *NeuroImage*, *38*(1), 95-113. doi: 10.1016/j.neuroimage.2007.07.007

Ashburner, J., Barnes, G., Chen, C. C., Daunizeau, J., Flandin, G., Friston, K., ... Zeidman, P. (2015). Spm12 manual [Computer software manual]. Retrieved from http://www.fil.ion.ucl.ac.uk/spm/doc/manual.pdf

Ashburner, J., & Friston, K. (2005). Unified segmentation. *NeuroImage*, *26*(3), 839-851. doi: 10.1016/j.neuroimage.2005.02.018

Atkinson-Clement, C., Pinto, S., Eusebio, A., & Coulon, O. (2017). Diffusion tensor imaging in parkinson's disease: Review and meta-analysis. *NeuroImage: Clinical*, *16*, 98–110. doi: 10.1016/j.nicl.2017.07.011

Auning, E., Kjærvik, V. K., Selnes, P., Aarsland, D., Haram, A., Bjørnerud, A., ... Fladby, T. (2014). White matter integrity and cognition in parkinson's disease: a cross-sectional study. *BMJ Open*, *4*(1). doi: 10.1136/bmjopen-2013-003976

Bach, J. P., Ziegler, U., Deuschl, G., Dodel, R., & Doblhammer-Reiter, G. (2011). Projected numbers of people with movement disorders in the years 2030 and 2050. *Movement Disorders*, *26*(12), 2286-2290. doi: 10.1002/mds.23878

Bangen, K. J., Clark, A. L., Edmonds, E. C., Evangelista, N. D., Werhane, M. L., Thomas, K. R., ... Delano-Wood, L. (2017). Cerebral blood flow and amyloid-β interact to affect memory performance in cognitively normal older adults. *Frontiers in Aging Neuroscience*, *9*(181). doi: 10.3389/fnagi.2017.00181

Barone, P., Antonini, A., Colosimo, C., Marconi, R., Morgante, L., Avarello, T. P., ... Dotto, P. D. (2009). The priamo study: A multicenter assessment of nonmotor symptoms and their impact on quality of life in parkinson's disease. *Movement Disorders*, *24*(11), 1641-1649. doi: 10.1002/mds.22643

Barreto, G. E., Iarkov, A., & Moran, V. E. (2014). Beneficial effects of nicotine, cotinine and its metabolites as potential agents for parkinson's disease. *Frontiers in Aging Neuroscience*, *6*(340). doi: 10.3389/fnagi.2014.00340

Basser, P. J., & Özaslan, E. (2009). Introduction to diffusion mr. In *Diffusion MRI* (p. 1-10). Academic Press.

Becker, G. A., Ichise, M., Barthel, H., Luthardt, J., Patt, M., Seese, A., ... Sabri, O. (2013). PET quantification of 18F-florbetaben binding to β-amyloid deposits in human brains. *Journal of Nuclear Medicine*, *54*(5), 723-731.

Benedictus, M. R., Leeuwis, A. E., Binnewijzend, M. A., Kuijer, J. P., Scheltens, P., Barkhof, F., ... Prins, N. D. (2017). Lower cerebral blood flow is associated with faster cognitive decline in alzheimer's disease. *European Radiology*, *27*(3). doi: 10.1007/s00330-016-4450-z

Berg, D., Postuma, R. B., Bloem, B., Chan, P., Dubois, B., Gasser, T., ... Deuschl, G. (2014). Time to redefine PD? Introductory statement of the MDS task force on the definition of parkinson's disease. *Movement Disorders*, *29*(4), 454-462. doi: 10.1002/mds.25844

Berman, J. I., Lanza, M. R., Blaskey, L., Edgar, J. C., & Roberts, T. P. (2013). High angular resolution diffusion imaging probabilistic tractography of the auditory radiation. *American Journal of Neuroradiology*, *34*(8), 1573-1578. doi: 10.3174/ajnr.A3471

Betarbet, R., Sherer, T. B., MacKenzie, G., Garcia-Osuna, M., Panov, A., & Greenamyre, J. T. (2000). Chronic systemic pesticide exposure reproduces features of parkinson's disease. *Nature Neuroscience*, *3*(12), 1301-1306. doi: 10.1038/81834

Bohnen, N. I., & Albin, R. L. (2011). White matter lesions in parkinson disease. *Nature Reviews Neurology*, *7*(4), 229-236. doi: 10.1038/nrneurol.2011.21

Braak, H., Del Tredici, K., Rüb, U., de Vos, R. A., Jansen Steur, E. N., & Braak, E. (2003). Staging of brain pathology related to sporadic parkinson's disease. *Neurobiology of Aging*, *24*(2), 197-211. doi: 10.1016/S0197-4580(02)00065-9

Brown, R. W., Cheng, Y.-C. N., Haacke, E. M., Thompson, M. R., Venkatesan, R., & service), W. I. O. (2014). *Magnetic resonance imaging: physical principles and sequence design* (Second ed.). Hoboken, New Jersey: John Wiley & Sons, Inc. doi: 10.1002/9781118633953.ch4

Bullich, S., Seibyl, J., Catafau, A. M., Jovalekic, A., Koglin, N., Barthel, H., ... Santi, S. D. (2017). Optimized classification of 18F-florbetaben PET scans as positive and negative using an suvr quantitative approach and comparison to visual assessment. *NeuroImage: Clinical*, *15*, 325-332. doi: 10.1016/j.nicl.2017.04.025

Buongiorno, M., Compta, Y., & Martí, M. J. (2011). Amyloid-β and τ biomarkers in parkinson's disease-dementia. *Journal of the Neurological Sciences*, *310*(1-2), 25-30.

Bürkner, P.-C. (2017). brms: An R package for bayesian multilevel models using stan. *Journal of Statistical Software*, *80*(1), 1-28.

Bushberg, J. T., Seibert, J. A., Jr., E. M. L., & Boone, J. M. (2012). *The essential physics of medical imaging* (Third ed.). Philadelphia, Pennsylvania: Lippincott Williams & Wilkins, a Wolters Kluwer business.

Button, K. S., Ioannidis, J. P. A., Mokrysz, C., Nosek, B. A., Flint, J., Robinson, E. S. J., & Munafò, M. R. (2013). Power failure: why small sample size undermines the reliability of neuroscience. *Nature Reviews Neuroscience*, *14*(5), 365-376. doi: 10.1038/nrn3475

Chaudhuri, K. R., Clough, C. G., & Sethi, K. D. (2011). *Fast facts: Parkinson's disease* (Third ed.). Oxford, UK: Health Press Limited.

Chaudhuri, K. R., Martinez-Martin, P., Schapira, A. H., Stocchi, F., Sethi, K., Odin, P., ... Olanow, C. W. (2006). International multicenter pilot study of the first comprehensive self-completed nonmotor symptoms questionnaire for parkinson's disease: The NMSQuest study. *Movement Disorders*, *21*(7), 916-923. doi: 10.1002/mds.20844

Chen, Y., & An, H. (2017). Attenuation correction of PET/MR imaging. *Magnetic Resonance Imaging Clinics of North America*, *25*(2), 245-255. doi: 10.1016/j.mric.2016.12.001

Chen, Y., Nasrallah, I., Akhtar, R., Rick, J., Chen-Plotkin, A., Trojanowski, J., ... Dubroff, J. (2017). Comparing patterns of brain amyloid deposition in parkinson's disease to alzheimer's disease and cognitively normal controls using [18F] florbetapir PET imaging. *Journal of Nuclear Medicine*, *58*(supplement 1), 416-416.

Choy, S. W., Bagarinao, E., Watanabe, H., Ho, E. T. W., Maesawa, S., Mori, D., ... Sobue, G. (2020). Changes in white matter fiber density and morphology across the adult lifespan: A cross-sectional fixel-based analysis. *Human Brain Mapping*, *41*(12), 3198-3211. doi: 10.1002/hbm.25008

Collignon, A., Maes, F., Delaere, D., Vandermeulen, D., Suetens, P., & Marchal, G. (1995). Automated multi-modality image registration based on information theory. *In: Bizais*.

Compta, Y., Ibarretxe-Bilbao, N., B Pereira, J., Junqué, C., Bargalló, N., Tolosa, E., ... Jose Martí, M. (2012). Grey matter volume correlates of cerebrospinal markers of alzheimer-pathology in parkinson's disease and related dementia. *Parkinsonism & Related Disorders*, *18*(8), 941-947.

Compta, Y., Parkkinen, L., Kempster, P., Selikhova, M., Lashley, T., Holton, J. L., ... Revesz, T. (2014). The significance of α-synuclein, amyloid-β and tau pathologies in parkinson's disease progression and related dementia. *Neurodegenerative Diseases*, *13*(2-3), 154-156.

Compta, Y., Parkkinen, L., O'Sullivan, S. S., Vandrovcova, J., Holton, J. L., Collins, C., ... Revesz, T. (2011). Lewy-and alzheimer-type pathologies in parkinson's disease dementia: Which is more important? *Brain*, *134*(5), 1493-1505.

Compta, Y., Pereira, J., Ríos, J., Ibarretxe-Bilbao, N., Junqué, C., Bargalló, N., ... Martí, M. (2013). Combined dementia-risk biomarkers in parkinson's disease: A prospective longitudinal study. *Parkinsonism & Related Disorders*, *19*(8), 717-724. doi: 10.1016/j.parkreldis.2013.03.009

Daducci, A., Canales-Rodrı´guez, E. J., Descoteaux, M., Garyfallidis, E., Gur, Y., Lin, Y., ... Thiran, J. (2014). Quantitative comparison of reconstruction methods for intra-voxel fiber recovery from diffusion MRI. *IEEE Transactions on Medical Imaging*, *33*(2), 384-399. doi: 10.1109/TMI.2013.2285500

Dai, W., Garcia, D., de Bazelaire, C., & Alsop, C. D. (2008). Continuous flow-driven inversion for arterial spin labelling using pulsed radio frequency and gradient fields. *Magnetic Resonance in Medicine*, *60*(6), 1488-1497. doi: 10.1002/mrm.21790

Dale, A. M., Fischl, B., & Sereno, M. I. (1999). Cortical surface-based analysis: I. segmentation and surface reconstruction. *NeuroImage*, *9*(2), 179-194. doi: 10.1006/nimg.1998.0395

Danielmeier, C., Eichele, T., Forstmann, B. U., Tittgemeyer, M., & Ullsperger, M. (2011). Posterior medial frontal cortex activity predicts post-error adaptations in task-related visual and motor areas. *Journal of Neuroscience*, *31*(5), 1780-1789. doi: 10.1523/JNEUROSCI.4299-10.2011

de Lau, L. M. L., & Breteler, M. M. B. (2006). Epidemiology of parkinson's disease. *The Lancet Neurology*, *5*(6), 525-535.

de Schipper, L. J., Hafkemeijer, A., Bouts, M. J., van der Grond, J., Marinus, J., Henselmans, J. M., & van Hilten, J. J. (2019). Age- and disease-related cerebral white matter changes in patients with parkinson's disease. *Neurobiology of Aging*, *80*, 203-209. doi: 10.1016/j.neurobiolaging.2019.05.004

Descoteaux, M. (2015). High angular resolution diffusion imaging (HARDI). In *Wiley Encyclopedia of Electrical and Electronics Engineering* (p. 1-25). American Cancer Society. doi: 10.1002/047134608X.W8258

Desikan, R. S., Ségonne, F., Fischl, B., Quinn, B. T., Dickerson, B. C., Blacker, D., ... Killiany, R. J. (2006). An automated labeling system for subdividing the human cerebral cortex on MRI scans into gyral based regions of interest. *NeuroImage*, *31*(3), 968-980.

Detre, J. A., Leigh, J. S., Williams, D. S., & Koretsky, A. P. (1992). Perfusion imaging. *Magnetic Resonance in Medicine*, *23*(1), 37-45. doi: 10.1002/mrm.1910230106

Dhollander, T., & Connelly, A. (2016, May). A novel iterative approach to reap the benefits of multi-tissue csd from just single-shell (+b=0) diffusion MRI data. In *Proceedings of 24th International Society of Magnetic Resonance in Medicine.*

Dhollander, T., Mito, R., Raffelt, D., & Connelly, A. (2019). Improved white matter response function estimation for 3-tissue constrained spherical deconvolution. In *Proceedings of 27th International Society of Magnetic Resonance in Medicine.*

Dhollander, T., Raffelt, D., & Connelly, A. (2016, Sep). Unsupervised 3-tissue response function estimation from single-shell or multi-shell diffusion mr data without a co-registered T1 image. In *Proceedings of ISMRM Workshop on Breaking the Barriers of Diffusion MRI.*

Diaz, N. L., & Waters, C. H. (2009). Current strategies in the treatment of parkinson's disease and a personalized approach to management. *Expert Review of Neurotherapeutics*, *9*(12), 1781-1789. doi: 10.1586/ern.09.117

Dickson, D. W. (2012). Parkinson's disease and parkinsonism: Neuropathology. *Cold Spring Harbor Perspectives in Medicine*, *8*(2), a009258. doi: 10.1101/cshperspect.a009258.

Docherty, M. J., & Burn, D. J. (2010). Parkinson's disease dementia. *Current Neurology and Neuroscience Reports*, *10*(4), 292-298. doi: 10.1007/s11910-010-0113-7

Dolatshahi, M., Pourmirbabaei, S., Kamalian, A., Ashraf-Ganjouei, A., Yaseri, M., & Aarabi, M. H. (2018). Longitudinal alterations of alpha-synuclein, amyloid beta, total, and phosphorylated tau in cerebrospinal fluid and correlations between their changes in parkinson's disease. *Frontiers in Neurology*, *9*, 560. doi: 10.3389/fneur.2018.00560

Donaghy, P. C., Firbank, M. J., Thomas, A. J., Lloyd, J., Petrides, G., Barnett, N., ... O'Brien, J. T. (2018). Clinical and imaging correlates of amyloid deposition in dementia with lewy bodies. *Movement Disorders*, *33*(7), 1130-1138. doi: 10.1002/mds.27403

Drachman, D. (2014). The amyloid hypothesis, time to move on: Amyloid is the downstream result, not cause, of alzheimer's disease. *Alzheimer's & Dementia*, *10*, 372-80. doi: 10.1016/j.jalz.2013.11.003

Dugger, B., Serrano, G., Sue, L., Walker, D., Adler, C., Shill, H., ... Beach, T. (2012). Presence of striatal amyloid plaques in parkinson's disease dementia predicts concomitant alzheimer's disease: Usefulness for amyloid imaging. *Journal of Parkinson's Disease*, *2*(1), 57-65. doi: 10.3233/JPD-2012-11073

Eckert, T., Tang, C., & Eidelberg, D. (2007). Assessing the progression of parkinson's disease: A metabolic network approach. *The Lancet Neurology*, *6*(10), 956-932. doi: 10.1016/S1474-4422(07)70245-4

Edison, P., Ahmed, I., Fan, Z., Hinz, R., Gelosa, G., Ray Chaudhuri, K., ... Brooks, D. J. (2013). Microglia, amyloid, and glucose metabolism in parkinson's disease with and without dementia. *Neuropsychopharmacology*, *38*(6), 938-949. doi: 10.1038/npp.2012.255

Eidelberg, D. (2009). Metabolic brain networks in neurodegenerative disorders: A functional imaging approach. *Trends in Neurosciences*, *32*(10), 548-557. doi: 10.1016/j.tins.2009.06.003

Eidelberg, D., Moeller, J. R., Ishikawa, T., Dhawan, V., Spetsieris, P., Chaly, T., ... Fahn, S. (1995). Early differential diagnosis of parkinson's disease with ^{18}f-fluorodeoxyglucose and positron emission tomography. *Neurology*, *45*(11), 1996-2004.

Emre, M., Aarsland, D., Brown, R., Burn, D., Duyckaerts, C., Mizuno, Y., ... Dubois, B. (2007). Clinical diagnostic criteria for dementia associated with parkinson's disease. *Movement Disorders*, *22*(12), 1689-1707. doi: 10.1002/mds.21507

Erickson, K. I., Voss, M. W., Prakash, R. S., Basak, C., Szabo, A., Chaddock, L., ... Kramer, A. F. (2011). Exercise training increases size of hippocampus and improves memory. *Proceedings of the National Academy of Sciences*, *108*(7), 3017-3022. doi: 10.1073/pnas.1015950108

Farquharson, S., Tournier, J.-D., Calamante, F., Fabinyi, G., Schneider-Kolsky, M., Jackson, G. D., & Connelly, A. (2013). White matter fiber tractography: why we need to move beyond DTI. *Journal of Neurosurgery*, *118*(6), 1367-1377. doi: 10.3171/2013.2.JNS121294

Fiorenzato, E., Biundo, R., Cecchin, D., Frigo, A., Kim, J., Weis, L., ... Antonini, A. (2018). Brain amyloid contribution to cognitive dysfunction in early-stage parkinson's disease: The ppmi dataset. *Journal of Alzheimer's disease : JAD*, *66*(1), 229-237. doi: 10.3233/JAD-180390

Fischl, B., Sereno, M. I., & Dale, A. M. (1999). Cortical surface-based analysis: Ii: Inflation, flattening, and a surface-based coordinate system. *NeuroImage*, *9*(2), 195-207. doi: 10.1006/nimg.1998.0396

Fodero-Tavoletti, M. T., Brockschnieder, D., Villemagne, V. L., Martin, L., Connor, A. R., Thiele, A., ... Cappai, R. (2012). In vitro characterization of [18F]-florbetaben, an Aβ imaging radiotracer. *Nuclear Medicine and Biology*, *39*(7), 1042-1048. doi: 10.1016/j.nucmedbio.2012.03.001

Forstmann, B. U., Anwander, A., Schäfer, A., Neumann, J., Brown, S., Wagenmakers, E.-J., ... Turner, R. (2010). Cortico-striatal connections predict control over speed and accuracy in perceptual decision making. *Proceedings of the National Academy of Sciences*, *107*(36), 15916-15920. doi: 10.1073/pnas.1004932107

Frazier, J. A., Chiu, S., Breeze, J. L., Makris, N., Lange, N., Kennedy, D. N., ... Biederman, J. (2005). Structural brain magnetic resonance imaging of limbic and thalamic volumes in pediatric bipolar disorder. *American Journal of Psychiatry*, *162*(7), 1256-1265.

FreeSurfer. (2017). *FreeSurfer analysis pipeline overview.* Retrieved 2020-01-19, from http://surfer.nmr.mgh.harvard.edu/fswiki/FreeSurferAnalysisPipelineOverview

Fripp, J., Bourgeat, P., Acosta, O., Raniga, P., Modat, M., Pike, K. E., ... Ourselin, S. (2008). Appearance modeling of 11C PiB PET images: Characterizing amyloid deposition in alzheimer's disease, mild cognitive impairment and healthy aging. *NeuroImage*, *43*(3), 430-439. doi: 10.1016/j.neuroimage.2008.07.053

Friston, K. J., Ashburner, J. T., Kiebel, S. J., Nichols, T. E., & Penny, W. D. (2007). *Statistical parametric mapping: the analysis of functional brain images* (First ed.). London, UK: Academic Press.

Gerrits, N. J. H. M., van Loenhoud, A. C., van den Berg, S. F., Berendse, H. W., Foncke, E. M. J., Klein, M., ... van den Heuvel, O. A. (2016). Cortical thickness, surface area and subcortical volume differentially contribute to cognitive heterogeneity in parkinson's disease. *PLOS ONE*, *11*(2), 1-14. doi: 10.1371/journal.pone.0148852

Goldman, J. G., Andrews, H., Amara, A., Naito, A., Alcalay, R. N., Shaw, L. M., ... Kang, U. J. (2018). Cerebrospinal fluid, plasma, and saliva in the biofind study: Relationships among biomarkers and parkinson's disease features. *Movement Disorders*, *33*(2), 282-288. doi: 10.1002/mds.27232

Goldstein, J. M., Seidman, L. J., Makris, N., Ahern, T., O'Brien, L. M., Caviness Jr, V. S., ... Tsuang, M. T. (2007). Hypothalamic abnormalities in schizophrenia: sex effects and genetic vulnerability. *Biological Psychiatry*, *61*(8), 935-945.

Gomperts, S. N., Locascio, J. J., Makaretz, S. J., Schultz, A., Caso, C., Vasdev, N., ... Johnson, K. (2016). Tau positron emission tomographic imaging in the lewy body diseases. *JAMA Neurology*, *73*(11), 1334-1341. doi: 10.1001/jamaneurol.2016.3338

Gomperts, S. N., Locascio, J. J., Marquie, M., Santarlasci, A. L., Rentz, D. M., Maye, J., ... Growdon, J. H. (2012). Brain amyloid and cognition in lewy body diseases. *Movement Disorders*, *27*(8), 965-973. doi: 10.1002/mds.25048

Gomperts, S. N., Locascio, J. J., Rentz, D., Santarlasci, A., Marquie, M., Johnson, K. A., & Growdon, J. H. (2013). Amyloid is linked to cognitive decline in patients with parkinson disease without dementia. *Neurology*, *80*(1), 85-91. doi: 10.1212/WNL.0b013e31827b1a07

Gomperts, S. N., Rentz, D. M., Moran, E., Becker, J. A., Locascio, J. J., Klunk, W. E., ... Johnson, K. A. (2008). Imaging amyloid deposition in lewy body diseases. *Neurology*, *71*(12), 903-910. doi: 10.1212/01.wnl.0000326146.60732.d6

Grinberg, L. T., Rueb, U., Alho, A. T., & Heinsen, H. (2010). Brainstem pathology and non-motor symptoms in PD. *Journal of the Neurological Sciences*, *289*(1–2), 81-88. doi: 10.1016/j.jns.2009.08.021

Hanganu, A., Monchi, O., & Modugno, N. (2016). Structural neuroimaging markers of cognitive decline in parkinson's disease. *Parkinson's disease, 2016*, 3217960. doi: 10.1155/2016/3217960

Hansen, A. K., Damholdt, M. F., Fedorova, T. D., Knudsen, K., Parbo, P., Ismail, R., ... Borghammer, P. (2017). In vivo cortical tau in parkinson's disease using 18F-AV-1451 positron emission tomography. *Movement Disorders*, *32*(6), 922-927. doi: 10.1002/mds.26961

Hardy, J., & De Strooper, B. (2017). Alzheimer's disease: where next for anti-amyloid therapies? *Brain*, *140*(4), 853-855. doi: 10.1093/brain/awx059

Harrison, J. R., & Owen, M. J. (2016). Alzheimer's disease: The amyloid hypothesis on trial. *British Journal of Psychiatry*, *208*(1), 1–3. doi: 10.1192/bjp.bp.115.167569

Hasselmo, M. E. (2006). The role of acetylcholine in learning and memory. *Current Opinion in Neurobiology*, *16*(6), 710-715. doi: 10.1016/j.conb.2006.09.002

Hattori, T., Orimo, S., Aoki, S., Ito, K., Abe, O., Amano, A., ... Mizusawa, H. (2012). Cognitive status correlates with white matter alteration in parkinson's disease. *Human Brain Mapping*, *33*(3), 727-739. doi: 10.1002/hbm.21245

Hely, M. A., Reid, W. G., Adena, M. A., Halliday, G. M., & Morris, J. G. (2008). The sydney multicenter study of parkinson's disease: the inevitability of dementia at 20 years. *Movement Disorders*, *23*(6), 837-844.

Hernan, M. A., Takkouche, B., Caamaño-Isorna, F., & Gestal-Otero, J. J. (2002). A meta-analysis of coffee drinking, cigarette smoking, and the risk of parkinson's disease: Coffee, smoking, and PD. *Annals of Neurology*, *52*(3), 276-284.

Herrup, K. (2015). The case for rejecting the amyloid cascade hypothesis. *Nature Neuroscience*, *18*, 794-9. doi: 10.1038/nn.4017

Hong, J. Y., Yun, H. J., Sunwoo, M. K., Ham, J. H., Lee, J.-M., Sohn, Y. H., & Lee, P. H. (2014). Cognitive and cortical thinning patterns of subjective cognitive decline in patients with and without parkinson's disease. *Parkinsonism & Related Disorders*, *20*(9), 999-1003. doi: 10.1016/j.parkreldis.2014.06.011

Huang, C., Mattis, P., Tang, C., Perrine, K., Carbon, M., & Eidelberg, D. (2007). Metabolic brain networks associated with cognitive function in parkinson's disease. *NeuroImage*, *34*(2), 714-723. doi: 10.1016/j.neuroimage.2006.09.003

Huang, C., Tang, C., Feigin, A., Lesser, M., Ma, Y., Pourfar, M., ... Eidelberg, D. (2007). Changes in network activity with the progression of parkinson's disease. *Brain*, *130*(7), 1834-1846. doi: 10.1093/brain/awm086

Huertas, I., Jesús, S., García-Gómez, F. J., Lojo, J. A., Bernal-Bernal, I., Bonilla-Toribio, M., ... Mir, P. (2017). Genetic factors influencing frontostriatal dysfunction and the development of dementia in parkinson's disease. *PLOS ONE*, *12*(4), 1-11. doi: 10.1371/journal.pone.0175560

Hughes, A., Daniel, S., Kilford, L., & Lees, A. (1992). Accuracy of clinical diagnosis of idiopathic parkinson's disease: a clinico-pathological study of 100 cases. *Journal of Neurology, Neurosurgery & Psychiatry*, *55*(3), 181-184.

Hui, E. S., Cheung, M. M., Chan, K. C., & Wu, E. X. (2010). B-value dependence of DTI quantitation and sensitivity in detecting neural tissue changes. *NeuroImage*, *49*(3), 2366-2374. doi: 10.1016/j.neuroimage.2009.10.022

Iriarte, A., Marabini, R., Matej, S., Sorzano, C., & Lewitt, R. (2016). System models for PET statistical iterative reconstruction: A review. *Computerized Medical Imaging and Graphics*, *48*, 30-48. Retrieved from http://www.sciencedirect.com/science/article/pii/S0895611115001901 doi: https://doi.org/10.1016/j.compmedimag.2015.12.003

Irwin, D. J., Lee, V. M.-Y., & Trojanowski, J. Q. (2013). Parkinson's disease dementia: convergence of α-synuclein, tau and amyloid-β pathologies. *Nature Reviews Neuroscience*, *14*(9), 626.

Irwin, D. J., Xie, S. X., Coughlin, D., Nevler, N., Akhtar, R. S., McMillan, C. T., ... Trojanowski, J. Q. (2018). CSF tau and β-amyloid predict cerebral synucleinopathy in autopsied lewy body disorders. *Neurology*, *90*(12), e1038-e1046.

J., S. D. (2018). Determinants of dopaminergic neuron loss in parkinson's disease. *The FEBS Journal*, *285*(19), 3657-3668. doi: 10.1111/febs.14607

Jack, C. R., Wiste, H. J., Weigand, S. D., Therneau, T. M., Lowe, V. J., Knopman, D. S., ... Petersen, R. C. (2017). Defining imaging biomarker cut points for brain aging and alzheimer's disease. *Alzheimer's & Dementia*, *13*(3), 205-216.

Jankovic, J. (2005). Searching for a relationship between manganese and welding and parkinson's disease. *Neurology*, *64*(12), 2021-2028. doi: 10.1212/01.WNL.0000166916.40902.63

Jeffrey, S. (2014). *Fda approves third amyloid PET tracer for alzheimer's disease.* http://www.medscape.com/viewarticle/822370. (Accessed: 2016-04-11)

Jellinger, K. (2012). Heterogenous mechanisms of mild cognitive impairment in parkinson's disease. *Journal of Neural Transmission*, *119*(3), 381-382. doi: 10.1007/s00702-011-0716-4

Jellinger, K. A. (2015). Neuropathobiology of non-motor symptoms in parkinson disease. *Journal of Neural Transmission*, *122*(10), 1429-1440. doi: 10.1007/s00702-015-1405-5

Jenkinson, M., Beckmann, C. F., Behrens, T. E. J., Woolrich, M. W., & Smith, S. M. (2012). Fsl. *NeuroImage*, *62*(2), 782-790. doi: 10.1016/j.neuroimage.2011.09.015.

Jenner, P., & Olanow, C. W. (1996). Oxidative stress and the pathogenesis of parkinson's disease. *Neurology*, *47*(6 Suppl 3), 161S-170S. doi: 10.1212/WNL.47.6_Suppl_3.161S

Jeurissen, B., Leemans, A., Tournier, J.-D., Jones, D. K., & Sijbers, J. (2013). Investigating the prevalence of complex fiber configurations in white matter tissue with diffusion magnetic resonance imaging. *Human Brain Mapping*, *34*(11), 2747-2766. doi: 10.1002/hbm.22099

Jolliffe, I. T. (2002). *Principal component analysis* (2nd ed.). New York: Springer.

Jones, A. J., Kuijer, R. G., Livingston, L., Myall, D., Horne, K., MacAskill, M., ... Dalrymple-Alford, J. C. (2017). Caregiver burden is increased in parkinson's disease with mild cognitive impairment (PD-MCI). *Translational Neurodegeneration*, *6*(1), 17.

Kalaitzakis, M., Graeber, M., Gentleman, S., & Pearce, R. (2008). Striatal β-amyloid deposition in parkinson disease with dementia. *Journal of Neuropathology and Experimental Neurology*, *67*(2), 155-161. doi: 10.1097/NEN.0b013e31816362aa

Kamagata, K., Motoi, Y., Abe, O., Shimoji, K., Hori, M., Nakanishi, A., ... Hattori, N. (2012). White matter alteration of the cingulum in parkinson disease with and without dementia: Evaluation by diffusion tensor tract–specific analysis. *American Journal of Neuroradiology*, *33*(5), 890-895. doi: 10.3174/ajnr.A2860

Kang, J. H. (2018). Cerebrospinal fluid amyloid β 1-42, tau, and alpha-synuclein predict the heterogeneous progression of cognitive dysfunction in parkinson's disease. *Journal of Movement Disorders*, *9*(2), 89. doi: 10.14802/jmd.16017

Kellner, E., Dhital, B., Kiselev, V. G., & Reisert, M. (2016). Gibbs-ringing artifact removal based on local subvoxel-shifts. *Magnetic Resonance in Medicine*, *76*(5), 1574-1581. doi: 10.1002/mrm.26054

Kim, H. M., Nazor, C., Zabetian, C. P., Quinn, J. F., Chung, K. A., Hiller, A. L., ... Cholerton, B. (2019). Prediction of cognitive progression in parkinson's disease using three cognitive screening measures. *Clinical Parkinsonism & Related Disorders*, *1*, 91-97. doi: 10.1016/j.prdoa.2019.08.006

Klein, C., & Westenberger, A. (2012). Genetics of parkinson's disease. *Cold Spring Harbor*

Perspectives in Medicine, *2*(1). doi: 10.1101/cshperspect.a008888

Klein, J., Eggers, C., Kalbe, E., Weisenbach, S., Hohmann, C., Vollmar, S., ... Hilker, R. (2010). Neurotransmitter changes in dementia with lewy bodies and parkinson disease dementia in vivo. *Neurology*, *74*(11), 885-892. doi: 10.1212/WNL .0b013e3181d55f61

Klunk, W. E., Engler, H., Nordberg, A., Wang, Y., Blomqvist, G., Holt, D. P., ... Långström, B. (2004). Imaging brain amyloid in alzheimer's disease with pittsburgh compound-b. *Annals of Neurology*, *55*(3), 306-319. doi: 10.1002/ana.20009

Klunk, W. E., Koeppe, R. A., Price, J. C., Benzinger, T. L., Devous, M. D., Jagust, W. J., ... Mintun, M. A. (2015). The centiloid project: Standardizing quantitative amyloid plaque estimation by PET. *Alzheimer's & Dementia*, *11*(1), 1-15. doi: 10.1016/j.jalz.2014.07.003

Kotzbauer, P., Tu, Z., & Mach, R. (2017). Current status of the development of PET radiotracers for imaging alpha synuclein aggregates in lewy bodies and lewy neurites. *Clinical and Translational Imaging*, *5*(1), 3-14. doi: 10.1007/s40336-016-0217-4

Kotzbauer, P. T., Cairns, N. J., Campbell, M. C., Willis, A. W., Racette, B. A., Tabbal, S. D., & Perlmutter, J. S. (2012). Pathologic accumulation of α-synuclein and Aβ in parkinson disease patients with dementia. *Archives of Neurology*, *69*(10), 1326-1331.

Kulisevsky, J., de Bobadilla, R. F., Pagonabarraga, J., Martíínez-Horta, S., Campolongo, A., García-Sánchez, C., ... Villa-Bonomo, C. (2013). Measuring functional impact of cognitive impairment: Validation of the parkinson's disease cognitive functional rating scale. *Parkinsonism & Related Disorders*, *19*(9), 812-817. doi: 10.1016/j.parkreldis.2013.05.007

Kurz, M., Alves, G., Aarsland, D., & Larsen, J. P. (2003). Familial parkinson's disease: a community-based study. *European Journal of Neurology*, *10*(2), 159-163. doi: 10.1046/j.1468-1331.2003.00532.x

Lanskey, J. H., McColgan, P., Schrag, A. E., Morris, H. R., Acosta-Cabronero, J., Rees, G., & Weil, R. S. (2018). Can neuroimaging predict dementia in parkinson's disease? *Brain*, *141*(9), 2545-2560. doi: 10.1093/brain/awy211

Lashley, T., Holton, J. L., Gray, E., Kirkham, K., O'Sullivan, S. S., Hilbig, A., ... Revesz, T. (2008). Cortical α-synuclein load is associated with amyloid-β plaque burden in a subset of parkinson's disease patients. *Acta Neuropathologica*, *115*(4), 417-425.

Lee, S., Cho, H., Choi, J., Lee, J., Ryu, Y., Lee, M., & Lyoo, C. (2018). Distinct patterns of amyloid-dependent tau accumulation in lewy body diseases. *Movement Disorders*, *33*(2), 262-272. doi: 10.1002/mds.27252

Leuzy, A., Chiotis, K., Lemoine, L., Gillberg, P.-G., Almkvist, O., Rodriguez-Vieitez, E., & Nordberg, A. (2019). Tau PET imaging in neurodegenerative tauopathies - still a challenge. *Molecular Psychiatry*, *24*(8), 1112-1134. doi: 10.1038/s41380-018-0342-8

Li, X., Li, W., Liu, G., Shen, X., & Tang, Y. (2015). Association between cigarette smoking and parkinson's disease: A meta-analysis. *Archives of Gerontology and Geriatrics*, *61*(3), 510.

Liepelt, I., Reimold, M., Maetzler, W., Godau, J., Reischl, G., Gaenslen, A., ... Berg, D. (2009). Cortical hypometabolism assessed by a metabolic ratio in parkinson's disease

primarily reflects cognitive deterioration - [18F]FDG-PET. *Movement Disorders*, *24*(10), 1504-1511. doi: 10.1002/mds/22662

Lin, C., Bernstein, M., Huston, J., & Fain, S. (2001). Measurements of T1 relaxation times at 3.0T: Implications for clinical MRA. *Proceedings of the 9th Annual Meeting of ISMRM*, *9*, 1391.

Liston, C., Watts, R., Tottenham, N., Davidson, M. C., Niogi, S., Ulug, A. M., & Casey, B. (2005). Frontostriatal Microstructure Modulates Efficient Recruitment of Cognitive Control. *Cerebral Cortex*, *16*(4), 553-560. doi: 10.1093/cercor/bhj003

Litvan, I., Goldman, J. G., Tröster, A. I., Schmand, B. A., Weintraub, D., Petersen, R. C., ... Emre, M. (2012). Diagnostic criteria for mild cognitive impairment in parkinson's disease: Movement disorder society task force guidelines. *Movement Disorders*, *27*(3), 349-356. doi: 10.1002/mds.24893

Ma, Y., Tang, C., Spetsieris, P. G., Dhawan, V., & Eidelberg, D. (2007). Abnormal metabolic network activity in parkinson's disease: test-retest reproducibility. *Journal of Cerebral Blood Flow and Metabolism*, *27*(3), 597-605. doi: 10.1038/sj.jcbfm.9600358

Macphee, G. J. A., & Stewart, D. A. (2012). Parkinson's disease: treatment and non-motor features. *Reviews in Clinical Gerontology*, *22*, 243-260. doi: 10.1017/S0959259812000093

Mak, E., Su, L., Williams, G. B., Firbank, M. J., Lawson, R. A., Yarnall, A. J., ... O'Brien, J. T. (2015). Baseline and longitudinal grey matter changes in newly diagnosed Parkinson's disease: ICICLE-PD study. *Brain*, *138*(10), 2974-2986. doi: 10.1093/brain/awv211

Mak, E., Zhou, J., Tan, L. C. S., Au, W. L., Sitoh, Y. Y., & Kandiah, N. (2014). Cognitive deficits in mild parkinson's disease are associated with distinct areas of grey matter atrophy. *Journal of Neurology, Neurosurgery & Psychiatry*, *85*(5), 576-580. doi: 10.1136/jnnp-2013-305805

Makris, N., Goldstein, J. M., Kennedy, D., Hodge, S. M., Caviness, V. S., Faraone, S. V., ... Seidman, L. J. (2006). Decreased volume of left and total anterior insular lobule in schizophrenia. *Schizophrenia Research*, *83*(2-3), 155-171.

Malhotra, A., Sepehrizadeh, T., Dhollander, T., Wright, D., Castillo-Melendez, M., Sutherland, A. E., ... Miller, S. L. (2019). Advanced MRI analysis to detect white matter brain injury in growth restricted newborn lambs. *NeuroImage: Clinical*, *24*, 101991. doi: 10.1016/j.nicl.2019.101991

Mao, P., & Reddy, P. H. (2011). Aging and amyloid beta-induced oxidative dna damage and mitochondrial dysfunction in alzheimer's disease: Implications for early intervention and therapeutics. *Biochimica et Biophysica Acta (BBA) - Molecular Basis of Disease*, *1812*(11), 1359-1370. doi: https://doi.org/10.1016/j.bbadis.2011.08.005

Marsh, S., & Blurton-Jones, M. (2012). Examining the mechanisms that link β-amyloid and α-synuclein pathologies. *Alzheimer's Research & Therapy*, *4*(2). doi: 10.1186/alzrt109

Mashima, K., Ito, D., Kameyama, M., Osada, T., Tabuchi, H., Nihei, Y., ... Suzuki, N. (2017). Extremely low prevalence of amyloid positron emission tomography positivity in parkinson's disease without dementia. *European Neurology*, *77*(5-6),

231-237. doi: 10.1159/000464322

Mata, I. F., Leverenz, J. B., Weintraub, D., Trojanowski, J. Q., Hurtig, H. I., Van Deerlin, V. M., ... Zabetian, C. P. (2014). APOE, MAPT, and SNCA Genes and Cognitive Performance in Parkinson Disease. *JAMA Neurology*, *71*(11), 1405-1412. doi: 10.1001/jamaneurol.2014.1455

Mathis, C. A., Lopresti, B. J., Ikonomovic, M. D., & Klunk, W. E. (2017). Small-molecule PET tracers for imaging proteinopathies. *Seminars in Nuclear Medicine*, *47*(5), 553-575. doi: 10.1053/j.semnuclmed.2017.06.003

Mattsson, N., Tosun, D., Insel, P. S., Simonson, A., Jack, C. R., Beckett, L. A., ... Weiner, M. W. (2014). Association of brain amyloid-β with cerebral perfusion and structure in alzheimer's disease and mild cognitive impairment. *Brain*, *137*(Pt 5), 1550-1561. doi: 10.1093/brain/awu043

Mazziotta, J., Toga, A., Evans, A., Fox, P., Lancaster, J., Zilles, K., ... Mazoyer, B. (2001). A probabilistic atlas and reference system for the human brain: International consortium for brain mapping (icbm). *Philosophical Transactions of the Royal Society of London*, *356*(1412), 1293-1322. doi: 10.1098/rstb.2001.0915

McMillan, C. T., & Wolk, D. A. (2016). Presence of cerebral amyloid modulates phenotype and pattern of neurodegeneration in early parkinson's disease. *Journal of Neurology, Neurosurgery & Psychiatry*, *87*(10), 1112-1122. doi: 10.1136/jnnp-2015-312690

McRobbie, D. W., Moore, E. A., Graves, M. J., & Prince, M. R. (2002). *MRI: From picture to proton* (2nd ed.). New York, USA: Cambridge University Press.

Melzer, T. R. (2011). *Magnetic resonance imaging of cognition in parkinson's disease* (Unpublished doctoral dissertation). University of Otago, Christchurch, New Zealand.

Melzer, T. R., Stark, M. R., Keenan, R. J., Myall, D. J., MacAskill, M. R., Pitcher, T. L., ... Anderson, T. J. (2019). Beta amyloid deposition is not associated with cognitive impairment in parkinson's disease. *Frontiers in Neurology*, *10*, 391. doi: 10.3389/fneur.2019.00391

Melzer, T. R., Watts, R., MacAskill, M. R., Pearson, J. F., Rüeger, S., Pitcher, T. L., ... Anderson, T. J. (2011). Arterial spin labelling reveals an abnormal cerebral perfusion pattern in parkinson's disease. *Brain*, *134*(3), 845-855. doi: 10.1093/brain/awq377

Melzer, T. R., Watts, R., MacAskill, M. R., Pitcher, T. L., Livingston, L., Keenan, R. J., ... Anderson, T. J. (2012). Grey matter atrophy in cognitively impaired parkinson's disease. *Journal of Neurology, Neurosurgery & Psychiatry*, *83*(2), 188-194. doi: 10.1136/jnnp-2011-300828

Melzer, T. R., Watts, R., MacAskill, M. R., Pitcher, T. L., Livingston, L., Keenan, R. J., ... Anderson, T. J. (2013). White matter microstructure deteriorates across cognitive stages in parkinson disease. *Neurology*, *80*(20), 1841-1849. doi: 10.1212/WNL.0b013e3182929f62

Mergenthaler, P., Lindauer, U., Dienel, G. A., & Meisel, A. (2013). Sugar for the brain: the role of glucose in physiological and pathological brain function. *Trends in Neurosciences*, *36*(10), 587-597. doi: 10.1016/j.tins.2013.07.001

Meyer, J. S., Rauch, G., Rauch, R. A., & Haque, A. (2000). Risk factors for cerebral hypoperfusion, mild cognitive impairment, and dementia. *Neurobiology of Aging*,

21(2), 161-169. doi: 10.1016/S0197-4580(00)00136-6

Mito, R., Raffelt, D., Dhollander, T., Vaughan, D. N., Tournier, J.-D., Salvado, O., ... Connelly, A. (2018). Fibre-specific white matter reductions in Alzheimer's disease and mild cognitive impairment. *Brain*, *141*(3), 888-902. doi: 10.1093/brain/awx355

Mor, D. E., & Ischiropoulos, H. (2018). The convergence of dopamine and α-synuclein: Implications for parkinson's disease. *Journal of Experimental Neuroscience*, *12*. doi: 10.1177/1179069518761360

Mormina, E., Longo, M., Arrigo, A., Alafaci, C., Tomasello, F., Calamuneri, A., ... Granata, F. (2015). MRI tractography of corticospinal tract and arcuate fasciculus in high-grade gliomas performed by constrained spherical deconvolution: Qualitative and quantitative analysis. *American Journal of Neuroradiology*, *36*(10), 1853-1858. doi: 10.3174/ajnr.A4368

Moses, W. W. (2011). Fundamental limits of spatial resolution in PET. *Nuclear Instruments & Methods in Physics Research*, *648*(Supplement 1), S236-S240. doi: 10.1016/j.nima.2010.11.092

Myall, D., Pitcher, T., Pearson, J., Dalrymple-Alford, J., Anderson1, T., & MacAskill, M. (2017). Parkinson's in the oldest old: impact on estimates of future disease burden. *Parkinsonism & Related Disorders*, *42*, 78-84. doi: 10.1016/j.parkreldis.2017.06.018

Nestor, P. J., Fryer, T. D., Smielewski, P., & Hodges, J. R. (2003). Limbic hypometabolism in alzheimer's disease and mild cognitive impairment. *Annals of Neurology*, *54*(3), 343-351. doi: 10.1002/ana.10669

Niccolini, F., Su, P., & Politis, M. (2014). Dopamine receptor mapping with PET imaging in parkinson's disease. *Journal of Neurology*, *261*(12), 2251-2263.

Nishio, Y., Ishii, K., Kazui, H., Hosokai, Y., & Mori, E. (2007). Frontal-lobe syndrome and psychosis after damage to the brainstem dopaminergic nuclei. *Journal of the Neurological Sciences*, *260*(1), 271-274. doi: 10.1016/j.jns.2007.04.021

Nombela, C., Rowe, J. B., Winder-Rhodes, S. E., Hampshire, A., Owen, A. M., Breen, D. P., ... Barker, R. A. (2014). Genetic impact on cognition and brain function in newly diagnosed Parkinson's disease: ICICLE-PD study. *Brain*, *137*(10), 2743-2758. doi: 10.1093/brain/awu201

Nordberg, A. (2004). PET imaging of amyloid in alzheimer's disease. *The Lancet Neurology*, *3*(9), 519-527. doi: 10.1016/S1474-4422(04)00853-1

Oishi, K., Zilles, K., Amunts, K., Faria, A., Jiang, H., Li, X., ... Mori, S. (2008). Human brain white matter atlas: Identification and assignment of common anatomical structures in superficial white matter. *NeuroImage*, *43*(3), 447-457. doi: 10.1016/j.neuroimage.2008.07.009

Okamura, N., Harada, R., Ishiki, A., Kikuchi, A., Nakamura, T., & Kudo, Y. (2018). The development and validation of tau PET tracers: current status and future directions. *Clinical and Translational Imaging*, *6*(4), 305-316. doi: 10.1007/s40336-018-0290-y

Ossenkoppele, R., Jansen, W. J., Rabinovici, G. D., Knol, D. L., van der Flier, W. M., van Berckel, B. N. M., ... the Amyloid PET Study Group (2015). Prevalence of Amyloid PET Positivity in Dementia Syndromes: A Meta-analysis. *The Journal*

of the American Medical Association, *313*(19), 1939-1950. doi: 10.1001/jama.2015.4669

Pankratz, N., Byder, L., Halter, C., Rudolph, A., Shults, C. W., Conneally, P. M., ... Nichols, W. C. (2006). Presence of an APOE4 allele results in significantly earlier onset of parkinson's disease and a higher risk with dementia. *Movement Disorders*, *21*(1), 45-49. doi: 10.1002/mds.20663

Parkinson, J. (2002). An essay on the shaking palsy. 1817. *The Journal of Neuropsychiatry and Clinical Neurosciences*, *14*(2), 223-236. doi: 10.1176/jnp.14.2.223

Pascoal, T. A., Mathotaarachchi, S., Shin, M., Benedet, A. L., Mohades, S., Wang, S., ... Rosa-Neto, P. (2017). Synergistic interaction between amyloid and tau predicts the progression to dementia. *Alzheimer's & Dementia*, *13*(6), 644-653. doi: https://doi.org/10.1016/j.jalz.2016.11.005

Petrou, M., Bohnen, N., Müller, M., Koeppe, R., Albin, R., & Frey, K. (2012). Aβ-amyloid deposition in patients with parkinson disease at risk for development of dementia. *Neurology*, *79*(11), 1161-1167. doi: 10.1212/WNL.0b013e3182698d4a

Petrou, M., Dwamena, B. A., Foerster, B. R., MacEachern, M. P., Bohnen, N. I., Müller, M. L., ... Frey, K. A. (2015). Amyloid deposition in parkinson's disease and cognitive impairment: A systematic review. *Movement Disorders*, *30*(7), 928-935. doi: 10.1002/mds.26191

Petrovitch, H., Ross, G. W., Abbott, R. D., Sanderson, W. T., Sharp, D. S., Tanner, C. M., ... White, L. R. (2002). Plantation Work and Risk of Parkinson Disease in a Population-Based Longitudinal Study. *Archives of Neurology*, *59*(11), 1787-1792. doi: 10.1001/archneur.59.11.1787

Piechnik, S., Evans, J., Bary, L., Wise, R., & Jezzard, P. (2009). Functional changes in CSF volume estimated using measurement of water T2 relaxation. *Magnetic Resonance in Medicine*, *61*(3), 579-586. doi: 10.1002/mrm.21897

Pipe, J. (2009). Pulse sequences for diffusion-weighted MRI. In *Diffusion MRI* (p. 11-35). Academic Press.

Poldrack, R. A., Baker, C. I., Durnez, J., Gorgolewski, K. J., Matthews, P. M., Munafó, M. R., ... Yarkoni, T. (2017). Scanning the horizon: towards transparent and reproducible neuroimaging research. *Nature Reviews Neuroscience*, *18*(2), 115-126. doi: 10.1038/nrn.2016.167

Postuma, R. B., Berg, D., Stern, M., Poewe, W., Olanow, C. W., Oertel, W., ... Deuschl, G. (2015). MDS clinical diagnostic criteria for parkinson's disease. *Movement Disorders*, *30*(12), 1591-1601. doi: 10.1002/mds.26424

Pozorski, V., Oh, J. M., Adluru, N., Merluzzi, A. P., Theisen, F., Okonkwo, O., ... Gallagher, C. L. (2018). Longitudinal white matter microstructural change in parkinson's disease. *Human Brain Mapping*, *39*(10), 4150-4161. doi: 10.1002/hbm.24239

Raffelt, D., Smith, R., Ridgway, G., Tournier, J.-D., Vaughan, D., Rose, S., ... Connelly, A. (2015). Connectivity-based fixel enhancement: Whole-brain statistical analysis of diffusion MRI measures in the presence of crossing fibres. *NeuroImage*, *11*. doi: 10.1016/j.neuroimage.2015.05.039

Raffelt, D., Tournier, J.-D., Crozier, S., Connelly, A., & Salvado, O. (2012). Reorientation

of fiber orientation distributions using apodized point spread functions. *Magnetic Resonance in Medicine*, *67*(3), 844-855. doi: 10.1002/mrm.23058

Raffelt, D., Tournier, J.-D., Fripp, J., Crozier, S., Connelly, A., & Salvado, O. (2011). Symmetric diffeomorphic registration of fibre orientation distributions. *NeuroImage*, *56*(3), 1171-1180. doi: 10.1016/j.neuroimage.2011.02.014

Raffelt, D., Tournier, J.-D., Rose, S., Ridgway, G. R., Henderson, R., Crozier, S., ... Connelly, A. (2012). Apparent fibre density: A novel measure for the analysis of diffusion-weighted magnetic resonance images. *NeuroImage*, *59*(4), 3976-3994. doi: 10.1016/j.neuroimage.2011.10.045

Raffelt, D. A., Tournier, J.-D., Smith, R. E., Vaughan, D. N., Jackson, G., Ridgway, G. R., & Connelly, A. (2016). Investigating white matter fibre density and morphology using fixel-based analysis. *NeuroImage*, *144*, 58-73. doi: 10.1016/j.neuroimage.2016.09.029

Rajapakse, J., Giedd, J., & Rapoport, J. (1997). Statistical approach to segmentation of single-channel cerebral mr images. *IEEE Transactional Medical Imaging*, *16*(2), 176-186. doi: 10.1109/42.563663

Rau, Y.-A., Wang, S.-M., Tournier, J.-D., Lin, S.-H., Lu, C.-S., Weng, Y.-H., ... Wang, J.-J. (2019). A longitudinal fixel-based analysis of white matter alterations in patients with parkinson's disease. *NeuroImage: Clinical*, *24*, 102098. doi: 10.1016/j.nicl.2019.102098

Razifar, P., Muhammed, H. H., Engbrant, F., Svensson, P., Olsson, J., Bengtsson, E., ... Bergström, M. (2009). Performance of principal component analysis and independent component analysis with respect to signal extraction from noisy positron emission tomography data - a study on computer simulated images. *The Open Neuroimaging Journal*, *3*, 1-16. doi: 10.2174/1874440000903010001

Ringnèr, M. (2008). What is principal component analysis? *Nature Biotechnology*, *26*(3), 303-304. doi: 10.1038/nbt0308-303

Roberts, H. L., & Brown, D. R. (2015). Seeking a mechanism for the toxicity of oligomeric α-synuclein. *Biomolecules*, *5*, 282-305. doi: 10.3390/biom5020282

Roberts, R. E., Anderson, E. J., & Husain, M. (2010). Expert cognitive control and individual differences associated with frontal and parietal white matter microstructure. *Journal of Neuroscience*, *30*(50), 17063-17067. doi: 10.1523/JNEUROSCI.4879-10.2010

Roberts, R. E., Anderson, E. J., & Husain, M. (2013). White matter microstructure and cognitive function. *The Neuroscientist*, *19*(1), 8-15. doi: 10.1177/1073858411421218

Robin, X., Turck, N., Hainard, A., Tiberti, N., Lisacek, F., Sanchez, J.-C., & Müller, M. (2011). proc: An open-source package for r and s+ to analyze and compare roc curves. *BMC Bioinformatics*, *12*. doi: 10.1186/1471-2105-12-77

Rowe, C., Ellis, K., Rimajova, M., Bourgeat, P., Pike, K., Jones, G., ... Villemagne, V. (2010). Amyloid imaging results from the australian imaging, biomarkers and lifestyle (aibl) study of aging. *Neurobiology of Aging*, *31*(8), 1275-1283. doi: 10.1016/j.neurobiolaging.2010.04.007

Rowe, C. C., Doré, V., Jones, G., Baxendale, D., Mulligan, R. S., Bullich, S., ... Villemagne, V. L. (2017). 18F-florbetaben PET beta-amyloid binding expressed in centiloids. *European Journal of Nuclear Medicine and Molecular Imaging*, *44*(12), 2053-2059. doi: 10.1007/s00259-017-3749-6

Rullmann, M., Dukart, J., Hoffmann, K.-T., Luthardt, J., Tiepolt, S., Patt, M., ... Barthel, H. (2016). Partial-volume effect correction improves quantitative analysis of 18F-florbetaben β-amyloid PET scans. *Journal of Nuclear Medicine*, *57*(2), 198-203. doi: 10.2967/jnumed.115.161893

S., B., Villemagne, V. L., Catafau, A. M., Jovalekic, A., Koglin, N., Rowe, C. C., & De Santi, S. (2017). Optimal reference region to measure longitudinal amyloid-β change with 18F-florbetaben PET. *Journal of Nuclear Medicine*, *58*(8), 1300-1306. doi: 10.2967/jnumed.116.187351

Sabbagh, M. N., Adler, C. H., Lahti, T. J., Connor, D. J., Vedders, L., Peterson, L. K., ... Beach, T. G. (2009). Parkinson's disease with dementia: comparing patients with and without alzheimer pathology. *Alzheimer Disease and Associated Disorders*, *23*(3), 295.

Sabri, O., Sabbagh, M. N., Seibyl, J., Barthel, H., Akatsu, H., Ouchi, Y., ... Schulz-Schaeffer, W. J. (2015). Florbetaben PET imaging to detect amyloid beta plaques in alzheimer's disease: phase 3 study. *Alzheimer's & Dementia*, *11*(8), 964-974.

Sabri, O., Seibyl, J., Rowe, C., & Barthel, H. (2015). Beta-amyloid imaging with florbetaben. *Clinical and Translational Imaging*, *3*(1), 13-26. doi: 10.1007/s40336-015-0102-6

Saha, G. (2015). *Basics of PET imaging: Physics, chemistry, and regulations*. Springer International Publishing. Retrieved from https://books.google.co.nz/books?id=_pp6CwAAQBAJ

Salvadó, G., Molinuevo, J. L., Brugulat-Serrat, A., Falcon, C., Grau-Rivera, O., Suárez-Calvet, M., ... Gispert, J. D. (2019). Centiloid cut-off values for optimal agreement between PET and CSF core AD biomarkers. *Alzheimer's Research & Therapy*, *11*(1), 27. doi: 10.1186/s13195-019-0478-z

Scatton, B., Javoy-Agid, F., Rouquier, L., Dubois, B., & Agid, Y. (1983). Reduction of cortical dopamine, noradrenaline, serotonin and their metabolites in parkinson's disease. *Brain Research*, *275*(2), 321-328. doi: 10.1016/0006-8993(83)90993-9

Segura, B., Baggio, H. C., Marti, M. J., Valldeoriola, F., Compta, Y., Garcia-Diaz, A. I., ... Junque, C. (2014). Cortical thinning associated with mild cognitive impairment in parkinson's disease. *Movement Disorders*, *29*(12), 1495-1503. doi: 10.1002/mds.25982

Segura-Aguilar, J., Paris, I., Muñoz, P., Ferrari, E., Zecca, L., & Zucca, F. A. (2014). Protective and toxic roles of dopamine in parkinson's disease. *Journal of Neurochemistry*, *129*(6), 898-915. doi: 10.1111/jnc.12686

Seibyl, J., Catafau, A., Barthel, H., Ishii, K., Rowe, C., Leverenz, J., ... Sabri, O. (2016). Impact of training method on the robustness of the visual assessment of 18F-florbetaben PET scans: Results from a phase-3 study. *Journal of Nuclear Medicine*, *57*(6), 900-906. doi: 10.2967/jnumed.115.161927

Sergeant, N., Delacourte, A., & Buée, L. (2005). Tau protein as a differential biomarker

of tauopathies. *Biochimica et Biophysica Acta (BBA) - Molecular Basis of Disease*, *1739*(2), 179-197. doi: 10.1016/j.bbadis.2004.06.020

Shah, N., Frey, K. A., LTM Müller, M., Petrou, M., Kotagal, V., Koeppe, R. A., ... Bohnen, N. I. (2016). Striatal and c ortical β-a myloidopathy and c ognition in p arkinson's d isease. *Movement Disorders*, *31*(1), 111-117.

Siderowf, A., Xie, S., Hurtig, H., Weintraub, D., Duda, J., Chen-Plotkin, A., ... Clark, C. (2010). CSF amyloid β 1-42 predicts cognitive decline in parkinson disease. *Neurology*, *75*(12), 1055-1061.

Smid, S. C., McNeish, D., Miočević, M., & van de Schoot, R. (2020). Bayesian versus frequentist estimation for structural equation models in small sample contexts: A systematic review. *Structural Equation Modeling: A Multidisciplinary Journal*, *27*(1), 131-161. doi: 10.1080/10705511.2019.1577140

Smith, R. E., Tournier, J.-D., Calamante, F., & Connelly, A. (2013). Sift: Spherical-deconvolution informed filtering of tractograms. *NeuroImage*, *67*, 298-312. doi: 10.1016/j.neuroimage.2012.11.049

Smith, S. M. (2002). Fast robust automated brain extraction. *Human Brain Mapping*, *17*(3), 143-155. doi: 10.1002/hbm.10062

Stanisz, G. J., Odrobina, E. E., Pun, J., Escaravage, M., Graham, S. J., Bronskill, M. J., & Henkelman, R. M. (2005). T1, T2 relaxation and magnetization transfer in tissue at 3T. *Magnetic Resonance in Medicine*, *54*(3), 507-512. doi: 10.1002/mrm.20605

Stelzer, J., Chen, Y., & Turner, R. (2013). Statistical inference and multiple testing correction in classification-based multi-voxel pattern analysis (MVPA): Random permutations and cluster size control. *NeuroImage*, *65*, 69-82. doi: 10.1016/j.neuroimage.2012.09.063

Sterling, N. W., Du, G., Lewis, M. M., Swavely, S., Kong, L., Styner, M., & Huang, X. (2017). Cortical gray and subcortical white matter associations in parkinson's disease. *Neurobiology of Aging*, *49*, 100-108. doi: 10.1016/j.neurobiolaging.2016.09.015

Su, Y., Flores, S., Hornbeck, R. C., Speidel, B., Vlassenko, A. G., Gordon, B. A., ... Benzinger, T. L. (2018). Utilizing the centiloid scale in cross-sectional and longitudinal PiB PET studies. *NeuroImage: Clinical*, *19*, 406-416.

Surti, S. (2015). Update on time-of-flight PET imaging. *Journal of Nuclear Medicine: Official Publication of the Society of Nuclear Medicine*, *56*(1), 98-105. doi: 10.2967/jnumed.114.145029

Swanson, C. J., Zhang, Y., Dhadda, S., Wang, J., Kaplow, J., Lai, R. Y. K., ... Luthman, J. (2018). Treatment of early AD subjects with BAN2401, an anti-Aβ protofibril monoclonal antibody, significantly clears amyloid plaque and significantly reduces clinical decline. *Alzheimer's & Dementia: The Journal of the Alzheimer's Association*, *14*(7). doi: 10.1016/j.jalz.2018.07.009

Tachibana, M., Holm, M.-L., Liu, C.-C., Shinohara, M., Aikawa, T., Oue, H., ... Kanekiyo, T. (2019). APOE4-mediated amyloid-β pathology depends on its neuronal receptor lrp1. *The Journal of Clinical Investigation*, *129*(3), 1272-1277. doi: 10.1172/JCI124853

Taylor, K. S. M., Cook, J. A., & Counsell, C. E. (2007). Heterogeneity in male to female risk for parkinson's disease. *Journal of Neurology, Neurosurgery & Psychiatry*, *78*(8), 905-906. doi: 10.1136/jnnp.2006.104695

Tiepolt, S., Barthel, H., Butzke, D., Hesse, S., Patt, M., Gertz, H.-J., ... Sabri, O. (2012). Influence of scan duration on the accuracy of β-amyloid PET with florbetaben in patients with alzheimer's disease and healthy volunteers. *European Journal of Nuclear Medicine and Molecular Imaging*, *40*(2), 238-244. doi: 10.1007/s00259-012-2268-8

Tohka, J., Zijdenbos, A., & Evans, A. (2004). Fast and robust parameter estimation for statistical partial volume models in brain MRI. *NeuroImage*, *23*, 84-97. doi: 10.1016/j.neuroimage.2004.05.007

Toledo, J. B., Gopal, P., Raible, K., Irwin, D. J., Brettschneider, J., Sedor, S., ... Trojanowski, J. Q. (2016). Pathological α-synuclein distribution in subjects with coincident alzheimer's and lewy body pathology. *Acta Neuropathologica*, *131*(3), 393-409. doi: 10.1007/s00401-015-1526-9

Tournier, J. D. (2004). The biophysics of crossing fibres. In D. K. Jones (Ed.), *Diffusion MRI: Theory, Methods, and Application* (p. 465-481). Oxford; New York: Oxford University Press.

Tournier, J.-D., Calamante, F., & Connelly, A. (2007). Robust determination of the fibre orientation distribution in diffusion MRI: Non-negativity constrained super-resolved spherical deconvolution. *NeuroImage*, *35*(4), 1459-1472. doi: 10.1016/j.neuroimage.2007.02.016

Tournier, J.-D., Smith, R., Raffelt, D., Tabbara, R., Dhollander, T., Pietsch, M., ... Connelly, A. (2019). Mrtrix3: A fast, flexible and open software framework for medical image processing and visualisation. *NeuroImage*, *202*, 116137. doi: 10.1016/j.neuroimage.2019.116137

Tuch, D. S., Salat, D. H., Wisco, J. J., Zaleta, A. K., Hevelone, N. D., & Rosas, H. D. (2005). Choice reaction time performance correlates with diffusion anisotropy in white matter pathways supporting visuospatial attention. *Proceedings of the National Academy of Sciences*, *102*(34), 12212-12217. doi: 10.1073/pnas.0407259102

Tustison, N. J., Avants, B. B., Cook, P. A., Zheng, Y., Egan, A., Yushkevich, P. A., & Gee, J. C. (2010). N4itk: Improved n3 bias correction. *IEEE Transactions on Medical Imaging*, *29*(6), 1310-1320.

van der Hoek, T. C., Bus, B. A., Matui, P., van der Marck, M. A., Esselink, R. A., & Tendolkar, I. (2011). Prevalence of depression in parkinson's disease: Effects of disease stage, motor subtype and gender. *Journal of the Neurological Sciences*, *310*(1–2), 220-224. doi: 10.1016/j.jns.2011.07.007

Varoquaux, G. (2018). Cross-validation failure: Small sample sizes lead to large error bars. *NeuroImage*, *180*, 68-77. doi: 10.1016/j.neuroimage.2017.06.061

Vehtari, A., Gelman, A., & Gabry, J. (2016). Practical bayesian model evaluation using leave-one-out cross-validation and waic. *Statistics and Computing*, *27*(5), 1413–1432. doi: 10.1007/s11222-016-9696-4

Vehtari, A., Gelman, A., & Gabry, J. (2017). Practical bayesian model evaluation using leave-one-out cross-validation and waic. *Statistics and Computing*, *27*(5), 1413-1432.

Vehtari, A., Simpson, D., Gelman, A., Yao, Y., & Gabry, J. (2015). *Pareto smoothed importance sampling.*

Vennart, N. J., Bird, N., Buscombe, J., Cheow, H. K., Nowosinska, E., & Heard, S. (2017). Optimization of PET/CT image quality using the GE 'Sharp IR' point-spread function reconstruction algorithm. *Nuclear Medicine Communications*, *38*(6), 471-479. doi: 10.1097/MNM.0000000000000669

Veraart, J., Fieremans, E., & Novikov, D. S. (2016). Diffusion MRI noise mapping using random matrix theory. *Magnetic Resonance in Medicine*, *76*(5), 1582-1593. doi: 10.1002/mrm.26059

Veraart, J., Novikov, D. S., Christiaens, D., Ades-aron, B., Sijbers, J., & Fieremans, E. (2016). Denoising of diffusion MRI using random matrix theory. *NeuroImage*, *142*, 394-406. doi: 10.1016/j.neuroimage.2016.08.016

Villain, N. N. (2012). Regional dynamics of amyloid-β deposition in healthy elderly, mild cognitive impairment and alzheimer's disease: a voxelwise PiB-PET longitudinal study. *Brain*, *135*(7), 2126-2139. doi: 10.1093/brain/aws125

Villemagne, V. L., Mulligan, R. S., Pejoska, S., Ong, K., Jones, G., O'Keefe, G., ... Rowe, C. C. (2012). Comparison of 11C-PiB and 18F-florbetaben for Aβ imaging in ageing and alzheimer's disease. *European Journal of Nuclear Medicine and Molecular Imaging*, *39*(6), 983-989. doi: 10.1007/s00259-012-2088-x

Villemagne, V. L., Pike, K. E., Chételat, G., Ellis, K. A., Mulligan, R. S., Bourgeat, P., ... Rowe, C. C. (2011). Longitudinal assessment of Aβ and cognition in aging and alzheimer disease. *Annals of Neurology*, *69*(1), 181-192. doi: 10.1002/ana.22248

von Campenhausen, S., Bornschein, B., Wick, R., Bötzel, K., Sampaio, C., Poewe, W., ... Dodel, R. (2005). Prevalence and incidence of parkinson's disease in europe. *European Neuropsychopharmacology*, *15*(4), 473-490. doi: 10.1016/j.euroneuro.2005.04.007

Wang, Y., & Mandelkow, E. (2015). Tau in physiology and pathology. *Nature Reviews Neuroscience*, *17*, 22-35. doi: 10.1038/nrn.2015.1

Wang, Y. T., & Edison, P. (2019). Tau imaging in neurodegenerative diseases using positron emission tomography. *Current Neurology and Neuroscience Reports*, *19*(7). doi: 10.1007/s11910-019-0962-7

Williams-Gray, C. H., Goris, A., Saiki, M., Foltynie, T., Compston, D. A. S., Sawcer, S. J., & Barker, R. A. (2009). Apolipoprotein e genotype as a risk factor for susceptibility to and dementia in parkinson's disease. *Journal of Neurology*, *256*(3), 493-498. doi: 10.1007/s00415-009-0119-8

Winer, J. R., Maass, A., Pressman, P., Stiver, J., Schonhaut, D. R., Baker, S. L., ... Jagust, W. J. (2018). Associations between tau, β-amyloid, and cognition in parkinson disease. *JAMA Neurology*, *75*(2), 227-235. doi: 10.1001/jamaneurol.2017.3713

Winkler, A. M., Ridgway, G. R., Webster, M. A., Smith, S. M., & Nichols, T. E. (2014). Permutation inference for the general linear model. *NeuroImage*, *92*, 381-397. doi: 10.1016/j.neuroimage.2014.01.060

Wood, K.-L., Myall, D. J., Livingston, L., Melzer, T. R., Pitcher, T. L., MacAskill, M. R., ... Dalrymple-Alford, J. C. (2016). Different PD-MCI criteria and risk of dementia

in parkinson's disease: 4-year longitudinal study. *NPJ Parkinson's Disease*, *2*. doi: 10.1038/npjparkd.2015.27

Xie, S., Zuo, N., Shang, L., Song, M., Fan, L., & Jiang, T. (2015). How does b-value affect hardi reconstruction using clinical diffusion MRI data? *PLOS ONE*, *10*(3), 1-19. doi: 10.1371/journal.pone.0120773

Ye, F. Q., Berman, K. F., Ellmore, T., Esposito, G., van Horn, J. D., Yang, Y., ... McLaughlin, A. C. (2000). $H_2{}^{15}O$ PET validation of steady-state arterial spin tagging cerebral blood flow measurements in humans. *Magnetic Resonance in Medicine*, *44*(3), 450-456. doi: 10.1002/1522-2594(200009)44:3⟨450::AID-MRM16⟩3.0.CO;2-0

Zarei, M., Ibarretxe-Bilbao, N., Compta, Y., Hough, M., Junque, C., Bargallo, N., ... Martí, M. J. (2013). Cortical thinning is associated with disease stages and dementia in parkinson's disease. *Journal of Neurology, Neurosurgery & Psychiatry*, *84*(8), 875-882. doi: 10.1136/jnnp-2012-304126

Zhao, N., Attrebi, O. N., Ren, Y., Qiao, W., Sonustun, B., Martens, Y. A., ... Bu, G. (2020). APOE4 exacerbates α-synuclein pathology and related toxicity independent of amyloid. *Science Translational Medicine*, *12*(529). doi: 10.1126/scitranslmed .aay1809

Zhou, J., Gennatas, E. D., Kramer, J. H., Miller, B. L., & Seeley, W. W. (2012). Predicting regional neurodegeneration from the healthy brain functional connectome. *Neuron*, *73*(6), 1216-1227. doi: 10.1016/j.neuron.2012.03.004